

FINITE-QUARK-MASS EFFECTS ON THE HIGGS PRODUCTION CROSS SECTION IN THE GLUON-GLUON FUSION CHANNEL

Von der Fakultät für Mathematik, Informatik und Naturwissenschaften der
RWTH Aachen University zur Erlangung des akademischen Grades eines
Doktors der Naturwissenschaften genehmigte Dissertation

vorgelegt von

Tom Claus Rudolf Schellenberger
aus
Hamburg

Berichter: Prof. Dr. Michał Czakon
Prof. Dr. Robert Harlander

Tag der mündlichen Prüfung: 31. Juli 2025

Diese Dissertation ist auf den Internetseiten der Universitätsbibliothek verfügbar.

Finite-Quark-Mass Effects on the Higgs Production Cross Section in the Gluon-Gluon Fusion Channel

© Tom Claus Rudolf Schellenberger 2025

GUTACHTER DER DISSERTATION:

Prof. Dr. Michał Czakon
Prof. Dr. Robert Harlander

ZUSAMMENSEZUNG DER PRÜFUNGSKOMMISSION:

Prof. Dr. Michał Czakon
Prof. Dr. Robert Harlander
Prof. Dr. Mario Berta
Prof. Dr. Achim Stahl

VORSITZENDER DER PRÜFUNGSKOMMISSION:

Prof. Dr. Achim Stahl

DATUM DER DOKTORPRÜFUNG:

31. Juli 2025

DEKAN DER FAKULTÄT MIN:

Prof. Dr. Carsten Honerkamp

ABSTRACT

This PhD thesis presents a comprehensive analysis of the impact of finite top- and bottom-quark masses on the Higgs production cross section via gluon-gluon fusion. Our study substantially reduces the uncertainties previously associated with these mass effects on the cross section. We also explore the implications of different mass renormalization schemes, delivering results for both the $\overline{\text{MS}}$ and on-shell renormalization schemes. Furthermore, we provide an in-depth comparison between the 4-flavor and 5-flavor schemes to address the treatment of finite quark masses. An additional novel aspect of our research is the examination of how finite quark masses affect the Higgs-rapidity spectrum. Finally, we offer well-founded recommendations to guide future experimental and phenomenological research in this field.

ZUSAMMENFASSUNG

Diese Dissertation präsentiert eine umfassende Analyse des Einflusses endlicher Top und Bottom Quarkmassen auf den Wirkungsquerschnitt von hadronischer Higgsproduktion im Gluon-Gluon-Fusionskanal. Unsere Studie verringert erheblich die zuvor mit diesen Masseeffekten verbundenen Unsicherheiten bezüglich des Wirkungsquerschnitts. Wir untersuchen außerdem die Auswirkungen verschiedener Massenrenormalisierungsschemata und liefern Ergebnisse sowohl für das $\overline{\text{MS}}$ - als auch das On-Shell-Renormalisierungsschema. Darüber hinaus bieten wir einen detaillierten Vergleich zwischen dem 4-Flavor- und dem 5-Flavor-Schema, um die Behandlung endlicher Quarkmassen zu adressieren. Ein neuartiger Aspekt unserer Forschung ist zudem die Untersuchung, wie sich endliche Quarkmassen auf das Higgspapidityspektrum auswirken. Schließlich geben wir fundierte Empfehlungen, um zukünftige experimentelle und phänomenologische Forschung in diesem Bereich zu leiten.

ACKNOWLEDGMENTS

First and foremost, I would like to thank my supervisor, Prof. Dr. Michał Czakon. I think it is fair to say that he is the person who taught me the most about physics. His insightful advice and expertise have been invaluable in shaping my research and helping me grow as a scholar.

I would further like to thank Felix Eschment, who not only jointly worked with me on many of the results presented in this thesis, but also shared an office with me for almost 4 years—a time I will always look back to fondly.

I also wish to express my gratitude to my other collaborators, Marco Niggetiedt and Rene Poncelet, without whom this work would not have been possible. I especially thank Marco for providing Figs. 5.8 and 5.9.

Special thanks also go to Prof. Dr. Robert Harlander who second-supervised this thesis.

Furthermore, I would like to acknowledge the funding of my position by the Deutsche Forschungsgemeinschaft (DFG) under grant 396021762-TRR 257: Particle Physics Phenomenology after the Higgs Discovery, and grant 400140256-GRK 2497: The Physics of the Heaviest Particles at the LHC. Also, this work would not have been possible without the computing time provided at the NHR Center NHR4CES at RWTH Aachen University (project number p0020025). This is funded by the Federal Ministry of Education and Research, and the state governments participating on the basis of the resolutions of the GWK for national high performance computing at universities (www.nhr-verein.de/unsere-partner).

Last but not least, I would like to thank my family and my friends for their unwavering support. Your love and encouragement has helped me so much throughout my life, and I feel extremely grateful to have you in my life.

I especially, like to thank my father, to whom I dedicate this thesis. He was the role model throughout my life, and it is because of him that I found my love for physics.

PUBLICATIONS

During my PhD studies, I co-authored the following publications:

- [1] Michał Czakon, Felix Eschment, and Tom Schellenberger. “Revisiting the double-soft asymptotics of one-loop amplitudes in massless QCD.” In: *JHEP* 04 (2023), p. 065. DOI: [10.1007/JHEP04\(2023\)065](https://doi.org/10.1007/JHEP04(2023)065). arXiv: [2211.06465 \[hep-ph\]](https://arxiv.org/abs/2211.06465)
- [2] Michał Czakon, Felix Eschment, and Tom Schellenberger. “Subleading effects in soft-gluon emission at one-loop in massless QCD.” In: *JHEP* 12 (2023), p. 126. DOI: [10.1007/JHEP12\(2023\)126](https://doi.org/10.1007/JHEP12(2023)126). arXiv: [2307.02286 \[hep-ph\]](https://arxiv.org/abs/2307.02286)
- [3] Michał Czakon et al. “Top-Bottom Interference Contribution to Fully Inclusive Higgs Production.” In: *Phys. Rev. Lett.* 132.21 (2024), p. 211902. DOI: [10.1103/PhysRevLett.132.211902](https://doi.org/10.1103/PhysRevLett.132.211902). arXiv: [2312.09896 \[hep-ph\]](https://arxiv.org/abs/2312.09896)
- [4] Michał Czakon et al. “Quark mass effects in Higgs production.” In: *JHEP* 10 (2024), p. 210. DOI: [10.1007/JHEP10\(2024\)210](https://doi.org/10.1007/JHEP10(2024)210). arXiv: [2407.12413 \[hep-ph\]](https://arxiv.org/abs/2407.12413)

Among these, only the last two are directly relevant to this dissertation.

My personal contributions to the work presented here are described in detail in chapter 5. The only notable exceptions being the computation of the numerical grids for the real-virtual corrections with only one massive quark, and the adaptations for the 4FS.

CONTENTS

1	Introduction	1
2	Fundamentals	5
2.1	Cross Sections	5
2.1.1	The Hard Scattering Amplitude	5
2.1.2	The Parton Distribution Functions	8
2.1.3	The Phase-Space Integration	11
2.2	The Standard Model of Particle Physics	14
3	The Effective Higgs Potential & the Stability of our Universe	21
4	Hadronic Higgs Production	29
4.1	The Leading-Order Cross Section	31
4.2	The Heavy-Top Limit	35
4.2.1	Renormalization of Gauge Invariant Operators	36
4.2.2	Matching of Wilson Coefficients	43
4.2.3	Higher-Order Corrections	47
4.2.4	Phenomenological Application	52
4.3	Theory Status	54
4.3.1	Scale Uncertainties	56
4.3.2	PDF Uncertainties	59
4.3.3	Electroweak Corrections	62
4.3.4	Finite Top-Quark Mass Effects	63
4.3.5	Effect of Light Quarks	65
4.3.6	Differential Cross Sections	66
4.3.7	Summary	68
5	Computational Details	71
5.1	Computing the Amplitudes	71
5.1.1	The Real-Real Corrections	72
5.1.2	The Real-Virtual Corrections	73
5.1.3	The Virtual-Virtual Corrections	90
5.2	The 4-Flavour Scheme	94
5.3	$\overline{\text{MS}}$ -scheme	96
5.4	Performing the Phase-Space Integration	102
6	Results and Discussion	105
6.1	Total Cross Section	105
6.1.1	Effects of Finite Top-Quark Masses	105
6.1.2	Effects of Finite Bottom-Quark Masses	106
6.2	Differential Cross Section	112
6.3	Validation & Comparison With Other Works	114
6.4	Recommendations for Phenomenological Applications	116

7	Conclusions & Outlook	121
7.1	Conclusions	121
7.2	Outlook	122
A	Feynman Rules of the Standard Model	123
B	Feynman Integrals	127
C	Energy Scan of the Top-Bottom Interference Contribution	129
D	On-shell Results for the Differential Cross Section	131
	Bibliography	133

ACRONYMS

1PI	One-particle irreducible
BSM	Beyond the standard model
DM	Dark matter
DR	Dimensional regularization
FS	Flavor scheme
HEL	High-energy limit
HTL	Heavy-top limit
IBP	Integration-by-parts
IR	Infrared
LHC	Large hadron collider
LL	Leading logarithm
LME	Large mass expansion
LO	Leading order
MC	Monte-Carlo
MHOU	Missing higher order uncertainties
NLO	Next-to-leading order
NNLO	Next-to-next-to-leading order
OS	On-shell
PDF	Parton distribution function
QCD	Quantum chromodynamics
QED	Quantum electrodynamics
RG	Renormalization group
RGE	Renormalization group equation
rHTL	Rescaled heavy-top limit
SCET	Soft-collinear effective theory
SM	Standard model
SSB	Spontaneous symmetry breaking
UV	Ultraviolet
VEV	Vacuum expectation value

NOTATION, CONSTANTS AND CONVENTIONS

- In this thesis, I will be using the *Einstein summation convention*, by which any index—be it a Lorentz, color or flavor index—which appears twice is implicitly summed over.
- I will be using natural units

$$\hbar = c = 1. \quad (0.1)$$

- The electron charge is

$$-e, \quad e > 0. \quad (0.2)$$

- The metric is

$$g_{\mu\nu} = \begin{pmatrix} 1 & & & \\ & -1 & & \\ & & -1 & \\ & & & -1 \end{pmatrix}. \quad (0.3)$$

- The normalization of the Levi-Civita anti-symmetric tensor $\epsilon_{\mu\nu\rho\sigma}$ is

$$\epsilon_{0123} = +1 \quad (0.4)$$

- The Pauli matrices are defined as

$$\sigma^1 \equiv \begin{pmatrix} 0 & 1 \\ 1 & 0 \end{pmatrix}, \quad \sigma^2 = \begin{pmatrix} 0 & -i \\ i & 0 \end{pmatrix}, \quad \sigma^3 = \begin{pmatrix} 1 & 0 \\ 0 & -1 \end{pmatrix}, \quad \tau^i \equiv \sigma^i. \quad (0.5)$$

- Unless specifically specified otherwise we will use the following values for appearing physical constants

- $G_F = 1.16637 \times 10^{-5} \text{ GeV}^{-2}$
- $m_H = 125.00 \text{ GeV}$
- $m_t = 173.06 \text{ GeV}$
- $\overline{m}_t(\overline{m}_t) = 162.7 \text{ GeV}$
- $m_b = 4.78 \text{ GeV}$
- $\overline{m}_b(\overline{m}_b) = 4.18 \text{ GeV}$
- $\overline{m}_c(\overline{m}_c) = 1.27 \text{ GeV}$
- $m_Z = 91.1876 \text{ GeV}$
- We use the `NNPDF31_nnlo_as_0118` and `NNPDF31_nnlo_as_0118_nf_4` PDF set in the 5FS and 4FS respectively.
- α_s is extracted from the PDF set at the relevant scale.

1 | INTRODUCTION

After the great successes of quantum electrodynamics (QED), physicists in the 1950s sought a quantum field theoretical description of other fundamental forces, like strong and weak interactions. In 1954 Chen Ning Yang and Robert Mills proposed a theory which, similar to QED, relied on gauge invariance, but extended the idea to non-abelian gauge groups [5]. Although these theories provided a compelling foundation for encapsulating the strong and weak interactions under the banner of local gauge invariance, they also led to a conundrum: They theorized massless gauge bosons which were simply not there.

One way to resolve this problem is through the phenomenon of confinement pioneered by Murray Gell-Mann [6], and realized in quantum chromodynamics (QCD). Here, particles charged under the QCD gauge group are not observable at large distances since separating two colored particles will eventually trigger the creation of new particles, leading to the formation of color neutral states.

In 1961, Sheldon Glashow [7] and later Abdus Salam and John Ward [8] proposed models based on the $SU(2) \times U(1)$ gauge symmetry, which for the first time unified the electromagnetic and the weak interaction under a single theoretical framework. However, in their proposed models, the gauge symmetry was always explicitly broken by the masses of the gauge bosons. Consequently, their models turned out to be unrenormalizable.

The solution materialized in the early 1960s when several physicists—François Englert, Robert Brout [9], Peter Higgs [10], Gerald Guralnik, Carl Hagen, and Tom Kibble [11]—proposed spontaneous symmetry breaking (SSB) as a mechanism to impart mass to otherwise massless gauge bosons while preserving the core symmetry of the gauge theory. This so-called *Higgs mechanism* introduced a scalar field permeating spacetime that acquires a nonzero vacuum expectation value (VEV) that provided mass to the gauge bosons. Shortly afterward, Stephen Weinberg [12] applied the Higgs mechanism to the electroweak model and hence formulated the standard model (SM) of particle physics as we know and love it today¹.

A key prediction was the existence of a new particle, the *Higgs boson*, which would serve as empirical evidence of the models' validity. Yet, for decades, the Higgs boson remained the one missing piece of this otherwise extensively tested framework. It was not until 2012, using the unprecedented energies of the Large Hadron Collider (LHC) at CERN, that the ATLAS [13] and CMS [14] collaborations finally observed a new particle whose properties aligned with those predicted for the Higgs boson. This discovery not only completed the particle content of the SM but also confirmed how massive gauge bosons could arise naturally from gauge-invariant theories.

But all is not well in the SM. Although it is one of, if not the best tested model ever proposed, the SM has several shortcomings. For one, astrophysical and cosmological observations have collected an overwhelming amount of evidence for the existence of a new type of very weakly interacting matter, elusively called dark matter (DM). However, currently there is no member

¹ Though in his original publication, Weinberg did not include quarks since, famously, he did not believe in their existence at the time.

of the SM which could serve as a DM candidate. Since the masses of all fundamental particles in the SM are generated through the Higgs mechanism, it is plausible that at least a fraction of the DM's mass is generated in the same fashion. The Higgs boson thus takes a central place in the search for DM, as it might be the portal connecting the SM with the DM sector. One promising way to look for DM is therefore by searching for *invisible Higgs decays* [15, 16].

Another issue of the SM is related to the value of the Higgs mass itself. As it stands, radiative corrections result in an unstable Higgs potential [17], meaning that at some point there must be physics beyond the SM, which will at least meta-stabilize the potential. This implies that our universe could be in a meta-stable state and at some point in time transition into a vastly different universe.

Since this suggests that the Higgs is sensitive to some new physics scale, it also gives rise to another problem—the electroweak hierarchy problem. In a nutshell, it poses the question of why the Higgs mass is so much smaller than the Planck scale. If one were to believe that the SM is accurate up to the Planck scale, then perturbative corrections of the Higgs mass would make the bare Higgs mass quadratically sensitive to that scale. Hence, the renormalization constant must be fine-tuned to cancel this huge number, and render a renormalized mass at the electroweak scale. This huge cancellation seems unnatural to many physicists², and sparked lots of ideas for extensions of the SM, such as *supersymmetry*, *conformal models*, or *extra dimensions*. It should be noted though that all these models have been either excluded or have seen significant tension.

These selected examples demonstrate that Higgs research has not stopped with its discovery. On the contrary, the Higgs boson has proven to be a central figure in the search for physics beyond the Standard Model (BSM). Nevertheless, the absence of direct evidence for new physics at the LHC is likely going to persist in the near future. Physicists are therefore turning to more subtle signals, in the hope that BSM physics might hide behind small deviations from the SM. Since the Higgs discovery, the field of particle physics has thus transitioned into an era of precision measurements. This requires better colliders and detectors as well as highly sophisticated measurement strategies. But any comparison to the SM is rendered moot, if its predictions are not precise enough. Aware of this, theoretical particle physicists have launched an extensive program in the pursuit of improving the accuracy of our SM predictions.

A prime example of this pursuit can be seen in a central observable of Higgs physics phenomenology: *the gluon-gluon fusion Higgs production cross section*. First predicted by Georgi, Glashow, Machacek and Nanopoulos in 1978 [18] at leading order (LO), it has since been calculated at next-to-LO (NLO) [19, 20], next-to-NLO (NNLO) [21–23] and even next-to-NNLO ($N^3\text{LO}$) [24, 25], though the latter two were computed under the assumption of an infinitely heavy top quark. Today's cross section prediction is almost three times as large as what was originally proposed by Glashow et al., highlighting the importance of perturbative corrections in QCD. However, the story does not end here. The cross section has been pushed to next-to- $N^3\text{LO}$ ($N^4\text{LO}$) in the soft-virtual approximation [26], such that missing higher order uncertainties (MHOU) are now believed to be below 1.9% of the total cross section. Furthermore, electroweak corrections have been addressed both at LO [27, 28] and NLO QCD [29–34]. Finally, the cross section has been calculated without the assumption of an infinitely heavy top quark at NNLO [35].

Besides the MHOU, the largest source of uncertainty now stems from the light-quark induced Higgs production contribution. Here, the Higgs does not couple to the top quark, but to lighter quarks, like the bottom or charm quark. Since the coupling strength to the Higgs is proportional

² Myself excluded.

to the mass of the respective particle, these contributions are generally suppressed with respect to the top quark induced production channel. Nevertheless, for precision predictions, their contribution cannot be omitted. Recently, we reported results on this contribution at NNLO [3, 4], thereby eliminating this piece of uncertainty.

In this PhD thesis, we follow up on our previous work, explaining in detail the challenges of the computation and how we overcame them. Furthermore, we combine our findings with the above-mentioned contributions, and thoroughly investigate the associated uncertainties, to give a new best prediction for the gluon-gluon fusion cross section. This shall prove useful for any further research in Higgs physics phenomenology.

This thesis is structured as follows: In Chapter 2, we explain the basics of the SM and the Higgs mechanism. We also provide a roadmap on how to perform cross section calculations. The experienced reader may skip this chapter. Chapter 3 is dedicated to the Higgs potential, its perturbative corrections, and the resulting implications for our universe. Chapter 4 discusses the Higgs production cross section. We present simple LO and NLO cross section calculations. These introduce core concepts which will prove useful when going to NNLO. Since the heavy-top limit is so central for the gluon-gluon fusion cross section, we also thoroughly discuss it here. We conclude the chapter by providing an overview on the current status of the cross section. In Chapter 5, we discuss the computational details for the NNLO computation, before providing our results in Chapter 6. Finally, we give our conclusions and further outlook in Chapter 7.

2 | FUNDAMENTALS

2.1 CROSS SECTIONS

Cross sections offer the possibility to directly test the SM and many of the great successes of the SM are its cross section predictions. The cross section is simply defined as the probability to create some final state from some initial state per unit of time per target particle normalized by the incoming particle flux. This definition allows for straightforward measurement through counting experiments. For instance, experiments like CMS and ATLAS collide particles and count how often a particular final state is produced within a given time interval.

From a theoretical perspective, cross sections can be calculated using

$$d\hat{\sigma}_{ij \rightarrow n} = \frac{1}{F} d\Phi_n |\mathcal{M}_{ij \rightarrow n}|^2, \quad (2.1)$$

where F denotes the *flux factor*¹

$$F \equiv 4p_1 \cdot p_2, \quad (2.2)$$

$d\Phi_n$ is the *Lorentz invariant phase space measure*

$$d\Phi_n = \left[\prod_{i=1}^n \frac{d^4 q_i}{(2\pi)^4} (2\pi) \delta(q_i^2 - m_i^2) \Theta(q_i^0) \right] (2\pi)^4 \delta^{(4)} \left(p_1 + p_2 - \sum_{i=1}^n q_i \right), \quad (2.3)$$

and $\mathcal{M}_{ij \rightarrow n}$ is the *scattering amplitude* describing the short distance interactions.

The computation of cross sections involves three basic steps:

1. calculation of the hard scattering amplitude,
2. phase-space integration,
3. and the convolution with *parton distribution functions* (PDFs).

We will discuss each step in detail below.

2.1.1 The Hard Scattering Amplitude

The hard scattering amplitude describes the transition probability from a specific initial state to a particular final state. Since the scattering is **hard**, it implies that the energy transfer between particles during scattering is large compared to the QCD scale. Thus, we operate within the perturbative regime of QCD and can perform an expansion in terms of the coupling constant

$$\mathcal{M}_{ij \rightarrow n} = \alpha_s^{n_{\text{Born}}} \left(\mathcal{M}_{ij \rightarrow n}^{(0)} + \frac{\alpha_s}{\pi} \mathcal{M}_{ij \rightarrow n}^{(1)} + \left(\frac{\alpha_s}{\pi} \right)^2 \mathcal{M}_{ij \rightarrow n}^{(2)} + \mathcal{O}(\alpha_s^3) \right). \quad (2.4)$$

¹ In the following we assume that the initial-state particles are massless.

Here, n_{Born} denotes the power of the coupling constant at LO. One can of course perform a simultaneous expansion in the electromagnetic coupling constant α , however for processes involving color charged particles, the QCD corrections are typically much more significant due to the larger coupling strength of QCD. For high precision predictions, electroweak corrections are however important.

The coefficients in the series of Eq. (2.4) can be computed graphically using *Feynman rules*. These are the set of all allowed propagators and vertices together with the corresponding mathematical prescription. The Feynman rules for the complete SM are listed in Appendix A. To calculate the coefficient $\mathcal{M}_{ij \rightarrow n}^{(l)}$ for a specific process, one has to draw all possible connected and amputated Feynman diagrams with the initial state (i, j) and final state n which contain $2(n_{\text{Born}} + l)$ vertices². Then one uses the Feynman rules to get the mathematical translation, keeping in mind that momentum must be conserved at every vertex and also taking into account possible symmetry factors.

Beginning with $\mathcal{M}_{ij \rightarrow n}^{(1)}$, and in certain cases known as *loop induced processes*, even starting from $\mathcal{M}_{ij \rightarrow n}^{(0)}$, we will encounter loops within the diagrams. Inside a loop, the momentum of the edges cannot be uniquely determined through momentum conservation. Consequently, we must leave the momentum unspecified and integrate over all possible values. Typically, it is the computation of these *loop integrals* that makes the calculation of hard scattering amplitudes so challenging. A plethora of powerful techniques has been developed over the years to tackle this daunting task. Still, the computation of loop integrals remains a highly active field of research and two-loop amplitudes with 5 or more scales are only just becoming available. A detailed description of modern techniques is beyond the scope of this thesis. For a comprehensive overview see Ref. [36].

Loop integrals are notorious for exhibiting divergences. To tame these, we introduce *regulators*, i.e. we introduce a parameter such that the integral becomes a function of that parameter. For a suitable regulator, the integral will now converge if the regulator is set to an unphysical value, and exhibits a pole at the physical value. The most commonly used regularization scheme is *dimensional regularization* (DR). Here, we make the loop integral a function of the spacetime dimension by replacing

$$\int \frac{d^4 k}{(2\pi)^4} (\dots) \longrightarrow \bar{\mu}^{2\epsilon} \int \frac{d^d k}{(2\pi)^d} (\dots), \quad d \equiv 4 - 2\epsilon \in \mathbb{C}, \quad \gamma_E = 0.5772\dots \quad (2.5)$$

The dimensionally regularized integral satisfies the usual integral properties like linearity, translation invariance and rescaling. The mass scale,

$$\bar{\mu}^2 = \frac{\mu^2}{4\pi} e^{\gamma_E} \quad (2.6)$$

was introduced to retain the mass dimension of the integral to 4, while absorbing some common factors of loop integrals. The physical limit then corresponds to $\epsilon \rightarrow 0$. A divergent integral in four dimensions will hence have ϵ -poles in DR. The poles are categorized as *ultraviolet* poles if their origin are large loop momenta, i.e. the four dimensional integral diverges for $k \rightarrow \infty$. Further we categorize poles as *infrared* poles if the singularity arises from loop momenta which are either *soft* ($k \rightarrow 0$) or *collinear* ($k \cdot p_i \rightarrow 0$) to one of the external massless legs. UV and IR singularities are mutually exclusive since they originate from different regions of the phase space. This means that the poles do not multiply together, and we may only get a single UV

² Quartic vertices are counted twice.

pole per loop integration. The soft and collinear singularities are **not** exclusive, meaning that IR singularities can develop one double pole per loop integration.

The IR singularities cancel for inclusive observables as we shall discuss in detail in Section 2.1.3. UV poles, on the other hand, are removed through a method called *renormalization*. Renormalization hinges on the idea that the fields, constants, and masses we observe in nature are not necessarily the same as the ones in our Lagrangian. Instead, they are related through *renormalization constants*. In QCD for example, we have

$$\begin{aligned} A_\mu^{B,a} &= (Z_3^A)^{1/2} A_\mu^{R,a} \\ q^B &= Z_2^{1/2} q^R \\ g^B &= Z_g g^R \\ m^B &= Z_m m^R \end{aligned} \tag{2.7}$$

Here A is the gluon field, q denotes quark fields, g is the coupling constant of QCD, and m is the mass of the quark. In these equations B refers to *bare* quantities appearing within our Lagrangian while R signifies renormalized quantities that are finite by definition. In the SM, it can be shown [37, 38] that we can choose renormalization constants, such that *Green's functions*, i.e. vacuum expectation values of time ordered products of local renormalized fields, are free of UV divergences. Scattering amplitudes, generally do not depend on the unphysical fields, which is why the fields can be kept unrenormalized in this case. Since at LO Green's functions do not require renormalization, all renormalization constants are equal to the identity at this order.

The definition of the renormalization constants is not unique. Indeed, the renormalization constants were designed to absorb singularities, but the finite part is a priori unconstrained. We call a prescription which uniquely determines the renormalization constants a *renormalization scheme*. The most widely used renormalization scheme is the $\overline{\text{MS}}$ scheme. Here, beyond the leading 1 and a universal factor of $\bar{\mu}^{\epsilon\rho_i}$, the renormalization constants **only** consist of poles, i.e. the renormalization constants have the structure

$$Z_i(\alpha) = \bar{\mu}^{\epsilon\rho_i} \left(1 + \frac{z_1}{\epsilon} \frac{\alpha}{4\pi} + \left(\frac{z_{22}}{\epsilon^2} + \frac{z_{21}}{\epsilon} \right) \left(\frac{\alpha}{4\pi} \right)^2 + \dots \right). \tag{2.8}$$

ρ_i is the mass dimension of the operator in units of ϵ , so that the factor $\bar{\mu}^{\epsilon\rho_i}$ corrects for the mismatch in mass dimensions between the four-dimensional renormalized and the d -dimensional bare quantities. For example: the coupling constant g^B has mass dimension ϵ , hence the renormalized coupling g^R has mass dimension zero and $\rho_i = 1$.

$\overline{\text{MS}}$ -renormalized masses are generally different from the pole mass. The *on-shell* (OS) *renormalization* scheme is an alternative to the $\overline{\text{MS}}$ scheme specifically designed, such that the renormalized mass matches the pole mass. It is therefore the suitable choice for external particles that are asymptotically free. Bare quantities are independent of the chosen renormalization scheme. The invariance under the change of the renormalization scheme defines a group, the *renormalization group* (RG). In the $\overline{\text{MS}}$ scheme, the change from one scale $\bar{\mu}$ to another defines a continuous subgroup of the RG. This means we can formulate the invariance in terms of a differential equation

$$0 = \frac{d}{d \log \mu} a^B = a^R \frac{dZ_a^{\overline{\text{MS}}}}{d \log \mu} + Z_a^{\overline{\text{MS}}} \frac{da^R}{d \log \mu}, \tag{2.9}$$

where a could be a mass or a coupling. Eq. (2.9) is called the *renormalization group equation* (RGE), and it can be leveraged to determine the scale dependence—also called the *running*—of the observable.

The final step in calculating the hard scattering amplitude involves the application of the *Lehmann-Symanzik-Zimmermann* (LSZ) reduction formula. It relates the scattering amplitudes to Green's functions, and it is the reason why we only considered amputated Feynman diagrams. In practice, one just has to multiply each external field with the square root of the corresponding LSZ constant. These constants are defined as the proportionality factor between the propagator of the interacting and the free theory³. As such, they are numerically identical to the OS field renormalization constants.

2.1.2 The Parton Distribution Functions

In hadron collisions, the initial state is not made up of elementary particles, but are bound states thereof. This means that during an inelastic scattering event, the partons which take part in the short-range interaction only carry a fraction of the original hadron momentum

$$p_1 = x_1 P_1, \quad p_2 = x_2 P_2. \quad (2.10)$$

Here p_1 and p_2 denote the momenta of the partons, and P_1 and P_2 are the momenta of the hadrons. Since the momentum of the parton cannot be larger than that of the hadron, $x_{1,2}$ is restricted to be less than one. Furthermore, since the energy of the parton must be positive the momentum fraction must also be positive. Otherwise, the momentum fraction is a priori unconstrained. We therefore integrate over all allowed values of x_1 and x_2

$$\begin{aligned} d\sigma_{H_1 H_2 \rightarrow n}(S) &= \int_0^1 dx_1 dx_2 \sum_{ij} f_{H_1,i}(x_1) f_{H_2,j}(x_2) d\hat{\sigma}_{ij \rightarrow n}(x_1 P_1, x_2 P_2, \mu_R) \\ &= \int_0^1 \frac{d\tau}{\tau} \sum_{ij} \mathcal{L}_{ij}(\tau) d\hat{\sigma}_{ij \rightarrow n}(\tau S, \mu_R), \end{aligned} \quad (2.11)$$

where $S = 2P_1 \cdot P_2$ is hadronic center-of-mass energy, and n denotes a certain final state. $f_{H_k,i}(x_k)$ are the (unrenormalized) *parton distribution functions* (PDFs). They describe the probability of finding a parton i with momentum fraction x_k inside the hadron H_k . Lorentz invariance of the partonic cross section allowed us to conclude that it can only depend on the partonic center-of-mass energy s

$$d\hat{\sigma}_{ij \rightarrow n}(x_1 P_1, x_2 P_2, \mu_R) = d\hat{\sigma}_{ij \rightarrow n}(x_1 x_2 S, \mu_R). \quad (2.12)$$

We then defined the *partonic luminosity*

$$\mathcal{L}_{ij}(\tau) \equiv (\tilde{f}_{H_1,i} \otimes \tilde{f}_{H_2,j})(\tau) \equiv \int_0^1 dx_1 dx_2 \tilde{f}_{H_1,i}(x_1) \tilde{f}_{H_2,j}(x_2) \delta(\tau - x_1 x_2), \quad (2.13)$$

where $\tilde{f}_{H,i}(x) \equiv x f_{H,i}(x)$, to arrive at the second line of Eq. (2.11).

At this stage the partonic cross section can still exhibit singularities whenever a final state parton becomes collinear to one of the initial-state partons. At LO for example, the divergence due to initial-state collinear emissions reads

$$d\hat{\sigma}_{ab \rightarrow cn}(s, \mu_R) \Big|_{\text{div.}} = -\frac{\alpha_s}{2\pi} \frac{1}{\epsilon} \int_0^1 dz \sum_d \left(P_{db}^{(0)}(z) d\hat{\sigma}_{ad \rightarrow n}(zs, \mu_R) + P_{da}^{(0)}(z) \hat{\sigma}_{db \rightarrow n}(zs, \mu_R) \right), \quad (2.14)$$

³ The interacting field theory might have an additional continuous spectrum.

where $P_{ij}^{(0)}$ are the LO *Altarelli-Parisi splitting kernels*⁴:

$$\begin{aligned} P_{qq}^{(0)}(x) &= C_F \left[\frac{1+x^2}{(1-x)_+} + \frac{3}{2}\delta(1-x) \right], \\ P_{qg}^{(0)}(x) &= T_F [x^2 + (1-x)^2], \\ P_{gg}^{(0)}(x) &= C_F \left[\frac{1+(1-x)^2}{x} \right], \\ P_{gg}^{(0)}(x) &= 2C_A \left[\frac{x}{(1-x)_+} + \frac{1-x}{x} + x(1-x) \right] + \delta(1-x)\frac{\beta_0}{2}. \end{aligned} \quad (2.15)$$

We absorb these collinear singularities into the PDFs through a process called *collinear renormalization*, by defining the renormalized PDFs $f_{H,i}(x, \mu_F)$ via

$$f_{H,i}(x) \equiv (Z_{ij}(\cdot, \mu_F) \otimes f_{H,j}(\cdot, \mu_F))(x). \quad (2.16)$$

Beyond the pole term, the renormalization constants are generally scheme dependent. From Eq. (2.14) we see that the $\overline{\text{MS}}$ renormalization constant at NLO are given by

$$Z_{ij}(z, \mu_R, \mu_F) = \delta(1-z)\delta_{ij} + \frac{\alpha_s}{2\pi} \frac{1}{\epsilon} P_{ij}^{(0)}(z) + \mathcal{O}(\alpha_s^2). \quad (2.17)$$

Now the sum

$$\sum_c d\sigma_{H_1 H_2 \rightarrow cn} + d\sigma_{H_1 H_2 \rightarrow n} \quad (2.18)$$

is guaranteed to be free of initial-state collinear divergences at NLO, if $d\sigma_{H_1 H_2 \rightarrow n}$ does not have these divergences at Born level.

Since the initial-state collinear divergences are of a completely different origin than the UV divergences, we introduce a new scale μ_F , called the factorization scale. This scale separates the long-distance (non-perturbative) physics contained in the PDFs from the short-distance (perturbative) physics contained in the partonic cross sections.

The factorization theorem (2.11) is central in the SM as it tells us that the PDFs are universal quantities, i.e. they are not specific to any one process. It is a postulate of the parton model, in which hadrons are thought of as a collection of free elementary particles. In QCD however, the theorem requires proof [41]! The PDF for all light partons are displayed in Fig. 2.1. In Fig. 2.2 we show the partonic luminosity for exemplary parton combinations. PDF's describe long range interactions, a regime in which QCD is non-perturbative. As such, PDFs are non-perturbative objects which have to be measured in experiments or be calculated non-perturbatively, e.g. on the lattice.

The factorization scale is unphysical in the sense that it is not a parameter in our theory, nor can it be measured in an experiment. As usual, we can apply the RGE to determine the running of the renormalized PDFs

$$0 = \frac{d}{d \ln \mu_F} f_{H,i}(x) = \frac{d}{d \ln \mu_F} (Z_{ij} \otimes f_{H,j}(\cdot, \mu_F))(x). \quad (2.19)$$

⁴ The definition of β_0 can be found in Eq. (4.71)

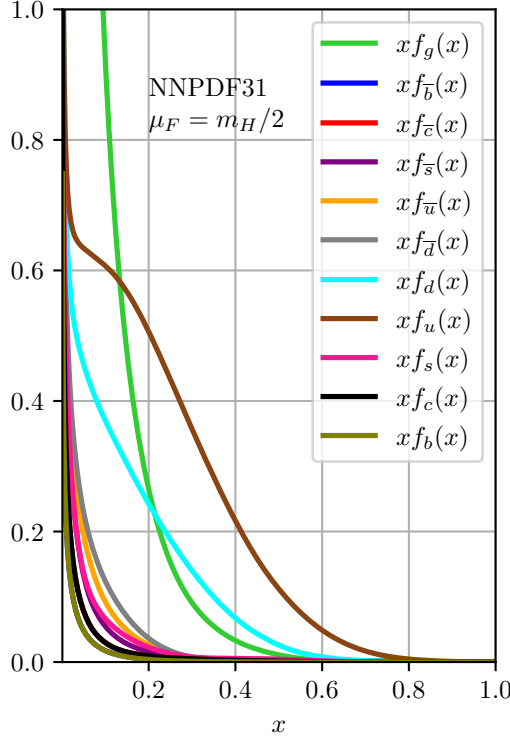


Figure 2.1: The various PDFs multiplied by x as a function of x . The plot was created using the LHAPDF6 [39] interface to the NNPDF31_nnlo_as_0118 [40] PDF set at a scale of $\mu_F = m_H/2$.

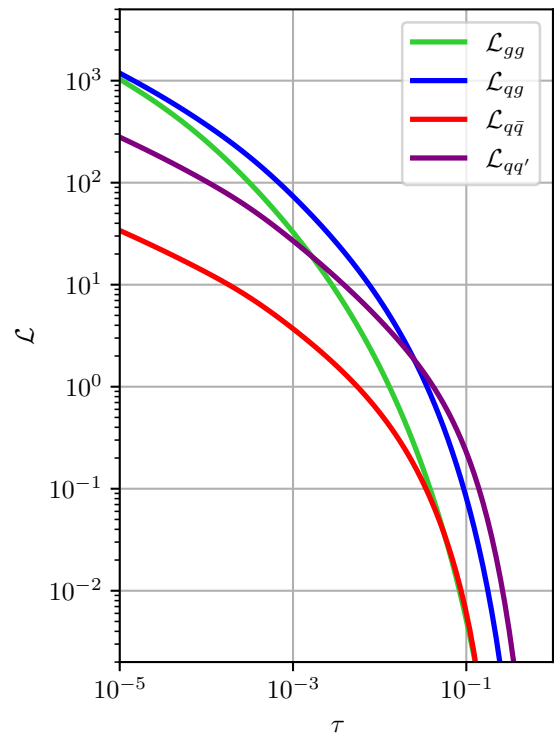


Figure 2.2: Displayed is the partonic luminosity for combinations of various partons. The luminosities are defined as $\mathcal{L}_{gg} = 2 \times \sum_i (\mathcal{L}_{q_i g} + \mathcal{L}_{\bar{q}_i g})$, $\mathcal{L}_{q\bar{q}} = 2 \times \sum_i \mathcal{L}_{q_i \bar{q}_i}$, $\mathcal{L}_{qq'} = \sum_{i,j} (\mathcal{L}_{q_i q_j} + \mathcal{L}_{q_i \bar{q}_j} + \mathcal{L}_{\bar{q}_i \bar{q}_j}) - \mathcal{L}_{q\bar{q}}$. The setup is the same as in Fig. 2.1.

This can be rewritten to

$$\begin{aligned} \frac{df_{H,i}(x, \mu_F)}{d \ln \mu_F} &= 2\alpha_s \left(Z_{ij}^{-1} \otimes \frac{dZ_{jk}^{(1)}}{d\alpha_s} \otimes f_{H,k}(\cdot, \mu_F) \right) (x) \\ &= \frac{\alpha_s}{\pi} \left(P_{ij}^{(0)} \otimes f_{H,j}(\cdot, \mu_F) \right) (x) + \mathcal{O}(\alpha_s^2), \end{aligned} \quad (2.20)$$

where $Z_{ij}^{(1)}$ is the residue of the renormalization constant. So even though the PDFs are not perturbative, their dependence on the factorization scale is. Eq. (2.20) is the famous *Dokshitzer-Gribow-Lipatow-Altarelli-Parisi-evolution equation* (DGLAP equations) [42–44].

In the derivation above, we have treated the partons inside the hadrons as massless, which leads to real collinear singularities. In reality, all quarks have finite masses, so the phase-space integration only yields logarithmic mass enhancements of the form $\ln(s/m_q^2)$ instead of actual singularities. The DGLAP equations then automatically resum these logarithms. For most applications at the LHC, the typical hard scattering scale is orders of magnitudes larger than all quark masses except for the top-quark mass. It is therefore beneficial to treat them as massless partons, as the appearance of the large logarithms would otherwise completely destroy the perturbative convergence. However, treating quarks as massless also implies that we neglect their mass-dependent effects in the hard-scattering matrix elements. If the scattering process is sensitive to the quark masses—for example, in processes involving Higgs couplings to quarks—these mass effects might be lost.

The number of quark flavors treated as active (massless) partons defines our *flavor scheme* (FS). For instance, if we treat the lightest four flavors (up, down, strange, charm) as massless, while considering the bottom and top quarks as massive, we are working in the 4FS. Analogously, if the bottom quark is also considered massless, we are working in the 5FS, and so on.

2.1.3 The Phase-Space Integration

Even after renormalization and collinear renormalization can the amplitude exhibit divergences. The scattering amplitude in and of itself is not a physical observable; therefore, it is not required to be finite. Physical observables are cross sections, which are obtained by performing phase-space integrations over the squared amplitudes. However, even after integrating over the phase space, the cross section is not guaranteed to be finite. The reason is that the Born process is indistinguishable from processes with additional infrared radiation. Indeed, no matter how precise a detector is, below a certain resolution, it becomes impossible to detect a very soft photon or to distinguish two highly collinear jets. Hence, computing a cross section with a fixed final state does not make physical sense. Instead, one must consider sufficiently inclusive observables—so called *IR-safe observables*. For these, Kinoshita, Lee and Nauenberg proved that in unitary theories all IR singularities cancel [45, 46]. This is known as the Kinoshita-Lee-Nauenberg (KLN) theorem.

An example of an observable which is trivially IR safe is the fully inclusive cross section

$$\hat{\sigma}_{ij \rightarrow n+X} = \sum_{k=1}^{\infty} \hat{\sigma}_{ij \rightarrow n+k}, \quad \text{for } \hat{\sigma}_{ij \rightarrow n}^{(0)} \text{ finite,} \quad (2.21)$$

where $n+k$ indicates that in addition to the final state n we now have k massless partons of whatever flavor. In perturbation theory, the infinite sum is truncated at a given order and each order

$$\hat{\sigma}_{ij \rightarrow n+X}^{(l)} = \sum_{k=0}^l \hat{\sigma}_{ij \rightarrow n+k}^{(l-k)}, \quad (2.22)$$

summed together with the contribution from collinear renormalization will be finite. For example at NLO, the finite inclusive cross section reads

$$\hat{\sigma}_{ij \rightarrow n+X}^{(1)} = \hat{\sigma}_{ij \rightarrow n}^R + \hat{\sigma}_{ij \rightarrow n}^V + \hat{\sigma}_{ij \rightarrow n}^C, \quad (2.23)$$

where

$$\hat{\sigma}_{ij \rightarrow n}^R = \frac{1}{F} \int d\Phi_{n+1} \sum_c |\mathcal{M}_{ij \rightarrow n+c}^{(0)}|^2 \quad (2.24)$$

is the real correction,

$$\hat{\sigma}_{ij \rightarrow n}^V = \frac{1}{F} \int d\Phi_n 2\text{Re} \left(\left(\mathcal{M}_{ij \rightarrow n}^{(0)} \right)^* \mathcal{M}_{ij \rightarrow n}^{(1)} \right) \quad (2.25)$$

is the virtual correction, and

$$\hat{\sigma}_{ij \rightarrow n}^C = \frac{1}{F} \int d\Phi_n \frac{\alpha_s}{2\pi} \frac{1}{\epsilon} \left(\frac{\mu_R^2}{\mu_F^2} \right)^\epsilon \sum_c \int_0^1 dz \left[P_{ci}^{(0)}(z) |\mathcal{M}_{cj \rightarrow n}^{(0)}|^2 + P_{cj}^{(0)}(z) |\mathcal{M}_{ic \rightarrow n}^{(0)}|^2 \right] \quad (2.26)$$

are the corrections from collinear renormalization. Figure 2.3 provides a pictorial representation of the required partonic cross sections for Higgs boson production in the gluon-gluon fusion channel at various perturbative orders.

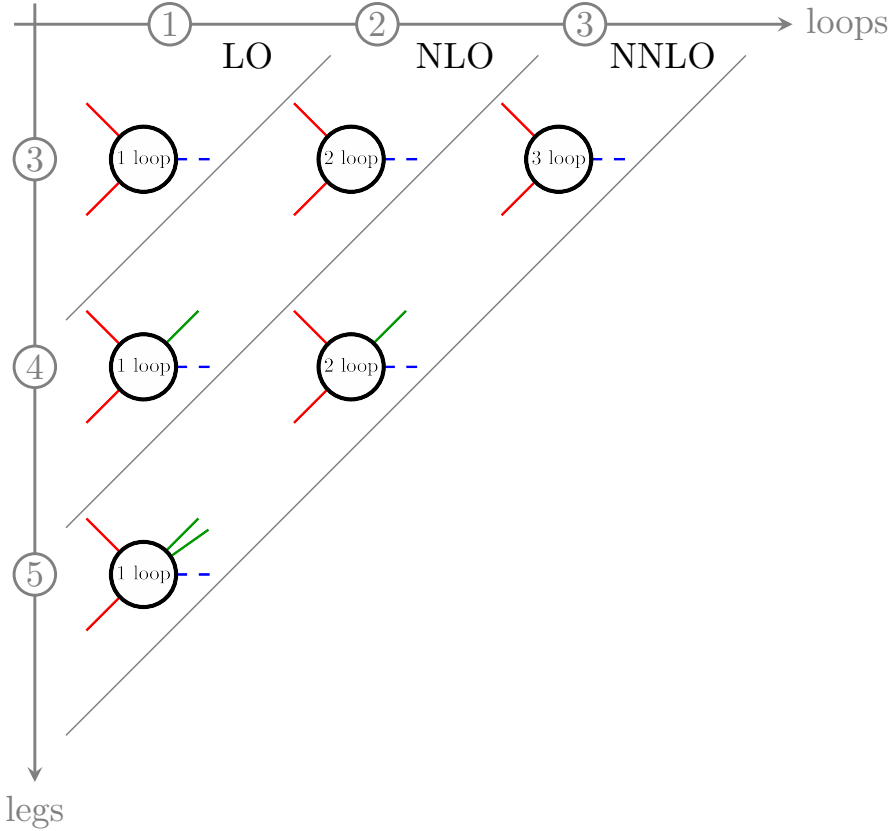


Figure 2.3: Pictorial representation of the needed partonic cross sections at various perturbative orders of the fully inclusive hadronic cross section. The graphic shows the example of Higgs production in the gluon-gluon fusion channel.

Although the sum of the contributions to the cross section is guaranteed to be finite due to the KLN theorem, the presence of IR singularities in the individual terms poses significant challenges for practical calculations. These singularities prevent a straightforward evaluation of the phase-space integrals. To overcome this, we once again have to introduce regulators (such as DR) to make the integrals well-defined. Over the years, numerous techniques have been developed to compute phase-space integrals efficiently. These techniques can generally be categorized into two main types: *Analytic methods*, and *numerical methods*.

As the name suggests, in the former class, the phase-space integrals are solved analytically. One noteworthy member of this class is the *reverse-unitarity method* [23], which was first applied to Higgs production in the gluon-gluon fusion channel. The method uses unitarity, to rewrite the phase-space integrals in terms of loop integrals over cut-propagators. One can then apply the remarkable techniques developed for Feynman integrals to these phase-space integrals and solve them analytically. The major downside of this approach is that it is highly process and observable dependent, meaning that for every process and every observable we have to start over from scratch. Furthermore, by the very nature of the method, you are always restricted to inclusive jet observables. Nevertheless, it has been successfully applied to, among others, Higgs-rapidity and Higgs- p_T distributions [47].

Among the numerical methods, there are two major approaches: *slicing* and *subtraction methods*. The former rely on a variable that isolates the IR-sensitive region of the phase space. Consider once again the example of Higgs production. Here, the IR-sensitive region of the

phase space corresponds to configurations where the transverse momentum of the Higgs boson, p_T , approaches zero. The phase-space integral can then be decomposed into

$$\int_0^{p_T} dk_T d\hat{\sigma}_{ij \rightarrow H+c} = \int_0^{p_T^{\text{cut}}} dk_T d\hat{\sigma}_{ij \rightarrow H+c} + \int_{p_T^{\text{cut}}}^{p_T} dk_T d\hat{\sigma}_{ij \rightarrow H+c}. \quad (2.27)$$

The second integral on the right-hand side is now finite and can be computed numerically, e.g. using *Monte-Carlo* (MC) techniques. If we choose p_T^{cut} small enough, then we can approximate the integrand in the first integral by its IR limit and solve the integral analytically. The pole of the integral should then cancel against the poles in the virtual integration and the counter term from collinear renormalization. The major advantage of this method is its simplicity. One big downside is its dependence on the unphysical cutoff scale. Ideally it is chosen very small such that the approximation introduces little to no error. But if chosen too small, the integrations will have huge logarithmic enhancements which can easily spoil the numerical precision. Another disadvantage is that not all processes or observables have easily identifiable slicing variables, or the analytic integration is very challenging. For example, p_T slicing only works for color singlet production, indeed if we have a jet in the final state, we can encounter collinear divergences also at finite transverse momenta of the jet. For processes involving jets, a possible slicing variable is the N -jettiness

$$\mathcal{T}_N \equiv \sum_k \min_i \left\{ \frac{2p_i \cdot q_k}{Q_i} \right\}, \quad (2.28)$$

with N , the number of jets, q_k , the momenta of the unresolved partons, p_i , the momenta of the resolved jets, and Q_i a normalization factor which can for example be set to the jet energy. However, in this instance the analytic integration below the cutoff becomes highly non-trivial and is a matter of active research. Currently, the N -jettiness beam functions are known at $N^3\text{LO}$ [48], the 0-jettiness soft function is known at $N^3\text{LO}$ [49, 50], and NNLO 1-jettiness soft functions and jet functions are known as well [51–54].

Subtraction methods, on the other hand, work by subtracting the infrared limits at the integrand level. In the *Frixione-Kunszt-Signer subtraction scheme* (FKS subtraction scheme) [55], one first isolates the IR divergence by partitioning the phase space into *sectors* using *selector functions*. These functions isolate specific infrared limits by approaching unity when a particular limit is approached (e.g. when an unresolved parton becomes soft or collinear), and vanish in other limits. For a single unresolved parton, a possible selector function is

$$\mathcal{S}_{n+1,k} \equiv \frac{1}{d_{n+1,k}} \left(\sum_j \frac{1}{d_{n+1,j}} \right)^{-1}, \quad \text{where} \quad d_{n+1,k} \equiv \left(\frac{E_{n+1}}{\sqrt{s}} \right)^\alpha (1 - \cos \theta_{n+1,k})^\beta. \quad (2.29)$$

The first index $n+1$ is the index of the unresolved parton, while the second index is the index of the reference parton. E_{n+1} denotes the energy of the unresolved parton, this factor therefore identifies soft singularities. Consequently, the power α can be set to zero if the unresolved parton is a quark. Other than that, the powers must be strictly positive $\alpha, \beta > 0$. If the $n+1$ -parton now becomes collinear to one of the other partons, say parton i , then the selector function $\mathcal{S}_{n+1,i}$ will approach one. And since the selector functions are strictly positive and form a decomposition of unity

$$\sum_k \mathcal{S}_{n+1,k} = 1, \quad (2.30)$$

all other selector functions will go to zero simultaneously.

The real emission cross section can then be written as a sum over sectors:

$$\hat{\sigma}_{ij \rightarrow n+u} = \frac{1}{F} \sum_k \int d\Phi_{n+1} |\mathcal{M}_{ij \rightarrow n+u}^{(0)}|^2 \mathcal{S}_{n+1,k}. \quad (2.31)$$

Now say we found a way to factorize the phase space such that the IR limits of a specific sector are isolated (see for example Ref. [56]). Then in each sector, we will have two unit integrations over ξ and η which parameterize the soft and collinear limit respectively, i.e. if $\xi \rightarrow 0$, then the momentum of the unresolved parton goes to zero and if $\eta \rightarrow 0$, the unresolved parton will become collinear to the reference momentum of that sector. The amplitude has the singular scaling $|\mathcal{M}_{ij \rightarrow n+u}^{(0)}|^2 \sim \xi^{-2}\eta^{-1}$, leading to an integral of the form

$$\int_0^1 \frac{d\eta}{\eta^{1+\epsilon}} \frac{d\xi}{\xi^{1+2\epsilon}} f(\eta, \xi, \dots), \quad (2.32)$$

where f is a function regular in the limits $\eta, \xi \rightarrow 0$. If we now apply the distributional identity

$$\frac{1}{x^{1-\epsilon}} = \frac{1}{\epsilon} \delta(x) + \sum_{k=0} \frac{\epsilon^k}{k!} \left(\frac{\ln^k x}{x} \right)_+, \quad (2.33)$$

we can explicitly carry out all integrations.

The *sector improved residue subtraction scheme* [56–58] extends the FKS subtraction scheme to NNLO. As of today, it is the only subtraction scheme capable of computing any QCD phase-space integral. Beyond NNLO, developing efficient and general subtraction schemes remains an open challenge in perturbative QCD.

2.2 THE STANDARD MODEL OF PARTICLE PHYSICS

The SM of particle physics is a theory that describes all known matter and their fundamental interactions, except for gravity. It unifies the electromagnetic, weak, and strong forces under a single theoretical framework. The matter content of the SM is classified into two primary groups: *fermions* and *bosons*. The fermions have spin 1/2, they are further subcategorized into *quarks* and *leptons*. Quarks participate in strong interactions, while leptons interact only via the electromagnetic and weak forces. In contrast, bosons have integer spin. There exists a single particle with spin 0—the Higgs boson—and four vector bosons, namely the gluon, the photon, and the W and Z bosons. The vector bosons act as force carrier for the strong, electromagnetic, and weak force respectively. Fermions are organized into three generations, with each generation containing two types of quarks (up-type and down-type) and two leptons (a charged lepton and its corresponding neutrino). These generations are shown in Fig. 2.4, along with their masses, charges, and spins.

The interactions between SM particles are described by a non-abelian gauge theory of the $SU(3)_C \times SU(2)_L \times U(1)_Y$ group. Here, $SU(3)_C$ governs the strong interactions. It applies to all *colored* particles, i.e. quarks and gluons. The quarks transform under the fundamental representation of the $SU(3)_C$ group, whereas the gluons—or more precisely its field strength

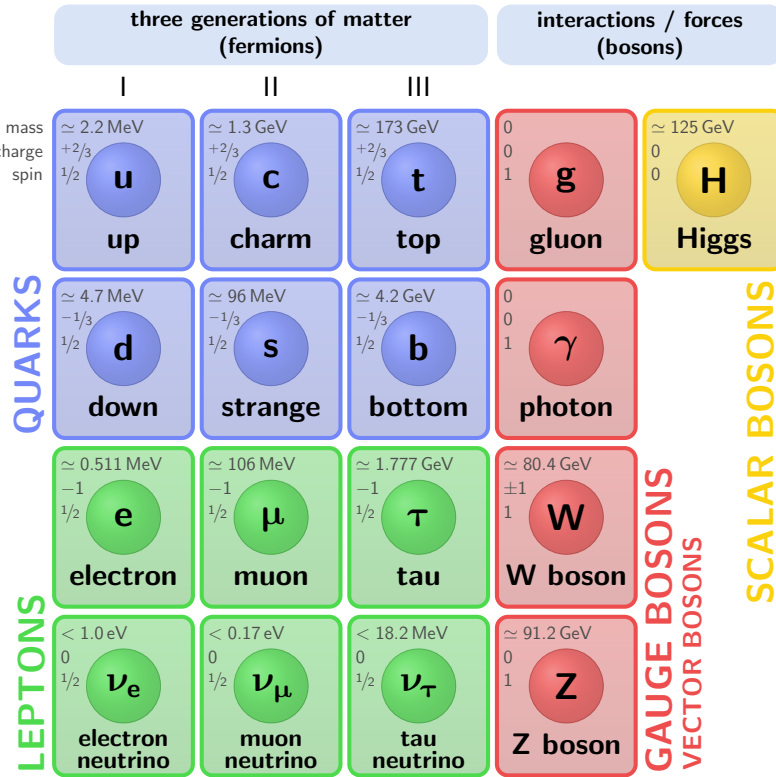


Figure 2.4: Elementary particles of the SM. The image was generated with the help of Ref. [59].

tensor—transforms under the adjoint representation. $SU(2)_L \times U(1)_Y$ governs electroweak interactions. The *left-handed* fermions form doublets under the $SU(2)_L$ group

$$L_{iL} \equiv \begin{pmatrix} \nu_{iL} \\ l_{iL} \end{pmatrix}, \quad Q_{iL} \equiv \begin{pmatrix} u_{iL} \\ d_{iL} \end{pmatrix}, \quad (2.34)$$

$$\nu_i = (\nu_e, \nu_\mu, \nu_\tau), \quad l_i = (e, \mu, \tau), \quad u_i = (u, c, t), \quad d_i = (d, s, b),$$

while right-handed fermions are singlets under the same group. The phase transformation $U(1)_Y$ acts on all particles except right-handed neutrinos according to their quantum number, the *hypercharge* Y .

The $SU(3)_C \times SU(2)_L \times U(1)_Y$ gauge symmetry is spontaneously broken into $SU(3)_C \times U(1)_Q$, where the $U(1)_Q$ group corresponds to gauge transformation of the electromagnetic interaction, hence the subscript Q indicating the *electric charge*. To ensure that the particles have the correct charges, the hypercharge must satisfy the *Gell-Mann–Nishijima relation*:

$$\frac{Y}{2} = Q - I^3. \quad (2.35)$$

With the particle charges displayed in Fig. 2.4, we find that the hypercharges of the SM particles are:

	L_{iL}	Q_{iL}	ν_{iR}	l_{iR}	u_{iR}	d_{iR}
$\frac{Y}{2}$	$-\frac{1}{2}$	$\frac{1}{6}$	0	-1	$\frac{2}{3}$	$-\frac{1}{3}$

The transformation properties of the gauge bosons is dictated by the covariance of the covariant derivative

$$D_\mu \equiv \partial_\mu - ig A_\mu^a T_R^a - ig_2 W_\mu^a I^a + ig_Y \frac{Y}{2} B_\mu$$

$$T_R^a = \begin{cases} T^a & \text{for quarks,} \\ 0 & \text{for leptons,} \end{cases} \quad I^a = \begin{cases} \frac{\tau^a}{2} & \text{for left-handed fermions,} \\ 0 & \text{for right-handed fermions,} \end{cases} \quad (2.36)$$

where T^a and τ^a are the *Gell-Mann* and *Pauli* matrices.

Before spontaneous symmetry breaking, the Lagrangian which governs the evolution of all matter fields must be invariant under the $SU(3)_C \times SU(2)_L \times U(1)_Y$ gauge group. Up to a \mathbb{CP} violating term⁵ the SM Lagrangian is the most general mass-dimension four Lagrangian for the described particle content which respects the above described gauge symmetries

$$\mathcal{L}_{\text{SM}} = \mathcal{L}_G + \mathcal{L}_F + \mathcal{L}_Y + \mathcal{L}_H. \quad (2.37)$$

The gauge-field Lagrangian \mathcal{L}_G describes the free propagation and in the case of the non-abelian groups $SU(3)_C$ and $SU(2)_L$ also the self-interaction of the gauge bosons. It is given by

$$\mathcal{L}_G = -\frac{1}{4} G_{\mu\nu}^a G^{a\mu\nu} - \frac{1}{4} W_{\mu\nu}^a W^{a\mu\nu} - \frac{1}{4} B_{\mu\nu} B^{\mu\nu},$$

$$G_{\mu\nu}^a \equiv \partial_\mu A_\nu^a - \partial_\nu A_\mu^a + g f^{abc} A_\mu^b A_\nu^c,$$

$$W_{\mu\nu}^a \equiv \partial_\mu W_\nu^a - \partial_\nu W_\mu^a + g_2 \epsilon^{abc} W_\mu^b W_\nu^c,$$

$$B_{\mu\nu} \equiv \partial_\mu B_\nu - \partial_\nu B_\mu. \quad (2.38)$$

The propagation of the fermions and their interaction with the gauge bosons is described by

$$\mathcal{L}_F = \bar{L}_{iL} i \not{D} L_{iL} + \bar{\nu}_{iR} i \not{D} \nu_{iR} + \bar{l}_{iR} i \not{D} l_{iR} + \bar{Q}_{iL} i \not{D} Q_{iL} + \bar{u}_{iR} i \not{D} u_{iR} + \bar{d}_{iR} i \not{D} d_{iR}. \quad (2.39)$$

The Higgs field is a doublet of the $SU(2)_L$ group. We want the field to acquire a non-vanishing VEV to dynamically generate the fermion and boson masses. Of course, the vacuum cannot carry an electric charge, which means that the Higgs field must be electrically neutral along the direction of SSB. We choose this to be the second component of the doublet. With the Gell-Mann–Nishijima relation we can then deduce that hypercharge of the doublet must be $Y = +1$. The Higgs doublet field thus takes the form

$$\Phi = \begin{pmatrix} \phi^+ \\ \phi^0 \end{pmatrix}, \quad (2.40)$$

where the superscript indicates the electric charge.

In order to generate a non-vanishing VEV, the Higgs field must be in a potential with a global minimum away from zero. Hence, the only gauge invariant mass-dimension four Lagrangian we can construct is

$$\mathcal{L}_H = (D_\mu \Phi)^\dagger (D^\mu \Phi) - V(\Phi) \quad (2.41)$$

$$V(\Phi) = \lambda (\Phi^\dagger \Phi)^2 - \mu^2 \Phi^\dagger \Phi, \quad \mu^2, \lambda > 0.$$

⁵ The absence of the \mathbb{CP} violating term $\theta \frac{g^2}{64\pi^2} \epsilon^{\mu\nu\alpha\beta} F_{\mu\nu}^a F_{\alpha\beta}^a$ is an unsolved problem of particle physics, known as the strong CP problem.

The restriction $\lambda > 0$, comes from the stability constrain of the potential, whereas $\mu^2 > 0$ is necessary in order to ensure that the global minimum of the potential is not at zero but at

$$\Phi_0^\dagger \Phi_0 = \frac{\mu^2}{2\lambda} \equiv \frac{v^2}{2} \neq 0. \quad (2.42)$$

After SSB we can expand the Higgs field around its minimum

$$\Phi = \begin{pmatrix} \phi^+ \\ \frac{1}{\sqrt{2}}(v + H + i\xi) \end{pmatrix}. \quad (2.43)$$

The real scalar field H is the famous Higgs boson, whereas the fields ϕ^\pm and ξ are unphysical since they can always be eliminated through a gauge transformation. Such a gauge fixing condition is called a unitarity gauge, and since the ϕ^\pm and ξ bosons decouple they are also called *would-be Goldstone bosons*. For calculations beyond tree-level it is however often advantageous to choose a non-physical gauge, in which these unphysical particles are not decoupled. After inserting the expansion in the Higgs Lagrangian, the mass of the Higgs can be read off from its square term, yielding

$$m_H = \sqrt{2}\mu. \quad (2.44)$$

SSB enables the generation of vector boson masses without breaking the gauge symmetry explicitly. If we insert the expanded Higgs field in the Higgs Lagrangian, we get quadratic terms of the gauge boson fields

$$\begin{aligned} \mathcal{L}_H &\supseteq \frac{v^2}{2} \left\{ g_2^2 \begin{pmatrix} 0 & 1 \end{pmatrix} I^a I^b \begin{pmatrix} 0 \\ 1 \end{pmatrix} W_\mu^a W^{b\mu} - g_2 g_Y \begin{pmatrix} 0 & 1 \end{pmatrix} I^a \begin{pmatrix} 0 \\ 1 \end{pmatrix} W_\mu^a B^\mu + \frac{g_Y^2}{4} B_\mu B^\mu \right\} \\ &= \frac{v^2}{2} \left\{ \frac{g_2^2}{4} [(W^1)^2 + (W^2)^2] + \frac{1}{4} \begin{pmatrix} B^\mu & W^{3\mu} \end{pmatrix} \begin{pmatrix} g_Y^2 & g_Y g_2 \\ g_Y g_2 & g_2^2 \end{pmatrix} \begin{pmatrix} B_\mu \\ W_\mu^3 \end{pmatrix} \right\}. \end{aligned} \quad (2.45)$$

The physical states can now be extracted by diagonalizing the mass matrix

$$\begin{pmatrix} A_\mu^\gamma \\ Z_\mu \end{pmatrix} = \begin{pmatrix} \cos \theta_W & -\sin \theta_W \\ \sin \theta_W & \cos \theta_W \end{pmatrix} \begin{pmatrix} B_\mu \\ W_\mu^3 \end{pmatrix}, \quad \cos \theta_W = \frac{g_2}{\sqrt{g_Y^2 + g_2^2}}, \sin \theta_W = \frac{g_Y}{\sqrt{g_Y^2 + g_2^2}}. \quad (2.46)$$

In this new basis, we have one massless boson A_μ^γ , which we identify as the photon and a charge neutral boson of mass

$$m_Z = \frac{v}{2} \sqrt{g_Y^2 + g_2^2}. \quad (2.47)$$

The vector bosons W^1 and W^2 are not eigenstates of the charge operator. We therefore define the new states

$$W_\mu^\pm = \frac{1}{\sqrt{2}} (W_\mu^1 \mp iW_\mu^2), \quad QW_\mu^\pm = \pm W_\mu^\pm, \quad (2.48)$$

which are eigenstates of Q and have mass

$$m_W = \frac{v}{2} g_2. \quad (2.49)$$

Last but not least, we discuss the Yukawa sector of the SM Lagrangian. Before SSB, fermions cannot generate masses because a mass term would mix the left- and right-handed components

of the fields, thereby breaking the chiral gauge symmetry. Here, once again, the Higgs field comes to the rescue: by coupling the fermions with the Higgs field through a Yukawa interaction⁶

$$\mathcal{L}_Y = - \left(y_{ij}^\nu \bar{L}_{iL} \Phi^c \nu_{jR} + y_{ij}^l \bar{L}_{iL} \Phi l_{jR} + y_{ij}^d \bar{Q}_{iL} \Phi d_{jR} + y_{ij}^u \bar{Q}_{iL} \Phi^c u_{jR} \right) + \text{h.c.}, \quad (2.50)$$

where Φ^c is the charge-conjugated field to Φ , we do not explicitly break the symmetry. However, after SSB this Lagrangian will generate exactly the required mixing between left- and right-handed fields to generate the fermion masses. The Yukawa-interaction matrices $y_{ij}^{\nu,l,d,u}$ can be shifted from the Yukawa sector to the fermion sector through a field redefinition. Indeed, if we apply the *singular value decomposition* of the Yukawa matrix

$$y = U_L^\dagger y_{\text{diag}} U_R, \quad \text{with} \quad (y_{\text{diag}})_{ij} = \sqrt{2} Y_i \delta_{ij} \quad \text{and} \quad U_{L,R} \in \text{U}(3), \quad (2.51)$$

and redefine our fermion fields to be

$$f_{iR} \rightarrow U_{Rij} f_{jR}, \quad f_{iL} \rightarrow U_{Lij} f_{jL}, \quad f = \nu, l, u, d \quad (2.52)$$

the Yukawa Lagrangian becomes

$$\mathcal{L}_Y = - \sum_i (m_{\nu_i} \bar{\nu}_i \nu_i + m_{l_i} \bar{l}_i l_i + m_{u_i} \bar{u}_i u_i + m_{d_i} \bar{d}_i d_i) \left(1 + \frac{H}{v} \right). \quad (2.53)$$

Here we identified the Yukawa coupling as $Y_i = m_i/v$ in order to generate the required mass terms. Consequently, we observe that the Yukawa coupling of the Higgs to the fermions is proportional to the mass of that fermion. The field redefinition is a change from a flavor eigenbasis, which is diagonal in the couplings to the gauge bosons, to a mass eigenbasis. In the mass eigenbasis the part of fermion Lagrangian which contains the interaction to the electroweak gauge bosons after SSB is

$$\begin{aligned} \mathcal{L}_F \supseteq & \sum_f (-Q_f) e \bar{f}_i \not{A}^\gamma f_i + \sum_f \frac{e}{\sin \theta_W \cos \theta_W} \bar{f}_i (I_f^3 \gamma^\mu P_L - \sin^2 \theta_W Q_f \gamma^\mu) f_i Z_\mu \\ & + \frac{e}{\sqrt{2} \sin \theta_W} \left(\bar{u}_i \gamma^\mu P_L (V_{\text{CKM}})_{ij} d_j W_\mu^+ + \bar{d}_i \gamma^\mu P_L (V_{\text{CKM}}^\dagger)_{ij} u_j W_\mu^- \right) \\ & + \frac{e}{\sqrt{2} \sin \theta_W} \left(\bar{\nu}_i \gamma^\mu P_L (V_{\text{PMNS}}^\dagger)_{ij} l_j W_\mu^+ + \bar{l}_i \gamma^\mu P_L (V_{\text{PMNS}})_{ij} v_j W_\mu^- \right). \end{aligned} \quad (2.54)$$

Here we identified the electromagnetic coupling constant

$$e = \frac{g_2 g_Y}{\sqrt{g_2^2 + g_Y^2}}, \quad (2.55)$$

as the factor in front of the photon interaction term. The operators $P_{L,R}$ are just the projectors onto the left- and right-handed components

$$P_{L,R} = \frac{1 \mp \gamma^5}{2}. \quad (2.56)$$

The *CKM* and *PMNS matrices*⁷ are the results of the field redefinitions

$$V_{\text{CKM}} \equiv U_L^{u\dagger} U_L^d, \quad V_{\text{PMNS}} \equiv U_L^{l\dagger} U_L^\nu. \quad (2.57)$$

⁶ In the original formulation of the SM, there are no neutrino Yukawa interactions since they were believed to be massless. Neutrino oscillation experiments have shown however that neutrinos do in fact have finite masses.

⁷ Named after Cabibbo, Kobayashi and Maskawa, and Pontecorvo, Maki, Nakagawa and Sakata.

Typically, one prefers to work in the mass eigenbasis of the quarks, while the neutrinos are kept in the flavor eigenbasis, in which case one encounters flavor changes (*neutrino oscillations*) through propagation. This is why the PMNS matrix is defined in terms of the complex conjugate of the CKM matrix equivalent in the lepton sector.

Beyond LO, the fields, coupling constants and masses require renormalization in order to give finite cross section predictions. The corresponding renormalization constants are

$$\begin{aligned}
W_\mu^{B,a} &= (Z_3^W)^{1/2} W_\mu^{R,a}, \\
B_\mu^B &= (Z_3^Z)^{1/2} B_\mu^R, \\
\Phi^B &= (Z^\Phi)^{1/2} \Phi^R, \\
Q_{iL}^B &= (Z_{2i}^L)^{1/2} Q_{iL}^R, \\
u_{iR}^{B,a} &= (Z_{2i}^{u,R})^{1/2} u_{iR}^{B,a}, \\
d_{iR}^{B,a} &= (Z_{2i}^{d,R})^{1/2} d_{iR}^{B,a}, \\
g_Y^B &= Z_Y g_Y^R, \\
g_2^B &= Z_2 g_2^R, \\
(\mu^2)^B &= Z_{\mu^2} (\mu^2)^R, \\
\lambda^B &= Z_\lambda \lambda^R, \\
y_{ij}^{d,B} &= Z_{y,ij}^d y_{ij}^{d,R}, \\
y_{ij}^{u,B} &= Z_{y,ij}^u y_{ij}^{u,R}.
\end{aligned} \tag{2.58}$$

3

THE EFFECTIVE HIGGS POTENTIAL & THE STABILITY OF OUR UNIVERSE

Like all other quantities in the SM Lagrangian, the parameters dictating the shape of the Higgs potential (2.41) require renormalization when we go to higher orders of perturbation theory. It was noticed by Coleman and E. Weinberg [60] that these radiative corrections can significantly alter the potential, and by extension the whole SM. In the following, we want to investigate the effect of these loop corrections and answer a very important question: is the Higgs potential stable?

As we showed in Section 2.2, the Goldstone bosons are not physical particles since they can be absorbed by a suitable gauge choice. The study of the Higgs potential hence boils down to its dependence on the Higgs field component which is invariant under the gauge transformation. Following our previous convention, this means we only have to consider the real part of the second component of the Higgs field, i.e. only the real scalar field $\phi = \frac{1}{\sqrt{2}} \text{Re}\Phi_2$. When expressed in terms of this field, the Higgs sector of the Lagrangian becomes

$$\begin{aligned} \mathcal{L}_H &= \frac{1}{2} D_\mu \phi D^\mu \phi - V(\phi) \\ V(\phi) &= \frac{1}{2} \mu^2 \phi^2 - \frac{\lambda}{4} \phi^4. \end{aligned} \tag{3.1}$$

One can show that a sufficient condition for SSB is that a non-vanishing VEV be a stationary point of the effective action

$$\frac{\delta \Gamma[\phi]}{\delta \phi} = 0, \quad \phi \neq 0. \tag{3.2}$$

Where the effective action is defined as the Legendre transform of the generating functional for connected Green's functions $W[J]$, i.e.

$$Z[J] \equiv \mathcal{N} \int \mathcal{D}\phi e^{i(S[\phi] + J \cdot \phi)} = e^{iW[J]} = e^{i(\Gamma[\phi] + J \cdot \phi)}, \quad \phi \equiv \frac{\delta W}{\delta J}. \tag{3.3}$$

We then define the effective potential as

$$\Gamma[\phi] \equiv \int d^4x (-V_{\text{eff}}(\phi) + \dots), \tag{3.4}$$

where the omitted terms contain derivatives of ϕ . The effective potential is the natural extension of the tree-level potential (3.1) since the SSB condition now translates into the condition that ϕ be minimum of the potential

$$\frac{dV_{\text{eff}}}{d\phi} = 0, \quad \frac{d^2V_{\text{eff}}}{d\phi^2} > 0, \quad \phi \neq 0. \tag{3.5}$$

The effective action can now be expanded around some arbitrary field value ω

$$\Gamma[\phi] = \sum_{n=1}^{\infty} \frac{1}{n!} \int \prod_{i=1}^n [dx_i (\phi(x_i) - \omega)] \Gamma^{(n)}(x_1, \dots, x_n). \tag{3.6}$$

Although ω is often assumed to be the VEV, it need not be. $\Gamma^{(n)}$ denotes the n -th functional derivative of the effective action evaluated at ω . Ergo, it is the 1-particle-irreducible (1PI) Green's function $-i \langle \Omega | T\{\phi(x_1) \dots \phi(x_n)\} | \Omega \rangle$, but in a new theory in which ϕ has been replaced by $\phi - \omega$. Comparison of Eqs. (3.4) and (3.6) then yields¹

$$V_{\text{eff}} = - \sum_{n=1}^{\infty} \frac{1}{n!} \Gamma^{(n)}(p_i = 0) (\phi - \omega)^n. \quad (3.7)$$

Note that the 1PI Green's function is now in its momentum space representation. If we now differentiate with respect to ω and then set $\phi = \omega$ we get

$$\left. \frac{dV_{\text{eff}}}{d\omega} \right|_{\phi=\omega} = \Gamma^{(1)}(p = 0). \quad (3.8)$$

The right-hand side is now just the 1PI tadpole amplitude in the shifted theory. The effective potential can thus be obtained by integrating this amplitude over ω and equating the result at $\omega = \phi$.

As an example, let us consider the scalar contribution to the effective Higgs potential at one loop. In the first step, the field ϕ is shifted to $\phi - \omega$, yielding a potential of

$$V = -\frac{1}{2}\mu^2(\phi - \omega)^2 + \frac{1}{4}\lambda(\phi - \omega)^4. \quad (3.9)$$

The field ϕ hence acquires an effective mass of $\mu^2 - 3\lambda\omega^2$. Furthermore, the shifted theory has a three-point vertex with coupling constant $-6i\omega\lambda$ and a four point vertex with the same coupling strength as in the un-shifted theory. Next, we compute the scalar contribution to the one-loop one-point 1PI Green's function, i.e. the first tadpole diagram in Fig. 3.1, the result reads

$$\Gamma^{(1)}(p = 0) = \bar{\mu}^{2\epsilon} \frac{1}{2} \int \frac{d^d k}{(2\pi)^d} \frac{-6i\lambda\omega}{k^2 - \mu^2 + 3\lambda\omega^2}. \quad (3.10)$$

The factor $1/2$ is the symmetry factor of the diagram. According to Eq. (3.8), the effective

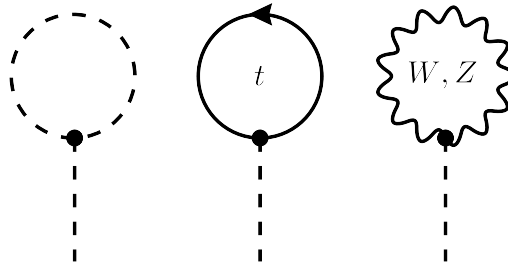


Figure 3.1: Tadpole Feynman diagrams at one loop. All Feynman diagrams in this thesis were created using **FeynGame** [61–63].

potential can now be obtained through integration over ω ,

$$V_{\text{eff}}^{(1)} \Big|_{\text{scalar}} = \frac{\mu_R^{2\epsilon}}{16\pi^2} e^{\epsilon\gamma_E} \int \frac{d^d k}{i\pi^{d/2}} \int^\phi d\omega \frac{3\lambda\omega}{k^2 - \mu^2 + 3\lambda\omega^2} = \frac{\mu_R^{2\epsilon}}{16\pi^2} e^{\epsilon\gamma_E} \int \frac{d^d k}{i\pi^{d/2}} \frac{1}{2} \ln \left(\frac{k^2 - \mu^2 + 3\lambda\phi^2}{k^2} \right). \quad (3.11)$$

¹ This can be seen easily after inserting Eq. (3.7) into (3.4). If one then takes functional derivatives in $\phi(x_i)$ and subsequently integrates over x_i , one regains the correct 1PI Green's function.

The lower bound of the ω integration is hereby irrelevant since it just results in a global shift of the potential. We chose the lower bound as $\sqrt{\mu^2/(3\lambda)}$ in order to have a particularly easy k -integration. To solve the k -integral, we perform a *Wick rotation* to Euclidean space, then the angular integration can be solved straightforwardly, resulting in

$$\begin{aligned} V_{\text{eff}}|_{\text{scalar}} &= \frac{\mu_R^{2\epsilon}}{16\pi^2} e^{\epsilon\gamma_E} \int_0^\infty dk_E k_E^{d-1} \ln\left(1 + \frac{\mu^2 - 3\lambda\phi^2}{k_E^2}\right) \int_{S_1^{d-1}} d\Omega \frac{1}{2\pi^{d/2}} \\ &= \frac{\mu_R^{2\epsilon}}{16\pi^2} e^{\epsilon\gamma_E} \int_0^\infty dk_E k_E^{d-1} \ln\left(1 + \frac{\mu^2 - 3\lambda\phi^2}{k_E^2}\right) \frac{1}{\Gamma(\frac{d}{2})} \\ &\stackrel{\text{IBP}}{=} \frac{\mu_R^{2\epsilon}}{16\pi^2} e^{\epsilon\gamma_E} \frac{2}{\Gamma(\frac{d}{2})} \int_0^\infty dk_E \frac{1}{d} k_E^{d-1} \frac{\mu^2 - 3\lambda\phi^2}{k_E^2 + \mu^2 - 3\lambda\phi^2} \\ &= \frac{\mu_R^{2\epsilon}}{16\pi^2} e^{\epsilon\gamma_E} \frac{1}{d\Gamma(\frac{d}{2})} (\mu^2 - 3\lambda\phi^2)^{d/2} \int_0^\infty dx x^{\frac{d}{2}-1} (1+x)^{-1} \end{aligned} \quad (3.12)$$

In the third line we integrated by parts. The boundary terms can be set to zero in dimensional regularization since we can always find a dimension for which the integrand vanishes suitably fast (here $d \in (0, 2)$), and then use analytic continuation to generalize to arbitrary dimensions. In the last step, we substituted $x = k_E^2/(\mu^2 - 3\lambda\phi^2)$. The resulting integral is *Euler's β -function* $B(\frac{d}{2}, 1 - \frac{d}{2})$. After expanding in ϵ , we find that the effective potential is

$$V_{\text{eff}}|_{\text{scalar}} = \frac{(\mu^2 - 3\lambda\phi^2)^2}{64\pi^2} \left[-\frac{1}{\epsilon} + \log\left(\frac{\mu^2 - 3\lambda\phi^2}{\mu_R^2}\right) - \frac{3}{2} + \mathcal{O}(\epsilon) \right]. \quad (3.13)$$

As usual, the poles can be removed through renormalization. The contributions from fermions and the vector bosons are computed analogously. The full one-loop effective potential in the $\overline{\text{MS}}$ scheme then reads

$$\begin{aligned} V_{\text{eff}} &= V_0 + V_1 \\ V_0 &= -\mu^2\phi^2 + \lambda\phi^4, \quad V_1 = \sum_i \frac{n_i}{64\pi^2} m_{i,\text{eff}}^4(\phi) \left[\log\left(\frac{m_{i,\text{eff}}^2(\phi)}{\mu_R^2}\right) - C_i \right], \end{aligned} \quad (3.14)$$

with $i = W, Z, t, H$ and

$$\begin{aligned} C_W &= C_Z = \frac{5}{6}, \quad C_t = C_H = \frac{3}{2}, \\ n_W &= 6, \quad n_Z = 3, \quad n_t = -12, \quad n_H = 1, \\ m_{W,\text{eff}}^2 &= \frac{1}{4}g_2^2\phi^2, \quad m_{Z,\text{eff}}^2 = \frac{1}{4}(g_2^2 + g_Y^2)\phi^2, \quad m_{t,\text{eff}}^2 = Y_t^2\phi^2, \quad m_{H,\text{eff}}^2 = \mu^2 - 3\lambda\phi^2. \end{aligned} \quad (3.15)$$

Numerically, the top quark has the largest impact on the radiative corrections, with smaller but significant corrections coming from the vector bosons. The Higgs self coupling is only of minor significance, due to the small value of λ , and only becomes relevant at smaller field values, where the constant μ^2 -term can become important.

The $\mu^2 = 0$ case is particularly interesting because it represents the only dimensionful parameter in the SM Lagrangian. If it could be set to zero, then the Lagrangian would be classically scale invariant, and all masses would be generated dynamically through radiative corrections. Models constructed under this assumption are called *conformal models*. They were fairly popular a couple of decades ago since the additional scaling symmetry would also solve the electroweak

hierarchy problem. If we assume $\mu^2 = 0$ and ignore the self-interaction of the Higgs, then the Higgs mass is easily calculable and reads

$$m_H^2 = \frac{3}{8\pi^2} v^2 \left[\frac{1}{16} (3g_2^4 + 2g_2^2 g_Y^2 + g_Y^4) - 4Y_t^4 \right]. \quad (3.16)$$

Unfortunately, the potential becomes unstable for top-quark masses above 125 GeV, and hence the model is not realized in nature.

If we want to study the stability of the Higgs potential, then we must look at its behavior at large field values. At large ϕ , logarithms of the form $\log(\phi^2/\mu_R^2)$ become large, and so our perturbative expansion becomes untrustworthy. To circumvent this, the appearing logarithms can be resummed to all orders by means of RGE methods. The potential cannot depend on the unphysical renormalization scale, and hence must satisfy

$$0 = \frac{dV(\phi)}{d \log \mu_R} = \left(\frac{\partial}{\partial \log \mu_R} + \beta_\lambda \frac{\partial}{\partial \lambda} - \gamma_{\mu^2} \mu^2 \frac{\partial}{\partial \mu^2} - \gamma \phi \frac{\partial}{\partial \phi} + \sum_{i=2,Y} \beta_i \frac{\partial}{\partial g_i} + \beta_{Y_t} \frac{\partial}{\partial Y_t} \right) V(\phi). \quad (3.17)$$

Here the β -functions are defined as

$$\beta_\lambda = \frac{d\lambda}{d \log \mu_R}, \quad \beta_i = \frac{dg_i}{d \log \mu_R}. \quad (3.18)$$

The anomalous dimensions of μ^2 and the field, are

$$\gamma_{\mu^2} = -\frac{d \log \mu^2}{d \log \mu_R}, \quad \gamma = -\frac{d \log \phi}{d \log \mu_R}. \quad (3.19)$$

The differential equation (3.17) can be solved via

$$\begin{aligned} V(\phi) &= -\frac{1}{2} \mu^2(t) G^2(t) \phi^2 + \frac{1}{4} \lambda(t) G^4(t) \phi^4, \quad t = \log \left(\frac{\phi}{\mu_R} \right), \\ G(t) &\equiv \exp \left(- \int_0^t dt' \gamma(g_i(t'), \lambda(t')) \right). \end{aligned} \quad (3.20)$$

If instead, we expand (3.17) in terms of couplings, we get

$$-\frac{\partial V_1(\phi)}{\partial \log \mu_R} = \left(\beta_\lambda \frac{\partial}{\partial \lambda} - \gamma_{\mu^2} \mu^2 \frac{\partial}{\partial \mu^2} - \gamma \phi \frac{\partial}{\partial \phi} + \sum_{i=2,Y} \beta_i \frac{\partial}{\partial g_i} + \beta_{Y_t} \frac{\partial}{\partial Y_t} \right) V_0(\phi). \quad (3.21)$$

Comparison of the quadratic and quartic terms then yields expressions for β_λ and γ_{μ^2}

$$\begin{aligned} \beta_\lambda &= 4\lambda\gamma + \frac{1}{16\pi^2} (24\lambda^2 + \frac{3}{2}g_2^4 + \frac{3}{8}(g_2^2 + g_Y^2)^2 - 24Y_t^4), \\ \gamma_{\mu^2} &= -2\gamma - \frac{3\lambda}{4\pi^2}. \end{aligned} \quad (3.22)$$

The Higgs anomalous dimension, can be easily derived from the two-point function. The result reads

$$\gamma = \frac{1}{64\pi^2} (-9g_2^2 - 3g_Y^2 + 12Y_t^2). \quad (3.23)$$

The remaining β -functions are

$$\begin{aligned}\beta_{Y_t} &= \frac{1}{16\pi^2} \left(\frac{9}{2} Y_t^3 - 8g_s^2 Y_t - \frac{9}{4} g^2 Y_t - \frac{17}{2} g_Y^2 Y_t \right), \quad \beta_s = -\frac{7}{16\pi^2} g_s^3, \\ \beta_{g_2} &= -\frac{19}{96\pi^2} g_2^3, \quad \beta_{g_Y} = \frac{41}{96\pi^2} g_Y^3.\end{aligned}\tag{3.24}$$

We thus obtained a system of differential equations for all the couplings. Once solved, the results can be inserted into (3.20) to obtain the resummed effective potential. At one-loop the system of differential equations is already in a triangular form, meaning that the system of equations is already more or less decoupled. Furthermore, the RGEs for g_s , g_2 and g_Y are simple enough to be solved analytical. The results can then be inserted into the RGE of Y_t , which is typically solved numerically. One then proceeds analogously with the RGEs of λ and μ^2 . The boundary conditions on the coupling constants can be set from measurements, whereas the boundary conditions on the μ^2 and λ are given by the requirement that

$$\left. \frac{dV_{\text{eff}}}{d\phi} \right|_{\phi=v} = 0, \quad \left. \frac{d^2V_{\text{eff}}}{d\phi^2} \right|_{\phi=v} = m_H^2.\tag{3.25}$$

The renormalization scale dependence of the various couplings at one-loop accuracy are displayed in Fig. 3.4.

The resulting potential should now be accurate for very large field values, even reaching up to the *Planck scale* if there is no beyond the SM physics entering in between. We can study the stability of the effective potential by studying its large ϕ limit at various scales. If we assume the SM to be an accurate description of nature up to the Planck scale, then the effective potential should be bounded from below, or else the VEV would not be stable. Furthermore, the effective potential can develop a second minimum. If this minimum has at a lower energy than our VEV, then the universe would at some point in time transition from our current “false” vacuum to the true minimum of the potential. The various scenarios are illustrated in Fig. 3.2. In Fig. 3.3, we show the stability of the Higgs potential in the

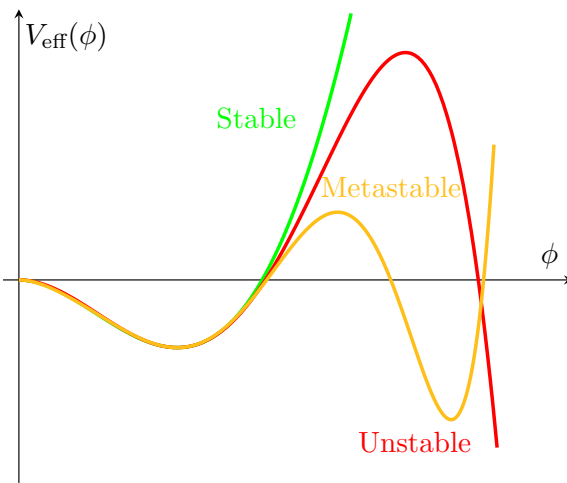


Figure 3.2: Illustration of effective Higgs potential for various scenarios.

(m_H, m_t) plane. We note that the stability bounds are notorious for being extremely sensitive to the chosen boundary conditions. We can see that due to the negative minus sign of the fermionic contributions to the effective potential (see n_t in Eq. (3.15)), the potential becomes unstable if the top-quark mass becomes too large. We also observe that for the SM Higgs

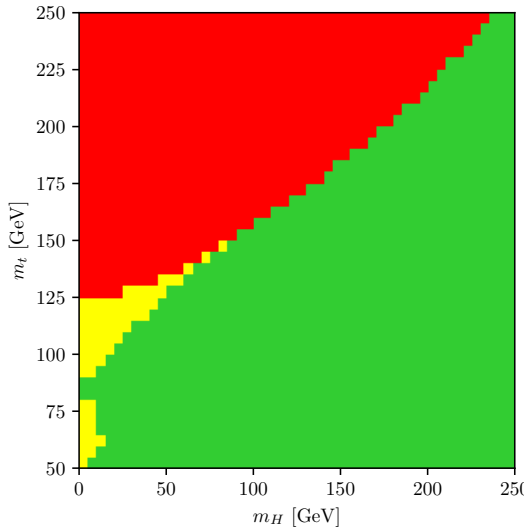


Figure 3.3: Stability of the Higgs potential as a function of the Higgs and top-quark mass. Red areas are unstable, yellow areas are metastable, and green areas are stable. The computational setup described in the Conventions.

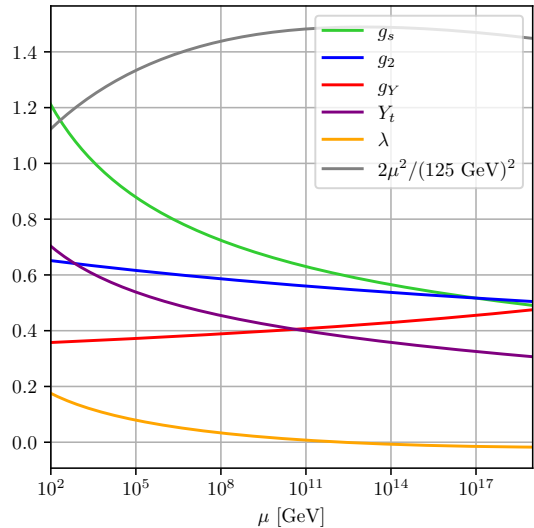


Figure 3.4: Scale dependence at one-loop accuracy of the various couplings for the SM values of the Higgs and top-quark mass. The computational setup described in the Conventions.

and top-quark masses, the potential is unstable but very close to the stability bound. With a two-loop calculation, absolute stability is now excluded at the 3σ -level [17]. Since an unstable vacuum is impossible, there must be some new physics mechanism which ensures that the potential is bounded from below. If the new physics scale is smaller than the scale at which the quartic Higgs coupling becomes negative ($\sim 10^{12}$ GeV see Fig. 3.4), then the potential would become absolutely stable once again. If, on the other hand, new physics only enters at even larger scales, then the potential exhibits a second VEV and our universe is metastable.

If our vacuum is truly metastable, then a) there must be a mechanism which ensured that the correct “false” vacuum was chosen, and b) the false vacuum must be sufficiently stable to have survived for at least the age of our universe (13.8 billion years). The first point could for example be explained, if today’s vacuum started off as the true vacuum and only became the false vacuum as the universe cooled down. How exactly the mechanism is realized is however highly model specific. The second point, that the false vacuum is sufficiently long-lived to have survived this long, is highly dependent on the new physics scale. Generally speaking, a higher new physics scale, results in a lower vacuum tunneling rate, that means the loosest bounds on SM parameters are therefore derived assuming that new physics only enters at the Planck scale. Since the SM is so close to the stability bound, it turns out that the Planck scale suffices to make the universe stable enough to have survived this long [17]. To address the question posed at the beginning of this chapter regarding the stability of the Higgs potential: surprisingly, within the framework of the SM, it is not stable. However, by making minimal assumptions about BSM physics, there exists a vast parameter space where the VEV is sufficiently stable to have persisted throughout the lifetime of the universe.

Lastly, we comment on the Landau pole of the quartic Higgs coupling. If β_λ is positive, then λ will at some point become large. If λ approaches unity, we lose perturbative convergence, the β_λ function will then become even larger and the Landau pole is quickly reached after losing

perturbative convergence². From Eq. (3.22), we can see that the β_λ -function becomes larger for larger λ , ergo for larger Higgs-boson masses, but decreases for larger top-quark masses. For the SM top-quark mass, one finds that the Higgs quartic coupling becomes non-perturbative at $m_H > 175$ GeV [17].

In conclusion, the Higgs boson is intricately connected to numerous fundamental concepts in physics, serving as a cornerstone in our understanding of particle interactions and symmetry breaking. Its properties not only illuminate aspects of the SM but also offer valuable insights into BSM theories. By examining the stability of the effective Higgs potential, we can impose significant constraints on both SM and BSM parameter spaces, guiding future research and deepening our comprehension of the universe's underlying principles.

² Since the RGE was derived perturbatively, it is, however, by no means clear that the pole would actually be reached.

4 | HADRONIC HIGGS PRODUCTION

In hadron-hadron collisions, a single Higgs boson can be produced via five main channels, listed below in descending order according to their cross sections:

1. Gluon-gluon fusion ($pp \rightarrow H$),
2. Vector-boson fusion ($pp \rightarrow qqH$),
3. Higgs Strahlung ($pp \rightarrow WH$ or $pp \rightarrow ZH$),
4. $t\bar{t}$ or $b\bar{b}$ associated production ($pp \rightarrow t\bar{t}H$, or $b\bar{b}H$),
5. Single-top associated production ($pp \rightarrow tH$).

Examples of leading-order (LO) Feynman diagrams for these channels are shown in Fig. 4.1. The cross sections for these processes span nearly three orders of magnitude, as illustrated

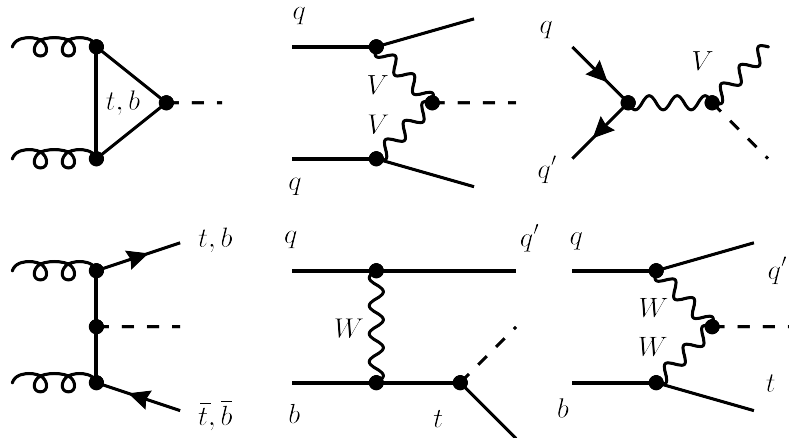


Figure 4.1: Example LO Feynman diagrams for the various hadronic Higgs-production channels. From top-left to bottom-right: gluon-gluon fusion, vector-boson fusion, Higgs Strahlung, $t\bar{t}$ or $b\bar{b}$ associated production, and the last two diagrams correspond to single-top associated production. V labels electroweak vector bosons, i.e. either a Z or W boson. In case a fermion line is drawn without an arrow, it indicates that both fermion flows are valid. q and q' mark massless quarks.

in Fig. 4.2. At the lower end is single-top associated Higgs production, with a cross section of about 0.08 pb at a center-of-mass energy of 13 TeV. The next rarest channels, with cross sections of approximately 0.5 pb, are $t\bar{t}$ and $b\bar{b}$ associated production, followed closely by the two Higgs-strahlung processes ($pp \rightarrow WH$ and $pp \rightarrow ZH$). Vector-boson fusion ranks second in magnitude, with a cross section of around 3.8 pb.

However, all other channels are dwarfed in comparison to the gluon-gluon-fusion channel with a cross section of approximately 46 pb. This channel alone accounts for nearly 90% of all produced Higgs bosons at the LHC.

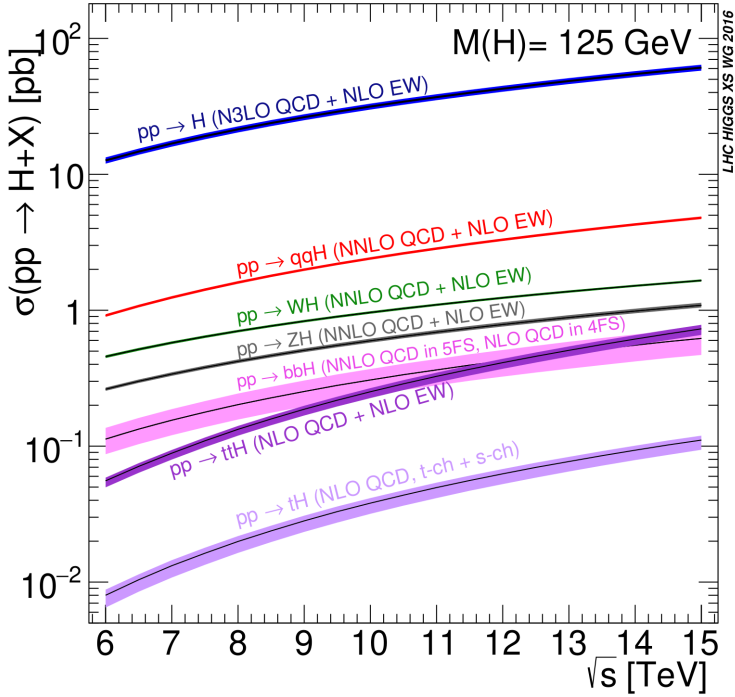


Figure 4.2: Inclusive Higgs production cross section as a function of the hadronic center-of-mass energy for various Higgs production channels. The figure was taken from Ref. [64].

The relatively large production cross section of the Higgs boson has enabled experimentalists to measure it with remarkable precision. Today, its most precise determination (under the assumption of SM branching ratios) was reported in Ref. [65] and reads

$$\sigma_{pp \rightarrow H}(13 \text{ TeV}) = 47.1 \pm 3.8 (\pm 8\%) \text{ pb.} \quad (4.1)$$

A key theoretical tool for describing the production and decay of the Higgs is the narrow width approximation, $\Gamma_H/m_H \approx 3 \times 10^{-5} \ll 1$. Under this approximation, the cross section for producing a Higgs boson and observing it in a particular decay mode can be factorized as

$$\sigma_{pp \rightarrow H \rightarrow X} = \sigma_{pp \rightarrow H} \frac{\Gamma_{H \rightarrow X}}{\Gamma_H}, \quad (4.2)$$

where Γ_H denotes the total decay width of the Higgs, and $\Gamma_{H \rightarrow X}$ is the partial decay width for the final state X .

Looking to the future, the planned high-luminosity phase of the LHC (HL-LHC) offers the prospect of even more precise cross-section measurements. As shown in Table 4.1, uncertainties below 4% are expected in some decay modes.

Such high-precision measurements are critical for searches beyond the SM, as experimental results must be compared closely with theoretical predictions. Any deviation from the SM expectation may serve as a hint of new physics, whereas agreement at this unprecedented level of accuracy places stronger constraints on extensions of the SM. Since the discovery of the Higgs boson in 2012 [13, 14], there has therefore been a continual drive to reduce the theoretical uncertainties of the SM predictions. Among the various Higgs production mechanisms, the gluon-gluon-fusion channel stands out as the most precisely measured and is thus particularly important for these ongoing efforts.

Decay Mode	CMS [%]	ATLAS [%]
$H \rightarrow \gamma\gamma$	± 2 (stat.) ± 3 (sys.)	± 2 (stat.) ± 3 (sys.)
$H \rightarrow ZZ^*$	± 2 (stat.) ± 3 (sys.)	± 2 (stat.) ± 4 (sys.)
$H \rightarrow WW^*$	± 1 (stat.) ± 3 (sys.)	± 1 (stat.) ± 4 (sys.)
$H \rightarrow b\bar{b}$	± 3 (stat.) ± 5 (sys.)	± 3 (stat.) ± 4 (sys.)
$H \rightarrow \mu^+\mu^-$	± 9 (stat.) ± 2 (sys.)	$^{+12}_{-13}$ (stat.) ± 3 (sys.)
$H \rightarrow \tau\tau$	± 3 (stat.) ± 5 (sys.)	± 3 (stat.) $^{+12}_{-10}$ (sys.)

Table 4.1: Projected relative statistical and systematic uncertainties on the Higgs production cross section in the gluon-gluon-fusion channel and its subsequent decays for the high-luminosity phase of the LHC, according to Ref. [66].

In the next sections, we concentrate solely on the gluon-gluon-fusion channel. We present explicit calculations of its cross section at leading order (LO) and approximate next-to-leading order (NLO), and we provide an overview of the current theoretical status along with the remaining challenges.

4.1 THE LEADING-ORDER CROSS SECTION

Having established that the gluon-gluon-fusion Higgs production cross section is central for many phenomenological applications, we now want to perform the actual LO calculation, which was first demonstrated by Georgi et al. in 1978 [18]. The calculation not only serves as an instructive example on cross section calculation, and thereby allows us to put our experience from Section 2.1 to good use, but it already introduces many important concepts we can transfer to the NNLO computation.

At LO, there are only two possible Feynman diagrams, depicted in Fig. 4.3. As we can see,

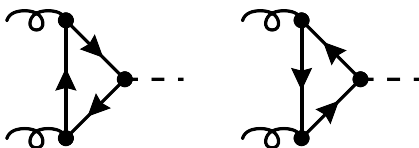


Figure 4.3: LO Feynman diagrams for Higgs production in the gluon-gluon-fusion channel.

gluon-gluon fusion is a loop induced process with two scales: the mass of the quark running in the loop m_q , and the Higgs mass m_H which must simultaneously represent the partonic center-of-mass energy. The initial-state gluons carry the on-shell momenta p_1 and p_2 . Let us then define the amputated amplitude via

$$i\mathcal{M} \equiv i\mathcal{M}^{\mu\nu,ab}\varepsilon_\mu^a(p_1)\varepsilon_\nu^b(p_2). \quad (4.3)$$

With the Feynman rules presented in Appendix A, we find that the amplitude reads

$$\begin{aligned} i\mathcal{M}^{\mu\nu,ab} = & - \int \frac{d^4 k}{(2\pi)^4} \\ & \times \text{Tr} \left[\frac{-im_q}{v} \delta_{ij} \frac{i(\not{k} + \not{p}_1 + \not{p}_2 + m_q)}{(k + p_1 + p_2)^2 - m_q^2} (ig\gamma^\nu T_{ik}^a) \frac{i(\not{k} + \not{p}_1 + m_q)}{(k + p_1)^2 - m_q^2} (ig\gamma^\mu T_{kj}^b) \frac{i(\not{k} + m_q)}{k^2 - m_q^2} \right] \quad (4.4) \\ & + \{p_1 \longleftrightarrow p_2, \mu \longleftrightarrow \nu, a \longleftrightarrow b\}. \end{aligned}$$

The extra minus sign in front of the integral stems from the closed fermion loop.

Even without performing the explicit calculation, we can already anticipate the general structure of the amplitude. Color wise, the amplitude must be proportional to δ^{ab} because it is the only available rank-two tensor. Since it is a symmetric tensor, the Lorentz structure must also be symmetric or else the amplitude would not respect *Bose symmetry*. The amputated amplitude must therefore satisfy

$$\mathcal{M}^{\mu\nu,ab}(p_1, p_2) = \mathcal{M}^{\nu\mu,ba}(p_2, p_1). \quad (4.5)$$

The only symmetric rank two tensors we have available are $g^{\mu\nu}$, $(p_1^\mu p_2^\nu + p_2^\mu p_1^\nu)$, $p_1^\mu p_1^\nu$, and $p_2^\mu p_2^\nu$. But since just the transverse parts give rise to physical amplitudes, the only relevant tensors are $g^{\mu\nu}$ and $p_2^\mu p_1^\nu$. Lastly, we know that the amplitude must satisfy the *Ward identity*. This allows us to restrict the tensor structure even further, such that we end up with

$$i\mathcal{M}^{\mu\nu,ab} = i\frac{\alpha_s}{\pi} \frac{1}{v} \delta^{ab} (p_2^\mu p_1^\nu - (p_1 \cdot p_2) g^{\mu\nu}) \mathcal{C}(m_H, m_q). \quad (4.6)$$

Notice that we have only made use of very general properties of the amplitude. This is why the decomposition in Eq. (4.6) will hold at every order of α_s . The function $\mathcal{C}(m_H, m_q)$ is called the *Higgs-gluon form factor*. It has mass dimension 0, i.e. its functional dependence on m_q and m_H must enter through a mass ratio

$$\mathcal{C}(m_H, m_q) = \mathcal{C}(z), \quad \text{with} \quad z \equiv \frac{m_H^2}{4m_q^2}. \quad (4.7)$$

The factor of 1/4 was introduced, so that the *normal threshold* is located at $z = 1$. Mathematically, this means that $z = 1$ is a solution of the *Landau equations*. Physically, we can interpret the singularity as the point where we have enough energy to produce the quark pair on-shell.

The form factor can now be extracted through a simple projection

$$\mathcal{C}(z) = \frac{\pi v}{i\alpha_s N_c^2 - 1} \delta^{ab} \frac{1}{(p_1 \cdot p_2)^2(d-2)} (p_2^\mu p_1^\nu - (p_1 \cdot p_2) g_{\mu\nu}) i\mathcal{M}^{\mu\nu,ab}. \quad (4.8)$$

Let us further define a perturbative expansion of the Higgs-gluon form factor

$$\mathcal{C} = \mathcal{C}^{(0)} + \frac{\alpha_s}{\pi} \mathcal{C}^{(1)} + \left(\frac{\alpha_s}{\pi} \right)^2 \mathcal{C}^{(2)} + \dots \quad (4.9)$$

If we now insert the LO expression of Eq. (4.4) and perform some basic manipulations, we find for the leading coefficient

$$\begin{aligned} \mathcal{C}^{(0)}(z) = & T_F \frac{1}{2-2\epsilon} \frac{1}{z} \int \frac{d^d k}{i\pi^{d/2}} \frac{1}{[k^2 - m_q^2 + i0^+] [(k + p_1 + p_2)^2 - m_q^2 + i0^+]} \\ & \times \left(2\epsilon + \frac{m_H^2}{[(k + p_1)^2 - m_q^2 + i0^+]} \left(\frac{1}{z} + \epsilon - 1 \right) \right), \quad (4.10) \end{aligned}$$

which, after solving the appearing integrals (see Appendix B) and expanding in ϵ , finally reduces to

$$\mathcal{C}^{(0)}(z) = T_F \frac{1}{z} \left\{ 1 - \left(1 - \frac{1}{z}\right) \left[\frac{1}{2} \ln \left(\frac{\sqrt{1-1/z}-1}{\sqrt{1-1/z}+1} \right) \right]^2 + \mathcal{O}(\epsilon) \right\}. \quad (4.11)$$

The LO Higgs-gluon form factor is plotted in Fig. 4.4 along with the NLO and NNLO corrections. As expected from the Landau equations, we pick up an imaginary part starting from the normal threshold at $z = 1$.

Since the two incoming gluons are vector bosons which subsequently form a spinless final state, we would expect them to always carry opposite spins. This intuition is indeed confirmed by the tensor structure of the amplitude (4.6), as it always vanishes once contracted with two polarization vectors of the same helicity¹.

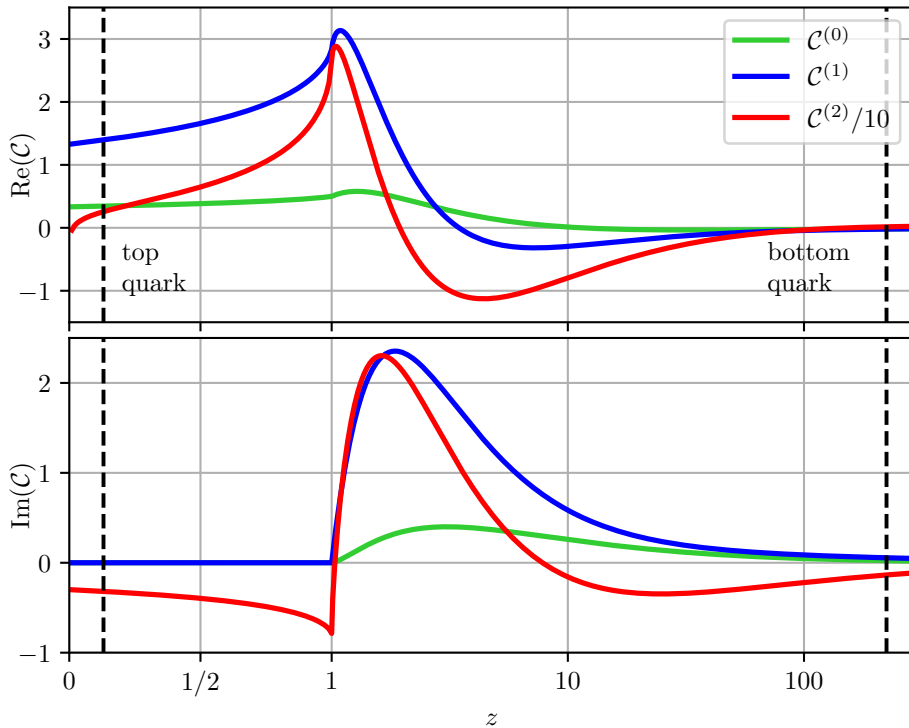


Figure 4.4: Real and imaginary part of the renormalized Higgs-gluon form factor at various perturbative orders. NNLO is divided by ten for better visibility. NNLO results also depend on the number of light-quark flavors which has been set to 5 (5FS). The top-quark mass is renormalized in the OS scheme. Infrared divergences are subtracted in the $\overline{\text{MS}}$ scheme with the help of the \mathbf{Z} operator (see e.g. Ref. [58]). Vertical dashed lines indicate the z -values for the top- (m_t) and bottom-quark ($\overline{m}_b(m_H/2)$) masses. The renormalization scale is set to $\mu_R = -m_H$, in order to eliminate some appearing logarithms and their analytic continuation. The plot was created using the results of Ref. [67].

If we expand the form factor around large quark masses, i.e. we perform a *large mass expansion* (LME), we find that it approaches a constant

$$\mathcal{C}^{(0)}(z) = T_F \left(\frac{2}{3} + \frac{7}{45}z + \frac{4}{63}z^2 + \mathcal{O}(z^3) \right). \quad (4.12)$$

¹ This can be seen easily by boosting to the center-of-mass frame and using $\epsilon^\mu(-\mathbf{p}, \lambda) \propto \epsilon^\mu(\mathbf{p}, -\lambda)$.

We will discuss the leading term of the expansion, i.e. the infinite mass limit, in more detail in Section 4.2. On the other side of the spectrum, we can see that if the mass of the Higgs is far greater than the mass of the internal quark, the form factor is approximately

$$\mathcal{C}^{(0)}(z) = \frac{T_F}{4z} \left[4 - \log^2(-4z) + \frac{1}{z} (\log(-4z) + \log^2(-4z)) + \mathcal{O}(1/z^2) \right]. \quad (4.13)$$

This expansion is known as the *high-energy limit* (HEL) of the Higgs-gluon form factor. In this limit, the Higgs-gluon form factor is roughly proportional to the square of the mass of the quark running in the loop. One power of m_q is hereby picked up from the Yukawa coupling. The other factor m_q is a consequence of the scalar coupling to the Higgs. Indeed, without the quark mass, the trace in Eq. (4.4) would contain an odd number of gamma matrices and vanish consequently. Physically, we can interpret this as a helicity flip of the internal quark at the Higgs interaction vertex. And since massless QCD conserves helicity, the other helicity flip is provided by the mass. The appearing double logarithms $\log^2(m_q^2/m_H^2)$ originate from a soft quark exchange (For a formal proof see Ref. [68]). In fact, the quark mass acts as an infrared regulator of the integral in Eq. 4.10, so the appearance of these logarithms is not entirely unexpected. Numerically, these logarithms can be very large. The bottom quark, for example, will yield a double logarithm of about 46. I.e., although suppressed by a factor of m_q^2/m_H^2 , the contributions from lighter quark flavors are logarithmically enhanced and hence highly significant for precision predictions.

If we now apply Eq. (2.1) and perform the phase space integration, which for a single particle is trivial because of the momentum conserving delta function, we get for the partonic cross section

$$\hat{\sigma}_{gg \rightarrow H}(\tau S) = \frac{\pi}{64v^2} m_H^2 \left(\frac{\alpha_s}{\pi} \right)^2 |\mathcal{C}(z)|^2 \delta(\tau S - m_H^2) \frac{1}{1-\epsilon}. \quad (4.14)$$

The initial state was averaged over spin and color. In conventional dimensional regularization, the gluons have $d - 2 = 2(1 - \epsilon)$ spin degrees. Finally, after the convolution with the partonic luminosity, we arrive at the LO cross section

$$\sigma_{pp \rightarrow HX}^{\text{LO}}(S) = \frac{\pi}{64v^2} \left(\frac{\alpha_s}{\pi} \right)^2 \mathcal{L}_{gg} \left(\frac{m_H^2}{S} \right) |\mathcal{C}^{(0)}(z)|^2. \quad (4.15)$$

From Fig. 4.4, we can see that the top-quark exerts the largest impact on the Higgs-gluon form factor and hence the LO hadronic cross section. We can read off the partonic luminosity from Fig. 2.2 and find that the cross section for the top-quark induces Higgs production reads²

$$\sigma_{pp \rightarrow HX}^{\text{LO}}(t) = 16.30 \text{ pb} \quad (4.16)$$

at a hadronic center-of-mass energy of 13 TeV. Although expected to have a less significant impact, we can also include the effects of finite bottom-quark masses by coherently summing together the corresponding form factors. With m_t and $\bar{m}_b(m_H/2)$, we find

$$\sigma_{pp \rightarrow HX}^{\text{LO}}(t+b) = 15.23 \text{ pb}, \quad (4.17)$$

i.e. the bottom quark lowers the cross section by around 6.5% at LO.

To quantify the impact of the individual quarks flavors, we can decompose the cross section in terms of the respective Yukawa couplings Y_i :

$$\sigma_{pp \rightarrow HX} = \sum_{i \leq j} Y_i Y_j \sigma_{ij}. \quad (4.18)$$

² Values of masses and coupling constants are provided in the Conventions.

Without the inclusion of electroweak corrections this decomposition is always possible. We call

$$\sigma_{i \times j} = Y_i Y_j \sigma_{ij}, \quad (4.19)$$

the *i-j-interference contribution* and

$$\sigma_i = Y_i^2 \sigma_{ii} \quad (4.20)$$

the *pure-i contribution* to the cross section. Both contributions are depicted at LO in Fig. 4.5. Clearly, the dominant contribution for the lighter quark flavors comes from the interference with

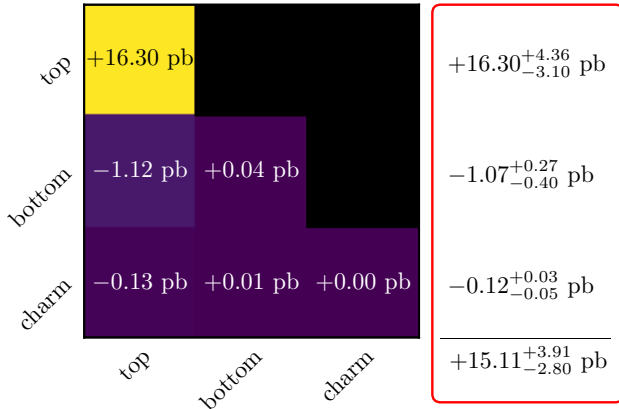


Figure 4.5: σ_i (diagonals) and $\sigma_{i \times j}$ (off-diagonals) at LO for the three heaviest quark flavors at 13 TeV. The red box indicates the sum of each row, and hence the combined effects of each additional flavor. The computational setup is described in the Conventions. We use the on-shell mass value for the top-quark and $\overline{\text{MS}}$ masses for the bottom- and charm-quark. Scale uncertainties are computed with 7-point-variation.

the top-quark. The pure-bottom contribution is already below a percent and the pure-charm quark mass effects are completely negligible. The inclusion of the charm quark lowers the total cross section by around 1%.

4.2 THE HEAVY-TOP LIMIT

The computation of the Higgs production cross section in full QCD is quite challenging. As we saw above, even at leading order we encounter loop integrals with two mass scales. It is therefore maybe not surprising that the first NLO corrections to this process were actually computed in an approximation framework [19]. In the approximation, we assume that the quark, which is coupling to the Higgs is much heavier than the Higgs $z \ll 1$. That means we are only interested in the leading term of the LME. In the SM, the top quark is the only quark for which this approximation is applicable, which is why it is often referred to as the *heavy-top limit* (HTL).

The finite distance interaction of the gluon and the Higgs will therefore shrink down to a point like vertex which we can describe with the effective Lagrangian

$$\mathcal{L}_{\text{HTL}}^{(0)} = \mathcal{L}_{\text{QCD}}^{(n_f-1)} - C_1 \frac{H}{v} \frac{1}{4} G_{\mu\nu}^a G^{a\mu\nu}. \quad (4.21)$$

We see that the coupling constant now has mass dimension -1 , so the theory will not be UV renormalizable. That means that we cannot absorb all UV divergences into multiplicative

renormalization constants as we did for the SM (see Eq. (2.58)). Instead, additional independent terms must appear in our Lagrangian to cancel the arising divergences. On the other hand, as long as we focus solely on QCD corrections and single-operator insertions, the color-singlet Higgs can be treated as a classical field, and we only need to renormalize the gauge-invariant dimension-four operator

$$\mathcal{O}_1 \equiv -\frac{1}{4}G_{\mu\nu}^a G^{a\mu\nu}. \quad (4.22)$$

To indicate the perturbative order, we gave the Lagrangian in Eq. (4.21) a superscript. The superscript $n_f - 1$ of the QCD Lagrangian specifies the number of active flavors. It was reduced by one since the heaviest quark flavor was integrated out. The constant C_1 is called a *Wilson coefficient*, and it needs to be matched to the full theory in the infinite-quark-mass limit. At LO for example, we find that the Higgs-gluon form factor in the effective theory simply reads

$$\mathcal{C}^{(0)} = -\frac{\pi}{\alpha_s} C_1. \quad (4.23)$$

If we compare this to the leading term of our LME (4.12), we find

$$C_1 = -\frac{\alpha_s}{\pi} \frac{2}{3} T_F + \mathcal{O}(\alpha_s^2). \quad (4.24)$$

The main benefit of the approximation lies in the reduced complexity. By integrating out the heavy quark, we have reduced a loop-induced process to a tree-level process. Moreover, the heavy-quark mass is eliminated as a scale; hence, the appearing Feynman integrals will generally be much simpler to solve.

4.2.1 Renormalization of Gauge Invariant Operators

Beyond LO, gauge invariant operators, such as \mathcal{O}_1 , can mix under renormalization not only with other gauge invariant operators but also, notably, with operators that are not gauge invariant. To understand this phenomenon, let us consider the following partition function:

$$\begin{aligned} Z[J, K] &\equiv e^{iW[J, K]} \equiv \mathcal{N} \int \mathcal{D}\Phi e^{i(S[J, K] + J \cdot \Phi + K \cdot \delta_{\text{BRS}}\Phi)}, \quad Z[0, 0] = 1, \\ J &= (J_\mu^a, \bar{J}^a, J^a, J_B^a, \eta, \bar{\eta}, \phi), \quad \Phi = (A^{a\mu}, c^a, \bar{c}^a, B^a, \bar{\psi}, \psi, \mathcal{O}_1), \quad K = (K_\mu^a, L^a), \\ J \cdot \Phi &\equiv \int d^d x [J_\mu^a(x) A^{a\mu}(x) + \bar{J}^a(x) c^a(x) + J^a(x) \bar{c}^a(x) + J_B^a(x) B^a(x) \\ &\quad + \bar{\psi}(x) \eta(x) + \bar{\eta}(x) \psi(x) + \phi(x) \mathcal{O}_1(x)], \\ K \cdot \delta_{\text{BRS}}\Phi &\equiv \int d^d x [K_\mu^a(x) \delta_{\text{BRS}} A^{a\mu}(x) + L^a(x) \delta_{\text{BRS}} c^a(x)], \end{aligned} \quad (4.25)$$

where J represents various sources coupled to the fields Φ , and K is a source specifically coupled to the *Becchi-Rouet-Stora* (BRS) variation of the gauge and ghost field. The BRS transformation is defined by

$$\delta_\lambda \equiv \lambda \delta_{\text{BRS}}, \quad \text{with } \lambda \text{ Grassmann odd, and}$$

$$\delta_\lambda \psi = i\lambda g c^a T^a \psi, \quad \delta_\lambda A_\mu^a = \lambda (D_\mu c)^a, \quad (4.26)$$

$$\delta_\lambda c^a = -\frac{1}{2} \lambda g f^{abc} c^b c^c, \quad \delta_\lambda \bar{c}^a = \lambda B^a, \quad \delta_\lambda B^a = 0.$$

The field B^a is the *Nakanishi-Lautrup* auxiliary field

$$B^a = -\frac{1}{\xi} \partial^\mu A_\mu^a. \quad (4.27)$$

Its introduction causes the BRS-variation to be degree-two instead of degree-three nilpotent, i.e. $\delta_{\text{BRS}}^2 = 0$.

As usual, we can define the effective action as the Legendre transform of the generating functional for connected Green's functions $W[J, K]$. Notice that we do not transform the BRS-variation of the fields, so the effective action is still a functional of K . Since the gauge-fixing Lagrangian does not receive quantum corrections, let us also define

$$\hat{\Gamma}[\Phi, k_\mu^a \equiv K_\mu^a + \partial_\mu \bar{c}^a, L^a] \equiv \Gamma[\Phi, k_\mu^a, L^a] - S_{\text{GF}} = \Gamma[\Phi, k_\mu^a, L^a] - \int d^d x \left(-\partial^\mu B^a A_\mu^a + \frac{\xi}{2} B^a B^a \right). \quad (4.28)$$

Here, we also utilized that the BRS variation of the gauge field only couples to the combination $k_\mu^a = K_\mu^a + \partial \bar{c}_\mu^a$. This effective action satisfies the famous *Zinn-Justin equation* [69]

$$0 = \frac{\delta \hat{\Gamma}}{\delta A_\mu^a} \cdot \frac{\delta \hat{\Gamma}}{\delta k^{a\mu}} + \frac{\delta \hat{\Gamma}}{\delta c^a} \cdot \frac{\delta \hat{\Gamma}}{\delta L^a}. \quad (4.29)$$

At NLO, the bare effective action $\hat{\Gamma}$ can be decomposed into the Born contribution $\hat{S} = S - S_{\text{GF}}$, the finite part of the one-loop correction $\hat{\Gamma}_{\text{fin}}^{\text{1-loop}}$, and the divergent part of the one-loop correction $\hat{\Gamma}_{\text{div}}^{\text{1-loop}}$

$$\hat{\Gamma} = \hat{S} + \hat{\Gamma}_{\text{fin}}^{\text{1-loop}} + \hat{\Gamma}_{\text{div}}^{\text{1-loop}} + \mathcal{O}(\hbar^2). \quad (4.30)$$

If we insert this into the Zinn-Justin equation (4.29), truncate the expression at one-loop, and only consider the divergent part we get

$$0 = \left[\frac{\delta \hat{S}}{\delta A_\mu^a} \cdot \frac{\delta}{\delta k^{a\mu}} + \frac{\delta \hat{S}}{\delta c^a} \cdot \frac{\delta}{\delta L^a} + \frac{\delta \hat{S}}{\delta k^{a\mu}} \cdot \frac{\delta}{\delta A_\mu^a} + \frac{\delta \hat{S}}{\delta L^a} \cdot \frac{\delta}{\delta c^a} \right] \hat{\Gamma}_{\text{div}}^{\text{1-loop}} \equiv s \hat{\Gamma}_{\text{div}}^{\text{1-loop}}. \quad (4.31)$$

Here, we also defined the *linearized Slavnov operator* s . The operator is an extension of the BRS transformation, and is also degree-2 nilpotent. Renormalization iteratively removes the divergences at each loop order; therefore, it is straightforward to see that Eq. (4.31) actually holds at every loop order. This equation tells us that although the counter terms of the effective action are not required to be gauge invariant, they must be vanishing under the action of s . Since counter terms are also polynomial in the external fields and have ghost number zero, one can then show [70–72], using *Becchi-Rouet-Stora-Tyutin* (BRST) *cohomology*, that the counter terms are linear combinations of BRST-exact, and gauge invariant operators

$$\hat{\Gamma}_{\text{ct}} = sF + \text{gauge invariant operators}. \quad (4.32)$$

Since s is nilpotent, it is easy to see that the first term automatically satisfies the Zinn-Justin equation. Moreover, the equation can now be leveraged to determine a complete operator basis. Since we are not interested in Green's functions of the BRS variation of fields, we can set $K_\mu^a = L^a = 0$ for all practical purposes. We can then make the general Ansatz

$$\begin{aligned} sF \Big|_{L^a=0, k_\mu^a=\partial_\mu \bar{c}^a} &= s(f[A_\mu^a, c^a, \partial_\mu \bar{c}^a] + g^a[A_\mu^a, c^a, \partial_\mu \bar{c}^a]L^a) \Big|_{L^a=0, k_\mu^a=\partial_\mu \bar{c}^a} \\ &= \left[\frac{\delta \hat{S}}{\delta A_\mu^a} \cdot \frac{\delta f}{\delta (\partial^\mu \bar{c}^a)} + \frac{\delta \hat{S}}{\delta (\partial^\mu \bar{c}^a)} \cdot \frac{\delta f}{\delta A_\mu^a} + \frac{\delta \hat{S}}{\delta L^a} \cdot \frac{\delta f}{\delta c^a} + \frac{\delta \hat{S}}{\delta c^a} \cdot g^a \right]_{L^a=0}. \end{aligned} \quad (4.33)$$

The functional derivatives can be worked out straightforwardly. The action and the Lagrangian can be decomposed into a gauge, a *Faddeev-Popov*, a matter, and a source sector

$$\hat{S} = S_G + S_{FP} + S_M + S_S = \int d^d x (\mathcal{L}_G + \mathcal{L}_{FP} + \mathcal{L}_M + \mathcal{L}_S). \quad (4.34)$$

The gauge-fixing term has been subtracted, so it does not appear on the right-hand side. The Lagrangians are

$$\begin{aligned} \mathcal{L}_G &= -\frac{1}{4} G_{\mu\nu}^a G^{a\mu\nu} = \frac{1}{2} A_\mu^a (g^{\mu\nu} \square - \partial^\mu \partial^\nu) A_\nu^a - g f^{abc} \partial^\mu A^{a\nu} A_\mu^b A_\nu^c - \frac{1}{4} g^2 f^{abe} f^{cde} A^{a\mu} A^{b\nu} A_\mu^c A_\nu^d, \\ \mathcal{L}_{FP} &= \partial \bar{c} \cdot D c = \partial_\mu \bar{c}^a D^{ab\mu} c^b, \\ \mathcal{L}_M &= \sum_{i=1}^{n_l} \bar{q}_i (i \not{D} - m_i) q_i, \\ \mathcal{L}_S &= L^a \delta_{\text{BRS}} c^a + \phi \mathcal{O}_1. \end{aligned} \quad (4.35)$$

Note that the source Lagrangian does not contain the term proportional to $K_\mu^a \delta_{\text{BRS}} A^{a\mu}$ since we defined the effective action $\hat{\Gamma}$ as a functional of k_μ^a , and we set $k_\mu^a = \partial_\mu \bar{c}^a$. It is then straightforward to work out the relevant functional derivatives

$$\begin{aligned} \frac{\delta S_G}{\delta A_\mu^a} &= (g^{\mu\nu} \square - \partial^\mu \partial^\nu) A_\nu^a - g f^{abc} \left(-\partial^\mu A^{b\nu} A_\nu^c + \partial^\nu A^{b\mu} A_\nu^c - \partial^\nu (A_\nu^b A^{c\mu}) \right) \\ &\quad - g^2 f^{abe} f^{cde} A^{b\nu} A^{c\mu} A_\nu^d \\ &= D_\nu^a G^{b\nu\mu}, \\ \frac{\delta S_{FP}}{\delta A_\mu^a} &= -f^{abc} \partial^\mu \bar{c}^b c^c, \\ \frac{\delta S_M}{\delta A_\mu^a} &= g \sum_{i=1}^{n_l} \bar{q}_i \gamma^\mu T^a q_i, \\ \frac{\delta S_{FP}}{\delta c^a} &= D^{ab\mu} \partial_\mu \bar{c}^b, \\ \frac{\delta S_{FP}}{\delta (\partial_\mu \bar{c}^a)} &= D^{ab\mu} \bar{c}^b = \delta_{\text{BRS}} A^{a\mu}, \\ \frac{\delta S_S}{\delta L^a} &= \delta_{\text{BRS}} c^a. \end{aligned} \quad (4.36)$$

Note that $\delta/\delta(c^a)$ and $\delta/\delta(\partial_\mu \bar{c}^a)$ are *Grassmann odd*; that is, we get an additional minus sign whenever we permute the derivatives with other ghost fields. This explains, for example, the lack of a minus sign in $\delta S_{FP}/\delta c^a$. All derivatives not explicitly shown in Eq. (4.36) vanish either identically or after setting $L^a = 0$. These functional derivatives can now be inserted into Eq. (4.33), yielding

$$\begin{aligned} sF &= \left\{ \left[D_\nu^a G^{b\nu\mu} - f^{abc} \partial^\mu \bar{c}^b c^c + g \sum_{i=1}^{n_l} \bar{q}_i \gamma^\mu T^a q_i \right] \cdot \frac{\delta}{\delta (\partial^\mu \bar{c}^a)} \right. \\ &\quad \left. + \delta_{\text{BRS}} A^{a\mu} \cdot \frac{\delta}{\delta A^{a\mu}} + \delta_{\text{BRS}} c^a \cdot \frac{\delta}{\delta c^a} \right\} f + D^{ab\mu} \partial_\mu \bar{c}^b \cdot g^a. \end{aligned} \quad (4.37)$$

The structure of the functionals $f[A_\mu^a, c^a, \partial_\mu \bar{c}^a]$ and $g^a[A_\mu^a, c^a, \partial_\mu \bar{c}^a]$ is almost entirely dictated by the mass dimension and the ghost number. Indeed, the effective action must be dimensionless and have vanishing ghost number. A quick inspection of the linearized Slavnov operator (4.31) shows that it must satisfy

$$\dim(s) = -3, \quad \text{and} \quad \text{gh}(s) = 1. \quad (4.38)$$

Consequently, the functionals f and g^a must fulfil

$$\dim(f) = 3, \quad \text{gh}(f) = -1, \quad \dim(g^a) = 1, \quad \text{and} \quad \text{gh}(g^a) = 1. \quad (4.39)$$

So up to a factor, the only possible local functionals are

$$f[A_\mu^a, c^a, \partial_\mu \bar{c}^a](x) = \partial^\mu \bar{c}^a(x) A_\mu^a(x), \quad g^a[A_\mu^a, c^a, \partial_\mu \bar{c}^a](x) = c^a(x). \quad (4.40)$$

In the end, we are only interested in a basis of independent operators, so we can consider f and g^a independently from one another. Setting g^a to zero yields

$$\begin{aligned} sF &= \left[D_\nu^{ab} G^{b\nu\mu} - f^{abc} \partial^\mu \bar{c}^b c^c + g \sum_{i=1}^{n_l} \bar{q}_i \gamma^\mu T^a q_i \right] A_\mu^a + \delta_{\text{BRS}} A^a{}^\mu \partial_\mu \bar{c}^a \\ &= D_\nu^{ab} G^{b\nu\mu} A_\mu^a + g \sum_{i=1}^{n_l} \bar{q}_i \not{A} q_i - \partial^\mu \bar{c}^a \partial_\mu c^a \\ &\equiv \mathcal{O}_4, \end{aligned} \quad (4.41)$$

where the minus sign in front of the last term of the second line stems from the anti-commutativity of the ghost fields. Similarly, setting f to zero and $g^a = c^a$ yields

$$sF = D^{ab\mu} \partial_\mu \bar{c}^b c^a = (D^\mu \partial_\mu \bar{c})^a c^a = \mathcal{O}_5. \quad (4.42)$$

In addition, the counter terms can contain additional gauge-invariant operators like

$$\mathcal{O}_2 = \sum_{i=1}^{n_l} m_i \bar{q}_i q_i. \quad (4.43)$$

These operators are only unique up to operators vanishing by the classical equations of motions. Ergo, counter terms to \mathcal{O}_1 can also contain operators of the form

$$\mathcal{O}_3 = \sum_{i=1}^{n_l} \bar{q}_i \left(\frac{i}{2} \not{D} - m \right) q_i. \quad (4.44)$$

Additional gauge invariant operators like $\sum_i \bar{q}_i \not{D} q_i$ are now no longer independent, and can be expressed in terms of linear combinations of other operators, in this case by \mathcal{O}_2 and \mathcal{O}_3 . Note also that the operator \mathcal{O}_5 is gauge invariant, vanishes by the classical equations of motion, and—as we showed above—is BRST-exact.

The BRST-transformation generated by the linearized Slavnov-operator is a symmetry of the action. The associated conserved charge defines the physical space, i.e. physical states are in the kernel of the charge operator. The matrix element of BRST-exact operators between physical states is thus vanishing. This is crucial, as it assures that the gauge-variant operators do not enter the computation of physical observables.

In summary, we can distinguish three types of operators: *type-I operators* which are gauge invariant and have non-zero matrix elements, *type-II_a operators* which are gauge invariant but give zero matrix elements due to the equation of motion, and finally *type-II_b operators* which are gauge variant but BRST-exact and thus also give zero when applied to physical states.

In the present case, the complete operator basis reads

$$\begin{aligned} \mathcal{O}_I & \left\{ \begin{array}{l} \mathcal{O}_1 = -\frac{1}{4}G_{\mu\nu}^a G^{a\mu\nu}, \\ \mathcal{O}_2 = \sum_{i=1}^{n_l} m_i \bar{q}_i q_i, \end{array} \right. \\ \mathcal{O}_{II_a} & \left\{ \begin{array}{l} \mathcal{O}_3 = \sum_{i=1}^{n_l} \bar{q}_i \left(\frac{i}{2} \overleftrightarrow{\not{D}} - m \right) q_i, \end{array} \right. \\ \mathcal{O}_{II_b} & \left\{ \begin{array}{l} \mathcal{O}_4 = A^{a\mu} D^\nu G_{\nu\mu}^a + g \sum_{i=1}^{n_l} \bar{q}_i \not{A} q_i - \partial^\mu \bar{c}^a \partial_\mu c^a, \\ \mathcal{O}_5 = (D_\mu \partial^\mu \bar{c})^a c^a. \end{array} \right. \end{aligned} \quad (4.45)$$

The operator basis is constructed only of light fields, and the light fields are defined in a decoupled theory. As previously discussed, the operator \mathcal{O}_5 is BRST-exact, gauge invariant, and vanishes due to the equations of motion. It thus classifies both as a type-II_a and a type-II_b operator.

Since operators of type-II cannot generate non-vanishing S -matrix elements through renormalization, the renormalization matrix must have the following general structure:

$$\begin{pmatrix} \mathcal{O}_I^R \\ \mathcal{O}_{II}^R \end{pmatrix} = \begin{pmatrix} z^{I,I} & z^{I,II} \\ 0 & z^{II,II} \end{pmatrix} \begin{pmatrix} \mathcal{O}_I^B \\ \mathcal{O}_{II}^B \end{pmatrix}. \quad (4.46)$$

Therefore, the final form of our effective Lagrangian reads

$$\mathcal{L}_{\text{HTL}} = \mathcal{L}_{\text{QCD}}^{(5)} + \frac{H}{v} \sum_{i=1}^5 C_i^B \mathcal{O}_i^B. \quad (4.47)$$

As usual, we replace the bare operators by their renormalized counterparts

$$C_i^B \mathcal{O}_i^B = C_i^B Z_{ij}^{-1} \mathcal{O}_j^R. \quad (4.48)$$

We can hence identify the renormalized Wilson coefficients as

$$C^R = (Z^{-1})^T C^B. \quad (4.49)$$

Using the RGE, we find that the *anomalous dimension* matrix of the Wilson coefficients is determined through

$$\frac{dC^R}{d \ln \mu} = \left(Z \frac{d(Z^{-1})}{d \ln \mu} \right)^T C^R = - \left(\frac{dZ}{d \ln \mu} Z^{-1} \right)^T C^R \equiv \gamma^T C^R. \quad (4.50)$$

With the structure of the renormalization matrix (4.46), we arrive at an important conclusion: The Wilson coefficients of type-II operators cannot mix into the Wilson coefficients of type-I operators through the running in the scale. Since the type-II operators render no contribution to the scattering matrix element, we can focus our attention on the gauge invariant operators and their Wilson coefficients.

We now want to determine the I, I part of the renormalization matrix $z^{I,I}$, in order to determine the running of the Wilson coefficients. Let us start by defining the generating functional

$$\begin{aligned} Z[J] &\equiv z[J]/z[0], \quad z[J] \equiv \int \prod_i \mathcal{D}\Phi_j e^{i(S+J\cdot\Phi)}, \quad S = S[A, c, \bar{c}, q, \bar{q}] \equiv \int d^d x \mathcal{L}, \\ J &= (J^\mu, \bar{J}, J, \bar{\eta}, \eta), \quad \Phi = \left(\frac{1}{g} A_\mu, c, \bar{c}, q, \bar{q} \right), \end{aligned} \quad (4.51)$$

with the Lagrangian

$$\mathcal{L} \equiv -\frac{1}{4g^2} G_{\mu\nu}^a G^{a\mu\nu} - \frac{1}{2\xi g^2} (\partial \cdot A)^2 + \partial^\mu \bar{c}^a (D_\mu c)^a + \bar{q} \left(\frac{i}{2} \not{D} - m_q \right) q. \quad (4.52)$$

The Lagrangian is the QCD Lagrangian with only one active quark flavor and rescaled gauge fields

$$A_\mu^a \longrightarrow \frac{1}{g} A_\mu^a. \quad (4.53)$$

Therefore, the covariant derivatives are now also defined in terms of the rescaled fields

$$D_\mu = \partial_\mu - iT_R^a A_\mu^a(x). \quad (4.54)$$

Green's functions of the operators \mathcal{O}_1 and \mathcal{O}_2 can now be generated by applying the differential operators³

$$\begin{aligned} D_1 &= -\frac{1}{2} g \frac{\partial}{\partial g} + \xi \frac{\partial}{\partial \xi} - \frac{1}{2} J_\mu \cdot \frac{\delta}{\delta J_\mu}, \\ D_2 &= -m_q \frac{\partial}{\partial m_q}, \end{aligned} \quad (4.55)$$

on the partition function, that means

$$-iD_k z[J] = \int \prod_j \mathcal{D}\Phi_j \hat{\mathcal{O}}_k(0) e^{i(S+J\cdot\Phi)} \equiv z_{\mathcal{O}_k}[J]. \quad (4.56)$$

Here $\hat{\mathcal{O}}_k(0)$ denotes the Fourier transform of the operator $\mathcal{O}_k(x)$ at zero momentum. The normalization of the generating functional then properly subtracts the vacuum expectation value of the operators

$$-iD_k Z[J] = \frac{1}{z[0]} \int \prod_j \mathcal{D}\Phi_j \left(\hat{\mathcal{O}}_k(0) - \langle \Omega | \mathcal{O}_k(0) | \Omega \rangle \right) e^{i(S+J\cdot\Phi)} \equiv Z_{\mathcal{O}_k}. \quad (4.57)$$

In the $\overline{\text{MS}}$ scheme, the R -operation commutes with the differential operators in Eq. (4.55), i.e. the renormalized operators can be generated from the renormalized generating functional

$$Z_{\mathcal{O}_k^R} = -iD_k Z^R[J], \quad (4.58)$$

which, on the other hand, is given by

$$\begin{aligned} Z^R[J] &= z^R[J]/z^R[0], \\ z^R[J] &= \int \prod_i \mathcal{D}\Phi_j e^{i(S^R+J\cdot\Phi)}, \\ S^R &\equiv S[Z_3'^{1/2} A^R, Z_3'^{-1/2} c^R, \tilde{Z}_3^{-1/2} \bar{c}^R, Z_2^{1/2} q^R, Z_2^{1/2} \bar{q}^R, Z_{gg}, Z_m m_q, Z_g^{-2} Z_3' \xi^R]. \end{aligned} \quad (4.59)$$

³ We only provide the operators for the type-I operators since they are the only ones necessary for computing physical amplitudes.

Using the chain rule, the derivatives can be reexpressed as

$$-iD_k z^R[J] = \int \prod_j \mathcal{D}\Phi_j \left[\hat{O}_k(0) + \sum_i (D_k \ln Z_i) \frac{\partial S^R}{\partial \ln Z_i} \right] e^{iS^R + J \cdot \Phi}, \quad (4.60)$$

where $Z_i \in \{Z'_3, \tilde{Z}_3, Z_2, Z_g, Z_m\}$.

With the Lagrangian of Eq. (4.52), the derivatives of the action can be computed explicitly, yielding

$$Z_g \frac{\partial S^R}{\partial Z_g} = -2\hat{O}_1(0), \quad \text{and} \quad Z_m \frac{\partial S^R}{\partial Z_m} = -\hat{O}_2(0). \quad (4.61)$$

We hence find that the renormalization constants are given by

$$\begin{aligned} z_{11}^{I,I} &= 1 - 2D_1 \ln Z_g = 1 + g \frac{\partial \ln Z_g}{\partial g}, & z_{12}^{I,I} &= -D_1 \ln Z_m = \frac{g}{2} \frac{\partial \ln Z_m}{\partial g} \\ z_{21}^{I,I} &= 0, & z_{22}^{I,I} &= 1. \end{aligned} \quad (4.62)$$

Here, we made use of the fact that the $\overline{\text{MS}}$ -renormalization constants are independent of the quark mass and the gauge parameter. We can rewrite the appearing derivatives in terms of the β -function and the mass-anomalous dimension. Indeed,

$$\begin{aligned} \frac{4\pi}{\alpha_s} \bar{\beta} &\equiv \frac{d \ln \alpha_s}{d \ln \mu} = -\frac{d \ln Z_{\alpha_s}}{d \ln \mu} = -\left(\frac{\partial \ln Z_{\alpha_s}}{\partial \ln \alpha_s} \frac{d \ln \alpha_s}{d \ln \mu} + \frac{\partial \ln Z_{\alpha_s}}{\partial \ln \mu} \right) = -\left(\frac{4\pi}{\alpha_s} \bar{\beta} \frac{\partial \ln Z_{\alpha_s}}{\partial \ln \alpha_s} + 2\epsilon \right) \\ &\Rightarrow \frac{\partial \ln Z_{\alpha_s}}{\partial \ln \alpha_s} = g \frac{\partial \ln Z_g}{\partial g} = -1 - 2\epsilon \frac{\alpha_s}{4\pi \bar{\beta}} = -1 + \frac{1}{1 - \frac{\beta}{2\epsilon} \frac{4\pi}{\alpha_s}}, \end{aligned} \quad (4.63)$$

where, in the last step, we used the relation between the d - and four-dimensional β -functions

$$\bar{\beta} = \beta - 2\epsilon \frac{\alpha_s}{4\pi}. \quad (4.64)$$

Similarly, we find

$$\begin{aligned} \gamma_m &\equiv -\frac{d \ln m_q}{d \ln \mu} = \frac{d \ln Z_m}{d \ln \mu} = \frac{\partial \ln Z_m}{\partial \ln \alpha_s} \frac{d \ln \alpha_s}{d \ln \mu} = \frac{\partial \ln Z_m}{\partial \ln \alpha_s} \frac{4\pi}{\alpha_s} \bar{\beta} \\ &\Rightarrow \frac{\partial \ln Z_m}{\partial \ln \alpha_s} = \frac{g}{2} \frac{\partial \ln Z_m}{\partial g} = \frac{\alpha_s}{4\pi} \frac{1}{\bar{\beta}} \gamma_m = -\frac{\gamma_m}{2\epsilon} \frac{1}{1 - \frac{\beta}{2\epsilon} \frac{4\pi}{\alpha_s}} \end{aligned} \quad (4.65)$$

Finally, we want to use the above results to calculate the anomalous dimension matrix in Eq. (4.50). The entries of the renormalization constant matrix depend only on the renormalization scale through the coupling constant, i.e.

$$\gamma^{I,I} = -\frac{dz^{I,I}}{d \ln \mu} (z^{I,I})^{-1} \Big|_{\epsilon=0} = -\frac{\partial z^{I,I}}{\partial \alpha_s} (z^{I,I})^{-1} 4\pi \bar{\beta} \Big|_{\epsilon=0} = \frac{\partial z^{I,I(1)}}{\partial \alpha_s} 2\alpha_s. \quad (4.66)$$

Where we used that $z^{I,I}$ consists only of poles in the $\overline{\text{MS}}$ scheme, and once again applied the relation between the β -functions given in Eq. (4.64). $z^{I,I(1)}$ denotes the residue of the renormalization matrix

$$z^{I,I} = \mathbb{1} + \sum_{i=1} z^{I,I(i)} \epsilon^{-i}. \quad (4.67)$$

We then obtain the following form for the anomalous dimension matrix:

$$\gamma^{I,I} = \begin{pmatrix} 4\pi\alpha_s \frac{d}{d\alpha_s} \left(\frac{\beta}{\alpha_s} \right) & -\alpha_s \frac{d\gamma_m}{d\alpha_s} \\ 0 & 0 \end{pmatrix}. \quad (4.68)$$

The structure of this matrix reveals that the C_1 Wilson coefficient, which is the relevant coefficient for the HTL, is completely independent of the other Wilson coefficients. The RGE for the Wilson coefficient (4.50) can now be written as:

$$\frac{\partial C_1}{\partial \alpha_s} 4\pi\beta + \frac{\partial C_1}{\partial \ln \mu} = 4\pi\alpha_s \frac{d}{d\alpha_s} \left(\frac{\beta}{\alpha_s} \right) C_1. \quad (4.69)$$

The β -function has the general expansion

$$\beta = \left(\frac{\alpha_s}{4\pi} \right)^2 \sum_{i=0} \beta_i \left(\frac{\alpha_s}{4\pi} \right)^i. \quad (4.70)$$

For example, at one-, and two-loop level, it can be shown [73–78]

$$\begin{aligned} \beta_0 &= -\frac{11}{3}C_A + \frac{4}{3}T_F n_f, \\ \beta_1 &= -\frac{34}{3}C_A^2 + \frac{20}{3}C_A T_F n_f + 4C_F T_F n_f. \end{aligned} \quad (4.71)$$

We can solve the partial differential equation in Eq. (4.69) perturbatively by proposing the Ansatz

$$\begin{aligned} C_1 &= \frac{\alpha_s}{4\pi} C_1^{(0,0)} + \left(\frac{\alpha_s}{4\pi} \right)^2 \left(C_1^{(1,0)} + C_1^{(1,1)} \ln \frac{\mu}{\mu_0} \right) \\ &\quad + \left(\frac{\alpha_s}{4\pi} \right)^3 \left(C_1^{(2,0)} + C_1^{(2,1)} \ln \frac{\mu}{\mu_0} + C_1^{(2,2)} \ln^2 \frac{\mu}{\mu_0} \right) + \dots. \end{aligned} \quad (4.72)$$

The coefficients without logarithms, $C_1^{(i,0)}$, mark the initial conditions; they need to be matched to the full theory in the infinite mass limit. The coefficients of the logarithms, on the other hand, can be determined through a comparison of coefficients; they read:

$$\begin{aligned} C_1^{(1,1)} &= 0, \\ C_1^{(2,1)} &= C_1^{(0,0)} \beta_1 - C_1^{(1,0)} \beta_0, \quad C_1^{(2,2)} = 0, \\ C_1^{(3,1)} &= 2C_1^{(0,0)} \beta_2 - 2C_1^{(2,0)} \beta_0, \quad C_1^{(3,2)} = \beta_0^2 C_1^{(1,0)} - \beta_0 \beta_1 C_1^{(0,0)}, \quad C_1^{(3,3)} = 0. \end{aligned} \quad (4.73)$$

It is clear from the structure of the differential equation that all coefficients $C_1^{(i,i)}$ are indeed zero except for $C_1^{(0,0)}$.

4.2.2 Matching of Wilson Coefficients

By expanding the Higgs-gluon form factor for large quark masses, we were able to determine the LO Wilson coefficient (see Eq. (4.24)). Of course, if we needed the full Higgs-gluon form factor to determine the Wilson coefficient, the HTL would be of little use, as it would not provide any simplifications. Fortunately, the large quark mass limit can already be used at the

integrand level using the large mass expansion, thus tremendously simplifying the computation of the amplitudes.

Alternatively, one may find the matching coefficients by means of a *low-energy theorem* [79–81], which states:

$$-iG_{\mathcal{O}_1, \dots, \mathcal{O}_n, \bar{q}_i q_i}^B(p_1, \dots, p_{n-1}, 0) = \frac{\partial}{\partial m_i^B} G_{\mathcal{O}_1, \dots, \mathcal{O}_n}^B(p_1, \dots, p_{n-1}). \quad (4.74)$$

Here, $\mathcal{O}_1, \dots, \mathcal{O}_n$ are local operators and $G_{\mathcal{O}_1, \dots}$ denotes the momentum space representation of the corresponding Green's functions

$$\begin{aligned} & \int \left(\prod_{i=1}^n d^d x_i e^{ip_i \cdot x_i} \right) \langle \Omega | T [\mathcal{O}_1^B(x_1) \dots \mathcal{O}_n^B(x_n)] | \Omega \rangle \\ & \equiv (2\pi)^d \delta^{(d)} \left(\sum_{i=1}^n p_i \right) G_{\mathcal{O}_1, \dots, \mathcal{O}_n}^B(p_1, \dots, p_{n-1}). \end{aligned} \quad (4.75)$$

$|\Omega\rangle$ hereby denotes the vacuum state of the interacting theory and T is the *time ordering operator*. The theorem relates the mass derivative of a Green's function to a Green's function of the same operators but with the insertion of $\bar{q}_i q_i$ at zero momentum.

The theorem follows upon application of the *Gell-Mann–Low formula*

$$\begin{aligned} \frac{\partial}{\partial m_i^B} \langle \Omega | T [\mathcal{O}_1^B(x_1) \dots \mathcal{O}_n^B(x_n)] | \Omega \rangle &= \mathcal{N} \langle 0 | T [\mathcal{O}_{1,I}^B(x_1) \dots \mathcal{O}_{n,I}^B(x_n) \\ &\times (-i) \int d^d x \left(1 + \frac{H_I^B(x)}{v} \right) \bar{q}_i^B(x) q_i^B(x) \exp \left(-i \int d^d z \mathcal{H}_{\text{int},I}^B(z) \right)] | 0 \rangle. \end{aligned} \quad (4.76)$$

The subscript I indicates interaction picture fields, $|0\rangle$ is the vacuum state, now of the free theory, and \mathcal{H}_{int} is the interaction part of the *Hamiltonian*. The normalization factor \mathcal{N} is defined as

$$\mathcal{N}^{-1} = \langle 0 | T \exp \left(-i \int d^d z \mathcal{H}_{\text{int},I}^B(z) \right) | 0 \rangle, \quad (4.77)$$

and it cancels the disconnected contributions of the numerator on the right-hand side of Eq. (4.76). In the absence of electroweak corrections, we can omit the field of the Higgs⁴ in the integral of Eq. (4.76). This also implies that none of the operators $\mathcal{O}_1, \dots, \mathcal{O}_n$, contain any electroweak fields, which would cause *Wick contractions* with the Higgs. After switching to momentum space, we then immediately arrive at Eq. (4.74).

Since the proof relied on relations at the level of the Lagrangian, the statement is true only for bare amplitudes and Green's functions beyond LO. It can be straightforwardly generalized to include an arbitrary number of massive particles by simply summing over all massive particles. Lastly, we note that the differential operator does not act on any masses present within the operators themselves.

⁴ Not to be confused with the Higgs field.

We can now apply the low-energy theorem to the gluon self-energy. Let us first consider the *amputated* Green's function of two gluons with the insertion of the composite operator $\mathcal{O}_h = \bar{h}^B h^B$, where h indicates a heavy quark field. In momentum space, it reads

$$\begin{aligned} G_{A,A,\mathcal{O}_h}^{B,ab\mu\nu}(p,0) \Big|_{\text{amp.}} &= \int d^d x d^d y e^{ip \cdot (x-y)} \langle \Omega | T \left[A^{B,a\mu}(x) A^{B,b\nu}(y) \mathcal{O}_h(0) \right] | \Omega \rangle \Big|_{\text{amp.}} \\ &\equiv \delta^{ab} \left[-g^{\mu\nu} p^2 G_{A,A,\mathcal{O}_h}^B(p^2) \Big|_{\text{amp.}} + \text{terms proportional to } p^\mu p^\nu \right], \end{aligned} \quad (4.78)$$

where T denotes the time ordering operator and p is the momentum along the gluon line. As discussed in detail above, in the limit of an infinite quark mass $m_h^B \rightarrow \infty$, the operator $\bar{h}^B h^B$ can be expressed as a linear combination of the operators $\mathcal{O}_1, \dots, \mathcal{O}_5$

$$\begin{aligned} G_{A,A,\mathcal{O}_h}^{B,ab\mu\nu}(p,0) \Big|_{\text{amp.}} &\simeq \\ &- \int d^d x d^d y e^{ip \cdot (x-y)} \langle \Omega | T \left[A^{B,a\mu}(x) A^{B,b\nu}(y) \frac{1}{m_h^B} \sum_{i=1}^5 C_i^B \mathcal{O}_i^B(0) \right] | \Omega \rangle \Big|_{\text{amp.}}. \end{aligned} \quad (4.79)$$

The \simeq symbol indicates that the relation holds only up to power corrections of order $1/m_h^B$.

As noted earlier, the operators $\mathcal{O}_1, \dots, \mathcal{O}_5$ are defined in a decoupled theory in which the heavy quark has been integrated out. In the $\overline{\text{MS}}$ scheme, the *Appelquist-Carazzone decoupling theorem* [82] does not hold in its naïve sense, i.e. heavy degrees of freedom, do not decouple at low energy. The standard method to circumvent this issue is by introducing decoupling constants. These relate quantities in the decoupled theory (denoted with a superscript (n_l)) with the full high energy theory:

$$\begin{aligned} g^{B,(n_l)} &= \zeta_g^B g^B, \quad m_i^{B,(n_l)} = \zeta_{m_i}^B m_i^B, \quad \xi^{B,(n_l)} - 1 = \zeta_3^B (\xi^B - 1), \\ q_i^{B,(n_l)} &= \sqrt{\zeta_2^B} q_i^B, \quad A_\mu^{B,(n_l),a} = \sqrt{\zeta_3^B} A_\mu^{B,a}, \quad c^{B,(n_l),a} = \sqrt{\zeta_3^B} c^{B,a}. \end{aligned} \quad (4.80)$$

The purpose of the decoupling constants is to absorb any residual logarithmic dependence on the decoupled fields. The decoupling relations therefore only hold up to power corrections of $1/m_h^2$. The decoupling constants are functions of g^B, m_i^B and the scale μ , but the function arguments are left implicit. The amputated Green's function then becomes⁵

$$\begin{aligned} G_{A,A,\mathcal{O}_h}^{B,ab\mu\nu}(p,0) \Big|_{\text{amp.}} &\simeq \\ &- \zeta_3^B \int d^d x d^d y e^{ip \cdot (x-y)} \langle \Omega | T \left[A^{B,(n_l),a\mu}(x) A^{B,(n_l),b\nu}(y) \frac{1}{m_h^B} \sum_{i=1}^5 C_i^B \mathcal{O}_i^B(0) \right] | \Omega \rangle \Big|_{\text{amp.}} \end{aligned} \quad (4.81)$$

At LO in α_s , we will have only contributions from the operators \mathcal{O}_1 and \mathcal{O}_4 , as all other operators would yield disconnected contributions

$$\begin{aligned} G_{A,A,\mathcal{O}_h}^{B,ab\mu\nu}(p,0) \Big|_{\text{amp.}} &\simeq \\ &- \frac{1}{m_h^B} \delta^{ab} \left(-g^{\mu\nu} p^2 \zeta_3^B (C_1^B + 2C_4^B) + \mathcal{O}(\alpha_s) \right) + \text{terms proportional to } p^\mu p^\nu. \end{aligned} \quad (4.82)$$

We now set the mass of light quarks in the QCD Lagrangian to zero; however, their masses as defined in Eq. (4.45) may still be non-vanishing. In the limit of vanishing gluon momentum

⁵ Note that the **amputated** Green's function scales with the inverse of the fields.

$p \rightarrow 0$, the coefficient of the transverse part does not receive any α_s -corrections in DR since all Feynman integrals involved are necessarily scaleless⁶. We have thus shown the all-orders result:

$$G_{A,A,\mathcal{O}_h}^B(0,0) \Big|_{\text{amp.}} \simeq -\frac{1}{m_h^B} \zeta_3^B (C_1^B + 2C_4^B). \quad (4.83)$$

By applying the LSZ reduction formula, we can rewrite the amputated Green's functions in terms of connected ones. The operator \mathcal{O}_h is hereby irrelevant as it is not considered to be external. Eq. (4.74) thus holds for regular, connected and 1PI Green's functions. Application of Eq. (4.74) then yields

$$(C_1^B + 2C_4^B) = \frac{\partial \ln \zeta_3^B}{\partial \ln m_h^B}. \quad (4.84)$$

We can repeat the same analysis for $G_{\bar{c},c,\mathcal{O}_h}(p,0)$ and $G_{\bar{c},c,g,\mathcal{O}_h}(p,p,0)$; in the limit as $p \rightarrow 0$, we obtain

$$\begin{aligned} (-C_4^B - C_5^B) &= \frac{\partial \ln \tilde{\zeta}_3^B}{\partial \ln m_h^B}, \\ (-C_5^B) &= \frac{\partial}{\partial \ln m_h^B} \ln \left(\tilde{\zeta}_3^B \sqrt{\zeta_3^B \zeta_g^B} \right). \end{aligned} \quad (4.85)$$

Eqs. (4.84) and (4.85) form a linear system of equations that we can solve for the Wilson coefficients. The solution for the physical Wilson coefficient reads

$$C_1^B = -\frac{\partial \ln \zeta_g^B}{\partial \ln m_h^B}. \quad (4.86)$$

In the $\overline{\text{MS}}$ scheme, the renormalization constant of the heavy-quark mass is independent of the mass; we can thus write

$$\frac{\partial}{\partial \ln m_h^B} = \frac{\partial}{\partial \ln m_h}. \quad (4.87)$$

With the renormalization matrix in Eq. (4.62), we can then find the renormalized version of Eq. (4.86)

$$C_1 = -\frac{\partial \ln \zeta_g^2}{\partial \ln m_h}. \quad (4.88)$$

The decoupling constants are known at two-, three-[83], and four-loop [84, 85] order. Note that we only require the logarithmic dependence of decoupling constants to obtain the Wilson coefficients. The logarithmic structure on the other hand may be reconstructed from lower order terms in combination with the β -function and the mass anomalous dimension [81]. The four-loop decoupling constant is therefore sufficient to match the Wilson coefficient up to

⁶ Typically, limits like $p \rightarrow 0$ do not permute with the integrals. However, as we are working in DR, we can always find a dimension d for which the appearing integral is vanishing in the limit $p \rightarrow 0$, as it can only depend on p^2 . Indeed, any such integral with positive mass dimension will necessarily vanish in this limit. We can then argue based on the identify theorem that the integral must in fact be vanishing for all d .

$N^4\text{LO}$. Here, we present only the Wilson coefficient up to $N^3\text{LO}$, as it is the highest order for which full cross section calculations are available at present:

$$\begin{aligned} C_1^{(0,0)} &= -\frac{4}{3}, \\ C_1^{(1,0)} &= -\frac{44}{3}, \\ C_1^{(2,0)} &= -\frac{5554}{27} + \frac{76}{3} \ln\left(\frac{m_h^2}{\mu^2}\right) + n_l \left[\frac{134}{9} + \frac{64}{9} \ln\left(\frac{m_h^2}{\mu^2}\right) \right], \\ C_1^{(3,0)} &= \frac{2892659}{486} - \frac{897943}{108} \zeta(3) + \frac{13864}{27} \ln\left(\frac{m_h^2}{\mu^2}\right) - \frac{836}{3} \ln^2\left(\frac{m_h^2}{\mu^2}\right) - \frac{64}{81} \ln^3\left(\frac{m_h^2}{\mu^2}\right) \\ &\quad + n_l \left[-\frac{40291}{243} + \frac{110779}{162} \zeta(3) + \frac{7040}{81} \ln\left(\frac{m_h^2}{\mu^2}\right) - \frac{184}{3} \ln^2\left(\frac{m_h^2}{\mu^2}\right) \right] \\ &\quad + n_l^2 \left[\frac{13730}{729} + \frac{308}{81} \ln\left(\frac{m_h^2}{\mu^2}\right) + \frac{128}{27} \ln^2\left(\frac{m_h^2}{\mu^2}\right) \right]. \end{aligned} \quad (4.89)$$

Notice that the decoupling constant ζ_g is a function of $\alpha_s^{(n_l+1)}$, i.e. we must recursively apply the decoupling relations (4.80) to express everything in terms of decoupled quantities. The heavy mass m_h is the $\overline{\text{MS}}$ mass.

4.2.3 Higher-Order Corrections

With the effective theory matched, we are ready to discuss higher order corrections to the Higgs production cross section. In the HTL, the cross section has been computed up to $N^3\text{LO}$ in the literature [19, 22, 23, 86]. Here, we will briefly recapitulate the NLO calculation, as it nicely illustrates the methods introduced in Section 2.1, and already allows for some important observations.

We start with the computation of the hard scattering amplitudes. At NLO, we require the one-loop Higgs-gluon form factor, and the tree-level amplitudes for $q\bar{q} \rightarrow Hg$, $qg \rightarrow Hq$, and $gg \rightarrow Hg$.

The careful reader might wonder why we do not need to compute the $q\bar{q} \rightarrow H$ amplitude. The reason is that these amplitudes will be zero at all orders. Indeed, the corresponding amplitude takes on a form

$$\mathcal{M}_{q\bar{q} \rightarrow H} = i \frac{\alpha_s}{\pi} \bar{v}(p_2) [\dots] u(p_1) \delta_{c_1 c_2} \frac{1}{v} \mathcal{C}_{q\bar{q}H}, \quad (4.90)$$

where the dots indicate an a priori unknown number of γ -matrices. However, since there is no external vector field, the γ -matrices must be contracted. The only available objects to contract a γ -matrix with are either other γ -matrices, or the momenta p_1 or p_2 . Contractions among γ -matrices can always be simplified by applying the anti-commutation relations provided by the Clifford algebra of the γ -matrices. Afterwards, we are left only with contractions involving p_1 and p_2 . These, on the other hand, vanish in Eq. (4.90) due to the equation of motion.

The virtual contributions to the cross sections result from evaluating the Feynman diagrams in Fig. 4.6. The result is the NLO correction to the Higgs-gluon form factor in the HTL and reads

$$\mathcal{C}(0) = \frac{1}{3} \left\{ 1 + \frac{\alpha_s}{\pi} \left(-\frac{m_H^2 + i0^+}{\mu^2} \right)^{-\epsilon} \left(-\frac{3}{2} \frac{1}{\epsilon^2} + \frac{11}{4} + \frac{\pi^2}{8} \right) \right\}. \quad (4.91)$$

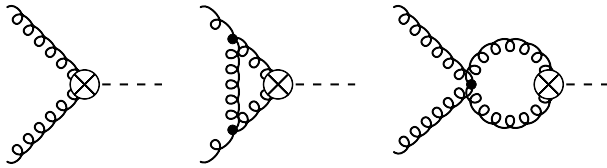


Figure 4.6: One-loop corrections to the Higgs-gluon form factor. The first diagram contributes through the NLO Wilson coefficient.

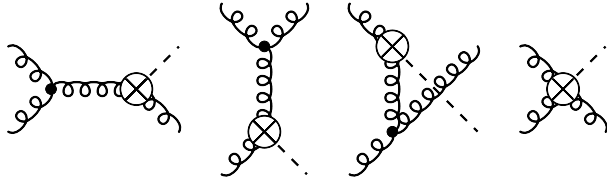


Figure 4.7: Feynman diagrams for the real-radiation corrections in the gluon-gluon channel.

Using Eq. (4.14) for the partonic $gg \rightarrow H$ cross section, we then find

$$\hat{\sigma}_{gg \rightarrow H} = \frac{\pi}{576v^2} \xi \left(\frac{\alpha_s}{\pi} \right)^2 \delta(1-\xi) \times \left[(1+\epsilon + \mathcal{O}(\epsilon^2)) + \frac{\alpha_s}{\pi} \left(\frac{m_H^2}{\mu^2} \right)^{-\epsilon} \left(-\frac{3}{\epsilon^2} - \frac{3}{\epsilon} + \frac{5}{2} + \frac{7\pi^2}{4} + \mathcal{O}(\epsilon) \right) + \mathcal{O}(\alpha_s^2) \right] \quad (4.92)$$

where we defined ξ as the square of the Higgs mass over the partonic center-of-mass energy

$$\xi = \frac{m_H^2}{s} = \frac{m_H^2}{\tau S}. \quad (4.93)$$

As expected, the NLO partonic cross section is not finite by itself because the IR divergences only cancel in inclusive observables. Therefore, we must also compute the real-radiation corrections as well as the contributions from collinear renormalization. For the former, we evaluate the diagrams shown in Fig. 4.7 and obtain the averaged squared amplitude

$$\overline{|\mathcal{M}_{gg \rightarrow Hg}|^2} = \frac{1}{N_A^2 4(1-\epsilon)^2} \frac{\alpha_s^3}{v^2} \left(\frac{32}{3\pi} \right) \left[(1-2\epsilon) \frac{m_H^8 + s^4 + t^4 + u^4}{stu} + \frac{\epsilon}{2} \frac{(m_H^4 + s^2 + t^2 + u^2)^2}{stu} \right], \quad (4.94)$$

where N_A is the dimension of the adjoint representation, i.e. $N_A = N^2 - 1$ for $SU(N)$ groups. The symbols s , t and u denote the usual *Mandelstam variables*. Since the Mandelstam variables are not completely independent, as they must satisfy

$$s + t + u = m_H^2, \quad (4.95)$$

the squared matrix element only depends on the final state momenta through t or u . The phase-space integral is $2 \times d$ dimensional. We can reduce one of the d dimensional integrals via the momentum conserving delta function. Using spherical coordinates and the remaining two delta functions which ensure on-shellness of the Higgs and the final state gluon, we can carry out the energy and momentum-magnitude integral explicitly. This is particularly simple

in the center-of-mass frame. We are hence left with an integral over the S_1^{d-2} sphere. If we now apply the recursion relation

$$\int_{S_1^{d-2}} d\Omega = \int_{-1}^1 d\cos\theta \sin^{d-4}\theta \int_{S_1^{d-3}} d\Omega, \quad (4.96)$$

and use that the amplitude only depends on the azimuthal angle, i.e. the scattering angle of the Higgs (or gluon), we can carry out the integral over the S_1^{d-3} sphere explicitly. In the end, the phase-space integral becomes a single one-dimensional integral

$$\text{P.S.} = \frac{1}{8\pi} \frac{1}{\Gamma(1-\epsilon)} \left(\frac{s}{\mu^2 e^{\gamma_E}} \right)^{-\epsilon} (1-\xi)^{1-2\epsilon} \Theta(1-\xi) \int_0^1 d\omega \omega^{-\epsilon} (1-\omega)^{-\epsilon}, \quad (4.97)$$

where ω is related to the scattering angle of the Higgs via

$$\omega = \frac{1 + \cos\theta}{2}. \quad (4.98)$$

The amplitude in Eq. (4.94) is proportional to $1/tu$, i.e. it diverges if the final state gluon becomes collinear to one of the initial-state gluons. Consequently, we expect the appearance of poles once we perform the phase-space integration. Indeed, we find after a straightforward integration

$$\begin{aligned} \hat{\sigma}_{gg \rightarrow Hg} &= \frac{1}{576\pi^2} \frac{\alpha_s}{v^2} (1-\xi)^{-1-2\epsilon} \left(\frac{s}{\mu^2} \right)^{-\epsilon} \Theta(1-\xi) \\ &\times \left[-\frac{3}{\epsilon} (1+\xi^4 + (1-\xi)^4) - \frac{11}{2} (1-\xi)^4 - 6(1-\xi + \xi^2)^2 + \epsilon \left(\frac{3\pi^2}{2} - 6 + (1-\xi) \cdot (\dots) \right) \right]. \end{aligned} \quad (4.99)$$

The cross section also has a soft singularity at $\xi \rightarrow 1$, which can be regulated by applying the distributional identity in Eq. (2.33). The $\mathcal{O}(\epsilon)$ terms proportional to $(1-\xi)$ that are only hinted at in Eq. (4.99) will hence not contribute as they are only integrated together with the delta function $\delta(1-\xi)$. The final result then reads

$$\begin{aligned} \hat{\sigma}_{gg \rightarrow Hg} &= \frac{1}{576\pi^2} \frac{\alpha_s^3}{v^2} \left(\frac{s}{\mu^2} \right)^{-\epsilon} \Theta(1-\xi) \left\{ \left[\frac{3}{\epsilon^2} + \frac{3}{\epsilon} + 3 - \frac{3\pi^2}{4} \right] \delta(1-\xi) \right. \\ &- \frac{6\xi}{\epsilon} \left[\frac{\xi}{(1-\xi)_+} + \frac{1-\xi}{\xi} + \xi(1-\xi) \right] (1+\epsilon) - \frac{11}{2} (1-\xi)^3 \\ &\left. + 6 \left(\frac{\log(1-\xi)}{1-\xi} \right)_+ [1 + \xi^4 + (1-\xi)^4] \right\}. \end{aligned} \quad (4.100)$$

The poles proportional to the delta function $\delta(1-\xi)$ exactly cancel between real (4.100) and virtual contributions (4.92). The remaining divergences should cancel after coupling and collinear renormalization. According to Eq. (2.26), the additional contribution from collinear renormalization is

$$\hat{\sigma}_{gg \rightarrow Hg}^C = 2 \times \frac{\alpha_s}{2\pi} \frac{1}{\epsilon} \int_0^1 dz P_{gg}^{(0)}(z) \hat{\sigma}_{gg \rightarrow H}(zs) = \frac{1}{576\pi^2} \frac{\alpha_s^3}{v^2} \frac{1}{\epsilon} \xi P_{gg}(\xi) (1+\epsilon). \quad (4.101)$$

With the definition of the splitting kernel in Eq. (2.15), we see that the remaining poles in the real-radiation contribution are indeed canceled. The additional pole introduced by the

collinear renormalization is finally canceled by the charge renormalization. Gathering the fruits of our labor, we determined that the inclusive partonic cross section at NLO reads

$$\begin{aligned} \hat{\sigma}_{gg \rightarrow HX} = & \frac{\alpha_s^2}{576\pi v^2} \Theta(1-\xi) \left\{ \delta(1-\xi) \right. \\ & + \frac{\alpha_s}{\pi} \left[\delta(1-\xi) \left(\pi^2 + \frac{11}{2} \right) - \frac{11}{2} (1-\xi)^3 + 6 (1+\xi^4 + (1-\xi)^4) \left(\frac{\log(1-\xi)}{1-\xi} \right)_+ \right. \\ & \left. \left. + \xi P_{gg}(\xi) \log \left(\frac{s}{\mu^2} \right) \right] \right\}. \end{aligned} \quad (4.102)$$

We can carry out the same analysis for the $q\bar{q}$ and qg channel. The relevant Feynman diagrams are depicted in Fig. 4.8. The amplitude for $q\bar{q} \rightarrow Hg$ does not exhibit any collinear or soft

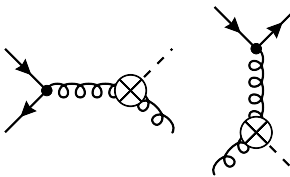


Figure 4.8: Feynman diagrams contributing to the $q\bar{q}$ (left) and qg (right) channel of the Higgs production cross section.

divergences, rendering collinear renormalization unnecessary. The result for the cross section reads

$$\hat{\sigma}_{q\bar{q} \rightarrow Hg} = \frac{1}{486\pi^2} \frac{\alpha_s^3}{v^2} \Theta(1-\xi) (1-\xi)^3. \quad (4.103)$$

The qg -channel, on the other hand, has a collinear divergence when the final state quark becomes collinear to the initial-state quark. After collinear renormalization, we find for the cross section

$$\begin{aligned} \hat{\sigma}_{qg \rightarrow Hg} + \hat{\sigma}_{qg \rightarrow Hg}^C = & \frac{\alpha_s^3}{576\pi^2 v^2} \Theta(1-\xi) \\ & \times \left\{ (1-\xi) \frac{3\xi-7}{3} + \frac{1}{2} \xi P_{qg}(\xi) \left[1 + \log \left(\frac{s}{\mu^2} \right) + 2 \log(1-\xi) \right] \right\}. \end{aligned} \quad (4.104)$$

After convolution of the partonic cross section with the partonic luminosity we get the hadronic cross section, which is displayed in Fig. 4.9 as a function of the hadronic center-of-mass energy. The cross section is split into the various channels. The soft + virtual channel denotes all contributions which originate from integrating the delta function $\delta(1-\xi)$ and irreducible plus distributions, i.e. terms of the form

$$\left(\frac{f(\xi)}{1-\xi} \right)_+ \mathcal{O}((1-\xi)^0). \quad (4.105)$$

At NLO, only gluon-induced Higgs production (see Eq. (4.102)) contributes to the soft + virtual channel.

The majority of the hadronic cross section is due to a gluon-gluon initial state, making up more than 95% of the total cross section over the full spectrum of energies. Roughly half of

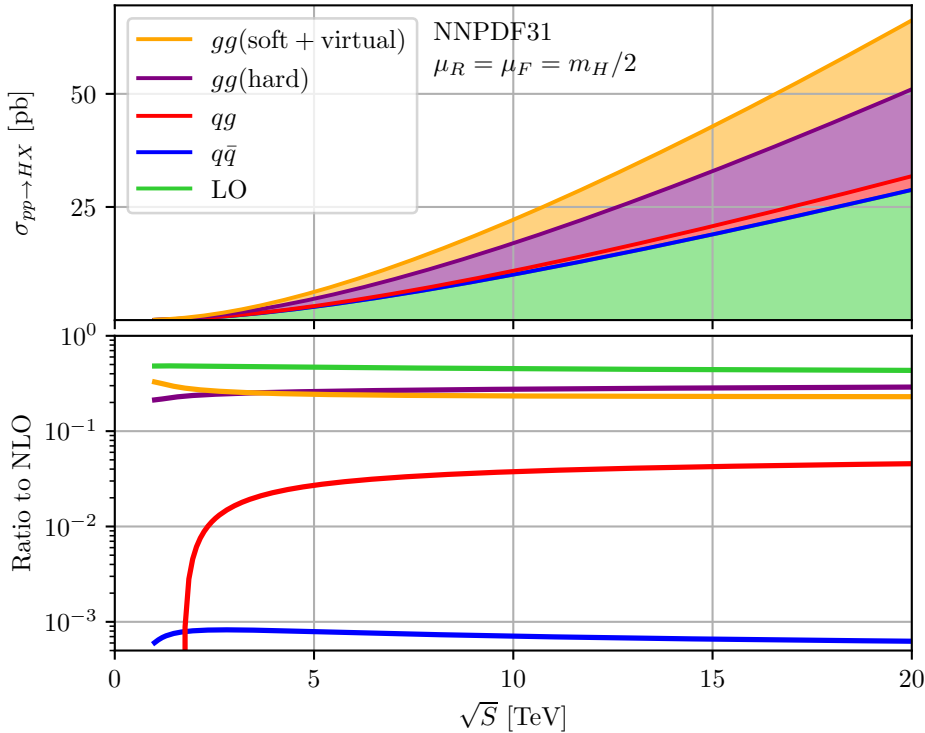


Figure 4.9: Hadronic cross section as a function of the hadronic center-of-mass energy. The total cross section is partitioned into its various channels. The channel denoted *soft + virtual* collects the leading terms of the threshold expansion around $(1 - \xi)$ in Eq. (4.102), that is all terms proportional to $\delta(1 - \xi)$ and irreducible plus distributions. The lower plot shows the ratio of the various channels to the NLO cross section. The computational setup is described in the Conventions.

this contribution comes from LO. The other half is composed, yet again, of roughly two equal parts, the soft + virtual contribution and the remaining real-radiation part. The quark-gluon initial state has the second-largest impact, whereas quark-quark induced Higgs production is completely negligible, contributing below 1%. The large suppression of the $q\bar{q}$ channel is almost entirely due to the reduced partonic luminosity of the channel. Indeed, from Fig. 2.2, we see that the $q\bar{q}$ flux is roughly 30 times smaller than the qg one. This is also the order of magnitude of the ratio of the qg and $q\bar{q}$ induced Higgs production cross section.

The gluon-gluon and quark-gluon luminosities, on the other hand, are rather similar, especially close to the production threshold, where most of the contributions to the cross section originate, as larger values of ξ are suppressed by \mathcal{L}/τ . Yet, we observe that the quark-gluon channel contributes almost an order of magnitude less than the gluon-gluon channel. To investigate the origin of this suppression, we can look at the coefficient of the logarithm $\log(\mu^2)$ which is predetermined by the RGE

$$\frac{\partial \hat{\sigma}_{qg \rightarrow Hq}}{\partial \log \mu^2} = -\frac{\alpha_s}{2\pi} \int_0^1 d\xi P_{qg}(\xi) \hat{\sigma}_{gg \rightarrow H}, \quad \frac{\partial \hat{\sigma}_{gg \rightarrow Hg}}{\partial \log \mu^2} = -2 \times \frac{\alpha_s}{2\pi} \int_0^1 d\xi P_{gg}(\xi) \hat{\sigma}_{gg \rightarrow H}. \quad (4.106)$$

At the threshold, the ratio of the logarithmic coefficients of the quark-gluon and the gluon-gluon channel is thus $C_F/(4C_A) = 1/9$. Incidentally, this is also roughly the ratio we observe between the cross sections of the two channels. The origin of the suppression is thus partly due to the difference in the color factor and the additional combinatorial factors in the gluon-gluon channel.

Since the NLO corrections are of the same magnitude as the LO cross section, the perturbative result is not yet reliable. One would need to go to even more loops and higher multiplicities in the hope to reach perturbative convergence.

4.2.4 Phenomenological Application

Having discussed the HTL at length, it is important to investigate how well the approximation works for phenomenological applications. In Fig. 4.10, we show the relative error of the cross section in the HTL compared to the results with a finite quark mass for different powers of α_s in the various partonic channels.

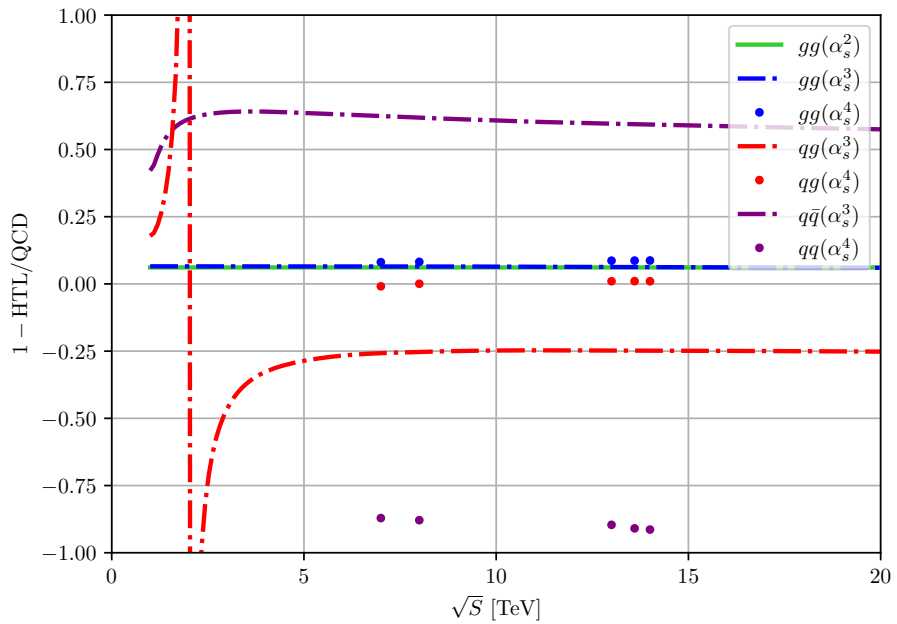


Figure 4.10: Relative error of the HTL compared to the results with finite top-quark mass for various center-of-mass energies. Displayed are contributions to the cross section in each partonic channel. The computational setup is described in the Conventions. The methods to compute the NNLO results with finite top-quark mass are described in Chapter 5.

At LO, the HTL underestimates the cross section by around 6.5%. In the HTL, the Higgs-gluon form factor is accurate up to power corrections of order $z = m_H^2/4m_t^2 \approx 13\%$, so the observed accuracy of the approximation aligns with our expectations. For radiative corrections, $m_H^2/m_t^2 \approx 52\%$ is the more natural expansion parameter and the quark-gluon as well as the quark-quark channel show that they are indeed only roughly 50% accurate.

The gluon-gluon channel on the other hand shows a remarkable property: the accuracy of the HTL stays quite constant across perturbative orders in α_s . In our opinion, this feed is explained by the fact that much of the structure of the perturbative corrections is dictated by lower orders, and that, for this channel in particular, these kinds of corrections turn out to be numerically large. Indeed, we can apply *Catani's I operator* [87] to predict the poles, as well

as the overall factor $(-m_H^2/\mu^2)^{-\epsilon}$, of the Higgs-gluon form factor in Eq. (4.91). So the part of the partonic cross section which is derived from LO reads

$$\begin{aligned} \hat{\sigma}_{gg \rightarrow H} \Big|_{\infty \sigma_{gg \rightarrow H}^{(0)}} &= \frac{\pi}{576v^2} \xi \left(\frac{\alpha_s}{\pi} \right)^2 \delta(1 - \xi) \\ &\times \left[(1 + \epsilon + \mathcal{O}(\epsilon^2)) + \frac{\alpha_s}{\pi} \left(\frac{m_H^2}{\mu^2} \right)^{-\epsilon} \left(-\frac{3}{\epsilon^2} - \frac{3}{\epsilon} - 3 + \frac{3\pi^2}{2} + \mathcal{O}(\epsilon) \right) + \mathcal{O}(\alpha_s^2) \right]. \end{aligned} \quad (4.107)$$

Numerically, the finite part is largely dominated by the π^2 term which originated from the analytic continuation of the Sudakov (double) logarithm. The analytic continuation needed at time-like momentum transfer thus causes a large logarithm. The logarithm, on the other hand, stems from a soft-gluon exchange in the loop.

For the real-radiation cross section, we can once again already anticipate the initial-state-collinear as well as the soft divergences

$$\begin{aligned} \hat{\sigma}_{gg \rightarrow Hg} &= \frac{1}{576\pi^2} \frac{\alpha_s}{v} (1 - \xi)^{-1-2\epsilon} \left(\frac{s}{\mu^2} \right)^{-\epsilon} \Theta(1 - \xi) \\ &\times \left[-\frac{1}{\epsilon} \xi (1 - \xi) P_{gg}^{(0)}(\xi) \frac{2(-1+2\epsilon)\Gamma(-\epsilon)}{\Gamma(3-2\epsilon)} + (1 - \xi)^2 \cdot (\dots) \right]. \end{aligned} \quad (4.108)$$

The $(1 - \xi)^2$ terms, which we denoted by (\dots) are finite and regular in the soft limit $\xi \rightarrow 1$. We know that there cannot be any terms of order $(1 - \xi)$ apart from those in the splitting function because every term in the matrix element (4.94) which is constant in the soft limit, still has collinear divergences in the phase-space. I.e. all next to soft contributions are captured in the splitting function. In fact, if we compare with the cross section in Eq. (4.99), then we see that the actual lowest order term is even $(1 - \xi)^4$.

The partonic luminosity together with the factor $1/\tau$ causes a strong enhancement of the phase-space region close to the threshold $\xi \rightarrow 1$ or $\tau \rightarrow m_H^2/S$. Therefore, the hadronic cross section will be well approximated by convolving the inclusive cross section

$$\begin{aligned} \hat{\sigma}_{gg \rightarrow HX} \Big|_{\infty \sigma_{gg \rightarrow H}^{(0)}} &= \frac{\alpha_s^2}{576\pi v^2} \Theta(1 - \xi) \left\{ \delta(1 - \xi) \right. \\ &+ \frac{\alpha_s}{\pi} \left[\delta(1 - \xi) \pi^2 \left(\frac{3}{4} + \mathcal{O}(1/\pi^2) \right) + 6 (1 + \xi^4 + (1 - \xi)^4) \left(\frac{\log(1 - \xi)}{1 - \xi} \right)_+ \right. \\ &\quad \left. \left. + \xi P_{gg}(\xi) \log \left(\frac{s}{\mu^2} \right) \right] \right\}. \end{aligned} \quad (4.109)$$

Numerically, we find that the approximation is around 90% accurate at NLO. The main deviations are caused by the soft-virtual channel. We can therefore expect to see deviations in the rescaling factor

$$r^{N^n \text{LO}} = \frac{\sigma_{pp \rightarrow HX}^{\text{QCD}, N^n \text{LO}}}{\sigma_{pp \rightarrow HX}^{\text{HTL}, N^n \text{LO}}} \quad (4.110)$$

across perturbative orders of the order of $10\% \times m_H^2/4m_t^2 \approx 1\%$ based on the gluon-gluon channel alone. The quark-gluon channel contributed only 3% to the cross section at NLO, and the accuracy of the HTL is only about 50% accurate in this channel. In total, we can therefore expect to see deviations in $r^{N^n \text{LO}}$ of the order of 2% across perturbative orders.

Strictly speaking, our discussion was limited to NLO. However, we claim that most of the arguments are transferable to higher orders in perturbation theory. Indeed, the factor π^2 we received from analytic continuation of the Sudakov logarithm will also be encountered at higher order, and the effects can be resummed to all orders [88]. Ergo, the driving contribution is indeed proportional to the Born cross section. This procedure is also sometimes referred to as π^2 -*resummation* (see Section 4.3.1 for more details). At high orders of perturbation theory, it was demonstrated [86] that the quality of the resummation deteriorates, meaning that the Sudakov logarithms are no longer the driving contributor to the soft-virtual contribution. We can therefore expect to see larger deviations from the exact rescaling at higher orders of perturbation theory. Similarly, our discussion on how to obtain the leading coefficients of the threshold expansion by requiring cancellation of initial-state collinear divergences can also be transferred to higher orders of perturbation theory [89] (see Section 4.3.1 for more details). This way, at $N^n\text{LO}$, it is in principle possible to correctly predict the first n leading logarithms from lower orders, and the leading logarithm is dictated by the LO cross section.

We can exploit the fact that the rescaling parameter only receives small corrections in order to improve the HTL cross section results. This works by rescaling the HTL results by

$$\sigma_{pp \rightarrow HX}^{\text{rHTL}, N^n\text{LO}} = r^{\text{LO}} \sigma_{pp \rightarrow HX}^{\text{HTL}, N^n\text{LO}}, \quad (4.111)$$

where the superscript “rHTL”, now refers to the *rescaled heavy-top limit*. Since the gluon-gluon channel is the dominant production channel and here the rescaling factor remains quite constant across the perturbative orders, the rHTL cross section yields a good approximation ($\sim 2\%$) for the Higgs production cross section⁷.

4.3 THEORY STATUS

Having analyzed the gluon-gluon-fusion Higgs production cross section at LO, and NLO in the HTL, we are now equipped with all concepts to discuss state-of-the-art theory predictions.

As already mentioned, the most precise theoretical predictions come from $N^3\text{LO}$ cross sections in the rHTL [24, 86]. They apply the method of reverse unitarity (see section 2.1.3) to perform the phase-space integration fully analytically. The cross section is calculated in terms of a deep expansion in the threshold parameter $(1 - \xi)$

$$\hat{\sigma}_{ij \rightarrow HX} = \delta_{ig}\delta_{jg}\hat{\sigma}_{\text{SV}} + \sum_{n=0}^N c_{ij}^{(n)}(1 - \xi)^n, \quad (4.112)$$

where $\hat{\sigma}_{\text{SV}}$ is the leading term, the soft-virtual contribution we already encountered, which only constitutes δ -functions and plus-distributions. The soft-virtual contribution has been calculated at $N^3\text{LO}$ in Ref. [90]. Because the partonic luminosity is concentrated heavily around the threshold region, one would expect to see good convergence of the threshold expansion of the hadronic cross section. Indeed, Ref. [24] computed the first 37 terms of the threshold expansion, and found that the hadronic cross section is already well approximated by the first five terms.

In the meantime, results without reliance on the threshold expansion have become available [25], confirming the expected accuracy of the threshold expansion and shifting the total cross section by around $+0.10$ pb at 13 TeV.

⁷ Excluding the effects from light quarks and electroweak corrections.

In Fig. 4.11 we show the results for the gluon-gluon-fusion cross section in the rHTL at various perturbative orders as a function of the hadronic center-of-mass energy.

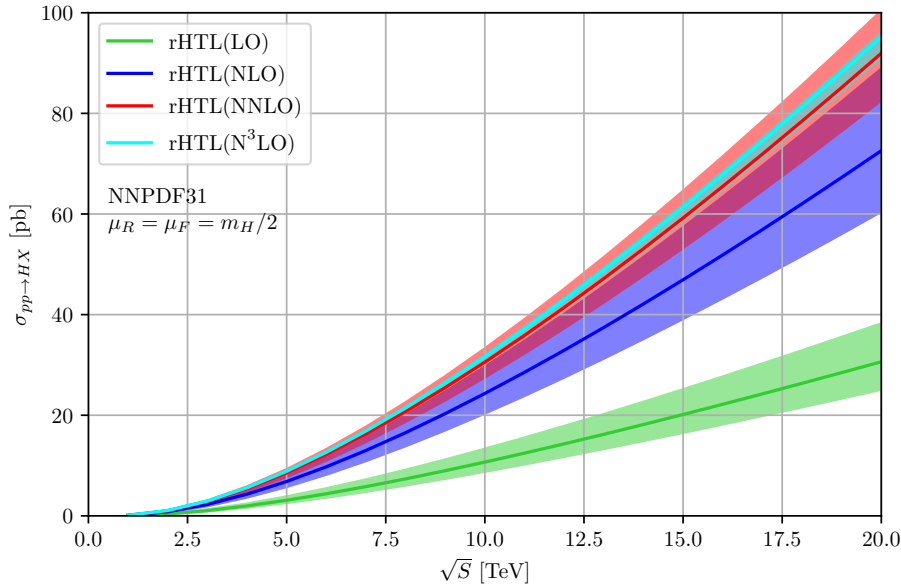


Figure 4.11: Gluon-gluon-fusion hadronic cross section as a function of the center-of-mass energy. Displayed are results computed in the rHTL at various perturbative orders. Transparent bands indicate the scale uncertainty calculated by variation of μ_R in the range $[m_H/4, m_H]$. The computational setup is described in the Conventions. The plot was created with the help of `SusHi` [91, 92].

As we discussed before, the NLO cross section is about twice as large as predicted in the Born approximation. NNLO corrections are still sizeable, contribution roughly 20% to the cross section. The NLO scale uncertainties underestimate the effect of higher orders, as the central NNLO cross section is outside the previous uncertainty bands. Only when we go to N^3LO do we see perturbative convergence and corrections consistent with the previous scale uncertainty bands. The scale uncertainties at this order are below 4% for the displayed collision energies.

At this level of precision, it becomes important to investigate other sources of uncertainty and perform a careful evaluation of their impact on the cross section. The most important sources are:

- The scale uncertainties,
- The PDF uncertainties,
- Uncertainties related to electroweak corrections,
- Uncertainties related to finite top-quark masses,
- Uncertainties related to light quarks.

In the following we will discuss them one-by-one.

4.3.1 Scale Uncertainties

Scale uncertainties serve as an estimate of MHOU. They are typically computed by a 7-point scale variation, meaning that the cross section is evaluated at a central scale μ and the additional 6 points $(\mu_R, \mu_F) = (\mu/2, \mu/2), (\mu/2, \mu), (\mu, \mu/2), (2\mu, \mu), (\mu, 2\mu), (2\mu, 2\mu)$. The envelope of the cross section at the seven points then forms the scale uncertainty. Since neither the renormalization nor the factorization scale are physical, observables like the cross section are in principle independent of these scales. However, as we are truncating the perturbative series at some fixed order, we are left with some residual scale dependence. The scale dependence is therefore a good indicator of missing higher orders. Even so, especially at low orders, the scale uncertainties cannot always be trusted as Fig. 4.11 illustrates instructively.

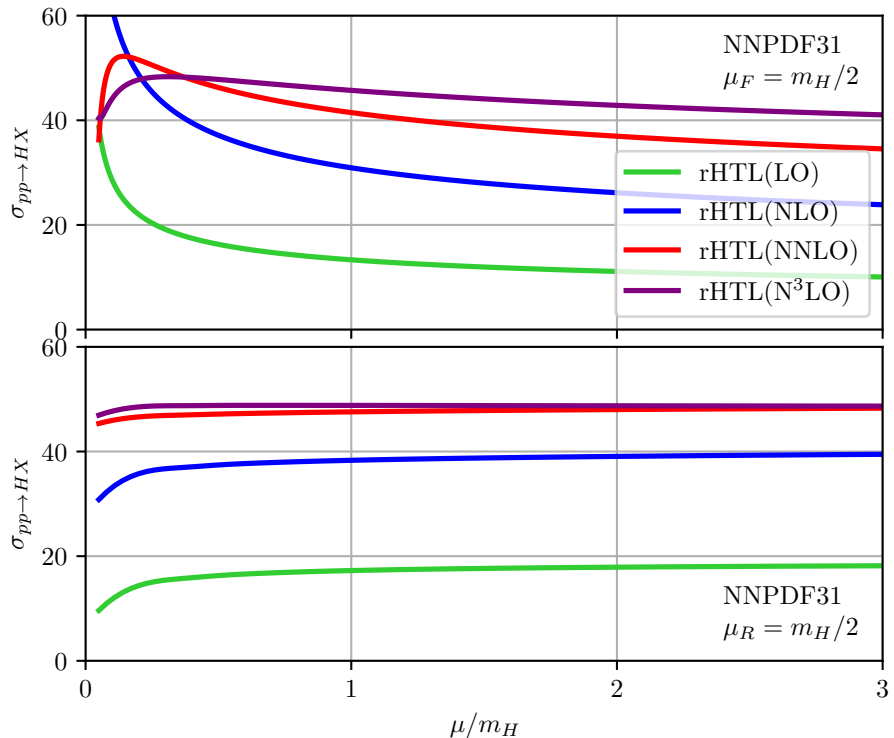


Figure 4.12: Hadronic cross section as a function of the renormalization scale (top panel) and factorization scale (bottom panel). The respective other scale is kept fixed at $m_H/2$. The computational setup is described in the Conventions. The plot was created with the help of `SusHi` [91, 92].

Fig. 4.12 shows the functional dependence of the hadronic cross section on the renormalization and factorization scale for various perturbative orders. We see that there is very little dependence on the factorization scale, i.e. the vast majority of the scale uncertainties derive from the variation of renormalization scale. This also justifies why the scale uncertainties in Fig. 4.11 are computed by only varying the renormalization scale, while the factorization scale was kept fixed at the central value. We also observe that the dependence on the scale nicely stabilizes as we increase the perturbative precision. For the central scale, $\mu_R = \mu_F = m_H/2$ has become the de facto standard for the inclusive cross section and is also the recommendation of the Higgs Working Group [64]. The observed functional dependence in Fig. 4.12 supports this choice, as the N^3LO corrections are minor at this scale and the cross section is particularly flat in this regime. It should be noted that the minor dependence on the factorization scale is

only observed for the total cross section. If instead, we are considering individual production channels, the functional dependence remains very large because the DGLAP equations mix the quark and gluon PDFs.

The scale uncertainties can be further reduced by including higher order corrections. Although full N⁴LO predictions are still beyond the current state-of-the-art in computational capabilities, we can predict at least some parts of the higher order corrections.

Results in the soft-virtual approximation

Since the partonic luminosity is sharply peaked around the threshold (see Fig. 2.2), corresponding to $\xi \rightarrow 1$ (or alternatively $\tau \rightarrow m_H^2/S$), we can get a good approximation of the hadronic cross section by expanding the partonic cross section around the threshold as seen in Eq. (4.112). The leading term, i.e. the soft-virtual approximation has already been computed up to four loops [26] in the HTL. In Tab. 4.2, we show a comparison of the cross section in the

	σ_{rHTL} [pb]	$\Delta\sigma_{\text{rHTL}}$ [pb]	$\Delta\sigma_{\text{s.-v.}}$ [pb]	$\Delta\sigma_{\text{s.-v.}}/\Delta\sigma_{\text{rHTL}}$
LO	16.3	16.3	+16.3	1
NLO	35.1	18.8	+7.8	0.42
NNLO	44.3	9.1	+3.4 ± 4.8	0.37
N ³ LO	45.8	1.6	+1.2 ± 2.2	0.83
N ⁴ LO			+0.14 ± 0.24	

Table 4.2: Comparison of the cross section computed in the full rHTL (σ_{rHTL}) and in the soft-virtual approximation ($\sigma_{\text{s.-v.}}$). $\Delta\sigma_{\text{s.-v.}}$ and $\Delta\sigma_{\text{rHTL}}$ refer to the perturbative correction of the respective order. The assigned uncertainties are computed based on lower orders using $\delta(\Delta\sigma_{\text{s.-v.}}^{\text{N}^n\text{LO}}) = \max\{|1 - \Delta\sigma_{\text{rHTL}}^{\text{NLO}}/\Delta\sigma_{\text{s.-v.}}^{\text{NLO}}|, \dots, |1 - \Delta\sigma_{\text{rHTL}}^{\text{N}^{n-1}\text{LO}}/\Delta\sigma_{\text{s.-v.}}^{\text{N}^{n-1}\text{LO}}|\}\Delta\sigma_{\text{s.-v.}}^{\text{N}^n\text{LO}}$. Results up to N³LO have been computed with `SusHi` using the computational setup described in the Conventions at a hadronic center-of-mass energy of 13 TeV. The N⁴LO results for the soft-virtual approximation were taken from Ref. [26]. Note that the authors of that reference use a slightly altered computational setup.

soft-virtual approximation (rescaled) with the corresponding results in the rHTL. We can see that the approximation is only qualitative, meaning that it only captures the rough magnitude of the contribution. We assigned a conservative error of the soft-virtual approximation based on the order at which the approximation works the worst and then rescaled to the respective order. The soft-virtual approximation is therefore not suited for precision predictions, but can give us valuable insights into the order of magnitude of the corrections.

The soft-virtual approximation can be further improved. As we discussed in Section 4.2.4, the cancellation of initial-state collinear divergences can be leveraged to determine the leading logarithms of the cross section. For example at N⁴LO, the coefficients of the logarithms⁸

$$\log^7(1 - \xi), \log^6(1 - \xi), \text{ and } \log^5(1 - \xi) \quad (4.113)$$

in $c_{ij}^{(0)}$ can be determined. This is especially important to stabilize the factorization scale dependence since otherwise we would introduce an additional contribution to the cross section which is only present in one of the partonic channels, the gluon-gluon channel.

At the central scale of $\mu_R = \mu_F = m_H/2$, the partial N⁴LO contribution shifts the cross section by about +0.3%. Scale uncertainties are reduced from around 4% to below 2%. The systematic uncertainty coming from the truncation of the threshold expansion is estimated by

⁸ In fact, one can also get parts of the $\log^4(1 - \xi)$ coefficient.

comparing the full cross section results with the soft-virtual approximation at lower orders in perturbation theory, and rescaling the error to the N⁴LO correction (see Eq. (6.7)). The error is estimated to be around 0.5% of the total cross section.

Threshold Resummation

The threshold logarithms appearing in $c_{ij}^{(0)}$ can actually be resummed to all orders. The hadronic cross section can be cast into the form

$$\sigma(N) = \sum_{ij} f_i(N, \mu_F) f_j(N, \mu_F) \hat{\sigma}_{ij}(N, \mu_R, \mu_F), \quad (4.114)$$

where we switched from τ -space to N -space by means of a *Mellin transform*

$$\sigma(N) \equiv \int_0^1 d\tau \tau^{N-1} \frac{\sigma(\tau)}{\tau}. \quad (4.115)$$

In N -space, also called *Mellin space*, the threshold region $\tau \rightarrow m_H^2/S$ corresponds to the limit $N \rightarrow \infty$. In this limit, it can be shown [93–96] that the partonic cross section satisfies the resummed form

$$\hat{\sigma}_{ij}(N) = \delta_{ig} \delta_{jg} \hat{\sigma}_{gg \rightarrow H}^{\text{LO}} C_{gg} \exp[\mathcal{G}_H(\log N)] + \mathcal{O}(1/N). \quad (4.116)$$

C_{gg} collects all constant contributions for $N \rightarrow \infty$ and can therefore be extracted from lower orders in the large N limit. $\mathcal{G}_H(\log N)$ contains the threshold logarithms, which get resummed by exponentiation. It requires the cusp anomalous dimension—now known at four-loop accuracy [97]—making it possible to compute the full N³LO + next-to-next-to-next-to-leading logarithm cross section results. The results⁹ [86] show that at the central scale, the fixed and resummed cross section are nearly identical. This can be interpreted as additional validation of our scale choice. Additionally, it confirms the N⁴LO soft virtual approximation, which also found that the corrections at the central scale are very close to zero.

π^2 -Resummation

In Section 4.2.4, we showed that the soft-virtual contribution to the cross section is dominated by a Sudakov logarithm at time-like momentum transfer. This fact can be exploited to predict numerically large coefficients at higher orders and ultimately can be used to perform an all order resummation, sometimes referred to as π^2 -resummation [88].

Since the logarithm stems from a soft-gluon exchange, we can apply techniques from *soft-collinear effective theory* (SCET) [98, 99] to map the Higgs-gluon form factor to a Wilson coefficient of SCET. In SCET, we integrate out all the hard modes so that we can approximate

$$G_{\mu\nu}^a G^{a\mu\nu} \longrightarrow C_S(-q^2) \times (-q^2) g_{\mu\nu} \mathcal{A}_{n\perp}^{a\mu} \mathcal{A}_{\bar{n}\perp}^{a\nu}, \quad (4.117)$$

where $\mathcal{A}_{n\perp}^{a\mu}$ and $\mathcal{A}_{\bar{n}\perp}^{a\nu}$ are effective, gauge invariant operators representing gluons traveling along the light-like directions n and \bar{n} defined by the momenta of the incoming hadrons. q^2 is the square of the momentum of the operator and $C_S(Q^2)$ is the Wilson coefficient. The Higgs-gluon form factor in SCET, and hence the leading logarithmic contribution to the full Higgs-gluon form factor is then simply given by

$$\mathcal{C}(0) \Big|_{\text{SCET}} = C_S(-m_H^2 - i0^+), \quad (4.118)$$

⁹ The authors of that reference use a Padé approximation for the four-loop cusp anomalous dimension, as the full result was still unknown at that point in time. They claim that the approximation is highly accurate.

which we can use to match the Wilson coefficient

$$C_S(Q^2) = 1 + \frac{\alpha_s}{4\pi} C_A \left(-\ln^2 \left(\frac{Q^2}{\mu^2} \right) + \frac{\pi^2}{6} \right). \quad (4.119)$$

The key benefit of working in the SCET framework is that we can now apply RGE methods. Indeed, the Wilson coefficient satisfies the RGE

$$\frac{dC_S}{d \ln \mu} = \left[\Gamma_{\text{cusp}}^A \ln \frac{Q^2}{\mu^2} + \gamma_S^S \right] C_S, \quad (4.120)$$

where Γ_{cusp}^A is the cusp anomalous dimension of Wilson lines with light-like segments in the adjoint representation, and γ_S is the anomalous dimension of the operator. The solution of the differential equation therefore automatically yields a resummed expression of the Higgs-gluon form factor. The solution can be written in terms of the recursive equation

$$|C_S(-m_H^2)|^2 = U(m_H^2) |C_S(-m_H^2)|^2, \\ \text{with } \ln U(m_H^2) = \frac{\alpha_s(m_H^2)}{\pi} \frac{C_A \pi^2}{2} \left\{ 1 + \frac{\alpha_s(m_H^2)}{4\pi} \left[C_A \left(\frac{67}{9} - \frac{\pi^2}{3} \right) - T_F n_l \frac{20}{9} \right] + \mathcal{O}(\alpha_s^2) \right\}. \quad (4.121)$$

We see that the leading π^2 term matches our findings in Eq. (4.107).

The resummation drastically improves results at low order of perturbation theory. However, at higher orders, the quality of the resummation deteriorates. This indicates that at these orders the factors of π^2 are no longer dominant. The procedure should therefore **not** be used to “improve” the N³LO cross sections.

4.3.2 PDF Uncertainties

All results presented so far, were computed using NNLO PDF sets, including all N³LO cross section results. This creates a mismatch between the hard scattering matrix elements and the PDFs, so that the cross sections predictions do not, in fact, have full N³LO accuracy. The reason for applying PDF sets at NNLO accuracy is the lack thereof at N³LO.

PDFs are usually fitted to experimental data and then evolved to the desired scale using the DGLAP equation (2.20). To achieve N³LO accuracy, we therefore require

1. hard scattering amplitudes the PDFs can be matched to,
2. and the N³LO splitting functions for the DGLAP evolution.

Regarding the first point, the exact N³LO coefficient functions for *deep-inelastic scattering* in the massless limit have been known for a long time [100–105], whereas massive coefficient functions are only available in approximation frameworks [106, 107]. Furthermore, N³LO predictions for charged- and neutral-current *Drell-Yan* production are also available, both for the total [108–110] and for differential cross sections [111, 112]. These processes are especially valuable for the matching of the PDFs since they are experimentally very clean.

In Mellin space, the DGLAP equation (2.20) transforms from an integral-differential equation to a mere partial differential equation

$$\frac{\partial f_{H,i}}{\partial \log \mu} = -\gamma_{ij}(N, \alpha_s(\mu)) f_{H,j}(N, \mu), \quad (4.122)$$

where $\gamma_{ij}(N, \alpha_s)$ is related to the Mellin transform of the splitting functions

$$\gamma_{ij}(N, \alpha_s(\mu)) = -\frac{\alpha_s}{\mu} \int_0^1 dx x^{N-1} P_{ij}(x, \alpha_s(\mu)). \quad (4.123)$$

Much progress has been made in evaluating specific moments of the splitting functions [113–119]. Additionally, parts of the splitting functions can be predicted through resummation techniques at low Bjorken- x , at leading logarithmic [120] and next-to-leading logarithmic [121–123] accuracy. Very recently, all $1 \rightarrow 2$ splitting amplitudes were computed fully analytical by Mistlberger et al. [124], these describe the limit of amplitudes in which two of the external partons become collinear. It represents one important ingredient of the splitting kernel.

Although the evolution kernels are not yet fully known, the ingredients we do have can be still be used to at least construct an approximate N³LO PDF set. Results for such PDF sets were recently published by the MSHT [125] as well as the NNPDF [126] collaboration, which were then combined in Ref. [127]. They use the available data for deep-inelastic scattering and Drell-Yan production to fit the PDFs. For the running they use (most of) the known Mellin moments of the splitting kernels and smoothly interpolate between them.

In Fig. 4.13 and Tab. 4.3, we compare the gluon-gluon-fusion rHTL cross section results at N³LO computed with different approximate N³LO PDF sets. The NNPDF40_an3lo_as_01180_mhou

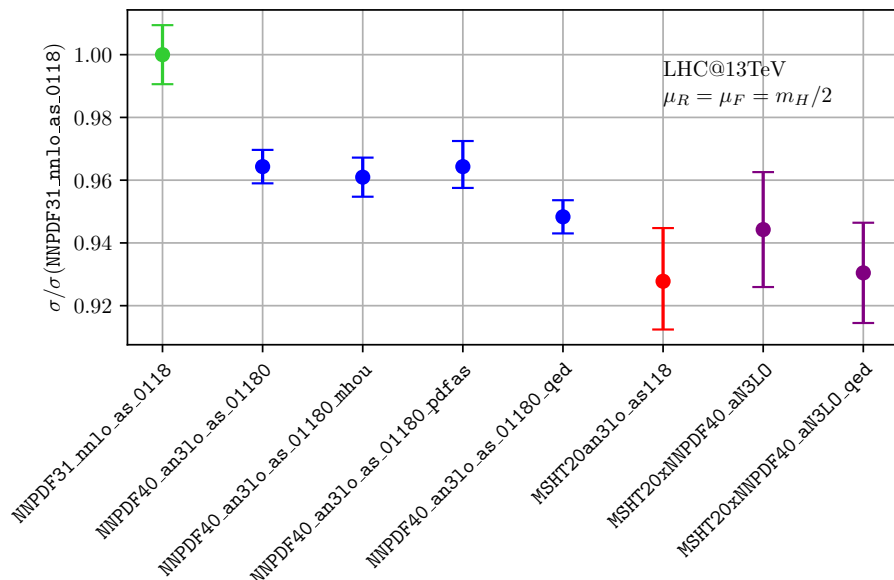


Figure 4.13: The gluon-gluon-fusion cross section at 13 TeV in the rHTL at N³LO for various PDF sets normalized by the cross section computed with the NNPDF31_nnlo_as_0118 PDF set. The provided uncertainties only include the PDF uncertainties. The uncertainty of the normalization is not propagated. The computational setup is described in the Conventions. Results were computed using `iHixs` 2 [128].

includes MHOU. This encompasses the scale uncertainties of the hard scattering matrix elements the PDFs are fitted to, and estimates of the omitted terms in the incomplete N³LO splitting kernels. In the NNPDF40_an3lo_as_01180_pdfas PDF set, the replicas are created with different values of α_s between $\alpha_s(m_Z) = 0.117$ and 0.119 , in order to estimate the α_s uncertainties. PDF sets ending with “_qed”, also include corrections from QED.

PDF	$\sigma_{gg \rightarrow HX}$ [pb]
NNPDF31_nnlo_as_0118	48.8 ± 0.46
NNPDF40_an3lo_as_01180	47.06 ± 0.26
NNPDF40_an3lo_as_01180_mhou	46.90 ± 0.30
NNPDF40_an3lo_as_01180_pdfas	$47.06^{+0.40}_{-0.33}$
NNPDF40_an3lo_as_01180_qed	46.28 ± 0.26
MSHT20an3lo_as118	$45.28^{+0.83}_{-0.75}$
MSHT20xNNPDF40_aN3LO	46.08 ± 0.89
MSHT20xNNPDF40_aN3LO_qed	45.41 ± 0.78

Table 4.3: The gluon-gluon-fusion cross section at 13 TeV in the rHTL at N³LO for various PDF sets. The provided uncertainties only include the PDF uncertainties. The computational setup is described in the Conventions. Results were computed using `iHixs` 2 [128].

Before the publication of aN³LO PDF sets, the uncertainty due to the mismatch of the PDFs was often estimated through lower orders rescaled to N³LO,

$$\delta(\text{PDF} - \text{th}) = \frac{1}{2} \left| \sigma_{gg \rightarrow HX}^{\text{NNLO,NNLO PDF}} - \sigma_{gg \rightarrow HX}^{\text{NNLO,NLO PDF}} \right|. \quad (4.124)$$

This is for example the recommendation of the Higgs Working Group [64]. The factor 1/2 is included as a conservative estimate of the rescaling factor, as the N³LO effect will be suppressed compared to the NNLO one. For the NNPDF31_nnlo_as_0118 PDF set at 13 TeV, this uncertainty turns out to be close to 1%. However, from Fig. 4.13, we can see that with this approach the impact of the N³LO PDFs is severely underestimated, as the results computed with the aN³LO PDFs is shifted by around 4-6%. This difference underscores why fully consistent N³LO PDF sets are crucial for accurate cross section predictions.

We can also see that the different approaches followed by the NNPDF and MSHT collaborations, yield central values which are not compatible within the associated uncertainty bands. Furthermore, the PDF-uncertainty estimates themselves differ significantly by about a factor of three.

Provided that the MHOU are well estimated by the NNPDF collaboration, the approximations of the splitting kernels by a finite number of Mellin-moments seems to be highly accurate, effecting the cross sections only on the level of 3%.

The α_s -uncertainties, make up about half of the total PDF uncertainty, as visible from the error increase between the NNPDF40_an3lo_as_01180 and NNPDF40_an3lo_as_01180_pdfs PDF set.

The inclusion of QED effects shifts the cross section by around -0.6 pb at 13 TeV.

Because of the sizeable difference between the PDFs of the two collaboration we advise using the combined PDF sets until the origin of the discrepancy has been identified or full N³LO PDF sets become available.

4.3.3 Electroweak Corrections

Besides the discussed QCD corrections, we can also consider electroweak corrections. These are generally suppressed because of the smaller coupling constant $\alpha(m_Z) \approx 1/127$, but the percentage-level precision of our predictions makes an investigation of electroweak effects indispensable.

The electroweak corrections to the LO QCD partonic cross section can be classified into two categories: the light-quark contributions and the top-quark contributions. The top-quark

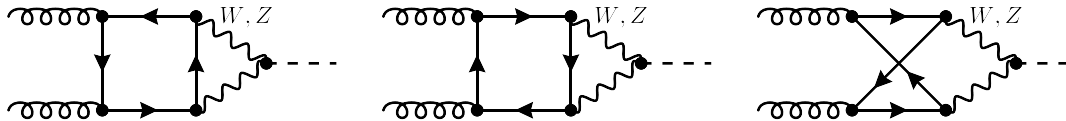


Figure 4.14: Light-quark contribution to the LO electroweak corrections of the gluon-gluon-fusion Higgs production cross section.

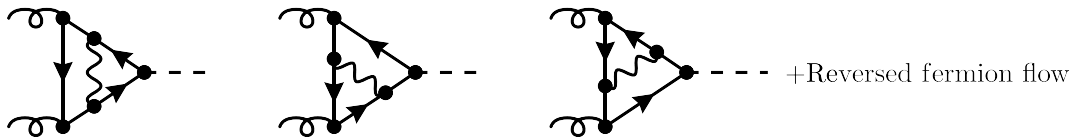


Figure 4.15: Top-quark contribution to the LO electroweak corrections of the gluon-gluon-fusion Higgs production cross section. The wavy line represents all electroweak gauge bosons (γ, W, Z).

contribution contains a Yukawa-coupling of the top, and the light-quark contributions contain all the remaining diagrams. The respective diagrams are depicted in Fig. 4.14 and 4.15. Real radiative electroweak corrections like those depicted in Fig. 4.16 do not contribute to the cross section, since two diagrams which only differ by the direction of the fermion flow exactly cancel. Even though the preconditions are not strictly met, this can be shown analogous to *Furry's theorem*¹⁰.

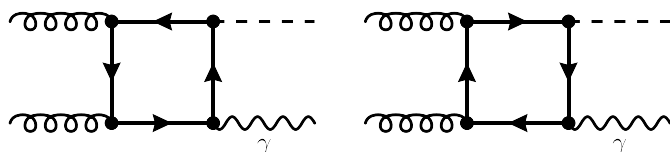


Figure 4.16: Example Feynman diagrams of radiative electroweak corrections to the gluon-gluon-fusion Higgs production cross section. The remaining four Feynman diagrams can be obtained by permutation of external gluon, photon and Higgs. Two diagrams which differ only by the direction of the fermion flow exactly cancel.

The two-loop light-quark contribution to the Higgs-gluon form factor was calculated in Ref. [27]. The top-quark contribution was then worked out in Refs. [28–30]. The latter reference also

¹⁰ Furry's theorem states that the abelian part of the sum of two diagrams that differ only by the direction of a closed fermion line vanishes, if there are an odd number of vertices proportional to the γ -matrices. In the present case, the color factor is $\delta^{c_1 c_2}$, i.e. it is fully abelian. There is an even number of vertices, however one of the vertices is a Yukawa interaction and hence does not introduce a γ -matrix. It is easy to show that with these conditions, Furry's theorem still applies.

includes the effect from finite bottom-quark masses, including diagrams in which we encounter flavor changes due to a W -boson exchange. The leading electroweak corrections increase the LO cross section by around 5%. Almost the entirety of this correction is due to the light-quark contribution.

Beyond LO in α_s , the hadronic cross section was first estimated at $\mathcal{O}(\alpha_s^3 \alpha)$ using the HTL and also treating the massive vector bosons as infinitely heavy [31]. Furthermore, since the top-quark contribution was negligible at LO, the authors omitted it in their calculation at NLO. With this approximation, the electroweak corrections can be incorporated through a modification of the Wilson coefficient

$$\begin{aligned} C_1 = & \left[\frac{\alpha_s}{4\pi} C_1^{(0)} + \left(\frac{\alpha_s}{4\pi} \right)^2 C_1^{(1)} + \mathcal{O}(\alpha_s^3) \right] \\ & + \frac{\alpha}{4\pi} \left[\frac{\alpha_s}{4\pi} C_{1,w}^{(0)} + \left(\frac{\alpha_s}{4\pi} \right)^2 C_{1,w}^{(1)} + \mathcal{O}(\alpha_s^3) \right]. \end{aligned} \quad (4.125)$$

One then finds for the electroweak coefficient

$$\begin{aligned} C_{1,w}^{(0)} = & -\frac{2}{\sin^2 \theta_W \cos^2 \theta_W} \left[\frac{5}{4} - \frac{7}{3} \sin^2 \theta_W + \frac{22}{9} \sin^4 \theta_W \right] - \frac{4}{\sin^2 \theta_W}, \\ C_{1,w}^{(1)} = & C_{1,w}^{(0)} \frac{14}{3}. \end{aligned} \quad (4.126)$$

The same contribution was later reevaluated in the limit of massless electroweak gauge bosons [32] as well as in the soft-gluon approximation [33]. Although the approximations make completely different assumptions about the mass spectrum, the phenomenological results turn out to be quite similar, increasing the NLO cross section between 5.4 and 5.2%. This shows that the cross section is not very sensitive to the mass of the vector bosons.

Still, results with finite vector-boson masses would be highly desirable and were recently reported in Ref. [34]. The authors found that the electroweak corrections increase the NLO cross section by around 5.1%, confirming that the previous approximations were indeed accurate. The $\mathcal{O}(\alpha_s^3 \alpha^2)$ QCD predictions are rescaled to order $\mathcal{O}(\alpha_s^5 \alpha^2)$ using the rHTL with electroweak corrected Wilson coefficients (see Eq. (4.125)). The electroweak corrections increase the N³LO rHTL cross section by $4.4 \pm 0.3\%$. By far, the dominating source of uncertainty of this contribution is the missing higher order uncertainty. Uncertainties related to the omission of the top-quark contribution, finite quark-mass effects, or partonic channels at $\mathcal{O}(\alpha_s^3 \alpha^2)$ are all below 0.1%.

4.3.4 Finite Top-Quark Mass Effects

So far our discussion of perturbative corrections was mainly focused on the HTL approximation. In Section 4.2.4, we explained how the approximation can be improved to also encompass some finite top-quark mass effects by means of rescaling the cross sections. We argued that in the dominant gluon-gluon channel especially, the rHTL approximation will be highly accurate. Nevertheless, we also saw significant deviations—in particular for the other partonic channels—which could yield important corrections to the rHTL cross section.

This makes the higher-order corrections with finite top-quark mass indispensable. The LO calculation with finite top-quark masses presented in Section 4.1 was extended to NLO in

channel	$\sigma_{\text{rHTL}}^{\text{NNLO}}$ [pb]	$(\sigma_t^{\text{NNLO}} - \sigma_{\text{rHTL}}^{\text{NNLO}})$ [pb]	$(\sigma_t^{\text{NNLO}} - \sigma_{1/m_t}^{\text{NNLO}})$ [pb]
	$\mathcal{O}(\alpha_s^2) + \mathcal{O}(\alpha_s^3) + \mathcal{O}(\alpha_s^4)$	$\mathcal{O}(\alpha_s^3)$	$\mathcal{O}(\alpha_s^4)$
$\sqrt{S} = 8 \text{ TeV}$			
gg	$7.39 + 8.58 + 3.88$	+0.0353	+0.0879
qg	$0.55 + 0.26$	-0.1397	-0.0153
qq	$0.01 + 0.04$	+0.0171	-0.0191
total	$7.39 + 9.14 + 4.18$	-0.0873	+0.0535
$\sqrt{S} = 13 \text{ TeV}$			
gg	$16.30 + 19.64 + 8.76$	+0.0345	+0.2431
qg	$1.49 + 0.84$	-0.3696	-0.0408
qq	$0.02 + 0.10$	+0.0322	-0.0501
total	$16.30 + 21.15 + 9.70$	-0.3029	+0.1522

Table 4.4: Comparison of cross sections computed in the rHTL (σ_{rHTL}), the cross section with finite top-quark masses (σ_t), and the cross section computed with power corrections (σ_{1/m_t}) at NNLO. The computational setup is described in the Conventions. Exact results were extracted from Ref. [35]. The power corrections were computed using `iHixs 2` [128]. The quark-quark channel is not yet available with power corrections, which is why we do not include it in the above table. The channel is suppressed by the PDFs, i.e. the total cross section will be left almost unaffected.

Refs. [20, 129]. Later, power corrections to the HTL of the form $\mathcal{O}(m_H^4/m_t^4)$ became available at NNLO [130–132]. Still, a residual theoretical uncertainty of about 1% of the total cross section persisted. Only with the computation of the exact top-quark mass dependence of the NNLO cross Section [35] was the uncertainty finally (effectively) eliminated.

The main results of that reference are displayed in Tab. 4.4 (also see Fig. 4.10). We also compare the cross sections with exact top-quark mass dependence with the m_H/m_t expansion. We see that the finite-top-quark-mass effects are small (< 0.4%). In the gluon-gluon channel, the rHTL works exceptionally well, approximating the NNLO cross section with percent-level accuracy. Again we expect this kind of accuracy on the basis of the rescaling procedure. In the other partonic channels the approximation works significantly worse, showing deviations of up to 19%. The sheer dominance of the gluon-gluon channel assures that the total cross section is approximated well by the rHTL.

The power corrections $\mathcal{O}(m_H^4/m_t^4)$ to the HTL do not significantly improve the rHTL, but they do get the order of magnitude as well as the sign right.

The residual theoretical uncertainty of the finite-top-quark-mass effects can be estimated from the scale uncertainty of the difference $\sigma_t - \sigma_{\text{rHTL}}$, taking into account all correlations.

Since the perturbative series of the cross section is truncated at some fixed order, it will have some residual renormalization scheme dependence. The scheme-dependence of the cross section was investigated in Refs. [4, 86] including our own analysis. The difference between the OS and $\overline{\text{MS}}$ schemes was found to be less than 1% of the total cross section, rendering also the uncertainty on the scheme dependence completely negligible.

4.3.5 Effect of Light Quarks

In Section 4.1, we investigated to what extent light quarks affect the gluon-gluon-fusion Higgs production cross section at LO. Here, we found that the main contribution arises from the interference with top-quark induced Higgs production. The inclusion of the bottom quark lowered the cross section by around 6.5% at 13 TeV. The next-heaviest quark—the charm—further reduced the cross section, this time by 1%.

Since perturbative corrections are typically quite large in gluon-gluon fusion, it is once again vital to also compute higher-order corrections to the interference. The NLO cross section for arbitrary quark masses was computed in Ref. [129].

Once again, we estimate the theoretical uncertainty from missing higher orders through the assigned scale uncertainties. The HWG, instead suggests estimating the uncertainty based on lower orders and rescale them to the $N^3\text{LO}$ correction in the rHTL. Since the light-quark-mass effects are not expected to scale with the cross section of the rHTL, we do not believe that this is a reliable estimate of the uncertainty and do not apply them going forward.

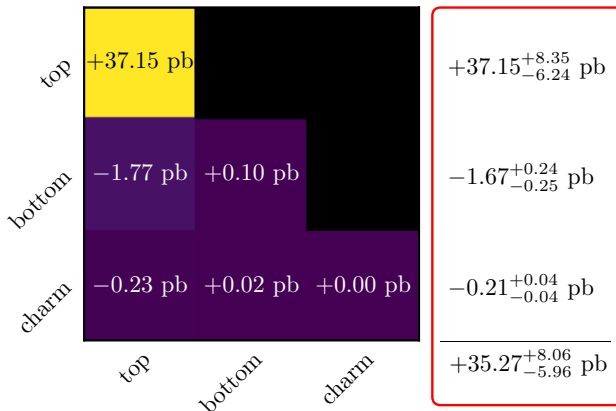


Figure 4.17: σ_i (diagonals) and $\sigma_{i \times j}$ (off-diagonals) at NLO for the three heaviest quark flavors at a hadronic center-of-mass energy of 13 TeV. The red box indicates the sum of each row, and hence the combined effects of each additional flavor. The computational setup is described in the Conventions. We use the on-shell scheme for the top-quark mass and the $\overline{\text{MS}}$ scheme for the charm- and bottom-quark masses. The scale uncertainties are computed using 7-point variation.

The NLO results for the pure-flavor and the interference effects are displayed in Fig. 4.17. We see that the top-bottom interference contribution to the cross section increased in magnitude by 58% from LO to NLO. We once again observe that the top-bottom interference contribution is by far the most significant one among the effects of light quarks. All other light-quark mass effects are still within the scale uncertainty of the top-bottom interference contribution. Improving these contributions beyond NLO is therefore completely unnecessary. Interestingly, we observe that the scale uncertainties of the pure-top and the top-bottom interference contribution are almost perfectly anti-correlated.

With the scale uncertainty, we estimate that effects of missing higher orders in the light-quark contribution are of the order of 7%. However, this estimate is too naïve. Indeed, if we

choose a different renormalization scheme for the bottom-quark mass, say the OS scheme, the top-bottom interference contribution at NLO becomes (again at $\sqrt{S} = 13$ TeV)

$$\sigma_{t \times b} = -2.42^{+0.19}_{-0.12} \text{ pb}, \quad (4.127)$$

which differs from our previous $\overline{\text{MS}}$ renormalized cross section contribution by -0.66 pb or 38%. The large discrepancy between the results is somewhat expected since the hard scattering amplitude in the high energy limit roughly scales with m_b^2 (see Eq. (4.13)) and the relation between the OS and the $\overline{\text{MS}}$ bottom-masses converges very poorly [133, 134]. Therefore, the cross section can only show a good perturbative convergence in one of the schemes if at all. At NLO, we have not determined enough coefficients of the perturbation series to make a reliable argument about the convergence, making higher order predictions indispensable. If we assign the error in a way to encompass both the on-shell- and $\overline{\text{MS}}$ -renormalized results, it will constitute a 1.7% uncertainty on the total cross section, making it one of the leading sources of uncertainty.

Eliminating this source of uncertainty by computing higher order corrections to the top-bottom interference contribution is one of the major aims of this PhD thesis. With these predictions we want to investigate the perturbative convergence in the different mass-renormalization schemes in order to assess which one works best for phenomenological applications.

The cross sections presented in this section were all computed in the 5FS, i.e. the bottom- and charm-quark were considered massless and could appear in the initial state. Since the hard scattering matrix element vanishes for massless particles, we then proceeded to set the light-quark masses to non-vanishing values in all closed quark loops which couple to the Higgs¹¹. This ad hoc introduction of quark masses has become the de facto standard for light-quark mass effects in gluon-gluon fusion, but well-grounded justifications of this procedure have been lacking so far. In this PhD thesis, we aim to close this gap and explore the validity of this massification procedure by comparing the results of top-bottom-interference contributions to the same but computed in the 4FS, in which the quark-masses are treated consistently.

4.3.6 Differential Cross Sections

Up to this point the main focus of our discussion has been the total cross section of the gluon-gluon-fusion channel. However, differential cross sections can shine some light on the production kinematics of the Higgs and additionally offer a plethora of rich phenomenology and experimental applications. In this section, we will briefly summarize the current status on differential cross sections of Higgs production in the gluon-gluon-fusion channel. The possibilities to study the Higgs production cross section in terms of its kinematics are endless, so our discussion is by no means complete, instead we will focus on the most phenomenologically relevant distributions.

The Higgs- p_T Distribution

Arguably the most important distribution is the Higgs- p_T distribution

$$\frac{d\sigma_{pp \rightarrow HX}}{dp_T}, \quad (4.128)$$

where p_T is the transverse momentum of the Higgs with respect to the beam axis. p_T -distributions have been calculated up to third order in perturbation theory using the rHTL [135,

¹¹ We will later show that this method indeed ensures gauge-invariant IR-safe cross sections.

[136], including subsequent decays to photons [137] and leptons [138]. The rHTL only provides a good approximation of the cross section up to $p_T \sim m_H$ since above this threshold, the top-quark running in the loop is getting resolved. For larger p_T , the partonic p_T -distribution is well described by a power law. This can be understood with a simple dimensional analysis. Indeed, at large p_T , the transverse momentum is the dominant scale, and we can neglect the top-quark mass. In order to match the mass dimension, -3 , of the differential partonic cross section $d\sigma_{pp \rightarrow HX}/dp_T$, we require the scaling behavior

$$\frac{d\hat{\sigma}_{ij \rightarrow HX}}{dp_T} \sim p_T^{-3}. \quad (4.129)$$

In the rHTL on the other hand, the coupling constant is proportional to $1/v^2$ and hence has a non-vanishing mass dimension. The large p_T scaling of the partonic cross section is therefore

$$\frac{d\hat{\sigma}_{ij \rightarrow HX}^{\text{rHTL}}}{dp_T} \sim v^{-2} p_T^{-1}. \quad (4.130)$$

Unfortunately, these power-laws no longer hold on the hadronic level because of the convolution with the partonic luminosities. However, since the partonic luminosity dies off extremely quickly, especially at larger values of τ (see Fig. 2.2), the largest contribution to the hadronic cross section will come from the region close to the threshold production. We can then expand the partonic cross section around the threshold yielding

$$\begin{aligned} \frac{d\sigma_{pp \rightarrow HX}}{dp_T} &= \int_{s_{\min}/S}^1 \frac{d\tau}{\tau} \sum_{ij} \mathcal{L}_{ij}(\tau) \frac{d\hat{\sigma}_{ij \rightarrow HX}(\tau S)}{dp_T} \\ &\approx \sum_{ij} \frac{d\hat{\sigma}_{ij \rightarrow HX}(s_{\min})}{dp_T} \int_{s_{\min}/S}^1 \frac{d\tau}{\tau} \mathcal{L}_{ij}(\tau), \end{aligned} \quad (4.131)$$

where $\sqrt{s_{\min}}$ denotes the minimum partonic center-of-mass energy

$$s_{\min} = \left(p_T + \sqrt{p_T^2 + m_H^2} \right)^2 \stackrel{m_H \ll p_T}{\approx} 4p_T^2. \quad (4.132)$$

In good approximation, the ratio of the hadronic cross sections in the rHTL and the exact theory must therefore satisfy

$$\frac{d\sigma_{pp \rightarrow HX}^{\text{rHTL}}}{dp_T} / \frac{d\sigma_{pp \rightarrow HX}}{dp_T} \sim p_T^2 / v^2 \quad (4.133)$$

at $p_T \gg m_H$. The inclusion of finite top-quark mass effects is therefore of immense importance especially at large p_T and has been studied up to NNLO in Refs. [139–141].

At smaller transverse momentum, $p_T \sim m_H/2$, we can resolve the effects of the lighter quark masses. This is particularly interesting because it demonstrates that this region is sensitive to the Yukawa coupling of the light quarks [142, 143]. In a recent study by the CMS collaboration [144]¹², the authors fitted experimental data to the Higgs- p_T spectrum and were able indirectly determine the following constraints on the coupling modifiers:

$$-1.2 < \kappa_b < 1.1, \quad -4.9 < \kappa_c < 4.8. \quad (4.134)$$

The effect of light-quark masses on the Higgs- p_T spectrum has been studied up to NNLO in Refs. [4, 146–148].

¹² Also see Ref. [145] for an updated analysis.

At LO and in all virtual corrections, the Higgs is produced with vanishing p_T because there is no other final state particle for the Higgs to recoil against. The LO and all virtual corrections will therefore only contribute to the zero-bin of the distribution. The transverse momentum hence acts as a slicing parameter. Consequently, at small transverse momentum, the cross section will receive large logarithmic enhancements because the cut-off threshold acts as an IR regulator. These logarithms cancel in the exact cross section, but because the perturbation series is truncated, fixed-order results still suffer from their appearance and yield inaccurate results whenever these logarithms become dominant. To stabilize the behavior in these phase-space regions, the logarithms can be resummed to all orders [139, 149–155].

The Higgs-Rapidity Distribution

The Higgs rapidity is defined as

$$\eta_H \equiv \frac{1}{2} \ln \frac{p_H^0 + p_H^3}{p_H^0 - p_H^3}, \quad (4.135)$$

where p_H is the momentum of the Higgs, and the z -axis aligns with the beam direction. For the Higgs-rapidity distribution, all channels, be it real or virtual, can contribute to any bin of the distribution. Consequently, the respective distribution will not show any logarithmic enhancements that require resummation, unlike in the p_T -distribution.

The Higgs-rapidity distribution has been calculated up to N³LO in the HTL [156, 157]. The effect of finite top-quark masses has been studied at NNLO in Ref. [155]. The effect of finite bottom-quark masses, on the other hand, was recently presented by us [4] and will be discussed in this PhD thesis.

4.3.7 Summary

The theory uncertainties of the fully inclusive gluon-gluon-fusion Higgs production cross section are summarized in Fig. 4.18. The errors on the various sources of uncertainty are assigned according to the above description (for details see Section 6.4). The uncertainty on the top-bottom interference contribution is assigned based on the difference between the NLO cross sections with OS and $\overline{\text{MS}}$ renormalized bottom-quark masses. The main source of uncertainty is the scale uncertainty, which still makes up almost 42% of the total error budget. The second most dominant source of uncertainty comes from the top-bottom interference contribution which makes up for about a third of the total error. The only other notable error comes from the soft-virtual approximation. Other sources of uncertainty are already reduced to a point where further improvements would no longer affect the total error significantly.

In order to significantly improve the uncertainty of the cross section, one can either refine the scale uncertainties, or the top-bottom interference contribution. The former is very challenging, as one would need to go to five-loop order. In the foreseeable future, this kind of computation seems out of reach. This leaves us only with the second option of improving the uncertainty of the top-bottom interference contribution, by performing the full NNLO cross section calculation with finite bottom-quark masses. This shall be the focus of this PhD thesis.

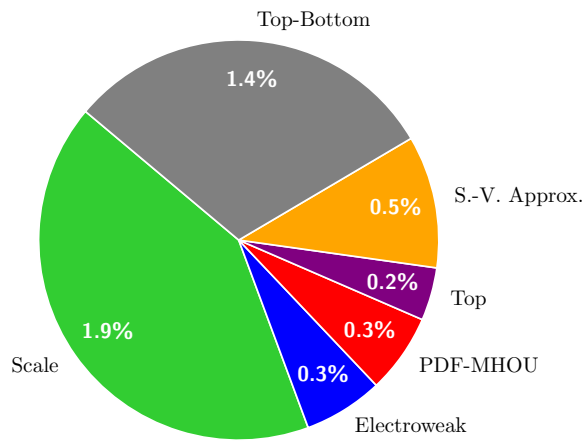


Figure 4.18: Total error budget of the fully inclusive gluon-gluon-fusion Higgs production cross section at 13 TeV. The errors on the various sources of uncertainty are estimated as described in Section 6.4. For the top-bottom interference contribution, the error is estimated based on the difference between NLO cross section with OS and $\overline{\text{MS}}$ -renormalized bottom-quark masses. For asymmetric uncertainty, we use the total span divided by two.

5

COMPUTATIONAL DETAILS

Our final goal is clear now: We want to investigate how finite top- and bottom-quark masses affect the Higgs production cross section, both on the inclusive and the differential cross section level. In particular, we want to study the impact of the mass renormalization scheme on the cross section to eliminate one of its main remaining uncertainties. Furthermore, aside from the commonly used 5FS, we want to explore the impact of alternative FSs to assess the validity of the treatment of light-quark masses in the 5FS.

In this chapter, we describe the necessary methods for computing the Higgs production cross section with full top- and bottom-quark mass dependence at NNLO.

5.1 COMPUTING THE AMPLITUDES

The base ingredients of the calculation are the scattering amplitudes. In addition to the LO amplitude for $gg \rightarrow H$ presented in Section 4.1 and the NLO amplitudes computed in Ref. [129], we require amplitudes for the following partonic processes

- real-real amplitudes (one-loop):
 1. $gg \rightarrow Hgg$;
 2. $gg \rightarrow Hq\bar{q}$;
 3. $q\bar{q} \rightarrow Hq'\bar{q}'$;
 4. $q\bar{q} \rightarrow Hq\bar{q}$;
 5. + processes related by crossing symmetry;
- real-virtual amplitudes (two-loop):
 1. $gg \rightarrow Hg$;
 2. $q\bar{q} \rightarrow Hg$;
 3. + processes related by crossing symmetry;
- virtual-virtual amplitudes (three-loop):
 1. $gg \rightarrow H$.

In the following, we discuss the computation of each amplitude one by one.

In this section, we work exclusively in the 5FS. The necessary modifications for adapting the amplitudes to the 4FS will be presented in Section 5.2. When working in the 5FS, the bottom-quark mass is generally zero. Since this would imply that the total top-bottom interference contribution would vanish, the mass is then set to its actual value in any closed quark loop

coupling to the Higgs. Therefore, in Feynman diagrams such as those in Fig. 5.3, the bottom quark is treated as massive; however, if the top and bottom quark are exchanged, the bottom-quark mass is set to zero. With a massification prescription like this, it is essential to verify that gauge invariance and IR safety are not lost in the process.

The proof that gauge invariance and IR safety are preserved proceeds via the *replica technique*. Consider the SM, but with the following quark content: n_b identical copies of the bottom quark, $n_{b'}$ massless quarks (denoted b') serving as our massless bottom quark, and the top quark. Without the inclusion of electroweak effects this theory is equivalent to QCD with the addition of a Yukawa interaction to the Higgs; ergo this theory is gauge invariant and free of IR-divergences. Furthermore, gauge invariance and IR safety also hold for each separate Yukawa coupling contribution (Y_t or Y_b) and each power of n_b and $n_{b'}$, as these are arbitrary parameters from the viewpoint of QCD. This means that the parts of the amplitude which are proportional to $Y_t n_b$ are separately gauge invariant, and so are the parts which are proportional to $Y_b n_b n_{b'}$, and so on. Examples of Feynman diagrams contributing to a selection of Y_t , Y_b , n_b , and $n_{b'}$ power-combinations are depicted in Fig. 5.1. Likewise, after squaring, the contribution

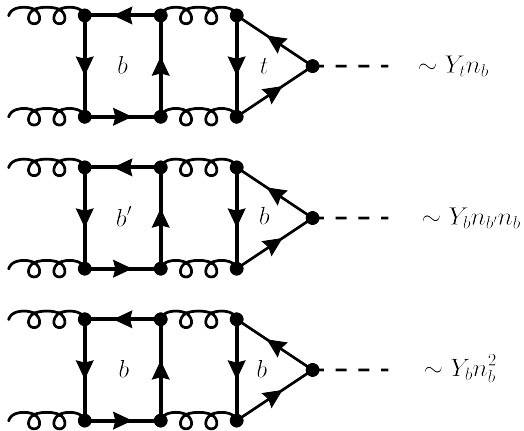


Figure 5.1: Example Feynman diagrams and their scaling with the Yukawa coupling, n_b , and $n_{b'}$.

$Y_t Y_b n_b n_{b'}$ is going to be separately IR finite. We have thus shown that contributions with a massive bottom-quark loop which does **not** couple to the Higgs do not mix gauge-dependent terms or IR divergences with the selected contribution from our massification procedure.

5.1.1 The Real-Real Corrections

The real-real corrections involve just a single loop containing either a top or a bottom quark. Examples of different Feynman diagrams for various partonic channels are depicted in Fig. 5.2.

As one-loop amplitudes, they can be computed numerically with publicly available libraries like **RECOLA** [158]. However, the real-real corrections often represent the bottleneck of the computation of the phase-space integrals, which makes an efficient evaluation of the amplitudes desirable. We therefore use an analytic form of the amplitude instead. We utilize the amplitude computed in Ref. [159] and its implementation provided by **MCFM** [160–162], which in turn uses **QCDLoop** [163, 164] for the evaluation of one-loop integrals.

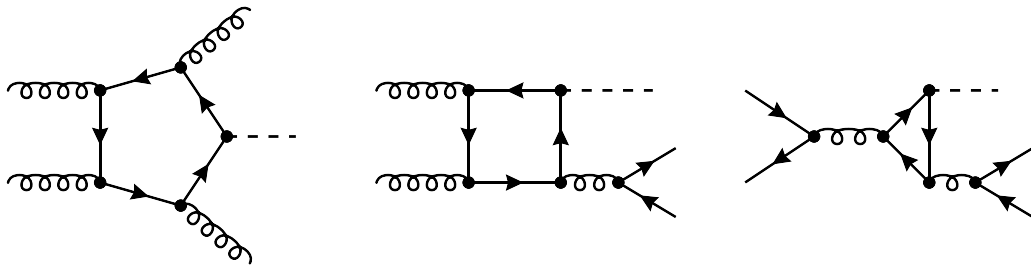


Figure 5.2: Example Feynman diagrams for one-loop real-real corrections in various partonic channels.

We found that using the analytic expressions speeds up the amplitude evaluation by a factor of 20 compared to the numerical evaluation in RECOLA.

5.1.2 The Real-Virtual Corrections

For the real-virtual corrections, we encounter—for the first time—Feynman diagrams that have two different mass scales in the loop. Fig. 5.3 shows all (up to inversion of the fermion flow inside the triangle loops) Feynman diagrams with two different quarks running in the loops. Naturally, we observe that all two-loop integrals actually factorize into two separate

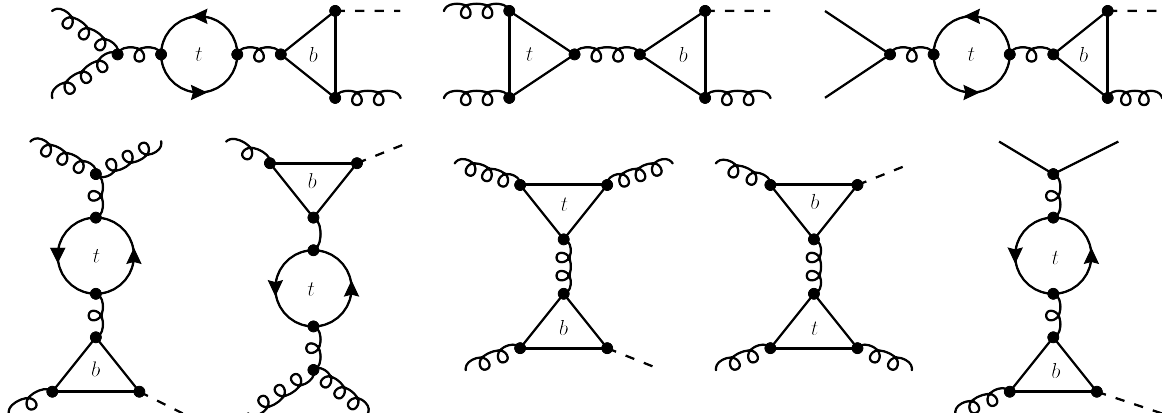


Figure 5.3: Feynman diagrams for the two-loop real-virtual corrections with two massive quarks. Fermion lines without arrows indicate that both fermion flows are valid. In the 5FS, the bottom quark is always coupling to the Higgs.

one-loop integrals making them quite straightforward to solve.

The contributions to the scattering amplitude containing only a single massive quark involve genuine two-loop integrals. Fig. 5.4 shows a selection of contributing Feynman diagrams. Two-loop integrals, especially non-planar ones, with three mass scales are very challenging to compute analytically, even with state-of-the-art methods. As of today, the analytic form of these amplitudes is still unknown; however approximations for a nearly massless bottom quark have been calculated relatively recently [165, 166]. We therefore decided to instead evaluate the appearing two-loop integrals numerically at fixed phase-space points and interpolate between them during the phase-space integration.

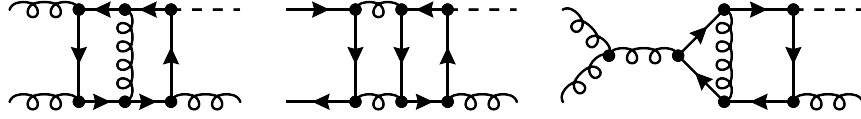


Figure 5.4: Example Feynman diagrams for the two-loop real-virtual corrections with a single massive quark in various partonic channels.

In any case, for both the one-mass and two-mass contributions, we first reduce the amplitude to form factors. To make potential symmetries more apparent, we cross the radiated parton to the initial state, i.e. we consider the amplitudes

$$g(p_1) + g(p_2) + g(p_3) \rightarrow H(p_4), \quad \bar{q}(p_1) + q(p_2) + g(p_3) \rightarrow H(p_4). \quad (5.1)$$

Projection to Form Factors

We can factor out the external polarization vectors, spinors and color factors to rewrite the amplitudes in terms of their amputated counterpart

$$\mathcal{M}_{ggg \rightarrow H} = \mathcal{M}_{\mu\nu\rho} \varepsilon_1^\mu \varepsilon_2^\nu \varepsilon_3^\rho f^{c_1 c_2 c_3}, \quad \mathcal{M}_{\bar{q}qg \rightarrow H} = \bar{v}(p_1) \mathcal{M}_\rho u(p_2) \varepsilon_3^\rho T_{c_1 c_2}^{c_3}. \quad (5.2)$$

After squaring the amplitude and summing over the color of the external partons, we get the color factors

$$f^{c_1 c_2 c_3} f^{c_1 c_2 c_3} = C_A N_A = 24, \quad T_{c_1 c_2}^{c_3} T_{c_2 c_1}^{c_3} = C_F N_c = 4. \quad (5.3)$$

It is convenient to choose polarization vectors which are cyclically transverse to the external momenta, i.e.

$$\varepsilon_1 = \varepsilon(p_1, p_2, \lambda_1), \quad \varepsilon_2 = \varepsilon(p_2, p_3, \lambda_2), \quad \varepsilon_3 = \varepsilon(p_3, p_1, \lambda_3), \quad (5.4)$$

where the second argument indicates the reference vector, and λ_i denotes the helicity of the i -th particle. We can then propose the form factor decomposition of the amplitudes

$$\begin{aligned} \mathcal{M}^{\mu\nu\rho} &= g^{\mu\nu} p_2^\rho F_1 + g^{\mu\rho} p_1^\nu F_2 + g^{\nu\rho} p_3^\mu F_3 + p_3^\mu p_1^\nu p_2^\rho F_4, \\ \bar{v}(p_1) \mathcal{M}^\rho u(p_2) &= \bar{v}(p_1) \left[\not{p}_3 p_1^\rho - (p_1 \cdot p_3) \gamma^\rho \right] u(p_2) G_1 + \bar{v}(p_1) \left[\not{p}_3 p_2^\rho - (p_2 \cdot p_3) \gamma^\rho \right] u(p_2) G_2. \end{aligned} \quad (5.5)$$

Here, we used the Ward identity, to restrict the tensor coefficients in \mathcal{M}^ρ .

The tensor coefficients span a vector space with respect to the scalar product

$$\langle a_{\mu_1 \dots \mu_{n_g}} | b^{\mu_1 \dots \mu_{n_g}} \rangle \equiv \sum_{\text{pol.}} a_{\mu_1 \dots \mu_{n_g}}^* \left[\prod_i^{n_g} \varepsilon_i^{*\mu_i} \varepsilon_i^{\nu_i} \right] b_{\nu_1 \dots \nu_{n_g}} \quad (5.6)$$

where n_g is the number of external gluons, i.e. $n_g = 3$ for $ggg \rightarrow H$ and $n_g = 1$ for $\bar{q}qg \rightarrow H$ and the summation is performed over the polarizations of all external particles. The tensor coefficients hence form a—not necessarily orthonormal—basis.

Any vector can be written as a linear sum over basis vectors

$$|v\rangle = \sum_i v_i |e_i\rangle. \quad (5.7)$$

Then the projector to the j -th basis vector can be found via

$$\langle e_j | P \equiv P_j = \sum_k G_{jk}^{-1} \langle e_k |, \quad (5.8)$$

where G is the *Gram-matrix*

$$G_{ij} = \langle e_i | e_j \rangle. \quad (5.9)$$

With this little interlude from linear algebra, it is then easy to verify that the projectors for the F_1, \dots, F_4 form factors are given by

$$\begin{aligned} P_1^{\mu\nu\rho} &= \frac{1}{d-3} \left(g^{\mu\nu} p_2^\rho \frac{t}{su} - p_3^\mu p_1^\nu p_2^\rho \frac{1}{su} \right), \\ P_2^{\mu\nu\rho} &= \frac{1}{d-3} \left(g^{\mu\rho} p_1^\nu \frac{u}{st} - p_3^\mu p_1^\nu p_2^\rho \frac{1}{st} \right), \\ P_3^{\mu\nu\rho} &= \frac{1}{d-3} \left(g^{\nu\rho} p_3^\mu \frac{s}{tu} - p_3^\mu p_1^\nu p_2^\rho \frac{1}{tu} \right), \\ P_4^{\mu\nu\rho} &= \frac{1}{d-3} \left(-g^{\mu\nu} p_2^\rho \frac{1}{su} - g^{\mu\rho} p_1^\nu \frac{1}{st} - g^{\nu\rho} p_3^\mu \frac{1}{tu} + p_3^\mu p_1^\nu p_2^\rho \frac{d}{stu} \right). \end{aligned} \quad (5.10)$$

Consequently, the form factors can be obtained by applying the projectors to the amplitudes

$$\begin{aligned} F_i = \langle e_i | P_{\mu\nu\rho} | \mathcal{M}^{\mu\nu\rho} \rangle &= P_i^{\mu_1\nu_1\rho_1} \left(-g_{\mu_1\mu_2} + \frac{p_1\mu_1 p_2\mu_2 + p_2\mu_1 p_1\mu_2}{p_1 \cdot p_2} \right) \\ &\times \left(-g_{\nu_1\nu_2} + \frac{p_2\nu_1 p_3\nu_2 + p_3\nu_1 p_2\nu_2}{p_2 \cdot p_3} \right) \left(-g_{\rho_1\rho_2} + \frac{p_3\rho_1 p_1\rho_2 + p_1\rho_1 p_3\rho_2}{p_3 \cdot p_1} \right) \mathcal{M}^{\mu_2\nu_2\rho_2}. \end{aligned} \quad (5.11)$$

Here, we used the standard identity

$$\sum_\lambda \varepsilon_\mu^*(p, n, \lambda) \varepsilon_\nu(p, n, \lambda) = -g_{\mu\nu} + \frac{p_\mu n_\nu + p_\nu n_\mu}{p \cdot n} \quad (5.12)$$

to rewrite the sum over the polarization vectors.

Similarly, using

$$\sum_\lambda u(p, \lambda) \bar{u}(p, \lambda) = \not{p}, \quad \text{and} \quad \sum_\lambda v(p, \lambda) \bar{v}(p, \lambda) = \not{p}, \quad (5.13)$$

we find for the projectors of G_1 and G_2 ¹

$$\begin{aligned} \bar{v}(p_1) P_1^\mu u(p_2) &= \frac{1}{2st(d-3)} \bar{v}(p_1) \left[\frac{d-2}{t} \left(\not{p}_3 p_1^\mu - \frac{t}{2} \gamma^\mu \right) - \frac{d-4}{u} \left(\not{p}_3 p_2^\mu - \frac{u}{2} \gamma^\mu \right) \right] u(p_2), \\ \bar{v}(p_1) P_2^\mu u(p_2) &= \frac{1}{2su(d-3)} \bar{v}(p_1) \left[\frac{d-2}{u} \left(\not{p}_3 p_2^\mu - \frac{u}{2} \gamma^\mu \right) - \frac{d-4}{t} \left(\not{p}_3 p_1^\mu - \frac{t}{2} \gamma^\mu \right) \right] u(p_2). \end{aligned} \quad (5.14)$$

These allow the extraction of the form factors via

$$G_i = \langle e_i | P_\mu | \mathcal{M}^\mu \rangle = \left(-g_{\mu_1\mu_2} + \frac{p_3\mu_1 p_1\mu_2 + p_1\mu_1 p_3\mu_2}{p_3 \cdot p_1} \right) \text{tr}\{ P_i^{\mu_1} \mathcal{M}^{\mu_2} \}, \quad (5.15)$$

where we have used Eq. (5.13) once again, to rewrite the polarization sum in terms of a Dirac-trace.

¹ Note that the projectors are defined as the entire left-hand side.

Helicity Amplitudes

Since the form factors depend on the choice of our tensor basis, we would rather express our end result in terms of helicity amplitudes

$$\begin{aligned}\mathcal{M}_{ggg \rightarrow H}^{\lambda_1 \lambda_2 \lambda_3} &= \mathcal{M}_{\mu\nu\rho} \varepsilon^\mu(p_1, p_2, \lambda_1) \varepsilon^\nu(p_2, p_3, \lambda_2) \varepsilon^\rho(p_3, p_1, \lambda_3), \\ \mathcal{M}_{\bar{q}qg \rightarrow H}^{\lambda_1 \lambda_2 \lambda_3} &= \bar{v}(p_1, \lambda_1/2) \mathcal{M}_\rho u(p_2, \lambda_2/2) \varepsilon^\rho(p_3, p_1, \lambda_3).\end{aligned}\quad (5.16)$$

To find the relation between the form factors and the helicity amplitudes, we consider all independent helicity configurations. We then use the *spinor-helicity formalism* (see Ref. [167] for a pedagogical introduction to the topic) to rewrite them in terms of spinor products like

$$\langle ij \rangle \equiv \bar{u}(p_i, -1/2) u(p_j, 1/2), \quad [ij] \equiv \bar{u}(p_i, 1/2) u(p_j, -1/2). \quad (5.17)$$

The results for the $ggg \rightarrow H$ amplitudes read

$$\begin{aligned}\mathcal{M}_{ggg \rightarrow H}^{+++} &= \frac{1}{\sqrt{2}} \frac{su}{\langle 12 \rangle \langle 23 \rangle \langle 31 \rangle} \left(F_1 + \frac{t}{u} F_2 + \frac{t}{s} F_3 + \frac{t}{2} F_4 \right), \\ \mathcal{M}_{ggg \rightarrow H}^{++-} &= \frac{1}{\sqrt{2}} \frac{[12]^3}{[13][23]} \frac{u}{s} \left(F_1 + \frac{t}{2} F_4 \right), \\ \mathcal{M}_{ggg \rightarrow H}^{+-+} &= \frac{1}{\sqrt{2}} \frac{[13]^3}{[12][23]} \frac{s}{t} \left(F_2 + \frac{u}{2} F_4 \right), \\ \mathcal{M}_{ggg \rightarrow H}^{-++} &= \frac{1}{\sqrt{2}} \frac{[23]^3}{[12][13]} \frac{t}{u} \left(F_3 + \frac{s}{2} F_4 \right).\end{aligned}\quad (5.18)$$

The other four helicity amplitudes can be determined via charge conjugation

$$\mathcal{M}^{\lambda_1, \lambda_2, \lambda_3} = \mathcal{M}^{-\lambda_1, -\lambda_2, -\lambda_3}|_{\langle ij \rangle \leftrightarrow [ji]}. \quad (5.19)$$

Similarly, for the $\bar{q}qg \rightarrow H$ process we find the helicity amplitudes

$$\begin{aligned}\mathcal{M}_{\bar{q}qg \rightarrow H}^{-++} &= -\frac{1}{\sqrt{2}} \frac{[13]^2}{[12]} s F_1, \\ \mathcal{M}_{\bar{q}qg \rightarrow H}^{+-+} &= \frac{1}{\sqrt{2}} \frac{[23]^2}{[12]} s F_2.\end{aligned}\quad (5.20)$$

The $+--$ and $-+-$ amplitudes can be determined with Eq. (5.19), and all other helicity configurations produce vanishing amplitudes due to the conservation of angular momentum.

The form factors, amplitudes and helicity amplitudes admit a perturbative expansion in α_s . We define

$$\mathcal{M}_{ijk \rightarrow H}^{\lambda_1 \lambda_2 \lambda_3} = \frac{4\pi}{v} \left(\frac{\alpha_s}{4\pi} \right)^{3/2} \sum_{i=0} \left(\frac{\alpha_s}{4\pi} \right)^i \mathcal{M}^{(i), \lambda_1 \lambda_2 \lambda_3}. \quad (5.21)$$

Mapping to Topologies and the Reduction to Master Integrals

We generate all diagrams with **DiaGen/IdSolver** [168], our in-house software tool for the generation of Feynman diagrams. As output, we obtain **FORM** [169, 170] code that we can further manipulate. We apply the color algebra and project to the form factors as described above. **DiaGen/IdSolver** is also capable to find *prototypes*, i.e. it automatically identifies a minimal set of integral families and assigns appearing integrals accordingly.

In principle, **DiaGen/IdSolver** is also able to find relations between appearing Feynman integrals, so-called *integration-by-parts identities* (IBP), by means of the *Laporta algorithm* [171].

However, due to the immense complexity of the problem at hand, intermediate expressions are prone to become very large. This makes solving the appearing linear system of equations by traditional methods, such as Gaussian elimination, highly inefficient. The appearance of large intermediate expressions can be circumvented by using *finite-field* methods. In a nutshell, one inserts fractional samples for the appearing kinematic invariants and then performs the Laporta algorithm with reduced kinematics, making it much simpler to solve. The final IBP identities relate the master integrals by rational functions. One can then reconstruct the functional dependence on the kinematic variables through repeated sampling, as in performing a fit. The rational values are mapped to finite fields—explaining the name of the method—which allows computations without loss of precision. We use this workflow implemented in the publicly available tool chain **Kira**⊕**Firefly** [172–174].

After applying the IBP identities, we end up with three integral families for amplitudes with a single internal massive quark. We adapt the definition provided in Ref. [165]. The propagators of each family are printed in Tab. 5.1. Note that the Feynman diagrams can never have more

#	Planar 1 (PL1)	Planar 2 (PL2)	Non-planar (NPL)
1	k_1^2	$k_1^2 - m^2$	$k_1^2 - m^2$
2	$(k_1 - p_1)^2$	$(k_1 - p_1)^2 - m^2$	$(k + p_1)^2 - m^2$
3	$(k_1 - p_1 - p_2)^2$	$(k_1 - p_1 - p_2)^2 - m^2$	$(k_1 - p_2 - p_3)^2 - m^2$
4	$(k_1 - p_1 - p_2 - p_3)^2$	$(k_1 - p_1 - p_2 - p_3)^2 - m^2$	$k_2^2 - m^2$
5	$k_2^2 - m^2$	$k_2^2 - m^2$	$(k_2 + p_1)^2 - m^2$
6	$(k_2 - p_1)^2 - m^2$	$(k_2 - p_1)^2 - m^2$	$(k_2 - p_3)^2 - m^2$
7	$(k_2 - p_1 - p_2)^2 - m^2$	$(k_2 - p_1 - p_2)^2 - m^2$	$(k_1 - k_2)^2$
8	$(k_2 - p_1 - p_2 - p_3)^2 - m^2$	$(k_2 - p_1 - p_2 - p_3)^2 - m^2$	$(k_1 - k_2 - p_2)^2$
9	$(k_1 - k_2)^2 - m^2$	$(k_1 - k_2)^2$	$(k_1 - k_2 - p_2 - p_3)^2$

Table 5.1: Integral families for all contributions with only one internal massive quark as defined in Ref. [165]. m is the mass of the internal top or bottom quark.

than seven internal lines, meaning that integrals appearing in physical amplitudes are missing at least two of the propagators. The physical subsectors of the integral families are depicted graphically in Figs. 5.5, 5.6, and 5.7. For the contributions containing two massive internal quarks, we do not provide the integral families since the two-loop integrals factorize to one-loop integrals.

UV-Renormalization, IR-Subtraction and LSZ-Reduction

So far our analysis has focused on bare amplitudes regulated in dimensional regularization. The UV-poles are eliminated through renormalization of the coupling constant and the quark masses. Following the description in Section 2.1, we replace the bare coupling constant and masses by their renormalized counterparts and subsequently expand in α_s . We isolate the $\alpha_s^{5/2}$ term to obtain the two-loop correction to the amplitude. We employ the $\overline{\text{MS}}$ scheme for α_s , and—for now—the OS scheme for all the quark masses.

To obtain physical amplitudes, we employ the LSZ reduction formula. This means for each external particle, multiplying by the square root of the corresponding LSZ-constant. In dimensional regularization, only heavy fields contribute to the LSZ constants, as other contributions necessarily lead to scaleless integrals. This means that the gluon LSZ constants are already non-trivial at one loop, whereas the quark LSZ constants only gets non-trivial corrections at two loop, which makes them irrelevant for the calculation at hand. Because bottom quarks are

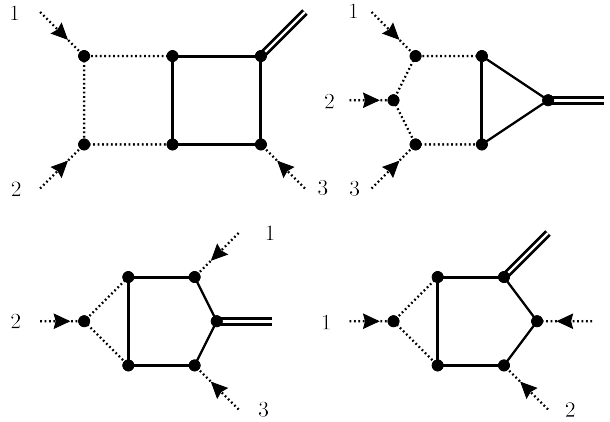


Figure 5.5: Graphical representation of the physical sectors embedded in the first integral family (PL1). Dotted lines represent massless propagators, while solid lines have the quark mass in the propagator.

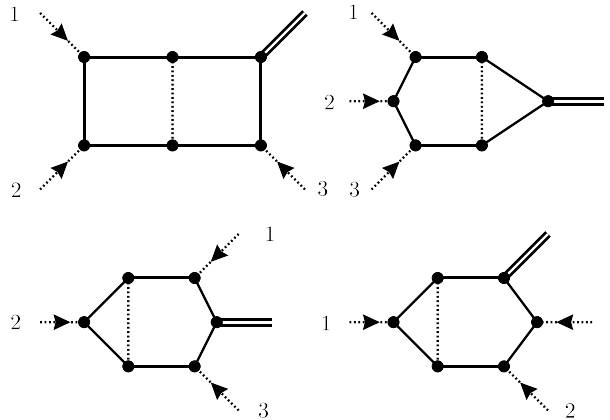


Figure 5.6: Same as Fig. 5.5 but for the second integral family (PL2).

treated as massless whenever they do not couple to the Higgs, they do not contribute to the LSZ constants. Hence, only the top-quark mass appears in these constants.

The remaining poles are of IR origin. They cancel against poles arising during phase-space integration, so we subtract them at the amplitude level. We employ the $\overline{\text{MS}}$ scheme and subtract only the divergences predicted by the \mathbf{Z} operator (see for example Ref. [58]).

Results for the Contributions with Two Heavy Quarks

Once all the above steps have been performed, we separate the contributions containing two heavy-quark loops from the rest of the amplitude. The IR-poles do not receive contributions from heavy internal lines and are therefore irrelevant for this contribution. The LSZ constants of the gluons on the other hand, do contribute. In the coupling renormalization constants, we single out the contributions from the top quark, i.e. we set the number of quarks to

$$n_f = n_l + n_h. \quad (5.22)$$

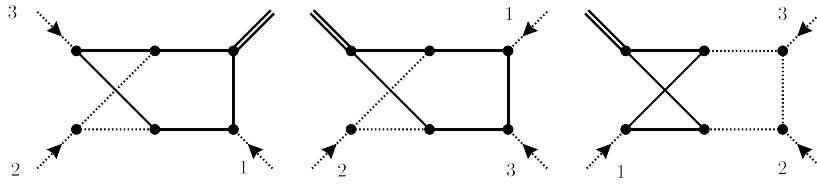


Figure 5.7: Same as Fig. 5.5 but for the third non-planar integral family (NPL).

Here n_l is the number of light quarks, and n_h is the number of heavy quarks. In the 5FS we have $n_l = 5$ and $n_h = 1$. The renormalization constant in the $\overline{\text{MS}}$ scheme then reads

$$Z_g = 1 - \frac{\alpha_s^{(n_f)}}{4\pi} 2\beta_0 \frac{1}{\epsilon} + \mathcal{O}(\alpha_s^2) = 1 + \frac{\alpha_s^{(n_f)}}{4\pi} \frac{1}{\epsilon} \left(-\frac{11}{6} C_A + \frac{2}{3} (n_l + n_h) T_F \right) + \mathcal{O}(\alpha_s^2). \quad (5.23)$$

To single out the contributions from the top quark we only take terms proportional to n_h and set n_h to one afterwards. We then apply the decoupling relations of Eq. (4.80) to replace the coupling constant with its decoupled counterpart in the lower order amplitudes². We can absorb these terms into the renormalization of the coupling constant, such that we end up with the effective renormalization constant

$$Z_g^{(n_l)}|_{\infty n_h} = \frac{\alpha_s}{4\pi} \frac{2}{3} T_F \left(\frac{1}{\epsilon} - \ln \left(\frac{m_t^2}{\mu^2} \right) \right) + \mathcal{O}(\alpha_s^2). \quad (5.24)$$

This is simply the top-quark contribution to the OS coupling renormalization constant. The decoupling constants were specifically introduced to cure the $\overline{\text{MS}}$ scheme from the appearance of non-decoupling effects. In the OS scheme this issue does not arise because of the Appelquist-Carrazzone theorem (see Section 4.2.2). The equality of the renormalization constants is therefore not accidental.

At one loop, the top-quark contribution to the renormalization constant is of abelian nature. In QED, the Ward identity implies the all order relation $Z_e = Z_3^{-1/2}$. We can therefore conclude, or verify explicitly that the one-loop renormalization constant is also related to the gluon LSZ constant

$$2(Z_g^{(n_l)} - 1)|_{\infty n_h} = -(Z_3 - 1) + \mathcal{O}(\alpha_s^2). \quad (5.25)$$

This has the profound effect that if the external number of gluons is identical to the power of the coupling constant (at lower order), then the contributions exactly cancel. This is for example the case in the $ggg \rightarrow H$ amplitude.

The result for the helicity amplitude of the $ggg \rightarrow H$ amplitude read

$$\begin{aligned} \mathcal{M}_{ggg \rightarrow H}^{(1),+++}|_{2 \text{ masses}} &= \frac{1}{\sqrt{2}} \frac{1}{\langle 12 \rangle \langle 23 \rangle \langle 31 \rangle} \left\{ -\frac{4m_t^2 stu}{(s+t)} \tilde{C}_0(u, m_t^2) \left[\tilde{B}(m_H^2, m_b^2) \right. \right. \\ &\quad \left. \left. + \frac{s+t}{u} + 2 \frac{m_b^2}{u} (4m_b^2 - s - t) \tilde{C}_1(u, m_H^2, m_b^2) - \frac{4m_b^2}{s+t} \tilde{B}(u, m_b^2) \right] \right. \\ &\quad \left. + (s \rightarrow t, t \rightarrow u, u \rightarrow s) + (s \rightarrow u, u \rightarrow t, t \rightarrow s) \right\} \end{aligned} \quad (5.26)$$

$$\begin{aligned} \mathcal{M}_{ggg \rightarrow H}^{(1),-+-}|_{2 \text{ masses}} &= -\frac{1}{\sqrt{2}} \frac{[23]^3}{[12][13]} \frac{4m_t^2 st}{u(s+t)} \tilde{C}_0(u, m_t^2) \left[\tilde{B}(m_H^2, m_b^2) \right. \\ &\quad \left. + \frac{s+t}{u} + 2 \frac{m_b^2}{u} (4m_b^2 - s - t) \tilde{C}_1(u, m_H^2, m_b^2) - \frac{4m_b^2}{(s+t)} \tilde{B}(u, m_b^2) \right] \end{aligned} \quad (5.27)$$

² In the renormalization constants we can simply set $\alpha_s^{(n_l+n_h)} = \alpha_s^{(n_l)}$ at this order in perturbation theory.

Where we defined the auxiliary functions³

$$\begin{aligned}\tilde{B}(s, m^2) &\equiv \beta(s, m^2) \log\left(-\frac{1 - \beta(s, m^2)}{1 + \beta(s, m^2)} + i0^+\right), \\ \tilde{C}_0(s, m^2) &\equiv \frac{1}{2s} \log^2\left(-\frac{1 - \beta(s, m^2)}{1 + \beta(s, m^2)} + i0^+\right) + \frac{2}{s} (\tilde{B}(s, m^2) + 2) + \frac{1}{6m^2}, \\ \tilde{C}_1(s_1, s_2, m^2) &\equiv \frac{1}{2} \frac{1}{s_1 - s_2} \left[\log^2\left(-\frac{1 - \beta(s_1, m^2)}{1 + \beta(s_2, m^2)} + i0^+\right) - \log^2\left(-\frac{1 - \beta(s_2, m^2)}{1 + \beta(s_2, m^2)} + i0^+\right) \right] \\ &\quad - \frac{s_1}{2m^2(s_1 - s_2)} \tilde{B}(s_2, m^2) + \frac{1}{2m^2}, \\ \text{with } \beta(s, m^2) &\equiv \sqrt{1 - \frac{4m^2}{s}}.\end{aligned}\tag{5.28}$$

All other helicity amplitudes are either related via charge conjugation (5.19), or by Bose symmetry

$$\mathcal{M}_{ggg \rightarrow H}^{+-+} = -\mathcal{M}_{ggg \rightarrow H}^{-++} \Big|_{p_1 \leftrightarrow p_2}, \quad \mathcal{M}_{ggg \rightarrow H}^{++-} = -\mathcal{M}_{ggg \rightarrow H}^{-++} \Big|_{p_1 \leftrightarrow p_3}.\tag{5.29}$$

Note that the Mandelstam variables are defined in terms of incoming gluon momenta, i.e.

$$s = (p_1 + p_2)^2, \quad t = (p_1 + p_3)^2, \quad u = (p_2 + p_3)^2.\tag{5.30}$$

For the quark channel the result reads

$$\begin{aligned}\mathcal{M}_{\bar{q}qg \rightarrow H}^{(1),-++} \Big|_{2 \text{ masses}} &= \frac{1}{\sqrt{2}} \frac{[13]^2}{[12]} \frac{4}{9(t+u)} \left(5s + 12m_t^2 + (3s + 6m_t^2)\tilde{B}(s, m_t^2) \right) \left[\tilde{B}(m_H^2, m_b^2) \right. \\ &\quad \left. + \frac{t+u}{s} + 2\frac{m_b^2}{s} (4m_b^2 - t - u) \tilde{C}_1(s, m_H^2, m_b^2) - \frac{4m_b^2}{t+u} \tilde{B}(s, m_b^2) \right].\end{aligned}\tag{5.31}$$

Once again all other amplitudes can be obtained through a relabeling of the external momenta and applying charge conjugation. We see that the functional dependence on the Mandelstams is identical in all amplitudes in Eqs. (5.26), (5.27), and (5.31). This is because the expression is related to the off-shell Higgs-gluon form factor, appearing in all Feynman diagrams of this contribution (see Fig. 5.3).

Contributions With One Heavy Quark

For completeness, we reproduce here the LO helicity amplitudes computed in Ref. [175]

$$\begin{aligned}\mathcal{M}_{ggg \rightarrow H}^{(0),+++} &= \frac{1}{\sqrt{2}} \frac{16m^2stu}{\langle 12 \rangle \langle 23 \rangle \langle 31 \rangle} \left\{ -8 \left[\frac{1}{ut} + \frac{1}{tt_1} + \frac{1}{uu_1} \right] - \frac{8}{s} \left[\frac{2s+t}{u_1^2} B_1(u) + \frac{2s+u}{t_1^2} B_1(t) \right] \right. \\ &\quad - \frac{2(s-4m^2)}{stu} [s_1 C_1(s) + (u-s)C_1(t) + (t-s)C_1(u)] - 16m^2 \left[\frac{1}{tt_1} C_1(t) + \frac{1}{uu_1} C_1(u) \right] \\ &\quad \left. + \frac{8m^2}{s} D(u, t) + \frac{s-4m^2}{stu} [stD(s, t) + usD(u, s) - utD(u, t)] - \frac{4}{s^2} E(u, t) \right\},\end{aligned}\tag{5.32}$$

³ The functions are closely related to the finite part of the bubble integrals, and the triangle integrals with one off-shell leg but otherwise on-shell external momenta. These functions are slightly modified to simplify the expressions, but we keep the standard notation B for bubble integrals and C for triangle integrals. The tilde is added to make the distinction from the original integrals more apparent.

$$\begin{aligned} \mathcal{M}_{ggg \rightarrow H}^{(0),-++} = & \frac{1}{\sqrt{2}} \frac{[23]^3}{[12][13]} \frac{16m^2st}{u} \left\{ \frac{8m_H^2}{stu} + \frac{2(m_H^2 - 4m^2)}{stu} [s_1C_1(s) + u_1C_1(u) + t_1C_1(t)] \right. \\ & \left. - \frac{m_H^2 - 4m^2}{stu} [stD(s,t) + usD(u,s) + utD(u,t)] \right\}, \end{aligned} \quad (5.33)$$

$$\mathcal{M}_{\bar{q}qg \rightarrow H}^{(0),-++} = \frac{1}{\sqrt{2}} \frac{[13]^2}{[12]} \frac{m^2}{s_1} \left[2 + 2 \frac{s}{s_1} B_1(s) + (4m^2 - u - t) C_1(s) \right]. \quad (5.34)$$

Here m is the internal quark mass and we defined

$$s_1 = s - m_H^2, \quad t_1 = t - m_H^2, \quad u_1 = u - m_H^2. \quad (5.35)$$

The appearing functions are directly linked to standard Feynman integrals which we provide in Appendix B.

Although there is one fewer scale in the contributions with only one quark mass, the two-loop amplitudes are substantially more complex because the integrals no longer factorize. Instead of attempting to solve the remaining integrals analytically, we followed a numerical approach, where the amplitudes are evaluated at fixed phase-space points. These points can then be used as grid points for interpolations during the phase-space integration. For the numerical evaluation of the master integrals we follow the strategy outlined in Ref. [35], which itself is based on methods presented in Ref. [176]. The general idea is to derive a system of differential equation for each integral family, find suitable boundary conditions analytically, and then solve the differential equations numerically.

The amplitude is a function of four variables, e.g. s, t, u and the quark mass m . The Higgs mass is not a free parameter, as it can be expressed as a sum over the Mandelstams. We can however simply factor out one scale—say the collision scale s —to make everything dimensionless, leaving us effectively with just three scales. We choose to parameterize the amplitude in terms of the dimensionless variables

$$z \equiv -\frac{t+u}{s}, \quad \lambda \equiv \frac{t}{t+u}, \quad x \equiv \frac{m^2}{s} = \frac{m^2}{m_H^2}(1-z). \quad (5.36)$$

These variables are advantageous because they parameterize soft and collinear limits. Indeed, soft limits are described with $z \rightarrow 0$, whereas the collinear limits are captured by $\lambda \rightarrow 0$ for the t -collinear and $\lambda \rightarrow 1$ for u -collinear. Furthermore, z and λ are bounded by

$$0 \leq z \leq 1, \quad 0 \leq \lambda \leq 1, \quad \text{and} \quad 0 \leq x \quad (5.37)$$

for physical production kinematics.

To apply the method of differential equations, we need to apply derivatives with respect to our variables, but the master integrals are functions of the external momenta. We can apply the chain rule to relate the derivatives

$$\begin{aligned} \left(z \frac{\partial}{\partial z} \right) &= \left(t \frac{\partial}{\partial t} \right) + \left(u \frac{\partial}{\partial u} \right) + \frac{t+u}{s+t+u} \left(x \frac{\partial}{\partial x} \right) \\ &= \left(p_3^\mu \frac{\partial}{\partial p_3^\mu} \right) - \frac{z}{1-z} \left(x \frac{\partial}{\partial x} \right), \\ \left(\lambda \frac{\partial}{\partial \lambda} \right) &= \left(t \frac{\partial}{\partial t} \right) - \frac{\lambda}{1-\lambda} \left(u \frac{\partial}{\partial u} \right) \end{aligned} \quad (5.38)$$

$$= \frac{1}{2} \left(\left(p_1^\mu \frac{\partial}{\partial p_1^\mu} \right) - \left(p_2^\mu \frac{\partial}{\partial p_2^\mu} \right) + (1 - 2\lambda) \left(p_3^\mu \frac{\partial}{\partial p_3^\mu} \right) \right). \quad (5.39)$$

The derivative with respect to x remains unchanged. One can now proceed to apply the differential operators onto the master integrals. The derivatives result in new integrals, which we can subsequently relate to our master integrals through the repeated use of IBPs.

We found that it is advantageous to shift almost all the appearing master integrals from $d = 4 - 2\epsilon$ to $d + 2$ dimensions, by application of *dimension-shift relations* (see Ref. [36] for a comprehensive introduction). This way, all spurious poles of the top-level sector are removed, and the integrals must only be computed up to ϵ^0 . As a byproduct, we found that the coefficients in front of the master integrals are significantly reduced in complexity.

In order to solve the differential equation, we need to find suitable boundary conditions. Because the HTL has already been extensively studied, we choose it as our boundary condition. To this end, we expand the integrals in the limit of a large internal mass $m, x \rightarrow \infty$ by means of the *large mass expansion* (see Ref. [177] for a comprehensive introduction). It allows expanding integrals in the limit of large masses already at the integral level, i.e. the remaining integrals are devoid of the large mass. The expansion is implemented in the workflow of **DiaGen/IdSolver**. The only required integrals are massless four-point functions and vacuum integrals which can be found in the appendix of Ref. [178].

The solutions found at the boundary $x \rightarrow \infty$ are then transported to the physical plane—i.e. to finite quark masses—by solving the differential equation in the x -direction. This strategy is illustrated in Fig. 5.8. The differential equation is solved numerically using the *Bulirsch-Stoer*

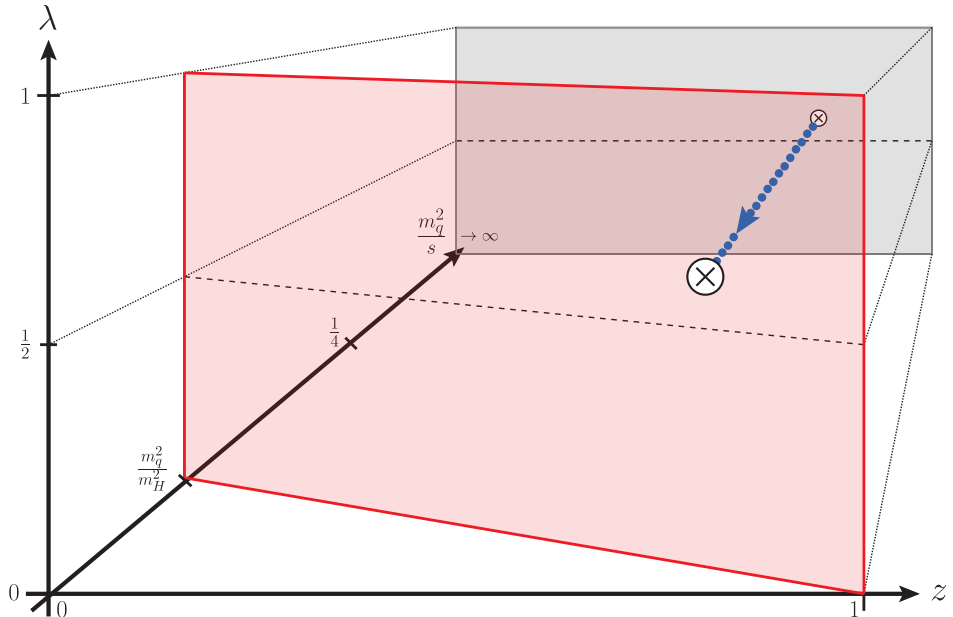


Figure 5.8: Graphical illustration of the parameter space and the strategy for transporting the boundary conditions at $x \rightarrow \infty$ to the physical plane shown in red. This figure was taken (with slight modification) from Ref. [178].

algorithm. Since we are working within the physical parameter space defined by Eq. (5.36), we can no longer relate the various matrix elements by means of the crossing relations in Eq. (5.29).

We will therefore have to switch to a physical momentum configuration, and compute all matrix elements⁴

$$\begin{aligned} \mathcal{M}_{gg \rightarrow gH}^{--+}, \mathcal{M}_{gg \rightarrow gH}^{++-}, \mathcal{M}_{gg \rightarrow gH}^{+-+}, \mathcal{M}_{gg \rightarrow gH}^{+++}, \\ \mathcal{M}_{\bar{q}q \rightarrow gH}^{--+}, \mathcal{M}_{\bar{q}q \rightarrow gH}^{++-}, \mathcal{M}_{g\bar{q} \rightarrow \bar{q}H}^{+-+}, \mathcal{M}_{g\bar{q} \rightarrow \bar{q}H}^{++-}, \mathcal{M}_{qg \rightarrow qH}^{+-+}, \mathcal{M}_{qg \rightarrow qH}^{--+} \end{aligned} \quad (5.40)$$

individually. Notice that we can still apply the charge conjugation identity in Eq. (5.19) if we first pull out the spinor-helicity factors. Nevertheless, the exchange of the first two momenta does not take us out of the physical parameter space and hence this crossing symmetry (followed by charge conjugation) can still be exploited

$$|\mathcal{M}_{gg \rightarrow gH}^{\lambda_1 \lambda_2 \lambda_3}|^2(\lambda, z, x) = |\mathcal{M}_{gg \rightarrow gH}^{\lambda_2 \lambda_1 \lambda_3}|^2(1 - \lambda, z, x), \quad (5.41)$$

$$|\mathcal{M}_{\bar{q}q \rightarrow gH}^{\lambda_1 \lambda_2 \lambda_3}|^2(\lambda, z, x) = |\mathcal{M}_{\bar{q}q \rightarrow gH}^{\lambda_2 \lambda_1 \lambda_3}|^2(1 - \lambda, z, x), \quad (5.42)$$

$$|\mathcal{M}_{qg \rightarrow qH}^{\lambda_1 \lambda_2 \lambda_3}|^2(\lambda, z, x) = |\mathcal{M}_{g\bar{q} \rightarrow \bar{q}H}^{\lambda_2 \lambda_1 \lambda_3}|^2(1 - \lambda, z, x). \quad (5.43)$$

We relate the squared amplitudes to avoid phase factors arising from the spinor-helicity factors. The physical parameter space is therefore effectively cut in half. Consequently, we only need to solve the amplitude for $1/2 \leq \lambda \leq 1$ and can infer the remaining domain using these symmetry relations.

We therefore choose initial conditions which are just above the symmetry line $\lambda = 1/2$, and then sample different values in z . The samples are then transported to the physical plane using the differential equation in the x -direction. The resulting solutions then serve as initial conditions for the differential equation in the λ -direction, allowing us to get samples in the entire physical parameter space. The strategy is illustrated in Fig. 5.9.

At $z \rightarrow 0$, we encounter soft divergences. These divergences will cancel in inclusive observables once we perform the phase-space integration. The large cancellations thus require particularly numerically accurate amplitudes. To minimize potential errors of the interpolation, we therefore sample z logarithmically, such that the grid points are especially dense in this region of the phase space. Similarly, for $z \rightarrow 1$, although there are no IR divergences, the differential equation still exhibits poles which for this region of the parameter space are located particularly close together. This is caused by the remapping of the phase-space to the unit square using the *Möbius transformation* in Eq. (5.36). Consequently, this region suffers from the appearance of large cancellations as well. So to avoid mismodelling the amplitudes we also sample points close to this boundary more densely. In the end we generated around 1000 values of z , ranging from 10^{-4} to $1 - 10^{-4}$.

The poles of the differential equation in λ are dealt with via a contour deformation in the complex plane. Once again we sample λ logarithmically, such that we obtain more points towards the IR-sensitive $\lambda \rightarrow 1$ region. In total, we sample around 500 λ -points, yielding in total, a dense grid of the physical plane of about 10^6 grid points.

As we highlighted repeatedly, around the IR sensitive regions $z \rightarrow 0$ and $\lambda \rightarrow 0, 1$, the amplitudes are dominated by the singularities $1/z$, $1/\sqrt{\lambda}$ and $1/\sqrt{1-\lambda}$, a contribution which will eventually cancel against other IR divergences. On the other hand, the dominance of the singularity will negatively impact the precision of the interpolation for the non-divergent terms. We would therefore like to subtract the IR-divergences before performing the interpolation.

⁴ The helicities are assigned to the partons in the order they appear in the corresponding process, i.e. the first helicity belongs to the first appearing parton, the second to the second, and the third to the third.

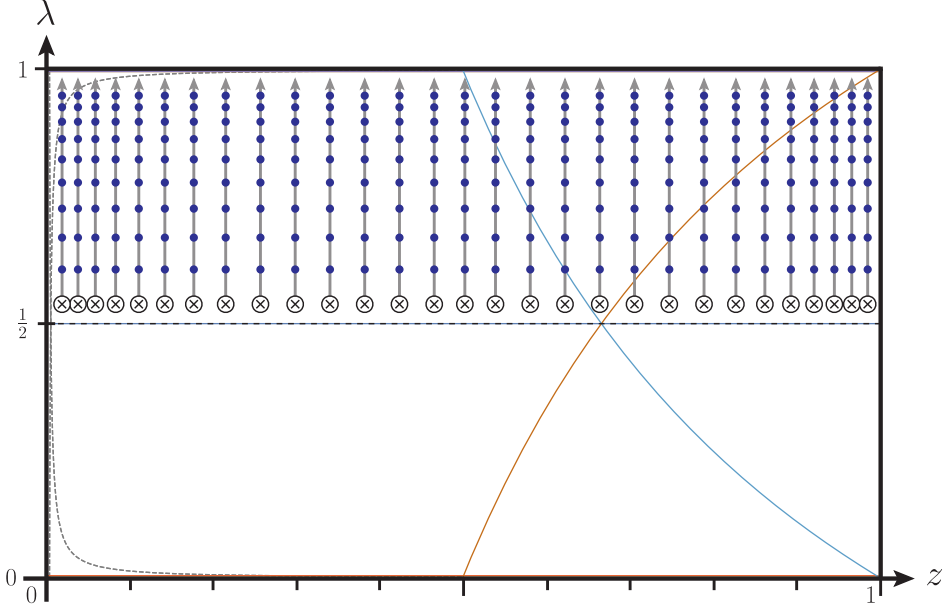


Figure 5.9: Illustration of the physical plane (shown in red in Fig. 5.8) for a bottom quark with a mass ratio of $m_b^2/m_H^2 = 1/684$. The colored thin lines indicate poles of the differential equation in λ . The circled crosses with the errors indicate the boundary condition for the differential equation in λ and the path along which the differential equation is solved. The integration paths are not to scale and are for illustrative purposes only.

It is well known that the leading IR behavior factorizes from the amplitude. Consider for example, the limit of two almost collinear outgoing partons with momenta

$$p_1^\mu = z_1 p^\mu + k_\perp^\mu - \frac{k_\perp^2}{z_1} \frac{n^\mu}{2p \cdot n}, \quad p_2^\mu = (1 - z_1)p^\mu - k_\perp - \frac{k_\perp^2}{1 - z_1} \frac{n^\mu}{2p \cdot n}, \quad (5.44)$$

where $k_\perp \cdot p = k_\perp \cdot n = 0$, and p and n are on-shell ($p^2 = n^2 = 0$). Further, p and n are not collinear, i.e. $p \cdot n \sim \mathcal{O}(p^0 n^0)$. The collinear limit is therefore parameterized by $k_\perp \rightarrow 0$. Then the leading power behavior of the one-loop averaged squared matrix element is given by

$$\begin{aligned} 2\text{Re}\overline{\langle \mathcal{M}_{a_1 a_2, \dots}^{(0)}(p_1, p_2, \dots) | \mathcal{M}_{a_1 a_2, \dots}^{(1)}(p_1, p_2, \dots) \rangle} &\simeq \\ 4\pi\alpha_s \frac{1}{p_1 \cdot p_2} \left[\langle P_{a_1 a_2}^{(0)}(z_1) \rangle \times 2\text{Re}\overline{\langle \mathcal{M}_{a, \dots}^{(0)}(p, \dots) | \mathcal{M}_{a, \dots}^{(1)}(p, \dots) \rangle} \right. \\ &\quad \left. + \frac{\alpha_s}{4\pi} \langle P_{a_1 a_2}^{(1)}(z_1) \rangle \overline{\langle \mathcal{M}_{a, \dots}^{(0)}(p, \dots) | \mathcal{M}_{a, \dots}^{(0)}(p, \dots) \rangle} \right]. \end{aligned} \quad (5.45)$$

Here a_1 and a_2 denote the flavor of the respective parton, while the flavor a is set by flavor conservation of the process $a \rightarrow a_1 a_2$. That means $(a_1 = q, a_2 = \bar{q})$ implies $a = g$, and further $(a_1 = g, a_2 = q) \Rightarrow a = q$, $(a_1 = g, a_2 = g) \Rightarrow a = g$, and so on. $\langle P_{a_1 a_2}^{(0,1)}(z_1) \rangle$ are the tree-level and one-loop averaged splitting functions. For reasons that will be explained below, the exact

structure of the one-loop splitting functions is of no concern to us. The tree-level averaged splitting functions in four dimensions read

$$\begin{aligned}\langle P_{gg}^{(0)}(z_1) \rangle &= 2C_A \left(\frac{z_1}{1-z_1} + \frac{1-z_1}{z_1} + z_1(1-z_1) \right), \\ \langle P_{q\bar{q}}^{(0)}(z_1) \rangle &= \langle P_{\bar{q}q}^{(0)}(z_1) \rangle = T_F (1 - 2z_1(1-z_1)), \\ \langle P_{qg}^{(0)}(z_1) \rangle &= \langle P_{\bar{q}g}^{(0)}(z_1) \rangle = C_F \frac{1+z_1^2}{1-z_1}, \\ \langle P_{gq}^{(0)}(z_1) \rangle &= \langle P_{g\bar{q}}^{(0)}(z_1) \rangle = \langle P_{qg}^{(0)}(1-z_1) \rangle.\end{aligned}\tag{5.46}$$

Initial-state collinear divergences can be recovered by replacing $p_2 \rightarrow -p_2$ as well as $P_{a_1 a_2} \rightarrow (-1)^{2s_a+2s_{a_1}} P_{a_1 a_2}$, where s_a and s_{a_1} are the spins of the respective partons.

Similarly, when one of the external gluons becomes soft, $q \rightarrow 0$, the factorization of the one-loop squared amplitude with external partons reads

$$\begin{aligned}2\text{Re} \langle \mathcal{M}_{g,a_1,\dots}(q,p_1,\dots) | \mathcal{M}_{g,a_1,\dots}^{(1)}(q,p_1,\dots) \rangle &\simeq \\ -4\pi\alpha_s \Bigg\{ &\sum_{(i,j)} (\mathcal{S}_{ij}(q) - \mathcal{S}_{ii}(q)) 2\text{Re} \langle \mathcal{M}_{a_1,\dots}(p_1,\dots) | \mathbf{T}_i \cdot \mathbf{T}_j | \mathcal{M}_{a_1,\dots}^{(1)}(p_1,\dots) \rangle \\ &+ \frac{\alpha_s}{4\pi} \Big[\sum_{(i,j)} (\mathcal{S}_{ij}(q) - \mathcal{S}_{ii}(q)) R_{ij} \langle \mathcal{M}_{a_1,\dots}(p_1,\dots) | \mathbf{T}_i \cdot \mathbf{T}_j | \mathcal{M}_{a_1,\dots}^{(0)}(p_1,\dots) \rangle \\ &- 4\pi \sum_{(i,j,k)} \mathcal{S}_{ik}(q) I_{ij} \langle \mathcal{M}_{a_1,\dots}(p_1,\dots) | f^{abc} \mathbf{T}_i^a \mathbf{T}_j^b \mathbf{T}_k^c | \mathcal{M}_{a_1,\dots}^{(1)}(p_1,\dots) \rangle \Big] \Bigg\}.\end{aligned}\tag{5.47}$$

The sums run over distinct parton indices. \mathbf{T}_i denotes the color operator of the i -th particle, i.e., it is the generator of the SU(3) group in the representation of that particle: fundamental for quarks, complex-conjugated for anti-quarks, adjoint for gluons and trivial for colorless particles. The ket $|\mathcal{M}\rangle$, denotes an abstract vector in color and spin space, i.e. the vector is related to the usual amplitudes via

$$|\mathcal{M}_{a_1,\dots,a_n}\rangle \equiv \sum_{\lambda_1,\dots,\lambda_n} \sum_{c_1,\dots,c_n} \mathcal{M}(\lambda_1, c_1; \dots; \lambda_n, c_n) |\lambda_1, \dots, \lambda_n; c_1, \dots, c_n\rangle.\tag{5.48}$$

Once again, the exact structure of the one-loop coefficients I_{ij} and R_{ij} is irrelevant for our purposes (see Ref. [58] for a definition). The eikonal factor is defined as

$$\mathcal{S}_{ij}(q) \equiv \frac{p_i \cdot p_j}{(p_i \cdot q)(p_j \cdot q)}.\tag{5.49}$$

We claim that the regulated, averaged squared amplitudes

$$\begin{aligned} \overline{\langle \mathcal{M}_{gg \rightarrow gH}^{(0)} | \mathcal{M}_{gg \rightarrow gH}^{(1)} \rangle}_{\text{regulated}} &\equiv \overline{\langle \mathcal{M}_{gg \rightarrow gH}^{(0)} | \mathcal{M}_{gg \rightarrow gH}^{(1)} \rangle} - \overline{\langle \mathcal{M}_{gg \rightarrow gH}^{(0),\text{rHTL}} | \mathcal{M}_{gg \rightarrow gH}^{(1),\text{rHTL}} \rangle} \\ &- \overline{\langle \mathcal{M}_{gg \rightarrow H}^{(0)} | \mathcal{M}_{gg \rightarrow H}^{(1)} - \mathcal{M}_{gg \rightarrow H}^{(1),\text{rHTL}} \rangle} \times \begin{cases} \frac{8\pi\alpha_s}{t} \langle P_{gg}^{(0)} \left(\frac{s}{s+u} \right) \rangle & \text{if } |t| < |u| \\ \frac{8\pi\alpha_s}{u} \langle P_{gg}^{(0)} \left(\frac{s}{s+t} \right) \rangle & \text{if } |u| < |t| \end{cases}, \\ \overline{\langle \mathcal{M}_{qg \rightarrow qH}^{(0)} | \mathcal{M}_{qg \rightarrow qH}^{(1)} \rangle}_{\text{regulated}} &\equiv \overline{\langle \mathcal{M}_{qg \rightarrow qH}^{(0)} | \mathcal{M}_{qg \rightarrow qH}^{(1)} \rangle} - \overline{\langle \mathcal{M}_{qg \rightarrow qH}^{(0),\text{rHTL}} | \mathcal{M}_{qg \rightarrow qH}^{(1),\text{rHTL}} \rangle} \\ &+ \overline{\langle \mathcal{M}_{gg \rightarrow H}^{(0)} | \mathcal{M}_{gg \rightarrow H}^{(1)} - \mathcal{M}_{gg \rightarrow H}^{(1),\text{rHTL}} \rangle} \times \frac{8\pi\alpha_s}{t} \langle P_{q\bar{q}}^{(0)} \left(\frac{s}{s+u} \right) \rangle, \\ \overline{\langle \mathcal{M}_{q\bar{q} \rightarrow gH}^{(0)} | \mathcal{M}_{q\bar{q} \rightarrow gH}^{(1)} \rangle}_{\text{regulated}} &\equiv \overline{\langle \mathcal{M}_{q\bar{q} \rightarrow gH}^{(0)} | \mathcal{M}_{q\bar{q} \rightarrow gH}^{(1)} \rangle} - \overline{\langle \mathcal{M}_{q\bar{q} \rightarrow gH}^{(0),\text{rHTL}} | \mathcal{M}_{q\bar{q} \rightarrow gH}^{(1),\text{rHTL}} \rangle}, \end{aligned} \quad (5.50)$$

are free of IR divergences.

By subtracting the amplitude in the rHTL we are eliminating all infrared divergences coming from one-loop splitting functions or soft functions in Eqs. (5.45) and (5.47). These functions now only act on the difference between the LO Higgs-gluon form factor in QCD and in the rHTL; however, that difference is zero by definition of the rHTL. Notice that the factor used for rescaling the cross section in the HTL for the interference contributions is now defined in terms of

$$r_{t \times b}^{\text{LO}} = \frac{\hat{\sigma}_{t \times b}^{\text{LO}}}{\hat{\sigma}_{t \times b}^{\text{LO,rHTL}}}, \quad (5.51)$$

which for on-shell masses yields approximately -0.129 . In contrast to the rescaling factor for the pure top-quark contribution, this rescaling factor has no direct phenomenological relevance, in the sense that it can incorporate finite-quark-mass effects, and is used only as a computational trick.

Even after subtraction of the rHTL squared amplitudes, the difference still exhibits divergences coming from tree-level splitting and soft functions. For the $gg \rightarrow gH$ amplitude the divergence can be handled by subtracting

$$\overline{\langle \mathcal{M}_{gg \rightarrow H}^{(0)} | \mathcal{M}_{gg \rightarrow H}^{(1)} - \mathcal{M}_{gg \rightarrow H}^{(1),\text{rHTL}} \rangle} \times \begin{cases} \frac{8\pi\alpha_s}{t} \langle P_{gg}^{(0)} \left(\frac{s}{s+u} \right) \rangle & \text{if } |t| < |u| \\ \frac{8\pi\alpha_s}{u} \langle P_{gg}^{(0)} \left(\frac{s}{s+t} \right) \rangle & \text{if } |u| < |t| \end{cases} \quad (5.52)$$

from the difference. To see this, consider the t -collinear limit ($p_1 \cdot p_3 \rightarrow 0$). We can choose the anti-collinear direction to be along p_2 , and then determine⁵

$$z_1 = \frac{p_1 \cdot p_2}{p_1 \cdot p_2 - p_3 \cdot p_2} = \frac{s}{s-u}. \quad (5.53)$$

Hence, Eq. (5.52) has exactly the structure required from a collinear limit (5.45). The u -collinear limit works analogously. In the soft limit, where t and u tend to zero, we can expand the splitting functions and get

$$(5.52) \rightarrow \overline{\langle \mathcal{M}_{gg \rightarrow H}^{(0)} | \mathcal{M}_{gg \rightarrow H}^{(1)} - \mathcal{M}_{gg \rightarrow H}^{(1),\text{rHTL}} \rangle} \times \frac{8\pi\alpha_s}{t} 2C_A \frac{s}{u}. \quad (5.54)$$

Remembering that the Higgs-gluon form factor was diagonal in color-space, i.e. proportional to $\delta^{c_1 c_2}$, we see that this is exactly the soft divergence predicted by Eq. (5.47).

⁵ Note that z_1 is only unique up to power corrections.

Since there is no $qg \rightarrow H$ process, the qg -channel cannot develop a soft divergence. The initial-state collinear divergence is subtracted with the corresponding splitting functions analogous to the gg channel. The different sign comes from the splitting function, which generates a minus sign if a fermion is crossed to the initial state.

Lastly, after subtraction of the squared amplitude of the rHTL, the $q\bar{q}$ -channel does not exhibit any IR singularity, due to the lack of available Born processes.

In Fig. 5.10 we present the results for the top-bottom interference contribution to the amplitudes, while Fig. 5.11 shows the results for the pure-top-quark contribution. Despite having subtracted

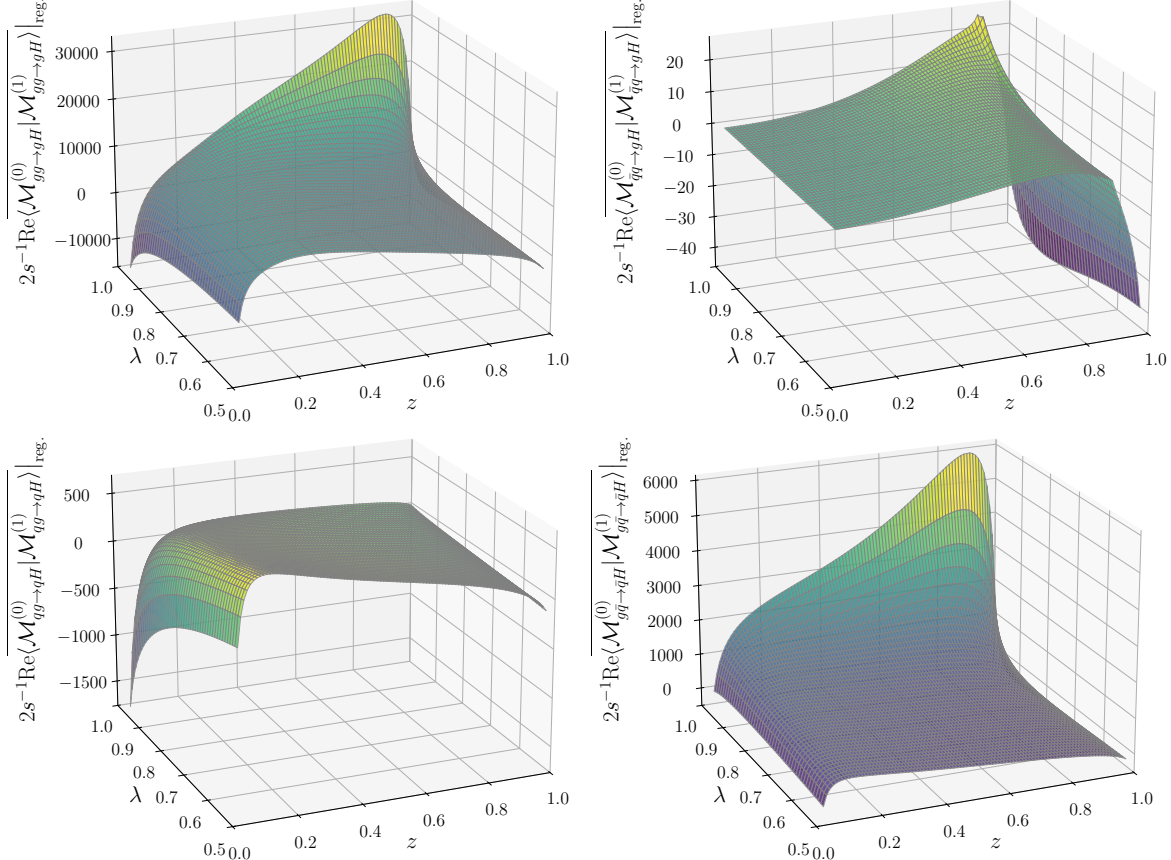


Figure 5.10: Top-bottom interference contribution to the amplitudes $gg \rightarrow gH$ (top left), $\bar{q}q \rightarrow gH$ (top right), $qg \rightarrow qH$ (bottom left) and $g\bar{q} \rightarrow \bar{q}H$ (bottom right) normalized by the partonic center-of-mass energy s . Displayed is only half of the parameter space $\lambda \in [0.5, 1]$; the other half can be obtained by means of the symmetry relations in Eqs. (5.41), (5.42) and (5.43). For better visibility, we only show grid points in the range of $\lambda \in [0.5, 0.98]$ and $z \in [0.02, 0.98]$. The amplitude is computed with on-shell renormalized quark-masses. The computational setup is described in the Conventions.

the IR-divergences, the amplitudes still exhibit some residual divergences in the IR-sensitive regions close to $z \rightarrow 0$ and $\lambda \rightarrow 1$. These divergences are however much better behaved, only showing logarithmic growth at the edges of the phase-space, and consequently can be integrated over. As expected, the $\bar{q}q$ -channel does not show logarithmic divergences in the soft limit $z \rightarrow 0$ since the $\bar{q}q \rightarrow H$ process was forbidden by the conservation of angular momentum (see discussion around Eq. (4.90)).

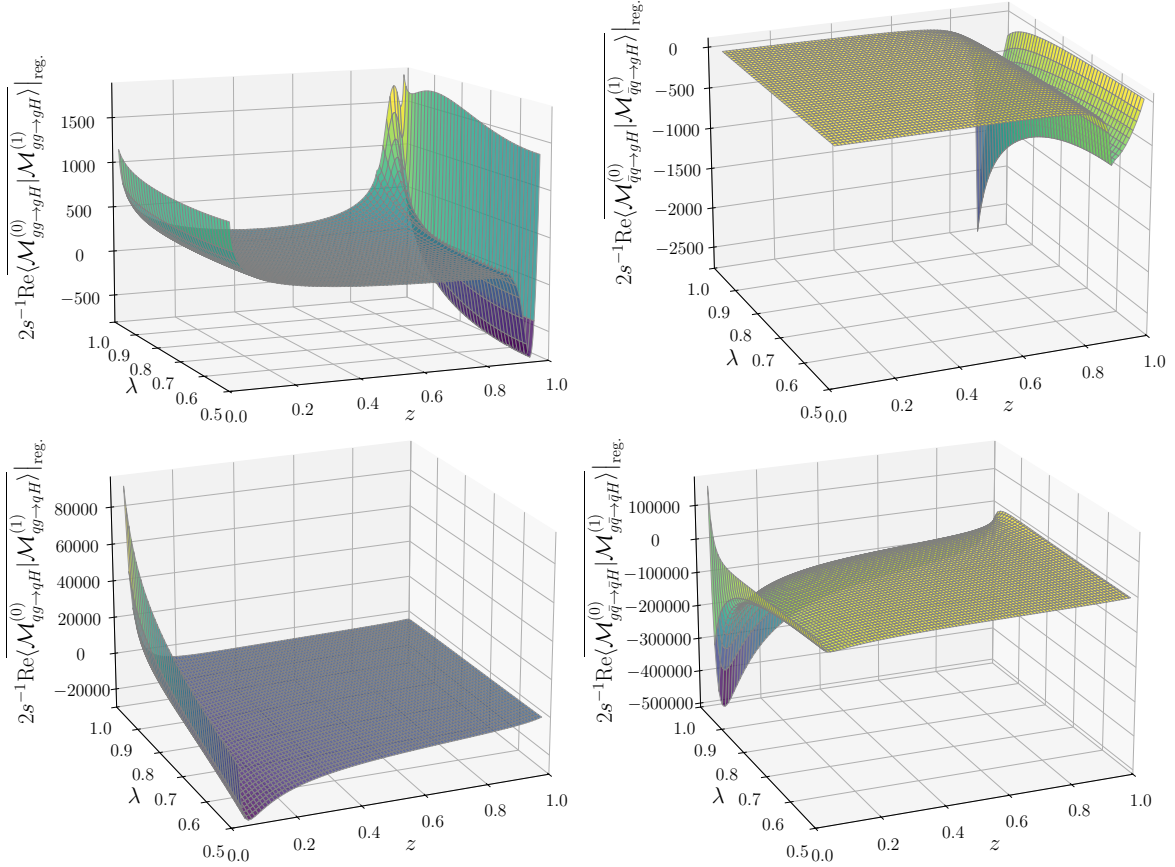


Figure 5.11: Same as in Fig. 5.10 but for the pure-top-quark contribution to the amplitudes. Plot range for the $gg \rightarrow gH$ has been changed to $z \in [0.002, 0.965]$ and $\lambda \in [0.5, 0.98]$, for better visibility.

In the pure-top-quark contribution, the $gg \rightarrow gH$ and $\bar{q}q \rightarrow qH$ amplitudes display their most prominent features around the $t\bar{t}$ -production threshold at $z_{\text{threshold}} = 1 - \frac{m_H^2}{4m_t^2} \approx 0.87$. This outcome aligns with our expectations, as Landau's equations predict a branch cut in the amplitude beginning at the production threshold. The amplitudes for the $qg \rightarrow qH$ and $g\bar{q} \rightarrow \bar{q}H$ processes do not exhibit this branch cut at LO since here the discontinuity lies outside the physical parameter space at $t = 4m_t^2 > 0$ and $u = 4m_t^2 > 0$. At NLO, the normal thresholds are nevertheless present. Since the normal threshold only enters via perturbative corrections, we can expect to see less pronounced features around it. For the top-bottom interference contributions, the threshold region is less feature rich since the amplitudes with top-quark induced Higgs production are no longer squared, but instead multiplied by the bottom-quark induced Higgs production. The latter do not have branch cuts at the $t\bar{t}$ -thresholds, causing a smoother behavior in this region of the parameter space.

Interpolation

During the phase-space integration, we require the amplitude at any point of the parameter space, not just at the grid points we computed. We can achieve a highly accurate approximation of the amplitudes by interpolating between the grid points. To do this, we first identify a 4×4 sub-grid, such that the target point lies inside the center square. We then construct one-dimensional cubic splines in the λ -direction for each fixed value of z using the relevant grid points. We can then use these spline fits to obtain approximations of the amplitude

at the target- λ value and the four fixed z -values. Next, we use these four values to build a second cubic spline in the z -direction, which can then be used to get an approximation of the amplitude at the target phase-space point. The method is illustrated in Fig. 5.12 and can be straightforwardly generalized to any dimension. Note that this method does not rely on a

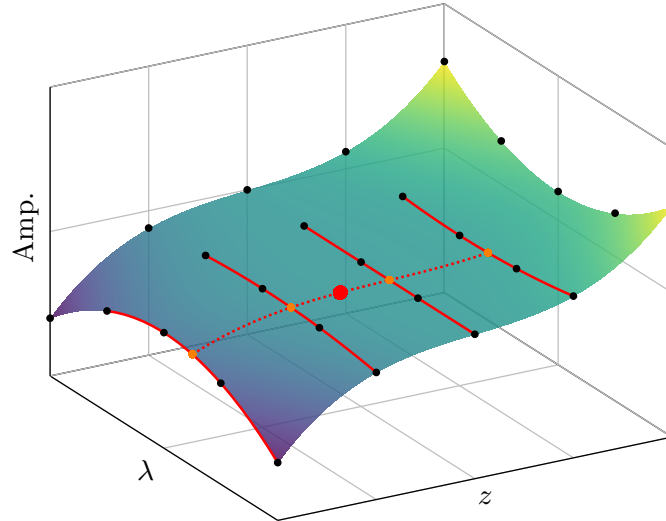


Figure 5.12: Graphical illustration of the method to perform multidimensional interpolations using cubic splines. The surface represents the actual amplitude; the black dots mark the computed grid points; the large red dot is the target phase-space point; the solid red line indicates the spline fit in the λ -direction; the orange dots mark the value of the λ -fits at the target- λ ; the dashed red line marks the spline fit in the z -direction.

rectangularly distributed grid samples—only that the samples lie in a straight line along one direction. This is important as our grid samples were distributed logarithmically. Furthermore, grid points which are located very close to poles of the differential equation are not being evaluated due to the contour deformation. But as the interpolation method does not rely on equidistant grid points, we can still interpolate these regions of the phase-space.

During the phase-space integration we will also encounter phase-space regions which lie outside our computed grid, making it necessary for us to extrapolate. In the IR-sensitive regions, the amplitude must grow double-logarithmically, whereas in the high-energy limit $z \rightarrow 1$ it can be shown [131, 179] that the amplitude grows as $\log^3(1 - z)$. One can therefore use a power-logarithmic *Ansatz* for the extrapolation of the amplitude. However, we found that extrapolations using the cubic splines yielded results compatible within the MC uncertainties, which is why we went with this simpler approach for our final results. The alternative extrapolation method serves as additional cross-check of the accuracy of our amplitudes in these regions of phase space.

After completing the interpolation, we reintroduce the subtraction terms from Eq. (5.50), which we know fully analytically across the entire phase-space, to obtain the full amplitudes.

5.1.3 The Virtual-Virtual Corrections

Lastly, we consider virtual-virtual corrections to the $gg \rightarrow H$ amplitudes—that is, the three-loop Higgs-gluon form factor. We can decompose the NNLO contribution to the form factor according to the quark loops of the respective Feynman diagrams as follows:

$$\begin{aligned} \mathcal{C}^{(2)} = & n_t \mathcal{C}_t^{(2)} + n_t^2 \mathcal{C}_{tt}^{(2)} + n_t n_l \mathcal{C}_{tl}^{(2)} \\ & + n_b \mathcal{C}_b^{(2)} + n_b^2 \mathcal{C}_{bb}^{(2)} + n_b n_l \mathcal{C}_{bl}^{(2)} \\ & + n_t n_b (\mathcal{C}_{tb}^{(2)} + \mathcal{C}_{bt}^{(2)}). \end{aligned} \quad (5.55)$$

Here, the first index indicates which quark flavor couples to the Higgs, and the second index—if present—marks the flavor of the other quark loop. That means contributions inside $\mathcal{C}_t^{(2)}$ are computed from Feynman diagrams with only a single quark loop containing the top quark. Example Feynman diagrams for this contribution are shown in Fig. 5.13. $\mathcal{C}_b^{(2)}$ is computed by the same means only with the top quark replaced by the bottom quark.

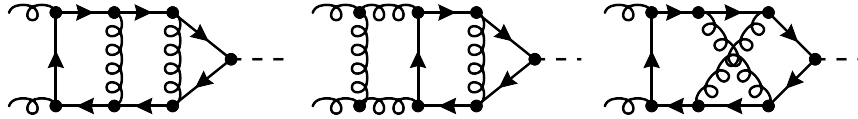


Figure 5.13: Example Feynman diagrams for contributions to $\mathcal{C}_t^{(2)}$, containing only a single heavy-quark loop.

Similarly, $\mathcal{C}_{tt}^{(2)}$ then contains two closed top-quark loops, $\mathcal{C}_{tl}^{(2)}$ one top-quark and one light-quark loop, and so on. All Feynman diagrams containing two closed quark-loops are depicted in Fig. 5.14. The $\mathcal{C}_t^{(2)}, \mathcal{C}_{tt}^{(2)}, \mathcal{C}_{tl}^{(2)}, \mathcal{C}_b^{(2)}, \mathcal{C}_{bb}^{(2)}$ and $\mathcal{C}_{bl}^{(2)}$ contributions are computed with only a single heavy-quark mass, making these contributions functions of only one dimensionless variable, namely

$$z_q = \frac{m_H^2}{4m_q^2}. \quad (5.56)$$

The $\mathcal{C}_{tb}^{(2)}$ and $\mathcal{C}_{bt}^{(2)}$ parts of the form factor, on the other hand, are now functions of both z_b and z_t . They are the only instance, where we encounter non-factorizable Feynman-integrals with two-different masses in the whole cross section calculation. Note that when working in the 5FS, the $\mathcal{C}_{tb}^{(2)}$ contribution is set to zero because the bottom-quark loop is not coupling to the Higgs.

Both the one- and two-quark-mass contributions have recently been computed [67, 180]. They apply a method similar to what we have described in the previous chapter. They derive a set of differential equations, this time in terms of z_q or z_b and z_t and subsequently solve the differential equations numerically. The heavy-top and the high-energy limit are used as boundary conditions of the differential equation. They derive a deep asymptotic expansion using a combination of the large-mass expansion and the method of regions [181]. For phenomenological application, both the bottom- and the top-quark mass are sufficiently far away from the threshold that the asymptotic expansions approximate the amplitude without a relevant loss of precision. We therefore use the provided series expansions for our computations. In the public version of Ref. [67], the amplitude is not provided with the $n_{t,b}$ tags, i.e. it is not possible to individually

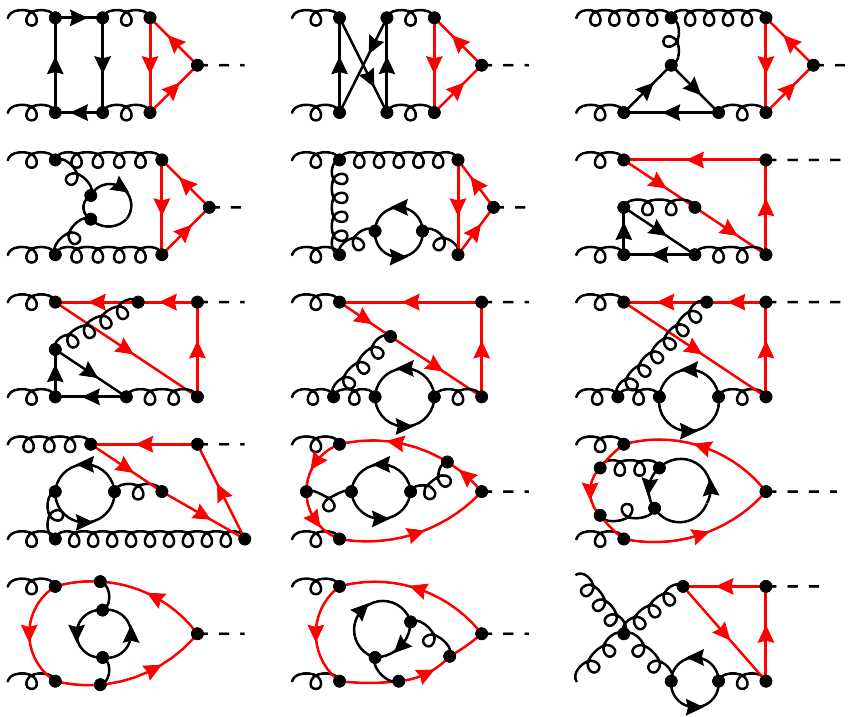


Figure 5.14: All Feynman diagrams with two closed quark loops. The quark loop coupling to Higgs, marked in red, must be a heavy-quark line, i.e. either a top or bottom quark. The black quark loop can be either a top, bottom, or light quark. Reversed fermion flows are not explicitly drawn.

extract the $\mathcal{C}_{bb}^{(2)}$ and $\mathcal{C}_b^{(2)}$ contribution. This is indispensable when working in the 5FS. We obtained the amplitudes with the relevant tags through private communication with the authors of Ref. [67].

The results for the various coefficients of the Higgs-gluon form factor are presented in Figs. 5.15 and 5.16. For the mixed contributions $\mathcal{C}_{tb}^{(2)}$ and $\mathcal{C}_{bt}^{(2)}$, we only display the results for a fixed OS mass of the quark which is not coupling to the Higgs. The full mass dependence of the mixed coefficients is displayed in Fig. 5.17. We can see that the dominant contribution to the Higgs-gluon form factor comes from \mathcal{C}_b in the high-energy limit. Since an additional fermion loop results in a power suppression of $1/N_c$, one can expect that the other coefficients $\mathcal{C}_{bb}^{(2)}$, $\mathcal{C}_{bl}^{(2)}$ and $\mathcal{C}_{bt}^{(2)}$ will be less significant. The observed discrepancy between the contributions is however larger than what can be expected from a mere color suppression, a phenomenon which is commonly observed in the computation of amplitudes. The mixed contribution $\mathcal{C}_{bt}^{(2)}$ is completely negligible, and is small even compared $\mathcal{C}_{bl}^{(2)}$ and $\mathcal{C}_{bb}^{(2)}$. This can be understood from the Appelquist-Carrazzone theorem, which implies that the amplitude should be suppressed by a factor of $m_H^2/4m_t^2$.

Below the threshold—i.e., in amplitudes where the Higgs couples to the top quark—the dominant coefficient stems from contributions without a second fermion loop. However, the imaginary part does receive significant corrections. The mixed coefficient $\mathcal{C}_{tb}^{(2)}$ is hereby also relevant since it is no longer suppressed by large quark masses.

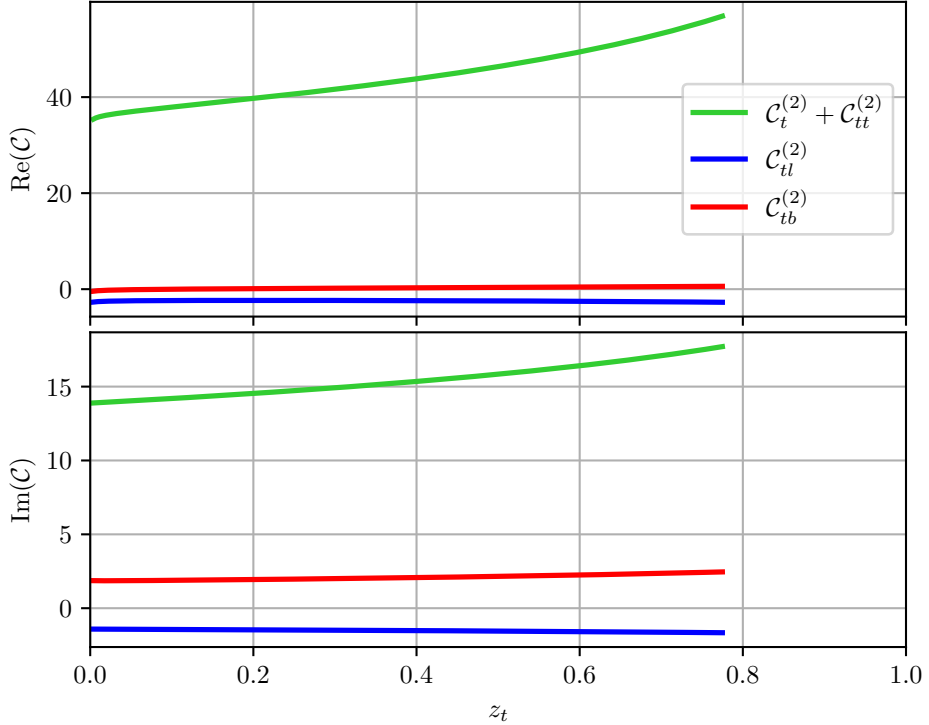


Figure 5.15: Coefficients of the Higgs-gluon form factor in the large-mass expansion. For the $\mathcal{C}_{tb}^{(2)}$ contribution, we set the bottom-quark mass to its OS-value. Both quark masses are renormalized in the OS scheme. IR divergences are subtracted in the $\overline{\text{MS}}$ scheme. The renormalization scale has been set to $\mu_R = m_H$. The computational setup is described in the Conventions.

Recently, it was noticed by Liu and Penin that the leading logarithms, i.e. logarithms of the form

$$\alpha_s^n \log^{n+1}(m_b^2/m_H^2), \quad (5.57)$$

of the high-energy limit of the virtual amplitudes can be predicted and resummed to all orders of perturbation theory [68]. They identified soft quark exchanges as the cause of the leading logarithm, and were able to rewrite the amplitude in terms of a *Sudakov form factor*. The Higgs gluon form factor in the high-energy limit at leading-logarithmic (LL) accuracy reads

$$\mathcal{C}(z_b) \Big|_{\text{LL}} = -Z_g^2 g(x) \left(\frac{3}{2} \frac{1}{4z_b} \ln^2 \left(-\frac{1}{4z_b} \right) \right) \mathcal{C}^{(0)}(0), \quad (5.58)$$

where

$$Z_g^2 = \exp \left[-\frac{C_A}{\epsilon^2} \frac{\alpha_s}{2\pi} \right], \quad g(x) = {}_2F_2(1, 1; 3/2, 2; x/2) = 2 \sum_{n=0}^{\infty} \frac{n!}{(2n+2)!} (2x)^n, \quad (5.59)$$

$$\text{and } x = \frac{\alpha_s}{4\pi} (C_A - C_F) \ln^2 \left(\frac{1}{4z_b} \right).$$

Here ${}_2F_2$ denotes a generalized hypergeometric function. If we expand this in α_s we recover the same high-energy limit (at LL accuracy) as in the fixed-order calculations. It is interesting to compare the full fixed-order results, with the leading-logarithmic approximation. On the one hand, it shows how much of the amplitude is dictated by the leading logarithm; on the

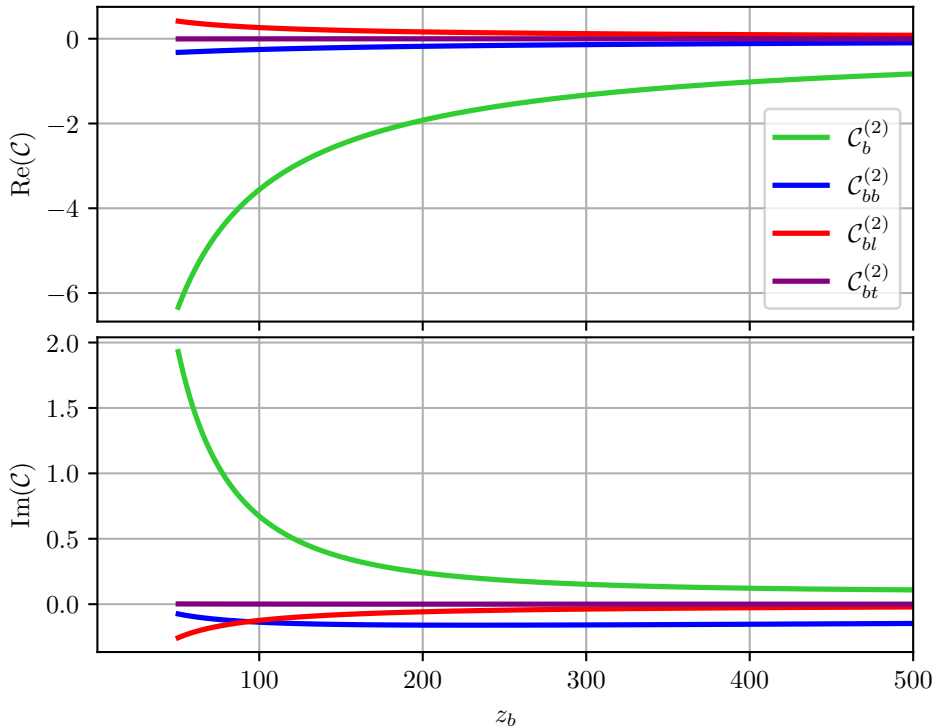


Figure 5.16: Same as in Fig. 5.15 but for high-energy limit. This time $\mathcal{C}_{bt}^{(2)}$ is computed using the fixed OS top-quark mass.

other hand, if accurate, it allows us to go to very high order of perturbation theory such that we can assess the quality of the perturbation series. At $\mu_R = m_H$, with an OS-renormalized bottom-quark mass and IR divergences subtracted in the $\overline{\text{MS}}$ scheme, the form factor is⁶

$$\begin{aligned} \mathcal{C}\left(\frac{m_H^2}{4m_b^2}\right) &= (-0.021 + 0.030i)\left\{1 + (9.237 - 0.442i)\frac{\alpha_s}{\pi} + (23.571 + 40.173i)\left(\frac{\alpha_s}{\pi}\right)^2\right\} \\ &= (-0.021 + 0.030i)\{1 + (0.329 - 0.016i) + (0.029 + 0.051i)\} \\ \mathcal{C}\left(\frac{m_H^2}{4m_b^2}\right)|_{\text{LL}} &= (-0.024 + 0.030i)\left\{1 + 10.36\frac{\alpha_s}{\pi} + 33.48\left(\frac{\alpha_s}{\pi}\right)^2\right. \\ &\quad \left.+ 79.44\left(\frac{\alpha_s}{\pi}\right)^3 + 153.93\left(\frac{\alpha_s}{\pi}\right)^4\right\} \\ &= (-0.024 + 0.030i)\{1 + 0.369 + 0.043 + 0.004 + 0.0002\}. \end{aligned} \tag{5.60}$$

We note that the full results hold in the 4FS, for better comparability, though numerically the differences between the schemes is very small. Similarly, we omit the effects from top-quark loops since these are also not accounted for in the LL approximation. Again, the numerical effect is almost negligible.

Eq. (5.60) shows that the LL approximation is quite accurate at low perturbative order, but the quality of the approximation deteriorates at higher orders. At NNLO only the order of magnitude of the real part is correctly predicted, whereas the imaginary part is completely off.

⁶ The computational setup is described in the Conventions.

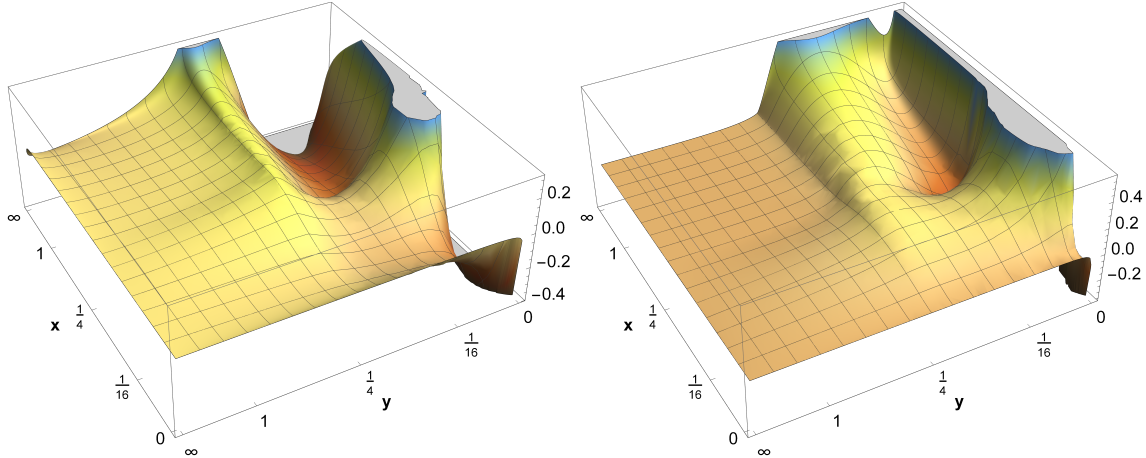


Figure 5.17: The coefficient $C_{tb}^{(2)}$ in the 4FS as a function of $x = m_t^2/m_H^2$ and $y = m_b^2/m_H^2$. Left plot shows the real part of the coefficient, right plot shows the corresponding imaginary part. This figure was taken from Ref. [180].

For the top-bottom interference contribution, the imaginary part of the NNLO corrections is, however, irrelevant since the LO amplitude below the $z = 1$ threshold is real. For precision predictions, the LL approximation is not suited, especially at high loop order.

The perturbative convergence of the amplitude seems to be relatively good. We can therefore conclude that logarithms of the form $\log^2(m_b^2/m_H^2)$ do not spoil the convergence and do not necessarily need to be resummed.

5.2 THE 4-FLAVOUR SCHEME

Up to this point, our discussion was mainly focused on the 5FS, where the bottom quark is considered to be a constituent of the proton. Consequently, to avoid the appearance of large logarithms, we have set the mass of the bottom quark to zero, except in closed bottom-quark loops that couple to the Higgs. To assess the validity of this prescription, we now investigate the alternative 4FS. Here the bottom quark is consistently treated as a massive particle, and by excluding the quark from the initial state, the large IR logarithms will cancel in sufficiently inclusive observables. In this section, we want to summarize the necessary adaptations of our calculation for the 4FS.

The Real-Real Corrections

In addition to the amplitudes already computed in the 5FS, the real-real corrections now include an additional channel, in which the Higgs is produced in association with a massive $b\bar{b}$ pair. Ergo, we need amplitudes for the processes $gg \rightarrow Hb\bar{b}$ and $q\bar{q} \rightarrow Hb\bar{b}$. The second and third diagram in Fig. 5.2 are examples of contributing Feynman diagrams. Note however that we still require the Higgs to couple to a closed quark loop. Hence, a contribution like the one displayed in Fig. 5.18 is **not** considered in the present calculation. Instead, they are considered in the interference of the bottom-bottom fusion- and gluon-gluon fusion-channel and were evaluated in the 4FS a long time ago [182].

The additional amplitudes are evaluated using the public amplitude library RECOLA [158]. However, the exclusion of the bottom-bottom fusion channel is not supported by RECOLA and

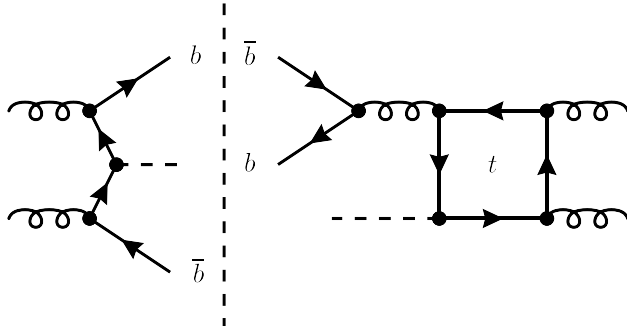


Figure 5.18: Example Feynman diagram for a contribution to the gluon-gluon-fusion–bottom–bottom-fusion interference at NLO in the 4FS. Because the Higgs does not only couple to closed quark loops, it is not considered a contribution to gluon-gluon fusion.

requires some out-of-the-box thinking. Our approach works by computing the amplitudes in the two-Higgs-doublet model instead of the SM. The details of the model are irrelevant for our purposes, the only important aspect is that the model now contains a second Higgs boson H_2 . We switch off any coupling to lighter quarks, including the bottom quark. Hence, we can compute the top-quark induced Higgs production in association with a massive $\bar{b}b$ pair. But how can we now obtain the amplitudes for the bottom-quark induced Higgs production? The solution is to couple the second Higgs boson to the top quark but rescale the momenta and masses to match the SM values. This means that we choose the mass of the second Higgs boson as

$$m_{H_2} = \frac{m_t}{m_b} m_H, \quad (5.61)$$

and rescale all external momenta by

$$p_i^\mu \rightarrow \frac{m_t}{m_b} p_i^\mu. \quad (5.62)$$

This ensures that the mass ratio of the Higgs boson to the internal quark running in the loop and to the external quarks matches the SM ratio of m_H to m_b . Since the mass dimension of the amplitude (without the inclusion of the VEV) is vanishing, the global rescaling has no effect on the numerical result of the amplitude.

The Real-Virtual Corrections

Let us follow the notation from Section 5.1.3 and introduce the bookkeeping parameters n_l , n_b and n_t to label light-, bottom-, and top-quark loops. The two-loop real-virtual amplitudes for the gluon-gluon fusion amplitudes then allow for the decomposition

$$\begin{aligned} \mathcal{M}_{ij \rightarrow kH}^{(1)} &= n_t \mathcal{M}_{ij \rightarrow kH}^{(1),t} + n_t^2 \mathcal{M}_{ij \rightarrow kH}^{(1),tt} + n_t n_l \mathcal{M}_{ij \rightarrow kH}^{(1),tl} \\ &\quad + n_b \mathcal{M}_{ij \rightarrow kH}^{(1),b} + n_b^2 \mathcal{M}_{ij \rightarrow kH}^{(1),bb} + n_b n_l \mathcal{M}_{ij \rightarrow kH}^{(1),bl} \\ &\quad + n_t n_b \left(\mathcal{M}_{ij \rightarrow kH}^{(1),tb} + \mathcal{M}_{ij \rightarrow kH}^{(1),bt} \right), \end{aligned} \quad (5.63)$$

where once again the first superscript indicates which quark flavor is coupling to the Higgs. In the 5FS both $\mathcal{M}_{ij \rightarrow kH}^{(1),tb}$ and $\mathcal{M}_{ij \rightarrow kH}^{(1),bt}$ were vanishing. For the 4FS we can get the $\mathcal{M}_{ij \rightarrow kH}^{(1),tb}$ contribution from $\mathcal{M}_{ij \rightarrow kH}^{(1),bt}$ upon exchanging the top and the bottom quark; this amounts to changing

$$m_t \longleftrightarrow m_b \quad (5.64)$$

in Eqs. (5.26), (5.27), and (5.31). $\mathcal{M}_{ij \rightarrow kH}^{(1),bb}$ could be computed in the same fashion, but instead we include it in our numerical grids. We thus reconstruct the full amplitude while keeping track of all bookkeeping parameters, preserving maximal flexibility and allowing us to seamlessly change between FSs.

The Virtual-Virtual Corrections

Similarly, the 3-loop Higgs-gluon form factor is known as a deep asymptotic series with full parametric dependence on n_l , n_b and n_t . The only necessary changes to adapt the amplitude to the 4FS are to include the $\mathcal{C}_{bb}^{(2)}$ and $\mathcal{C}_{tb}^{(2)}$ terms previously omitted.

5.3 $\overline{\text{MS}}$ -SCHEME

So far, our discussion of amplitudes was limited to OS-renormalized quark masses. In the OS scheme, the renormalized mass is identical to the pole mass, that means it corresponds to the position of the pole of the quark propagator. It is however not physical since quarks cannot exist as free asymptotic particles. Scattering matrices in QCD will therefore not exhibit poles at the OS mass.

As explained in Section 4.3.5, the top-bottom interference contribution is highly sensitive to the renormalization scheme, especially of the bottom-quark mass. One of our central aims was therefore to examine how the choice of the mass-renormalization scheme affects results at NNLO. In this section, we want to discuss the relevant adjustments necessary for the computation of the $\overline{\text{MS}}$ -renormalized amplitudes.

Strictly speaking, the $\overline{\text{MS}}$ scheme is actually a family of renormalization schemes, as every scale μ forms a new scheme. Since μ can be varied continuously, the RG invariance can be leveraged in the form of the RGE

$$0 = \frac{d \ln m_q^B}{d \ln \mu} \Rightarrow \frac{d \ln m_q}{d \ln \mu} = -\frac{d \ln Z_m}{d \alpha_s} \pi \bar{\beta} = 2\alpha_s \frac{d Z_m^{(1)}}{d \alpha_s} \equiv -\gamma_m. \quad (5.65)$$

Here, $\bar{\beta}$ is again the d -dimensional β function of Eq. (4.64), $Z_m^{(1)}$ is the residue in the ϵ -expansion of the mass-renormalization constant, and γ_m is the *mass anomalous dimension*. The solution of the RGE is given by

$$m_q(\mu) = m_q(\mu_0) \exp \left[- \int_{\mu_0}^{\mu} \frac{d\mu'}{\mu'} \gamma_m(\mu') \right], \quad (5.66)$$

which truncated at one-loop yields

$$m_q(\mu) = m_q(\mu_0) \left(\frac{\alpha_s(\mu)}{\alpha_s(\mu_0)} \right)^{-\gamma_0/\beta_0} = m_q(\mu_0) \left(1 - \frac{\alpha_s(\mu_0)}{4\pi} \beta_0 \ln \left(\frac{\mu}{\mu_0} \right) \right)^{\gamma_0/\beta_0}, \quad (5.67)$$

where $\gamma_0 = 6C_F$,

and β_0 as in Eq. (4.71). Beyond one-loop the differential equation becomes very challenging to solve analytically. We instead fall back to solving the differential equation numerically using the publicly available software tool `CRunDec` [183], at the highest available 4-loop accuracy. Around the top-quark $\overline{\text{MS}}$ mass, we observed that `CRunDec` encounters numerical instabilities, which we do not observe when using its `Mathematica` sister tool `RunDec` [184]. The Higgs

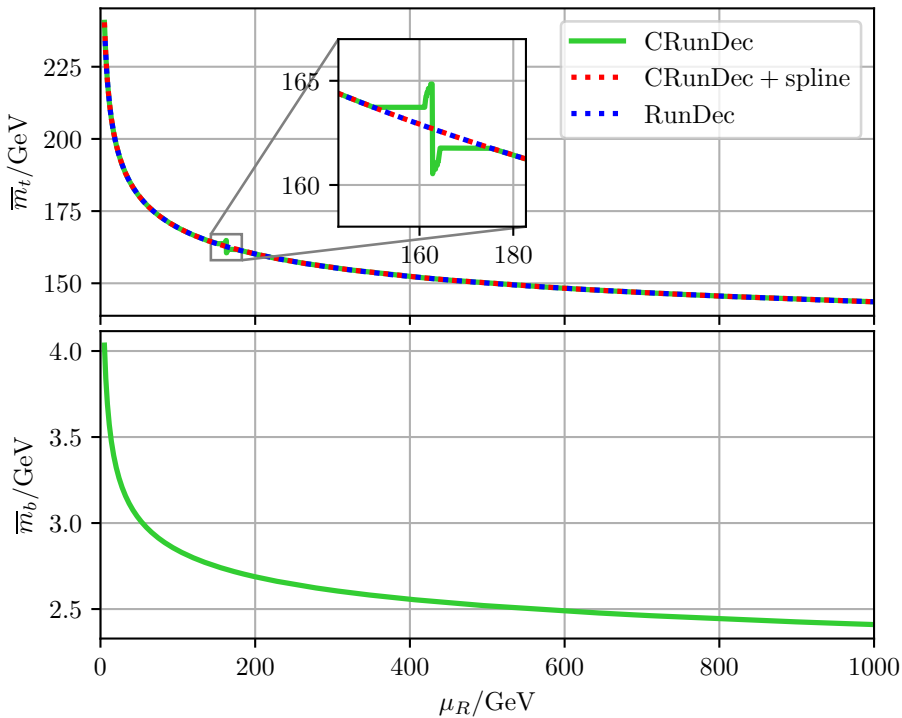


Figure 5.19: Running of the top (top panel) and bottom quark (bottom panel) mass. The solid green curve is the result computed with `CRunDec` at 4-loop accuracy. The dashed blue curve is the same but computed with `RunDec` [184]. The dashed red curve uses `CRunDec` except for the region $\mu_R \in [\bar{m}_t(\bar{m}_t) - 15 \text{ GeV}, \bar{m}_t(\bar{m}_t) + 15 \text{ GeV}]$, where we use a cubic spline instead. The computational setup is described in the Conventions.

production cross section is quite insensitive to the top-quark mass, hence we do not expect this to be of much importance. Especially considering that in the total cross section the standard scale choice $\mu_R = m_H/2$ is below this instability region even for the scale variation. Nevertheless, we will later also introduce dynamical scales which can exceed $\bar{m}_t(\bar{m}_t)$ for a large Higgs transverse momentum. For this reason, we bridge the problematic region around $\mu_R \in [\bar{m}_t(\bar{m}_t) - 15 \text{ GeV}, \bar{m}_t(\bar{m}_t) + 15 \text{ GeV}]$ using a cubic spline fit which we construct from the top-quark mass at $\bar{m}_t(\bar{m}_t) - 15 \text{ GeV}$, $\bar{m}_t(\bar{m}_t) - 14 \text{ GeV}$, $\bar{m}_t(\bar{m}_t) + 14 \text{ GeV}$, and $\bar{m}_t(\bar{m}_t) + 15 \text{ GeV}$. In Fig. 5.19, we can see that the spline fit correctly reproduces the results of `RunDec` in the unstable parameter window. The evolved quark masses then enter the computed amplitudes.

Since the real-virtual amplitudes containing only a single heavy-quark flavor were computed using a fixed mass ratio m_q^2/m_H^2 (see Section 5.1.2), we recompute the amplitude using a variety of different quark masses. In total, we computed the amplitude for nine different quark masses as listed in Tab. 5.2. Using the interpolation method discussed in Section 5.1.2, we are now able to very quickly compute all amplitudes with high precision in a large region of the parameter space. Note that the chosen grid masses have been selected explicitly to eliminate any interpolation error for the standard fixed scale choices. Hence, we rely on the interpolation only when using a dynamic scale. To assess the accuracy of our interpolation method, we removed each set of grid points corresponding to the masses $\bar{m}_b(m_H)$, $\bar{m}_b(m_H/2)$, $\bar{m}_b(m_H/4)$, m_t and reran the MC simulation. The results differed by less than the MC uncertainty, proving the robustness of our interpolation method.

Grid mass	Value [GeV]	Approximate ratio $m_{b,t}^2/m_H^2$	Relative error [%]
m_b	4.78	$\frac{1}{684}$	0.2
$\bar{m}_b(m_H)$	2.789	$\frac{1}{2011}$	0.9
$\bar{m}_b(m_H/2)$	2.961	$\frac{1}{1782}$	0.2
$\bar{m}_b(m_H/4)$	3.170	$\frac{1}{1557}$	1.0
\bar{m}_b^{\min}	1.67	$\frac{1}{5602}$	0.1
m_t	172.4	$\frac{23}{12}$	4
$\bar{m}_t(m_H)$	166.1	$\frac{136}{77}$	0.0
$\bar{m}_t(m_H/2)$	176.2	$\frac{149}{75}$	0.0
$\bar{m}_t(m_H/4)$	188.2	$\frac{213}{94}$	0.0

Table 5.2: Mass ratios squared, m_b^2/m_H^2 and m_t^2/m_H^2 , used for the generation of numerical values of the two-loop four-point amplitudes. We chose values corresponding to the OS masses, according to PDG recommendations [185], and $\overline{\text{MS}}$ masses at scales relevant for 7-point variation w.r.t. a central scale of $m_H/2$. For the latter, we used $\bar{m}_b(\bar{m}_b) = 4.18$ GeV as recommended by the PDG and $\bar{m}_t(\bar{m}_t) = 162.7$ GeV. The dynamic scale used for our differential cross-section predictions (see Eq. (6.1)) can exceed m_H , and reaches values of up to 1 TeV. At these high scales, the bottom-quark mass is $\bar{m}_b(1 \text{ TeV}) = 2.41$ GeV. To avoid extrapolations outside our numerical grids for the amplitudes, we therefore included another mass value, \bar{m}_b^{\min} , below this minimum.

Evaluating OS-renormalized amplitudes at the $\overline{\text{MS}}$ mass does not make them $\overline{\text{MS}}$ renormalized. We can however extract the $\overline{\text{MS}}$ -renormalized amplitudes by rewriting the OS mass in terms of the $\overline{\text{MS}}$ mass

$$m^{\text{OS}} = \bar{m}^{(n_m)}(\mu) \left(1 + c_1^{(n_m, n_l)}(\mu) \frac{\alpha_s^{(n_l)}(\mu)}{\pi} + c_2^{(n_m, n_l)}(\mu) \left(\frac{\alpha_s^{(n_l)}(\mu)}{\pi} \right)^2 + \mathcal{O}(\alpha_s^3) \right), \quad (5.68)$$

and then expand all amplitudes in α_s up to the required fix order. The superscripts n_m and n_l define which quark flavors have been decoupled from the mass and α_s . The relation between the quark masses in the different renormalization schemes can be extracted using the renormalization-scheme invariance of the bare quark mass, which yields the relation

$$Z_m^{\overline{\text{MS}}}(\mu) \bar{m}(\mu) = Z_m^{\text{OS}} m^{\text{OS}}. \quad (5.69)$$

Meaning that the coefficients c_1 and c_2 can simply be extracted from the $\left(\alpha_s^{(n_l)}\right)^1$ and $\left(\alpha_s^{(n_l)}\right)^2$ coefficients of the expanded ratio $Z_m^{\overline{\text{MS}}}(\mu)/Z_m^{\text{OS}}$. The OS-renormalization constant still has logarithmic dependencies on the OS masses. We eliminate any residual logarithmic dependence by recursively inserting the relation of Eq. (5.68). Note that if the quark with the mass m is not being decoupled from the running of α_s , then its mass is set to zero in all contributions to the renormalization constants which feature a closed quark loop of that flavor. This is to ensure consistency with our previous prescription of quark masses.

With the renormalization constants computed in Refs. [186, 187] we find

$$\begin{aligned}
c_1^{(n_f, n_l)}(\mu) &= C_F \left(1 - \frac{3}{4} \ln \left(\frac{\bar{m}^{(n_f)}(\mu)^2}{\mu^2} \right) \right), \\
c_2^{(n_f, n_l)}(\mu) &= -\frac{1}{384} C_F \left\{ \right. \\
&\quad + C_A \left(-132 \ln^2 \left(\frac{\bar{m}^{(n_f)}(\mu)^2}{\mu^2} \right) + 740 \ln \left(\frac{\bar{m}^{(n_f)}(\mu)^2}{\mu^2} \right) + 144\zeta(3) - 1111 + \pi^2 (32 - 96 \ln(2)) \right) \\
&\quad + 3C_F \left(-36 \ln^2 \left(\frac{\bar{m}^{(n_f)}(\mu)^2}{\mu^2} \right) - 36 \ln \left(\frac{\bar{m}^{(n_f)}(\mu)^2}{\mu^2} \right) - 96\zeta(3) + 71 + 8\pi^2 (8 \ln(2) - 5) \right) \\
&\quad + 4n_l T_F \left(12 \ln^2 \left(\frac{\bar{m}^{(n_f)}(\mu)^2}{\mu^2} \right) - 52 \ln \left(\frac{\bar{m}^{(n_f)}(\mu)^2}{\mu^2} \right) + 8\pi^2 + 71 \right) \left. \right\} \\
&- \sum_{i=n_l+1}^{n_f} \frac{1}{96} C_F T_F \left(12 \ln^2 \left(\frac{\bar{m}^{(n_f)}(\mu)^2}{\mu^2} \right) - 24 \ln \left(\frac{\bar{m}^{(n_f)}(\mu)^2}{\mu^2} \right) \ln \left(\frac{\bar{m}_i^{(n_f)}(\mu)^2}{\mu^2} \right) - 52 \ln \left(\frac{\bar{m}^{(n_f)}(\mu)^2}{\mu^2} \right) \right. \\
&\quad \left. + 32 \ln \left(\frac{\bar{m}_i^{(n_f)}(\mu)^2}{\mu^2} \right) + 48(x_i - 1)^2 (x_i^2 + x_i + 1) \text{Li}_2(1 - x_i) + 48x_i^4 \ln^2(x_i) + 48x_i^2 \ln(x_i) \right. \\
&\quad \left. - 48 (x_i^4 + x_i^3 + x_i + 1) (\text{Li}_2(-x_i) + \ln(x_i) \ln(x_i + 1)) - 16\pi^2 (x_i^3 + x_i) + 72x_i^2 + 71 \right),
\end{aligned} \tag{5.71}$$

where we defined $x_i = \frac{\bar{m}_i^{(n_f)}(\mu)}{\bar{m}^{(n_f)}(\mu)}$, n_f is the total number of quarks, i.e. $n_f = 6$ in the SM, and n_l is the number of light quarks, i.e. the number of quarks which have not been decoupled in the running of α_s . The sum therefore runs over all quark flavors which are decoupled from the running of α_s ; this includes the quark with mass $\bar{m}^{(n_f)}$ in case it is decoupled. This implies that the OS- $\overline{\text{MS}}$ -mass relation of the bottom quark somehow depends on the mass of the top quark. Since the top-quark mass is orders of magnitudes larger than the bottom-quark mass, this seems quite unphysical. The problem is that we relate the OS mass with the $\overline{\text{MS}}$ mass within the full $n_f = 6$ theory. Instead, we would like to relate the OS mass to the decoupled masses defined by

$$\begin{aligned}
\bar{m}^{(n_m)}(\mu) &= \zeta_m \left(\alpha_s^{(n_m+1)}(\mu), \ln \frac{(\bar{m}^{(n_m+1)})^2}{\mu^2} \right) \bar{m}^{(n_m+1)}(\mu), \\
\text{with } \zeta_m(\alpha_s, L) &= 1 + \left(\frac{\alpha_s}{\pi} \right)^2 T_F \left[\frac{89}{288} C_F + \frac{5}{24} C_F L + \frac{C_F}{8} L^2 \right].
\end{aligned} \tag{5.72}$$

Once we expand our relation in $x_i \gg 1$, which we can do anyway as all decoupling relations only hold up to power corrections, we find that all non-decoupling effects cancel as expected. The coefficients for general $n_m \leq n_f$ are therefore given by Eq. (5.71) upon replacing $n_f \rightarrow n_m$ on the left- and right-hand side.

In case we have a hierarchy among the mass scales for which $x_i \ll 1$, for example when considering the top-quark OS- $\overline{\text{MS}}$ -mass relation in the 4FS, we can expand the expression yielding

$$\begin{aligned}
c_1^{(n_m, n_l)}(\mu) &= C_F \left(1 - \frac{3}{4} \ln \left(\frac{\bar{m}^{(n_m)}(\mu)^2}{\mu^2} \right) \right), \\
c_2^{(n_m, n_l)}(\mu) &= -\frac{1}{384} C_F \left\{ \right. \\
&\quad + C_A \left(-132 \ln^2 \left(\frac{\bar{m}^{(n_m)}(\mu)^2}{\mu^2} \right) + 740 \ln \left(\frac{\bar{m}^{(n_m)}(\mu)^2}{\mu^2} \right) + 144\zeta(3) - 1111 + \pi^2 (32 - 96 \ln(2)) \right) \\
&\quad + 3C_F \left(-36 \ln^2 \left(\frac{\bar{m}^{(n_m)}(\mu)^2}{\mu^2} \right) - 36 \ln \left(\frac{\bar{m}^{(n_m)}(\mu)^2}{\mu^2} \right) - 96\zeta(3) + 71 + 8\pi^2 (8 \ln(2) - 5) \right) \\
&\quad + 4n_l T_F \left(12 \ln^2 \left(\frac{\bar{m}^{(n_m)}(\mu)^2}{\mu^2} \right) - 52 \ln \left(\frac{\bar{m}^{(n_m)}(\mu)^2}{\mu^2} \right) + 8\pi^2 + 71 \right) \left. \right\} \\
&\quad - \frac{1}{96} C_F T_F \left\{ 72 + \sum_{i=n_l+1}^{n_m} \left[71 - 20 \ln \left(\frac{\bar{m}^{(n_m)}(\mu)^2}{\mu^2} \right) - 12 \ln^2 \left(\frac{\bar{m}^{(n_m)}(\mu)^2}{\mu^2} \right) \right. \right. \\
&\quad \left. \left. + 8\pi^2 (1 - 3x_i) + 16 \ln(x_i) \left(4 - 3 \ln \left(\frac{\bar{m}^{(n_m)}(\mu)^2}{\mu^2} \right) \right) \right] \right\}.
\end{aligned} \tag{5.74}$$

The sum once again runs over all quark flavors decoupled from the running of α_s , with masses less or equal than m . We once again underscore that these are not the “standard” relations between the pole and the $\overline{\text{MS}}$ masses, due to our prescription of the bottom-quark mass in loops that do not couple to the Higgs. However, they follow upon replacing

$$n_l \longrightarrow n_l - 1 \tag{5.75}$$

in Eqs. (5.71) and (5.74).

For convenience, we also provide the numerical values for the top- and bottom-quark mass scheme relations in the 4 and 5FSs

$$\begin{aligned}
5\text{FS} : m_t &= \bar{m}_t^{(6)}(\bar{m}_t^{(6)}) \left(1 + 1.333 \times \frac{\alpha_s^{(5)}(\bar{m}_t)}{\pi} + 8.237 \times \left(\frac{\alpha_s^{(5)}(\bar{m}_t)}{\pi} \right)^2 + \mathcal{O}(\alpha_s^3) \right) \\
&= (162.7 + 7.493 + 1.608) \text{ GeV} = 171.793 \text{ GeV},
\end{aligned} \tag{5.76}$$

$$\begin{aligned}
4\text{FS} : m_t &= \bar{m}_t^{(6)}(\bar{m}_t^{(6)}) \left(1 + 1.333 \times \frac{\alpha_s^{(4)}(\bar{m}_t)}{\pi} + 8.864 \times \left(\frac{\alpha_s^{(4)}(\bar{m}_t)}{\pi} \right)^2 + \mathcal{O}(\alpha_s^3) \right) \\
&= (162.7 + 7.434 + 1.694) \text{ GeV} = 171.828 \text{ GeV},
\end{aligned} \tag{5.77}$$

$$\begin{aligned}
5\text{FS} : m_b &= \bar{m}_b^{(5)}(\bar{m}_b^{(5)}) \left(1 + 1.333 \times \frac{\alpha_s^{(5)}(\bar{m}_b)}{\pi} + 8.132 \times \left(\frac{\alpha_s^{(5)}(\bar{m}_b)}{\pi} \right)^2 + \mathcal{O}(\alpha_s^3) \right) \\
&= (4.18 + 0.398 + 0.174) \text{ GeV} = 4.752 \text{ GeV},
\end{aligned} \tag{5.78}$$

$$4\text{FS} : m_b = \bar{m}_b^{(5)}(\bar{m}_b^{(5)}) \left(1 + 1.333 \times \frac{\alpha_s^{(4)}(\bar{m}_b)}{\pi} + 9.278 \times \left(\frac{\alpha_s^{(4)}(\bar{m}_b)}{\pi} \right)^2 + \mathcal{O}(\alpha_s^3) \right)$$

$$= (4.18 + 0.443 + 0.245) \text{ GeV} = 4.869 \text{ GeV}. \quad (5.79)$$

The first two corrections in the expansion already suggest a relatively good perturbative convergence for the top quark. The bottom quark on the other hand receives quite large correction, indicating poor convergence of the perturbation series, a phenomenon which actually worsens with higher loop order [133, 134]. Although there exists no formal proof in QCD, it is believed that the perturbation series in Eq. (5.68) only converges asymptotically. Asymptotic expansions can sometimes be summed by means of a *Borel transform* defined by

$$f(\alpha_s) = \sum_{n=1}^{\infty} c_n \alpha_s^n \quad \Rightarrow \quad B[f](t) = \sum_{n=0}^{\infty} c_{n+1} \frac{t^n}{n!}. \quad (5.80)$$

The omission of the tree-level α_s^0 term is conventional. Formally, we then find

$$f(\alpha_s) = \int_0^{\infty} dt e^{-\frac{t}{\alpha_s}} B[f](t), \quad (5.81)$$

in the sense that this integral representation reproduces the expansion of f term by term. This way, we can analytically extend the domain of series beyond its classical radius of convergence. However, if the Borel transform of the series has a pole on the real positive axis—say at $t_0 > 0$ —then we cannot perform the integration in Eq. (5.81) right away. Even so, we can shift the pole away from the real axis by a small amount $\pm i0^+$, so that we can define the finite integral

$$f_{\pm}(\alpha_s) = \int_0^{\infty} dt e^{-\frac{t}{\alpha_s}} B[f](t \pm i0^+). \quad (5.82)$$

Since this shift is arbitrary, the result is not unique, and will generally result in the finite difference

$$f_+(\alpha_s) - f_-(\alpha_s) = 2\pi i \sum_{\substack{t \in \text{poles of } B[f] \\ \text{Re}(t) > 0, \text{Im}(t) = 0}} \text{Res}(B[f], t) e^{-\frac{t}{\alpha_s}}. \quad (5.83)$$

But if $t/\alpha_s \gg 1$, then this difference is exponentially suppressed. The leading pole, that is the pole on the positive real axis with the smallest real part, therefore results in the largest ambiguity. It is also called the *leading renormalon singularity*. In complete analogy, subsequent poles are called subleading renormalon singularities. It can be shown [188, 189] that the leading renormalon singularity of the OS- $\overline{\text{MS}}$ -mass relation in Eq. (5.68) is located at $t = -1/(2\beta_0)$. With the QCD scale $\Lambda_{\text{QCD}} \approx \mu \exp\left(-\frac{1}{2\beta_0\alpha_s}\right)$, we thus observe that the ambiguity is linear in $\Lambda_{\text{QCD}}/\bar{m}$. In QCD, the leading renormalon is of IR origin. Renormalization schemes, which are insensitive to the IR—such as the $\overline{\text{MS}}$ scheme—consequently do not suffer from these linear power ambiguities; they are *renormalon free*. The OS scheme on the other hand is IR sensitive. As a result, OS quark masses can never be determined more precisely than Λ_{QCD}/m [190]. For the top quark, this ratio is tiny ($\sim 1\%$) and therefore irrelevant for most phenomenological applications. For lighter quarks such as the bottom quark, the ratio becomes more sizable ($\sim 5\%$). Perturbation series in the OS scheme thus often exhibit particularly bad perturbative convergence.

Still, Eqs. (5.78) and (5.79) show that the OS bottom-quark mass is reproduced relatively well at $\mu_R = \bar{m}_b$. If we however evaluate the OS- $\overline{\text{MS}}$ -mass relation at $\mu_R = m_H/2$, we find (in the 5FS) $m_b = 4.29$ GeV, which already deviates significantly from the OS mass value

of $m_b = 4.78$ GeV. This can be seen as an additional indicator for poor convergence of the perturbation series. The top-quark mass is not relevantly affected by the choice of the FS, whereas we see a slight shift of the bottom-quark mass of around 2%.

Equipped with the coefficients in Eq. (5.71), we can now insert the OS- $\overline{\text{MS}}$ -mass relation into the OS-renormalized amplitudes. A subsequent expansion in α_s , then yields the relation between the amplitudes in the OS and the $\overline{\text{MS}}$ scheme

$$\begin{aligned} \mathcal{M}^{\overline{\text{MS}}}(\bar{m}(\mu)) &= \mathcal{M}^{\text{OS}}(\bar{m}(\mu)) + \delta\mathcal{M}(\bar{m}(\mu)), \\ \delta\mathcal{M}^{(1)}(\bar{m}(\mu)) &= \bar{m}(\mu)c_1(\mu)\frac{\alpha_s(\mu)}{\pi}\left.\frac{d\mathcal{M}^{\text{OS},(0)}}{dm}\right|_{m=\bar{m}(\mu)}, \\ \delta\mathcal{M}^{(2)}(\bar{m}(\mu)) &= \bar{m}(\mu)\left[c_1(\mu)\frac{\alpha_s(\mu)}{\pi}\left.\frac{d\mathcal{M}^{\text{OS},(1)}}{dm}\right|_{m=\bar{m}(\mu)} + c_2(\mu)\left(\frac{\alpha_s(\mu)}{\pi}\right)^2\left.\frac{d\mathcal{M}^{\text{OS},(0)}}{dm}\right|_{m=\bar{m}(\mu)}\right] \\ &\quad + \frac{1}{2}\left(\bar{m}(\mu)c_1(\mu)\frac{\alpha_s(\mu)}{\pi}\right)^2\left.\frac{d^2\mathcal{M}^{\text{OS},(0)}}{dm^2}\right|_{m=\bar{m}(\mu)}. \end{aligned} \tag{5.84}$$

The relevant LO and NLO amplitudes are known fully analytically. For the Higgs-gluon form factor at LO, the first and second derivative is performed fully analytically. At NLO, we use a deep asymptotic expansion in the high-energy or large-mass limit, and then perform the necessary mass derivatives fully automated using **Mathematica**. For the one-loop real corrections, we apply the derivatives already at the level of Feynman rules using **DiaGen/IdSolver**. Taking mass derivatives is necessary for the large-mass expansion, a feature already implemented in the framework of **DiaGen/IdSolver**, and we use the implementation therein to get the derivatives. They are then processed using the same tool chain described in Section 5.1.2. In a nutshell, we project to form factors, use IBPs to reduce the integrals to master integrals, and insert the solutions to the appearing one-loop integrals.

5.4 PERFORMING THE PHASE-SPACE INTEGRATION

Once we have collected all relevant amplitudes, we perform the phase-space integration to obtain cross sections. We carry out the phase-space integration numerically using MC methods. The IR singularities arising during the integration are handled using the *sector-improved residue subtraction scheme*⁷ [57], implemented in the private software package **Stripper**.

Typically, **Stripper** runs the MC simulation at a fixed renormalization scale and uses the provided lower-order amplitudes to automatically evolve the final result to other scales. However, this procedure only applies if the involved masses are renormalization-scale independent; therefore, it is not fully automated in the $\overline{\text{MS}}$ scheme. Each renormalization scale is therefore run individually.

For the top-quark-induced Higgs production cross section, we subtract the rHTL limit already on the integrand level. Since the rHTL already captures the bulk of the cross section, this massively improves the MC uncertainties. To get the total cross section, we then add back the rHTL cross section after performing the phase-space integration. The rHTL cross sections on

⁷ See Section 2.1.3 for a brief review on subtraction schemes.

the other hand can be evaluated extremely efficiently by public software tools like `SusHi` or `iHixs` 2. This combination of numerical phase-space integration with rHTL-based subtraction yields stable and efficient cross-section computations.

6 | RESULTS AND DISCUSSION

In this chapter, we present the main results of this PhD thesis. First, we show results for the total and differential top-bottom interference contributions to the gluon-gluon-fusion Higgs-production cross section in both the 4FS and the 5FS. We then compare the results in the OS and the $\overline{\text{MS}}$ renormalization schemes for the top- and bottom-quark masses. We also provide pure-top-quark-mass effects and, finally, compare our findings with other works.

We use two scale choices; for the fully-inclusive cross section we use the central scale of $\mu = m_H/2$, as it shows very good perturbative convergence as explained in Section 4.3.1. In differential cross sections we use the dynamic scale

$$\mu = \frac{H_T}{2} \equiv \frac{1}{2} \left(\sqrt{m_H^2 + p_T^2} + \sum_i p_{i,T} \right), \quad (6.1)$$

where p_T is the transverse momentum of the Higgs, and $p_{i,T}$ is the transverse momentum of the i -th final state parton. The scale was chosen on the one hand to match previous studies [141, 146, 148], and on the other hand to improve perturbative convergence at large p_T , where the Higgs mass alone is no longer the natural scale. This is evident, for example, in the phase-space measure of Eq. (4.97), which shows that at large transverse momentum, we encounter logarithms of the form $\log(\mu^2/s)$. Since H_T is the minimum partonic center-of-mass energy (see Eq. (4.132)), it will result in better convergence at large p_T .

Unless specified otherwise, we follow the computational setup described in the Conventions.

6.1 TOTAL CROSS SECTION

6.1.1 Effects of Finite Top-Quark Masses

As mentioned before, the finite top-quark mass effects on the Higgs production cross section in the OS-scheme have already been studied in Ref. [35]. Here, we reproduce the result computed therein and complement them with scale uncertainties. We further provide results for additional center-of-mass energies. The results are displayed in Tab. 6.1. Moreover, we compare the rHTL and the full QCD cross sections in the various partonic channels in Fig. 4.10 and Tab. 4.4.

As discussed earlier, the rHTL provides an excellent approximation of the cross section. By looking at Fig. 4.10, we see that this is especially true for the gluon-gluon channel, whereas the other channels show discrepancies of $\mathcal{O}(10)\%$. The dominance of the gluon-gluon channel then results in the remarkable accuracy of the rHTL when combining all partonic channels, yielding approximations with sub-percent precision. We observe that the NNLO correction of $\sigma_t - \sigma_{\text{rHTL}}$ has the opposite sign and roughly half the magnitude of the NLO correction. The lower scale uncertainties are reduced drastically by a factor of 4–6 going from NLO to NNLO, while the upper uncertainties increase slightly.

In Tab. 6.2, we show the difference between top-quark induced gluon-gluon fusion cross sections computed with a top-quark mass defined in the $\overline{\text{MS}}$ and the OS schemes. Based on the previous studies at LO and NLO, it was conjectured that the renormalization scheme of the top-quark mass has little effect on the cross section. We find this trend continued at NNLO, where the difference amounts to just -0.01 pb or 0.2% at 13 TeV . Based on our findings, we conclude that the scale uncertainties overestimate the uncertainty of the difference between the cross sections in the two schemes. The scale uncertainties themselves decrease slightly going from NLO to NNLO.

Lastly, we compare the pure-top-quark effects between the 4 and 5FS. In both schemes, the Higgs boson couples exclusively to the top quark; but the two schemes differ in the treatment of the bottom-quark mass. The results are displayed in Tab. 6.3. The differences between the two schemes are insignificant, reaching 0.03 pb at NLO and 0.01 pb at NNLO at a center-of-mass energy of 13 TeV . At NLO the only difference between the computations is the used PDF set and the additional $qg \rightarrow Hq$ channel in the 5FS. Only at NNLO do we have explicit dependence on the bottom-quark mass in the 4FS, which does, however, not give rise to significant deviations; in fact the NNLO results show even smaller deviations between the two schemes. We stress that the rHTL cross sections themselves decrease by a significant -1.16 pb when moving from the 5 to the 4FS (see Tab. 6.5).

6.1.2 Effects of Finite Bottom-Quark Masses

Tab. 6.4 shows one of the major findings of this work: the top-bottom interference contribution to the gluon-gluon fusion cross section at NNLO. Herein, we compare various computational setups, including results computed with $\overline{\text{MS}}$ - and OS-renormalized bottom- and top-quark masses as well as results in the 5 and 4FS.

In Appendix C, we provide results for additional collider energies relevant for LHC phenomenology.

Order	σ_{rHTL} [pb]	$(\sigma_t - \sigma_{\text{rHTL}})$ [pb]	$(\sigma_t - \sigma_{\text{rHTL}})/\sigma_{\text{rHTL}} [\%]$
$\sqrt{s} = 7 \text{ TeV}$			
$\mathcal{O}(\alpha_s^2)$	+5.85	–	–
LO	$5.85^{+1.56}_{-1.11}$	–	–
$\mathcal{O}(\alpha_s^3)$	+7.14	-0.0604	–
NLO	$12.99^{+2.89}_{-2.14}$	$-0.0604^{+0.021}_{-0.037}$	-0.5
$\mathcal{O}(\alpha_s^4)$	+3.28	+0.0386(2)	–
NNLO	$16.27^{+1.45}_{-1.61}$	$-0.0218(2)^{+0.035}_{-0.009}$	-0.1
$\sqrt{s} = 8 \text{ TeV}$			
$\mathcal{O}(\alpha_s^2)$	+7.39	–	–
LO	$7.39^{+1.98}_{-1.40}$	–	–
$\mathcal{O}(\alpha_s^3)$	+9.14	-0.0873	–
NLO	$16.53^{+3.63}_{-2.73}$	$-0.0873^{+0.030}_{-0.052}$	-0.5
$\mathcal{O}(\alpha_s^4)$	+4.19	+0.0523(2)	–
NNLO	$20.72^{+1.84}_{-2.06}$	$-0.0350(2)^{+0.048}_{-0.013}$	-0.2
$\sqrt{s} = 13 \text{ TeV}$			
$\mathcal{O}(\alpha_s^2)$	+16.30	–	–
LO	$16.30^{+4.36}_{-3.10}$	–	–
$\mathcal{O}(\alpha_s^3)$	+21.14	-0.303	–
NLO	$37.44^{+8.42}_{-6.29}$	$-0.303^{+0.10}_{-0.17}$	-0.8
$\mathcal{O}(\alpha_s^4)$	+9.72	+0.147(1)	–
NNLO	$47.16^{+4.21}_{-4.77}$	$-0.156(1)^{+0.13}_{-0.03}$	-0.3
$\sqrt{s} = 13.6 \text{ TeV}$			
$\mathcal{O}(\alpha_s^2)$	+17.47	–	–
LO	$17.47^{+4.67}_{-3.32}$	–	–
$\mathcal{O}(\alpha_s^3)$	+22.76	-0.338	–
NLO	$40.23^{+9.07}_{-6.77}$	$-0.338^{+0.11}_{-0.18}$	-0.8
$\mathcal{O}(\alpha_s^4)$	+10.47	+0.162(1)	–
NNLO	$50.70^{+4.53}_{-5.14}$	$-0.176(1)^{+0.14}_{-0.03}$	-0.3
$\sqrt{s} = 14 \text{ TeV}$			
$\mathcal{O}(\alpha_s^2)$	+18.26	–	–
LO	$18.26^{+4.88}_{-3.47}$	–	–
$\mathcal{O}(\alpha_s^3)$	+23.86	-0.362	–
NLO	$42.12^{+9.51}_{-7.10}$	$-0.362^{+0.12}_{-0.20}$	-0.9
$\mathcal{O}(\alpha_s^4)$	+10.98	+0.171(1)	–
NNLO	$53.10^{+4.75}_{-5.39}$	$-0.191(1)^{+0.15}_{-0.04}$	-0.4

Table 6.1: Total gluon-gluon fusion cross section in the rHTL and the pure-top-quark-mass effects for a selection of hadronic center-of-mass energies relevant for LHC phenomenology. The top-quark mass is renormalized in the OS-scheme. The computational setup is described in the Conventions. The scale uncertainties are determined with seven-point variation taking into account all correlations.

Order	$(\sigma_t^{\overline{\text{MS}}} - \sigma_t^{\text{OS}})$ [pb]
$\sqrt{s} = 13$ TeV	
$\mathcal{O}(\alpha_s^2)$	-0.04
LO	$-0.04^{+0.12}_{-0.17}$
$\mathcal{O}(\alpha_s^3)$	+0.02
NLO	$-0.02^{+0.14}_{-0.30}$
$\mathcal{O}(\alpha_s^4)$	+0.01
NNLO	$-0.01^{+0.12}_{-0.24}$

Table 6.2: Difference of cross sections for Higgs production through a closed top-quark loop with the top-quark mass defined either in the $\overline{\text{MS}}$ or the OS scheme. The results are computed for LHC @ 13 TeV using the computational setup described in the Conventions. The scale uncertainties are determined with seven-point variation taking into account all correlations.

Order	$(\sigma_t - \sigma_{\text{rHTL}})$ [pb]	
$\sqrt{s} = 13$ TeV		
	5FS	4FS
	$m_t = 173.06$ GeV	$m_t = 173.06$ GeV
	$\overline{m}_b(\overline{m}_b) = 4.18$ GeV	
LO	-	-
$\mathcal{O}(\alpha_s^3)$	-0.30	-0.27
NLO	$-0.30^{+0.10}_{-0.17}$	$-0.27^{+0.09}_{-0.16}$
$\mathcal{O}(\alpha_s^4)$	+0.14	+0.12
NNLO	$-0.16^{+0.13}_{-0.03}$	$-0.15^{+0.10}_{-0.02}$

Table 6.3: Effect of the finite top-quark mass on the gluon-gluon fusion cross section in the 4 and 5FS. The top-quark mass is defined in the OS-scheme, while the bottom-quark mass is defined in the $\overline{\text{MS}}$ scheme. The results are computed for LHC @ 13 TeV using the computational setup described in the Conventions. The scale uncertainties are determined with seven-point variation.

Order	$\sigma_{t \times b}$ [pb]				
	$\sqrt{s} = 13$ TeV				
	5FS	5FS	5FS	4FS	5FS
$m_t = 173.06$ GeV	$m_t = 173.06$ GeV	$\bar{m}_t(\bar{m}_t) = 162.7$ GeV	$m_t = 173.06$ GeV	$m_t = 173.06$ GeV	$m_t = 173.06$ GeV
$\bar{m}_b(\bar{m}_b) = 4.18$ GeV	$m_b = 4.78$ GeV	$\bar{m}_b(\bar{m}_b) = 4.18$ GeV	$\bar{m}_b(\bar{m}_b) = 4.18$ GeV	$m_b = 4.78$ GeV	$Y_b = \bar{m}_b/v$
$\mathcal{O}(\alpha_s^2)$	-1.11	-1.98	-1.12	-1.15	-1.223
LO	$-1.11^{+0.28}_{-0.43}$	$-1.98^{+0.38}_{-0.53}$	$-1.12^{+0.28}_{-0.42}$	$-1.15^{+0.29}_{-0.45}$	$-1.223^{+0.29}_{-0.44}$
$\mathcal{O}(\alpha_s^3)$	-0.65	-0.44	-0.64	-0.66	-0.623(1)
NLO	$-1.76^{+0.27}_{-0.28}$	$-2.42^{+0.19}_{-0.12}$	$-1.76^{+0.27}_{-0.28}$	$-1.81^{+0.28}_{-0.30}$	$-1.85^{+0.26}_{-0.26}$
$\mathcal{O}(\alpha_s^4)$	+0.02	+0.43	-0.02	-0.02	+0.019(5)
NNLO	$-1.74(2)^{+0.13}_{-0.03}$	$-1.99(2)^{+0.29}_{-0.15}$	$-1.78(1)^{+0.15}_{-0.03}$	$-1.83(2)^{+0.14}_{-0.03}$	$-1.83(1)^{+0.08}_{-0.03}$

Table 6.4: Top-bottom interference contribution to the gluon-gluon fusion cross section for various computational setups. The results are computed for LHC @ 13 TeV using the computational setup described in the Conventions. The scale uncertainties are determined with seven-point variation. Numbers in parentheses indicate the MC uncertainties on the last provided digit.

Using an $\overline{\text{MS}}$ renormalized bottom-quark mass, an OS renormalized top-quark mass, and the 5FS, we find that the central value is not shifted significantly going from NLO to NNLO. The result is therefore consistent within the previously estimated scale uncertainty bands. The latter are reduced significantly in this setup. The upwards scale variation is halved, reaching a precision of 7% whereas the lower uncertainty is reduced even further to about 2%. Overall, we observe a good perturbative convergence with this setup.

When the top-quark mass is renormalized in the $\overline{\text{MS}}$ scheme instead (3rd column of Tab. 6.4), we find only minor changes in the results. This is true both for the central value and the associated scale uncertainties. This aligns with our earlier observation for the pure-top-quark-mass effects, which also displayed very little dependence on the top-quark mass renormalization scheme.

The situation is very different for the renormalization scheme of the bottom-quark mass. At LO, the cross sections in the two renormalization schemes differ by almost 80%. At this order, the only difference during the computation is the numerical value of the bottom-quark mass. The OS mass of the bottom quark is $m_b = 4.78$ GeV, whereas the $\overline{\text{MS}}$ mass at the central scale can be read off Fig. 5.19 and reads about $\overline{m}_b(m_H/2) = 3.0$ GeV. The large difference at LO is therefore explained by the large discrepancy of the two mass values and the fact that the Higgs-gluon form factor shows a strong quadratic dependence on the quark mass in the HEL (see Eq. (4.13)). In principle, the difference should be mitigated when including higher orders in perturbation theory. However, the poor perturbative convergence of the OS- $\overline{\text{MS}}$ -mass relation in Eq. (5.78) often averts such mitigations in practice. Indeed, although we observe that the gap between the $\overline{\text{MS}}$ - and OS-results is reduced significantly, the results in the OS-scheme are unreliable, as the NNLO correction has nearly the same magnitude as the NLO correction but comes with the opposite sign. Alternating corrections of similar magnitude are a typical indicator of bad perturbative convergence. The NNLO corrections also lie outside the previously estimated uncertainty band. Additionally, we find that the scale uncertainties actually increase going from NLO to NNLO, giving us further evidence that the cross section does not stabilize in the OS-scheme. The main conclusion here is that the cross section results with an OS-renormalized bottom-quark mass are not trustworthy. The NNLO predictions therefore allowed us to eliminate the scheme-uncertainty previously associated with the gluon-gluon fusion cross section, by conclusively demonstrating that the $\overline{\text{MS}}$ scheme performs better in this instance.

To further investigate the origin of the improvements of the perturbative convergence in the $\overline{\text{MS}}$ scheme, we also computed results in a mixed renormalization scheme, where the bottom-quark mass is renormalized in the OS-scheme, but the Yukawa coupling of the Higgs and the bottom-quark is renormalized in the $\overline{\text{MS}}$ scheme. We stress that this scheme is formally inconsistent since in the SM, the Yukawa couplings are set by the mass via

$$Y = \frac{m}{v}. \quad (6.2)$$

Hence, the renormalization constant of the Yukawa coupling is fixed by those of the mass and the VEV. With the inclusion of electroweak corrections, this can result in problems of gauge invariance, but since our considerations are limited to QCD corrections, we can ignore these for our purposes. The results are much simpler to derive from the OS results than when using the $\overline{\text{MS}}$ scheme consistently because the Yukawa coupling only enters our cross section linearly.

That means that the derivatives in Eq. (5.84) are trivial, and the perturbative corrections can be obtained via

$$\begin{aligned}\sigma_{t \times b, \text{Mixed}}^{(0)} &= \frac{\bar{m}_b}{m_b} \sigma_{t \times b, \text{OS}}^{(0)} \\ \sigma_{t \times b, \text{Mixed}}^{(1)} &= \frac{\bar{m}_b}{m_b} \left[\sigma_{t \times b, \text{OS}}^{(1)} + c_1^{(5,5)} \frac{\alpha_s}{\pi} \sigma_{t \times b, \text{OS}}^{(0)} \right] \\ \sigma_{t \times b, \text{Mixed}}^{(2)} &= \frac{\bar{m}_b}{m_b} \left[\sigma_{t \times b, \text{OS}}^{(2)} + c_1^{(5,5)} \frac{\alpha_s}{\pi} \sigma_{t \times b, \text{OS}}^{(1)} + c_2^{(5,5)} \left(\frac{\alpha_s}{\pi} \right)^2 \sigma_{t \times b, \text{OS}}^{(0)} \right],\end{aligned}\quad (6.3)$$

with $\sigma_{t \times b}^{\text{NNLO}} = \sigma_{t \times b}^{(0)} + \sigma_{t \times b}^{(1)} + \sigma_{t \times b}^{(2)}$.

The results for the mixed renormalization scheme are displayed in the last column of Tab. 6.4. We can see that the main improvements on the perturbative convergence are already captured by the mixed scheme, as we no longer encounter alternating corrections of similar magnitude. The central values are compatible across all orders with the results computed using a consistent $\overline{\text{MS}}$ -renormalized bottom-quark mass within the provided scale uncertainties. The scale uncertainties themselves are generally also very similar, and even slightly smaller in the mixed scheme.

In the high-energy limit, the top-bottom interference contribution depends quadratically on the bottom-quark mass. The poor perturbative convergence of the interference contribution is therefore not entirely unexpected, as we observed similar problems in the OS- $\overline{\text{MS}}$ -mass relation of the bottom quark (see Eq. (5.78)). As to why it is the $\overline{\text{MS}}$ scheme which performs better: the standard argument is that logarithms of the form $\log(m_b^2/\mu^2)$ are automatically resummed to all orders in the $\overline{\text{MS}}$ scheme by means of the running of the bottom-quark mass. In the top-bottom interference contribution however, we also encounter Sudakov-type logarithms of the form $\log^2(m_b^2/m_H^2)$ (see for example Eq. (4.13)). These logarithms are of IR origin and should in principle dominate over the UV-logarithms, which renders the standard reasoning not directly applicable. Nevertheless, as shown in Section 5.1.3, for the Higgs-gluon form factor, the leading power of these Sudakov-type logarithms can be resummed to all orders of perturbation theory. Moreover, the resummation indicated that the perturbation series converges very quickly (see Eqs. (5.59) and (5.60)), scaling as

$$\frac{\alpha_s^n}{n! \times n^2} \log^{2n+2} \left(\frac{m_b^2}{m_H^2} \right) \quad (6.4)$$

in the large-loop limit. The UV logarithms, on the other hand, only scale as

$$\alpha_s^n n^{-\gamma_0/\beta_0} \log^n \left(\frac{m_b^2}{\mu^2} \right). \quad (6.5)$$

Thus, even if the UV logarithms $\log(m_b^2/\mu^2)$ themselves are not large compared to the IR logarithms $\log^2(m_b^2/m_H^2)$, the corresponding coefficients could make both contributions comparable in magnitude, especially at higher orders. The resummation of the UV logarithms by means of the RGE in the $\overline{\text{MS}}$ scheme could therefore still be the reason for the better convergence.

Alternatively, one could argue that in contrast to the OS scheme, the $\overline{\text{MS}}$ scheme is renormalon-free. Consequently, its asymptotic series must converge better at large loop order.

Lastly, let us compare the results of the different FSs. Similarly to the pure-top-quark-mass effects, we find that the differences are mild. Once again, at LO the only difference in the computation is the used PDF set. At NLO the computations additionally differ by the inclusion

of the $bg \rightarrow Hb$ channel in the 5FS, which due to the small PDF of the bottom-quark (see Fig. 2.1) does not impact the result significantly. Only at NNLO do we encounter differences in the calculation of amplitudes due to closed bottom-quark loops that do not couple to the Higgs. We observe that the 4 and 5FS are compatible within the provided uncertainties across all orders. The treatment of bottom-quark masses in the 5FS therefore seems to capture the effects from finite bottom-quark masses well. Intuitively, this seems reasonable because the massless limit $m_b \rightarrow 0$, works extremely well in QCD at LHC energies. We would hence expect the same for loops that do not couple to the Higgs. It is nevertheless important to verify this intuition, and validate that electroweak effects which are causing the strong mass dependence are not creeping into the parts of the amplitude which should be dictated by QCD physics.

6.2 DIFFERENTIAL CROSS SECTION

In addition to the total cross section, we also computed results for differential cross section distributions, specifically for the Higgs- p_T and the Higgs-rapidity distributions.

In Fig. 6.1, we show the top-bottom interference contribution to the two differential cross sections at NNLO¹. Herein, we compare results for OS and $\overline{\text{MS}}$ renormalized bottom-quark masses. Fig. 6.2 then presents the complete differential cross section, i.e. including the pure-top-quark and top-bottom interference contribution, and compares them to the respective results in the rHTL². The Higgs- p_T distribution is particularly interesting, as the various regions of p_T are sensitive to very different physics. At large p_T ($p_T \gg m_t$), we see that the rHTL completely breaks down and we are increasingly sensitive to finite top-quark mass effects. In Section 4.3.6, we explained that this is due to the non-vanishing mass dimension of the coupling in the HTL, resulting in a less suppressed high p_T -tail. Our analysis concluded that the ratio of the rHTL and SM differential cross section must grow quadratically in p_T (see Eq. (4.133)). We find this rough estimate confirmed in the ratio plot of the p_T distribution in Fig. 6.2. To validate this, we performed a linear fit of the logarithm of the cross-section ratio on a logarithmic p_T scale. The slope of such a fit thus indicates the power of a power-law. Our fit resulted in a slope of 1.95 within a p_T range of [500 GeV, 1000 GeV]. If the fit is performed in a higher p_T range, the slope becomes even closer to 2. The perturbative corrections are relatively constant across the spectrum for $p_T > 50$ GeV. The NNLO correction raises the distribution by roughly a factor of two, both for the rHTL and the SM calculations.

At lower transverse momentum ($p_T < m_t$), the top-quark running in the loop is not resolved, and the cross section is well approximated by the rHTL. This of course excludes the effects from the missing light-quarks, which are however only relevant for $p_T < 50$ GeV. At small transverse momenta, the fixed-order cross sections are logarithmically enhanced by $\log(p_T^2/m_H^2)$, which spoil the perturbative convergence. These kinds of logarithms can be resummed to all orders of perturbation theory. For the pure-top-quark effects, the fixed-order results can be compared to parton shower matched results [155], and one observes that resummation only becomes relevant below transverse momenta of 20 GeV. In the very low p_T region where $p_T \ll m_b$, the bottom quark is not resolved and the appearing logarithms can be resummed once again. However, this region is also sensitive to non-perturbative effects [191]. For intermediate transverse momenta $m_b < p_T < m_H$, the top-bottom interference contribution also picks up additional logarithms of the form $\log(p_T/m_b)$ and $\log(m_H/m_b)$, potentially further degrading the perturbative

¹ In Fig. 6.3 we also show OS-scheme results for a slightly altered computational setup, with a finer binning.

² In Fig. D.1 we present the analogous results for an OS renormalized bottom-quark mass.

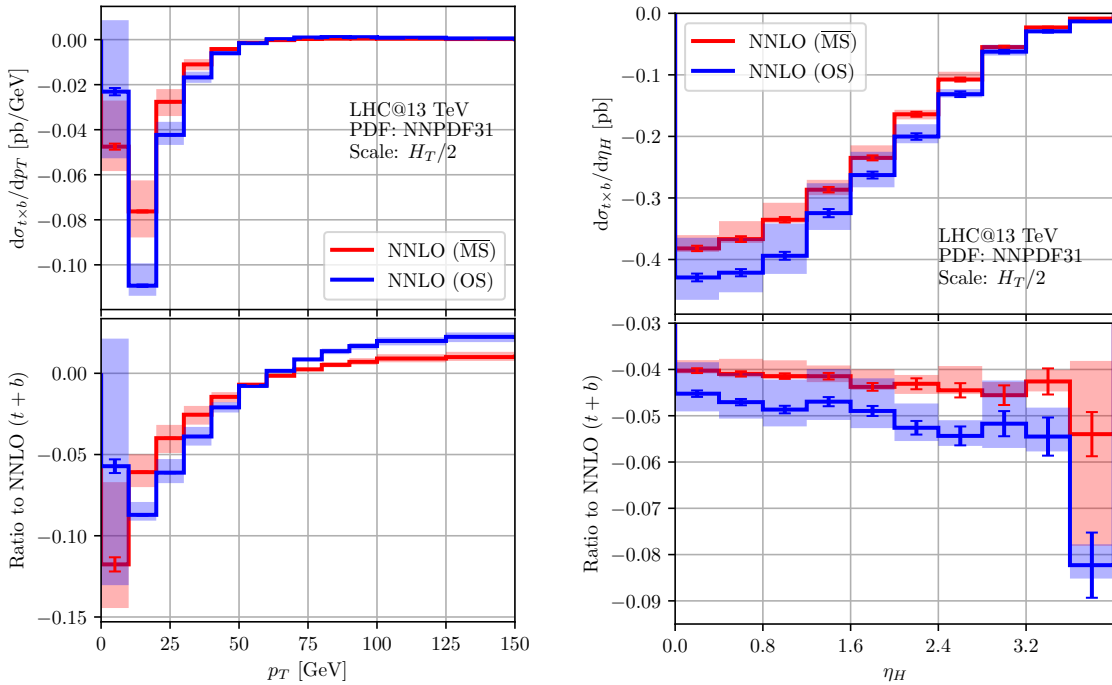


Figure 6.1: Higgs- p_T (left) and Higgs-rapidity (right) distributions for the top-bottom interference contribution to the gluon-gluon-fusion cross section. Compared are the 5FS results obtained with an $\overline{\text{MS}}$ renormalized bottom-quark mass (red) against those computed with an OS renormalized mass (blue). The results are computed for LHC @ 13 TeV using the computational setup described in the Conventions. The transparent bands indicate the scale uncertainties, whereas the error bars show the MC uncertainties.

convergence in this region. The origin and resummation of these are not well understood, however the resummation effects have been estimated in Ref. [147]. In this reference, the authors show that the effects are only relevant for transverse momenta below 20 GeV. Coincidentally, this also marked the threshold, where the resummation of top-quark logarithms can no longer be ignored. Our fixed-order results are hence reliable above this threshold.

Comparing the p_T -distributions of the top-bottom interference contribution computed with OS and $\overline{\text{MS}}$ renormalized bottom-quark masses (Fig. 6.1) reveals that the two schemes are compatible for transverse momenta above 30 GeV. Below this threshold, we observe significant deviations and a sharp spike at around 15 GeV in the OS scheme. In the $\overline{\text{MS}}$ scheme the spike is also visible but less pronounced and overall there is a smoother low- p_T behavior. This indicates that the main improvements on the perturbative convergence over the OS scheme come from this region of the phase-space.

The rapidity distribution is not subject to logarithmic enhancements and remains reliable across the entire range. The distribution overall is less feature rich. With an $\overline{\text{MS}}$ renormalized bottom-quark mass, the top-bottom interference contribution approximately results in a shift of -4% across the entire rapidity spectrum. In the OS scheme the shift is slightly larger—around -4.5% with a slight negative tilt towards larger rapidities. Relative scale uncertainties remain roughly constant and are significantly larger in the OS-scheme, as expected from our findings on the total cross section (see Tab. 6.4). In the right panel of Fig. 6.2, we can see that the NNLO corrections on the total cross section result in a shift of $+20\%$ across the entire rapidity spectrum, both for the rHTL and the SM cross section. This once again perfectly aligns with

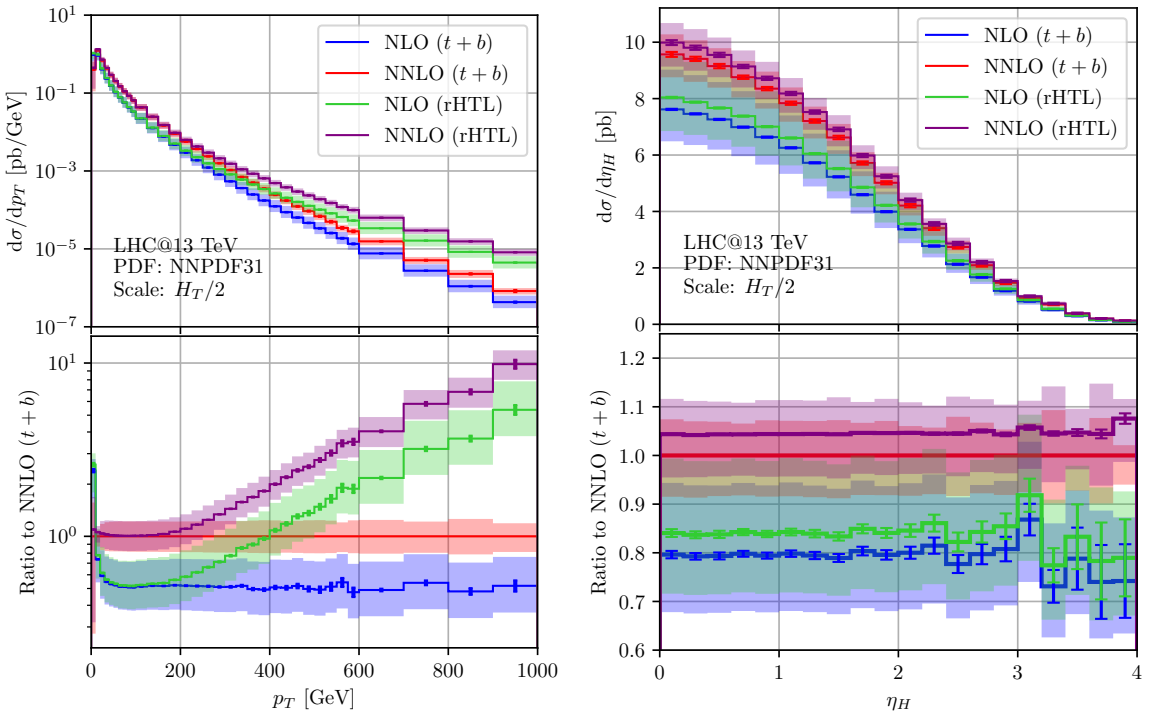


Figure 6.2: Higgs- p_T (left) and Higgs-rapidity (right) distributions for the gluon-gluon fusion channel. Compared are the 5FS results obtained in the rHTL with those including finite-quark-mass effects (pure-top-quark-mass effects + top-bottom interference contribution). The bottom-quark mass is renormalized in the $\overline{\text{MS}}$ scheme, while the top-quark mass is renormalized in the OS scheme. The results are computed for LHC @ 13 TeV using the computational setup described in the Conventions. The transparent bands indicate the scale uncertainties, whereas the error bars show the MC uncertainties.

the observed corrections in the total cross section in Tab. 6.1. Similarly, the rHTL differential cross section overshoots the full cross section by around 4 – 5% across the entire spectrum, aligning perfectly with the observed shift of the top-bottom interference contribution in the right panel Fig. 6.1.

6.3 VALIDATION & COMPARISON WITH OTHER WORKS

In the 4FS, the bottom-quark mass acts as an IR-regulator, resulting in huge logarithmic enhancements of the individual amplitudes. To check that these enhancements cancel in inclusive observables, we performed the calculation of the rHTL cross section for a number of small bottom-quark masses. This means that the cross section contains only contributions arising from the effective coupling of the Higgs to gluons, and the bottom-quark mass is only relevant in bottom-quark loops which are not coupling to the Higgs. These loops, however, are precisely the ones that give rise to the logarithmic enhancements. The results are displayed in Tab. 6.5. The results clearly show that there are no logarithmic enhancements on the cross section level, as there is no pronounced rise of the cross section for decreasing bottom-quark masses. We further observe that the 4FS results approach the 5FS results in the limit $m_b \rightarrow 0$. For realistic values of the bottom-quark mass (last two columns in Tab. 6.5), we see a significant

Order		$\sigma_{\text{rHTL}} [\text{pb}]$			
		$\sqrt{s} = 13 \text{ TeV}$			
	5FS	4FS $m_b = 0.01 \text{ GeV}$	4FS $m_b = 0.1 \text{ GeV}$	4FS $m_b = 4.78 \text{ GeV}$	4FS $\bar{m}_b(\bar{m}_b) = 4.18 \text{ GeV}$
$\mathcal{O}(\alpha_s^2)$	+16.30	+16.27	+16.27	+16.27	16.27
LO	$16.30^{+4.36}_{-3.10}$	$16.27^{+4.63}_{-3.22}$	$16.27^{+4.63}_{-3.22}$	$16.27^{+4.63}_{-3.22}$	$16.27^{+4.63}_{-3.22}$
$\mathcal{O}(\alpha_s^3)$	+21.14	+20.08(3)	+20.08(3)	+20.08(3)	+20.08(3)
NLO	$37.44^{+8.42}_{-6.29}$	$36.35(3)^{+8.57}_{-6.32}$	$36.35(3)^{+8.57}_{-6.32}$	$36.35(3)^{+8.57}_{-6.32}$	$36.35(3)^{+8.57}_{-6.32}$
$\mathcal{O}(\alpha_s^4)$	+9.72	+10.8(4)	+11.1(4)	+9.5(2)	+9.6(2)
NNLO	$47.16^{+4.21}_{-4.77}$	$47.2(4)^{+5.4}_{-5.4}$	$47.5(4)^{+5.4}_{-5.5}$	$45.9(2)^{+4.3}_{-4.9}$	$46.0(2)^{+4.4}_{-5.0}$

Table 6.5: rHTL cross section in the 5-flavour scheme and for different bottom-quark masses in the 4-flavour scheme. In the last column the cross section and the scale variation are computed with the $\overline{\text{MS}}$ mass. The results are computed for LHC @ 13 TeV using the computational setup described in the Conventions. The scale uncertainties are determined with seven-point variation. Numbers in parentheses indicate the MC uncertainties on the last provided digit. Results in the 5FS were computed using SusHi.

change from the 5 to the 4FS of around -2% , which is, however, still well within the associated scale uncertainties. Finally, results for OS and $\overline{\text{MS}}$ renormalized bottom-quark masses show no significant deviations.

To further validate our findings, we compared our Higgs- p_T spectra against existing Higgs+jet analysis. The top-bottom interference contribution with OS-renormalized top- and bottom-quark masses was compared to the results presented in Ref. [147]. In this reference, the authors approximate the real-virtual corrections using the HTL for the top-quark, and they work under the assumption of a nearly massless bottom-quark. Fig. 6.3 shows the comparison of the two results. We see that the approximations perform well for transverse momenta below 40 GeV, but result in an error of about 20% above this threshold. Since the approximation of a nearly massless bottom quark is expected to perform well in the limit $m_b \ll m_H, p_T$, the discrepancy is likely due to the HTL approximation. Since the p_T range $[0, 40 \text{ GeV}]$ is responsible for the majority of the top-bottom interference contribution—about 99%—, the approximation is still highly accurate for the total cross section. Additionally, we observe that the scale uncertainties of the first two bins are significantly larger in Ref. [147]. We were able to identify that this difference arises only from a single scale variation ($\mu_R/\mu = 1, \mu_F/\mu = 2$), but we have not found any error on our end that would account for this difference.

Furthermore, we compared our findings of the pure-top and the top-bottom-interference contribution with both quark-masses defined in the $\overline{\text{MS}}$ scheme with the results presented in Ref. [148]. The results show excellent agreement for transverse momenta $p_T \leq 400 \text{ GeV}$. Above this scale we find significant deviations. We were able to identify that the problem arises from the real-virtual amplitudes. Indeed, our numerical grids were only computed for top-quark masses up to a scale of $\mu_R = 125 \text{ GeV}$. If the scale exceeds this value, we are extrapolating from our grid. This then results in large errors for $p_T > 400 \text{ GeV}$. We stress that all our previous findings did not rely on this extrapolation, since we used fixed scales whenever we renormalized the top-quark mass in the $\overline{\text{MS}}$ scheme.

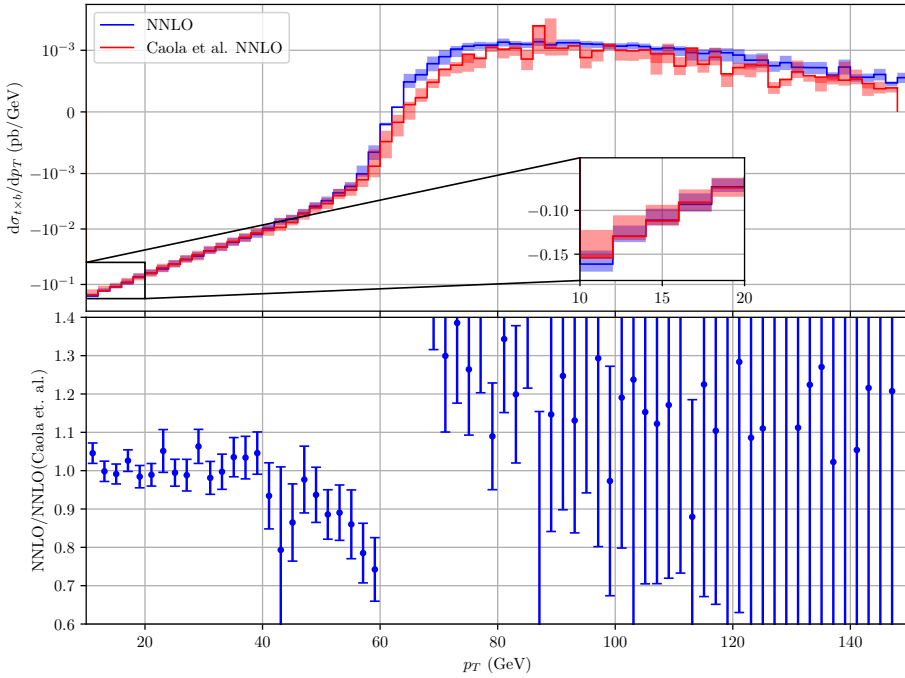


Figure 6.3: Top-bottom interference contribution to the Higgs production cross section. Displayed are our results (blue) and the results presented in Ref. [147] (red), with data provided by the authors. The authors of that reference used an OS top- and bottom-quark mass of $m_t = 173.2$ GeV, and $m_b = 4.75$ GeV, whereas we used $m_t = 173.05$ GeV and $m_b = 4.78$ GeV and the same Higgs mass of $m_H = 125$ GeV. For the sake of this comparison, we used the same PDF4LHC15_nlo_30 PDF set and a central scale of $\mu = \frac{1}{2}\sqrt{m_H^2 + p_T^2}$. The transparent bands indicate scale uncertainties, whereas the error bars in the lower panel indicate the MC uncertainties dominated by the uncertainties of Ref. [147].

6.4 RECOMMENDATIONS FOR PHENOMENOLOGICAL APPLICATIONS

We conclude this chapter by giving our recommendations for the total gluon-gluon fusion Higgs-production cross section for future phenomenological applications. We combine our findings with the full N³LO rHTL results, the partial N⁴LO results in the soft-virtual approximation, the available electroweak corrections, and the finite top-quark mass effects. The associated uncertainties of each contribution are carefully examined.

Following our discussion of Section 4.3.1, we suggest using $\mu = m_H/2$ as the central scale. Moreover, we recommend using the MSHT20xNNPDF40_aN3LO PDF set until full N³LO sets become available.

The top-bottom interference contribution proved to be quite independent of the chosen FS. We suggest using the 5FS going forward because large logarithms are automatically resummed in this FS by the running of the PDFs. The renormalization scheme of the top-quark mass also did not affect the cross section significantly. Both the $\overline{\text{MS}}$ and the OS scheme are therefore valid choices. In the following we provide results for the latter. The bottom-quark mass on the other hand, was very sensitive to the renormalization scheme, and the $\overline{\text{MS}}$ scheme showed significantly better perturbative convergence, which is why we strongly recommend using this scheme from now on.

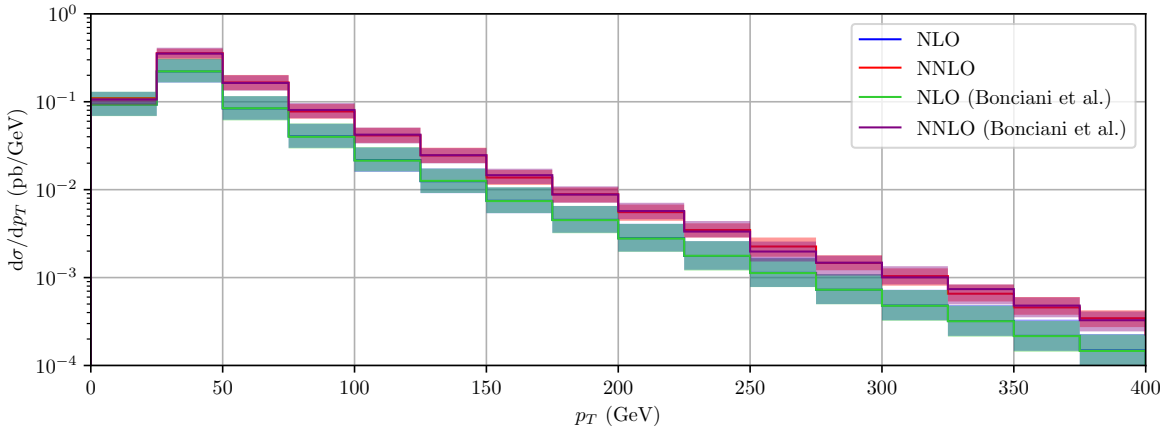


Figure 6.4: Comparison of the differential Higgs- p_T cross section of the gluon-gluon fusion channel between our findings and the results presented in Ref. [148]. The cross section constitutes the pure-top-quark, the top-bottom interference, and the pure-bottom-quark contributions, however, we neglect the pure-bottom-quark contribution for all NNLO corrections. For the sake of this comparison, we use the same computational setup as the authors of Ref. [148], namely top- and bottom-quark masses defined in the $\overline{\text{MS}}$ scheme with the masses $\bar{m}_t(\bar{m}_t) = 163.4$ GeV and $\bar{m}_b(\bar{m}_b) = 4.18$ GeV. The running of the quark-masses is computed at two-loop accuracy. The Higgs mass is set to $m_H = 125.25$ GeV. We apply the anti- k_T algorithm with a jet radius of $R = 0.4$ and use the central scale $\mu = \frac{1}{2} \left(\sqrt{m_H^2 + p_T^2} + \sum_i p_{i,T} \right)$, where the sum runs over all jet momenta. We use a p_T -cut on the jets, requiring that at least one of the jets satisfies $p_{i,T} > 20$ GeV. We use the `NNPDF40_nlo_as_01180` PDF set.

Our best prediction for the gluon-gluon fusion cross section is

$$\begin{aligned}
\sigma_{pp \rightarrow HX}(13 \text{ TeV}) = & + 15.33 \text{ pb } (+33.17\%) \quad (\text{LO rHTL}) \\
& + 19.99 \text{ pb } (+43.26\%) \quad (\text{NLO cor. rHTL}) \\
& + 9.20 \text{ pb } (+19.91\%) \quad (\text{NNLO cor. rHTL}) \\
& + 1.56 \text{ pb } (+3.38\%) \quad (\text{N}^3\text{LO cor. rHTL}) \\
& + 0.14 \text{ pb } (+0.30\%) \quad (\text{N}^4\text{LO cor. rHTL in s.-v. approx.}) \\
& + 2.02 \text{ pb } (+4.37\%) \quad (\text{NLO EW-QCD}) \quad (6.6) \\
& - 0.16 \text{ pb } (-0.35\%) \quad (\text{NNLO finite top-quark mass}) \\
& - 0.23 \text{ pb } (-0.50\%) \quad (\text{NLO top-charm interference}) \\
& + 0.10 \text{ pb } (+0.22\%) \quad (\text{NLO pure bottom-quark effects}) \\
& - 1.74 \text{ pb } (-3.77\%) \quad (\text{NNLO top-bottom interference}) \\
\hline
& 46.21 \text{ pb } (100\%).
\end{aligned}$$

Here, “cor.” refers to the correction of the respective perturbative order. The rHTL results were computed using `iHixs` 2. The N^4LO results were extracted from the K -factor with respect to N^3LO at 13 TeV, provided in Ref. [26]. In this reference, the authors use a slightly altered computational setup, including a different PDF set (`MSHT2014`). Since the N^4LO corrections are tiny, the final result should not be affected by this significantly. Similarly, the electroweak corrections were extracted from Ref. [34], where the authors used the `PDF4LHC15_nlo_30` PDF set and slightly different masses for the Higgs, and the top and bottom quark³. Once again, the electroweak corrections themselves are small, making the impact of a slightly altered

³ The authors also used a bottom-quark mass defined in the OS scheme.

computational setup non-essential. Finally, the effects from finite top- and bottom-quark masses were computed using the `NNPDF31_nnlo_as_0118` PDF set.

We estimate the MHOU, based on the μ_R variation⁴ of the N⁴LO cross section in the soft-virtual approximation in the range $[m_H/4, m_H]$ presented in Ref. [26]. The factorization-scale dependence was shown to be very small (see Fig. 4.12), making it an accurate estimate of MHOU. We can estimate the error of the soft-virtual approximation itself based on lower orders. We conservatively assign the uncertainty by taking the perturbative order at which the soft-virtual approximation yielded the worst estimate of the perturbative correction and then apply the resulting accuracy to the N⁴LO results,

$$\delta(\Delta\sigma_{\text{s.-v.}}^{\text{N}^n\text{LO}}) = \max\left\{\left|1 - \Delta\sigma_{\text{rHTL}}^{\text{NLO}}/\Delta\sigma_{\text{s.-v.}}^{\text{NLO}}\right|, \dots, \left|1 - \Delta\sigma_{\text{rHTL}}^{\text{N}^{n-1}\text{LO}}/\Delta\sigma_{\text{s.-v.}}^{\text{N}^{n-1}\text{LO}}\right|\right\} \Delta\sigma_{\text{s.-v.}}^{\text{N}^n\text{LO}}. \quad (6.7)$$

Here, $\Delta\sigma_{\text{s.-v.}}^{\text{N}^n\text{LO}}$ refers to the correction of the cross section at NⁿLO. We can see from Tab. 4.2 that this error estimate works reasonably well, as the differences between the soft-virtual and the full corrections is always within a 1.2σ interval. Uncertainties on the electroweak corrections are also dominated by MHOU, and we adopt the uncertainties assigned in Ref. [34]. Errors associated with missing higher orders in the PDF fits, including the missing ingredients for the DGLAP evolution equation, are estimated by comparing cross section results computed using the `NNPDF40_an3lo_as_01180_mhou` and the `NNPDF40_an3lo_as_01180` PDF sets, i.e. the uncertainty is calculated via

$$\delta(\text{PDF MHOU}) = \sqrt{\left(\sigma_{gg \rightarrow HX}^{\text{NNPDF40_an3lo_as_01180_mhou}}\right)^2 - \left(\sigma_{gg \rightarrow HX}^{\text{NNPDF40_an3lo_as_01180}}\right)^2}. \quad (6.8)$$

This assumes that the PDF-theory and the PDF uncertainties are uncorrelated. Uncertainties for finite quark-mass effects are determined through seven-point scale variation. The full theory uncertainty can be broken down as follows:

$$\begin{aligned} \delta(\text{theory}) = & \begin{array}{l} +0.10 \\ -1.73 \end{array} \text{ pb } \begin{array}{l} (+0.2\%) \\ (-3.7\%) \end{array} \text{ (scale)} \\ & \pm 0.24 \text{ pb } (\pm 0.5\%) \text{ (s.-v. approx.)} \\ & \pm 0.14 \text{ pb } (\pm 0.3\%) \text{ (electroweak)} \\ & \pm 0.16 \text{ pb } (\pm 0.3\%) \text{ (PDF MHOU)} \\ & \begin{array}{l} +0.13 \\ -0.03 \end{array} \text{ pb } \begin{array}{l} (+0.3\%) \\ (-0.1\%) \end{array} \text{ (finite top-quark mass)} \\ & \begin{array}{l} +0.13 \\ -0.03 \end{array} \text{ pb } \begin{array}{l} (+0.3\%) \\ (-0.1\%) \end{array} \text{ (top-bottom interference)} \\ \hline & \begin{array}{l} +0.35 \\ -1.76 \end{array} \text{ pb } \begin{array}{l} (+0.8\%) \\ (-3.8\%) \end{array}. \end{aligned} \quad (6.9)$$

For the final theory uncertainty, we added all individual errors in quadrature. In Section 4.3.5 we observed that the top-bottom interference contribution is actually anti-correlated with the pure-top-quark contribution. We do not take this anti-correlation into account here because the correlations among the other sources of uncertainty are currently unavailable. The error budget is illustrated in Fig. 6.5.

The uncertainty estimates are slightly different from the upcoming Higgs Working Group recommendation [193], mainly due to the fact that electroweak corrections are not incorporated with full NLO precision. Furthermore, the Higgs Working Group assumes maximal correlation among the various uncertainties. The uncertainty estimates presented here are therefore smaller by approximately 0.8% of the total cross section.

⁴ Recently, the MHOU were also estimated using theory nuisance parameters [192] at NNLO. The authors found the uncertainties to be compatible.

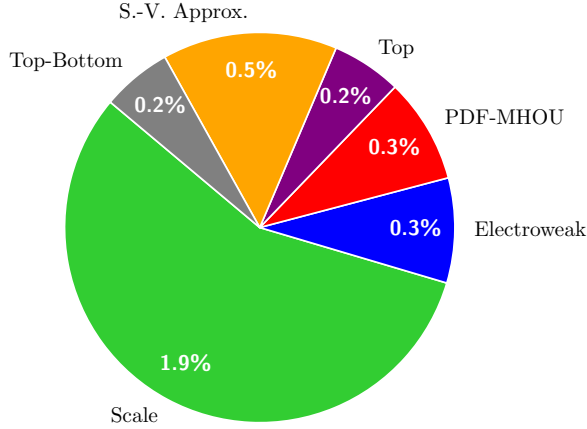


Figure 6.5: Total error budget of the fully inclusive gluon-gluon fusion Higgs production cross section at 13 TeV. Uncertainties are assigned as described in the text.

Finally, the uncertainties on the PDF sets are combined with the α_s uncertainties, assuming that the errors are uncorrelated. This not entirely realistic assumption is adopted out of necessity since the MSHT20xNNPDF40_aN3LO PDF set does not support correlations yet. The α_s -uncertainty is estimated by reevaluation of the N³LO rHTL cross section at $\alpha_s(m_Z) = 0.117$ and $\alpha_s(m_Z) = 0.119$, corresponding to the standard deviation of α_s [194], the resulting range is taken as the standard deviation. The combined uncertainty reads

$$\begin{aligned} \delta(\text{PDF} + \alpha_s) &= \sqrt{[\delta(\text{PDF})]^2 + [\delta(\alpha_s)]^2} = \sqrt{[0.88 \text{ pb (1.9\%)}]^2 + \left[\begin{array}{c} +1.23 \\ -1.21 \end{array} \text{ pb (+2.6\%)} \right]^2} \\ &= {}^{+1.52}_{-1.50} \text{ pb } {}^{(+3.3\%)}_{(-3.2\%)}. \end{aligned} \quad (6.10)$$

Our final best prediction for the gluon-gluon fusion cross at 13 TeV is

$$\boxed{\sigma_{pp \rightarrow HX}(13 \text{ TeV}) = 46.21^{+0.35}_{-1.76} \text{ (theory)} {}^{+1.52}_{-1.50} \text{ (PDF + } \alpha_s \text{) pb.}} \quad (6.11)$$

This is in excellent agreement with the current best measurement of the cross section (4.1).

7

CONCLUSIONS & OUTLOOK

7.1 CONCLUSIONS

In this work, we investigated the effect of finite bottom-quark masses on the Higgs production cross section in the gluon-gluon fusion channel. We computed the top-bottom interference contribution to the cross section at NNLO. In our recommended setup, where the bottom-quark mass is renormalized in the $\overline{\text{MS}}$ scheme and the bottom quark is included in the PDFs, the NNLO correction turned out to be tiny (+0.02 pb at 13 TeV), however the scale uncertainties were reduced significantly. This marks the final cornerstone in a long series of theoretical improvements to the cross section. The theoretical uncertainty is now at the level 2% of the total cross section.

We also investigated the effects of alternative renormalization schemes, both for the top- and for the bottom-quark mass. We found that the cross section is quite insensitive to the renormalization scheme of the top-quark mass. For the bottom-quark mass, on the other hand, the renormalization scheme proved crucial. The OS scheme failed to exhibit good perturbative convergence at NNLO, whereas the $\overline{\text{MS}}$ scheme succeeded. Nevertheless, the cross section predictions in the two renormalization schemes turned out to be compatible within a 2σ interval. This analysis removed the scheme ambiguity previously associated with the cross section contribution.

Additionally, we examined the impact of the chosen FS. This was particularly interesting for this process because it altered the treatment of the bottom-quark mass whenever it was not coupled to the Higgs. Our findings showed that the results in the 4 and 5FS were compatible, thus providing empirical evidence that the treatment of the bottom-quark mass in the 5FS is indeed justified.

Besides the total cross section, we also provided results for differential cross sections, namely for the Higgs- p_T and -rapidity spectra. Our results for the p_T spectrum aligned with what was found in previous studies [147, 148]. The top-bottom interference contribution as well as the effect of finite top-quark masses on the NNLO Higgs rapidity distribution represent new results. The combined effect shifted the rHTL results by around -4% across the entire rapidity spectrum.

Our analysis allowed us to give well-grounded recommendations for future research in this field. Finally, we combined our findings with other state-of-the-art computations and carefully assessed their theoretical uncertainties. The resulting prediction can be used for future experimental or phenomenological applications.

7.2 OUTLOOK

Since the theoretical uncertainty is now dominated by scale uncertainties, and this despite the fact that the cross section has been computed at partial N⁴LO, it is unlikely that we will see a further significant reduction of the total theory uncertainty. The only uncertainties that will probably be reduced in the near future are the MHOU in the PDFs, as well as the uncertainty on the soft-virtual approximation. The former partly arises from the incomplete N³LO DGLAP evolution kernels, i.e. once these have been worked out, we can see a further reduction of the error. However, it is unclear how much the uncertainty will actually improve, as the MHOU also include the uncertainties of the perturbative cross sections the PDFs are matched to. Moreover, even if the uncertainty were completely removed, the impact on the total error of the cross section is almost negligible. Regarding the error of the soft-virtual approximation, the latest *Les Houches wishlist* [195], named the N⁴LO Higgs production cross section as a major aim, and with tremendous progress in the calculation of the necessary amplitudes recently [196, 197], we can hope that the full N⁴LO cross section will become available in the coming years. And although the total uncertainty is likely not going to be reduced significantly, the full calculation is still highly desirable, in order to assess the quality of the soft-virtual approximation at this order.

The most promising way to make significant progress in the mitigation of the theory uncertainties, is by improving on the PDF and α_s uncertainties. We have seen in Section 4.3.2 that the PDF-uncertainty estimates of the NNPDF and MSHT collaborations are vastly different. If the small uncertainties of the NNPDF collaboration are to be believed, then the PDF+ α_s uncertainty, which is dominating for this progress, would be reduced by another factor of 2! Understanding the origin of this discrepancy could be key, not only for the Higgs production cross section, but for precision predictions in general.

The low- p_T region of the top-bottom interference contribution is particularly interesting since here the effects from finite bottom-quark masses are most noticeable. Consequently, it is the region most suited for the determination of the bottom-Yukawa coupling. The fixed-order p_T -distribution is however only reliable above $p_T \sim 20$ GeV. Below, large logarithms can no longer be ignored and require the resummation to all orders. The origin and resummation of these logarithms is not yet well understood and more research along the lines of Refs. [68, 147] is needed to improve our understanding as well as the precision of the cross section in this critical region of the phase space.

In experimental searches and measurements of Higgs boson properties, one typically considers only specific production and decay channels of the Higgs. Since the decay width of the Higgs is orders of magnitude smaller than its mass $\Gamma_H/m_H = 3 \times 10^{-5}$, one can apply the narrow width approximation (see Eq. (4.2)), such that production and decay of the Higgs boson become factorized. Our results therefore serve as a stepping stone for a more precise determination of the $pp \rightarrow H \rightarrow X$ cross sections. This will be crucial, especially in the light of the high luminosity phase of the LHC.

A

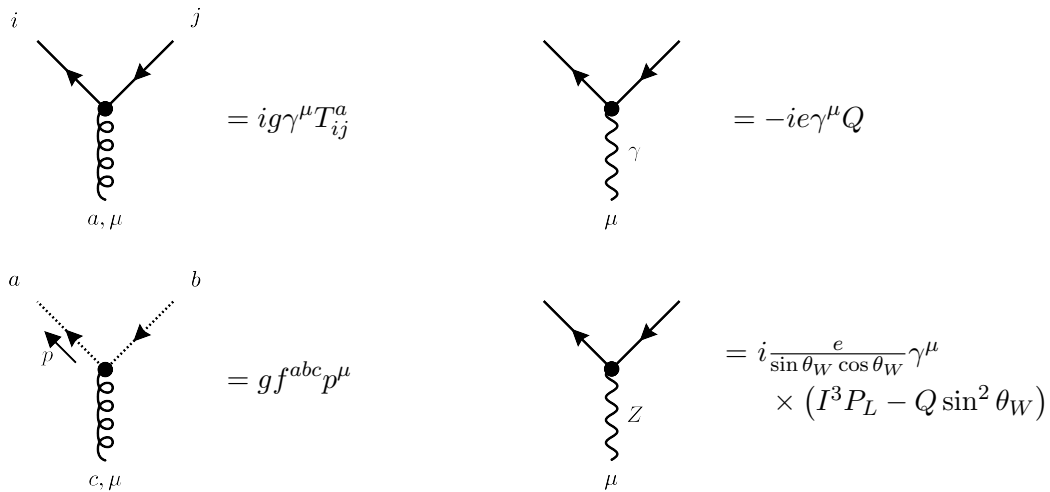
FEYNMAN RULES OF THE STANDARD MODEL

In this chapter we list all Feynman rules of the SM. We choose to work in a unitary gauge, meaning that the all Goldstone-bosons decouple and there are no unphysical particles in the electroweak sector. In the QCD sector, we work in the R_ξ gauge, i.e. we have unphysical particles in the form of *Faddeev-Popov ghosts*. If not otherwise specified, the momenta on every line are defined as incoming.

Propagators:

$$\begin{aligned}
 a, \mu & \quad \text{---} \xrightarrow[k]{} \text{---} b, \nu & = i \frac{\delta^{ab}}{k^2 + i0^+} \left[-g_{\mu\nu} + (1 - \xi) \frac{k_\mu k_\nu}{k^2 + i0^+} \right] \\
 i & \quad \xrightarrow[k]{} j & = i\delta_{ij} \frac{\not{k} + m}{k^2 - m^2 + i0^+} \\
 & \quad \text{---} \xrightarrow[k]{} \text{---} & = i \frac{1}{k^2 - m_H^2 + i0^+} \\
 \mu & \quad \text{---} \xrightarrow[k]{} \gamma & = i \frac{-g_{\mu\nu}}{k^2 + i0^+} \\
 \mu & \quad \text{---} \xrightarrow[k]{} W & = i \frac{1}{k^2 - m_W^2 + i0^+} \left(-g_{\mu\nu} + \frac{k_\mu k_\nu}{m_W^2 + i0^+} \right) \\
 \mu & \quad \text{---} \xrightarrow[k]{} Z & = i \frac{1}{k^2 - m_Z^2 + i0^+} \left(-g_{\mu\nu} + \frac{k_\mu k_\nu}{m_Z^2 + i0^+} \right) \\
 a & \quad \text{---} \xrightarrow[k]{} b & = i \frac{\delta^{ab}}{k^2 + i0^+}
 \end{aligned}$$

Fermion–Gauge-Boson Vertices:



$$\text{Left Diagram: } q_i^u \text{ and } q_j^d \text{ exchange } W \text{ (mu)} = i \frac{e(V_{CKM})_{ij}}{\sqrt{2} \sin \theta_W} \gamma^\mu P_L$$

$$\text{Right Diagram: } q_i^d \text{ and } q_j^u \text{ exchange } W \text{ (mu)} = i \frac{e(V_{CKM})_{ji}^*}{\sqrt{2} \sin \theta_W} \gamma^\mu P_L$$

Gauge-Boson Self Interactions:

$$\text{Top Row: } c, \rho \text{ and } b, \nu \text{ exchange } \rho \text{ (p}_3\text{) and } \rho \text{ (p}_2\text{) and } \rho \text{ (p}_1\text{) and } \rho \text{ (p}_1\text{).}$$

$$= g f^{abc} ((p_1^\rho - p_2^\rho) g^{\mu\nu} + (p_2^\mu - p_3^\mu) g^{\nu\rho} + (p_3^\nu - p_1^\nu) g^{\rho\mu})$$

$$\text{Bottom Row: } a, \mu \text{ and } b, \nu \text{ exchange } \rho \text{ (p}_3\text{) and } \rho \text{ (p}_2\text{) and } \rho \text{ (p}_1\text{) and } \rho \text{ (p}_1\text{).}$$

$$= -ig^2 (f^{abe} f^{cde} (g^{\mu\rho} g^{\nu\sigma} - g^{\mu\sigma} g^{\nu\rho}) + f^{ace} f^{bde} (g^{\mu\nu} g^{\rho\sigma} - g^{\mu\sigma} g^{\nu\rho}) + f^{ade} f^{bce} (g^{\mu\nu} g^{\rho\sigma} - g^{\mu\rho} g^{\nu\sigma}))$$

$$\text{W and W-gamma: } \mu \text{ and } \nu \text{ exchange } W^- \text{ (p}_2\text{), } W^+ \text{ (p}_3\text{), } \gamma, Z \text{ (p}_1\text{), and } \rho.$$

$$= i \frac{e}{\sin \theta_W} ((p_1^\rho - p_2^\rho) g^{\mu\nu} + (p_2^\mu - p_3^\mu) g^{\nu\rho} + (p_3^\nu - p_1^\nu) g^{\rho\mu}) \times \begin{cases} -\sin \theta_W & \text{for } \gamma \\ \cos \theta_W & \text{for } Z \end{cases}$$

$$\text{W and W-Z: } \mu \text{ and } \nu \text{ exchange } W^- \text{ (V}_1\text{), } W^+ \text{ (V}_2\text{), and } \rho \text{ (sigma).}$$

$$= i \frac{e^2}{\sin^2 \theta_W} (g^{\mu\sigma} g^{\nu\rho} + g^{\mu\rho} g^{\nu\sigma} - 2g^{\mu\nu} g^{\rho\sigma}) \times \prod_{i=1}^2 \begin{cases} -\sin \theta_W & \text{if } V_i = \gamma \\ \cos \theta_W & \text{if } V_i = Z \end{cases}$$

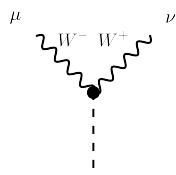
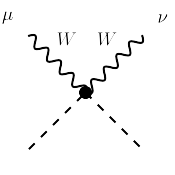
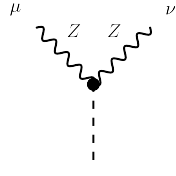
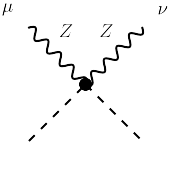
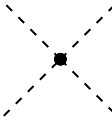
$$\text{W and W-W: } \mu \text{ and } \nu \text{ exchange } W^- \text{ (V}_1\text{), } W^+ \text{ (V}_2\text{), and } \rho \text{ (sigma).}$$

$$= i \frac{e^2}{\sin^2 \theta_W} (2g^{\mu\rho} g^{\nu\sigma} - g^{\mu\nu} g^{\rho\sigma} - g^{\mu\sigma} g^{\nu\rho})$$

Higgs Interactions:

$$\text{Left Diagram: } i \text{ and } j \text{ exchange } q\bar{q} = -i \frac{m_q}{v} \delta_{ij}$$

$$\text{Right Diagram: } i \text{ and } j \text{ exchange } H \text{ (dashed)} = -i \frac{3m_H^2}{v}$$

	$= i \frac{e}{\sin \theta_W} m_W g^{\mu\nu}$		$= i \frac{e^2}{2 \sin^2 \theta_W} g^{\mu\nu}$
	$= i \frac{e}{\sin \theta_W \cos \theta_W} m_Z g^{\mu\nu}$		$= i \frac{e^2}{2 \sin^2 \theta_W \cos^2 \theta_W} g^{\mu\nu}$
	$= -i \frac{3m_H^2}{v^2}$		

B | FEYNMAN INTEGRALS

In this appendix we collect some common one-loop Feynman integrals which appear repeatedly throughout this PhD thesis.

Bubble

We define the function $B(p^2)$ as the finite part of the bubble integral

$$B(p^2) = 2 - \log\left(\frac{m^2}{\mu^2}\right) + \beta(p^2, m^2) \log\left(-\frac{1 - \beta(p^2, m^2)}{1 + \beta(p^2, m^2)} + i0^+\right). \quad (\text{B.1})$$

The function $\beta(s, m^2)$ is defined in Eq. (5.28). We further define

$$B_1(p^2) \equiv B(p^2) - B(m_H^2). \quad (\text{B.2})$$

Triangle

The one-loop on-shell triangle integral is

$$\begin{aligned} C(s) = C(p_1, p_2) &= \int \frac{d^4 l}{i\pi^2} \frac{1}{[l^2 - m^2][(l + p_1)^2 - m^2][(l + p_1 + p_2)^2 - m^2]} \\ &= \frac{1}{2s} \log^2\left(-\frac{1 - \beta(p^2, m^2)}{1 + \beta(p^2, m^2)} + i0^+\right). \end{aligned} \quad (\text{B.3})$$

The triangle integral with one off-shell leg is related via

$$s_1 C_1(s) \equiv sC(s) - m_H^2 C(m_H^2). \quad (\text{B.4})$$

Box

The one-loop box integral reads

$$\begin{aligned} D(s, t) &= D(p_1, p_2, p_3) \\ &= \int \frac{d^4 l}{i\pi^2} \frac{1}{[l^2 - m^2][(l + p_1)^2 - m^2][(l + p_1 + p_2)^2 - m^2][(l + p_1 + p_2 + p_3)^2 - m^2]} \\ &= -\frac{2}{st\beta(-st/u, m^2)} \left\{ \text{Li}_2\left(\frac{1 - \beta(-st/u, m^2)}{-\beta(-st/u, m^2) - \beta(m_H^2, m^2)}\right) \right. \\ &\quad - \text{Li}_2\left(\frac{1 + \beta(-st/u, m^2)}{\beta(-st/u, m^2) - \beta(m_H^2, m^2)}\right) + \text{Li}_2\left(\frac{1 - \beta(-st/u, m^2)}{\beta(m_H^2, m^2) - \beta(-st/u, m^2)}\right) \\ &\quad - \text{Li}_2\left(\frac{1 + \beta(-st/u, m^2)}{\beta(m_H^2, m^2) + \beta(-st/u, m^2)}\right) \\ &\quad + \log\left(-\frac{1 - \beta(-st/u, m^2)}{1 + \beta(-st/u, m^2)}\right) \log\left(1 - \frac{m_H^2}{4m^2}(1 - \beta^2(-st/u, m^2) - i0^+)\right) \\ &\quad \left. - (m_H^2 \rightarrow s) - (m_H^2 \rightarrow t) \right\}, \end{aligned} \quad (\text{B.5})$$

where $p_1^2 = p_2^2 = p_3^2 = 0$. We further define the auxiliary function

$$E(u, t) = uC(u) + tC(t) + u_1 C_1(u) + t_1 C_1(t) - utD(u, t). \quad (\text{B.6})$$

C

ENERGY SCAN OF THE TOP-BOTTOM
INTERFERENCE CONTRIBUTION

In this appendix we provide additional results on the top-bottom interference contribution to the gluon-gluon fusion cross section. Specifically we provide the results for collider energies of 7, 8, 13, 13.6, and 14 TeV. In Tab. C.1 we present the results computed with a setup according to Higgs-Working-Group recommendations. Tab. C.2 show the results for an OS renormalized bottom-quark mass, as well as the results for a mixed renormalization scheme, where the bottom-quark Yukawa coupling has been renormalized in the $\overline{\text{MS}}$ -scheme.

	7 TeV	8 TeV	13 TeV	13.6 TeV	14 TeV
LO	$-0.39^{+0.10}_{-0.15}$ pb	$-0.50^{+0.12}_{-0.19}$ pb	$-1.09^{+0.27}_{-0.42}$ pb	$-1.17^{+0.29}_{-0.45}$ pb	$-1.22^{+0.31}_{-0.47}$ pb
NLO	$-0.66^{+0.11}_{-0.12}$ pb	$-0.82^{+0.13}_{-0.14}$ pb	$-1.72^{+0.26}_{-0.27}$ pb	$-1.84^{+0.28}_{-0.29}$ pb	$-1.91^{+0.29}_{-0.30}$ pb
NNLO	$-0.68^{+0.06}_{-0.02}$ pb	$-0.84^{+0.07}_{-0.01}$ pb	$-1.70^{+0.13}_{-0.01}$ pb	$-1.80^{+0.13}_{-0.01}$ pb	$-1.88^{+0.13}_{-0.01}$ pb

Table C.1: Top-bottom interference contribution to the fully-inclusive Higgs-production cross section for different collider energies and perturbative orders. The top-quark mass is renormalized in the OS-scheme with a pole mass of $m_t = 172.5$ GeV, except in the real-virtual corrections where we use a mass of $m_t = 173.18$ GeV. We reevaluated this contribution with a value of $m_t = 171.1$ GeV and found that the difference is below our MC uncertainties. The bottom-quark mass is renormalized in the $\overline{\text{MS}}$ -scheme with a mass of $\overline{m}_b(\overline{m}_b) = 4.18$ GeV. The Higgs mass was chosen as $m_H = 125.09$ GeV. The results were computed using the PDF4LHC21_40 PDF set. The scale uncertainties are determined with seven-point variation.

Order	$\sigma_{t \times b}$ [pb]	$\sigma_{t \times b}(Y_{b,\overline{\text{MS}}})$ [pb]	$\sigma_{t \times b}/\sigma_{\text{HEFT}}$ [%]
$\sqrt{s} = 7 \text{ TeV}$			
$\mathcal{O}(\alpha_s^2)$	-0.708	-0.439	
LO	$-0.708^{+0.13}_{-0.19}$	$-0.439^{+0.10}_{-0.16}$	-12
$\mathcal{O}(\alpha_s^3)$	-0.226	-0.264	
NLO	$-0.934^{+0.09}_{-0.07}$	$-0.703^{+0.11}_{-0.12}$	$-7.2^{+1.0}_{-0.8}$
$\mathcal{O}(\alpha_s^4)$	+0.121(3)	-0.026(2)	
NNLO	$-0.813(3)^{+0.10}_{-0.04}$	$-0.729(2)^{+0.04}_{-0.01}$	$-5.0^{+1.0}_{-0.8}$
$\sqrt{s} = 8 \text{ TeV}$			
$\mathcal{O}(\alpha_s^2)$	-0.895	-0.554	
LO	$-0.895^{+0.17}_{-0.24}$	$-0.554^{+0.13}_{-0.20}$	-12
$\mathcal{O}(\alpha_s^3)$	-0.268	-0.323	
NLO	$-1.163^{+0.10}_{-0.08}$	$-0.877^{+0.13}_{-0.14}$	$-7.0^{+1.0}_{-0.8}$
$\mathcal{O}(\alpha_s^4)$	+0.167(3)	-0.022(2)	
NNLO	$-0.996(3)^{+0.12}_{-0.05}$	$-0.899(2)^{+0.04}_{-0.02}$	$-4.8^{+0.9}_{-0.8}$
$\sqrt{s} = 13 \text{ TeV}$			
$\mathcal{O}(\alpha_s^2)$	-1.975	-1.223	
LO	$-1.98^{+0.38}_{-0.53}$	$-1.22^{+0.29}_{-0.44}$	-12
$\mathcal{O}(\alpha_s^3)$	-0.446(1)	-0.623(1)	
NLO	$-2.42^{+0.19}_{-0.12}$	$-1.85^{+0.26}_{-0.26}$	$-6.5^{+0.9}_{-0.8}$
$\mathcal{O}(\alpha_s^4)$	+0.434(8)	+0.019(5)	
NNLO	$-1.99(1)^{+0.30}_{-0.15}$	$-1.83(1)^{+0.08}_{-0.03}$	$-4.2^{+0.9}_{-0.8}$
$\sqrt{s} = 13.6 \text{ TeV}$			
$\mathcal{O}(\alpha_s^2)$	-2.117	-1.311	
LO	$-2.12^{+0.40}_{-0.57}$	$-1.31^{+0.31}_{-0.47}$	-12
$\mathcal{O}(\alpha_s^3)$	-0.464(1)	-0.659(1)	
NLO	$-2.58^{+0.20}_{-0.12}$	$-1.97^{+0.28}_{-0.28}$	$-6.4^{+0.9}_{-0.8}$
$\mathcal{O}(\alpha_s^4)$	+0.464(9)	+0.022(6)	
NNLO	$-2.12(1)^{+0.33}_{-0.16}$	$-1.95(1)^{+0.09}_{-0.03}$	$-4.2^{+0.9}_{-0.8}$
$\sqrt{s} = 14 \text{ TeV}$			
$\mathcal{O}(\alpha_s^2)$	-2.213	-1.370	
LO	$-2.21^{+0.42}_{-0.59}$	$-1.37^{+0.32}_{-0.49}$	-12
$\mathcal{O}(\alpha_s^3)$	-0.475(1)	-0.682(1)	
NLO	$-2.69^{+0.21}_{-0.13}$	$-2.05^{+0.29}_{-0.29}$	$-6.4^{+0.9}_{-0.8}$
$\mathcal{O}(\alpha_s^4)$	+0.488(9)	+0.027(6)	
NNLO	$-2.20(1)^{+0.34}_{-0.17}$	$-2.03(1)^{+0.09}_{-0.03}$	$-4.1^{+0.9}_{-0.8}$

Table C.2: Top-bottom interference contribution to the gluon-gluon fusion cross section for top- and bottom-quark masses defined in the OS-scheme, and in a mixed scheme, where the bottom-quark Yukawa coupling is renormalized in the $\overline{\text{MS}}$ -scheme. The results are computed for LHC @ 7,8,13,13.6 and 14 TeV using the computational setup is described in the Conventions. The scale uncertainties are determined with seven-point variation. Numbers in parentheses indicate the MC uncertainties on the last provided digit.

D

ON-SHELL RESULTS FOR THE DIFFERENTIAL CROSS SECTION

Here we present the results for the Higgs-transverse momentum and -rapidity spectra with the bottom-quark mass defined in the OS scheme. Since the relevant discrepancies between the

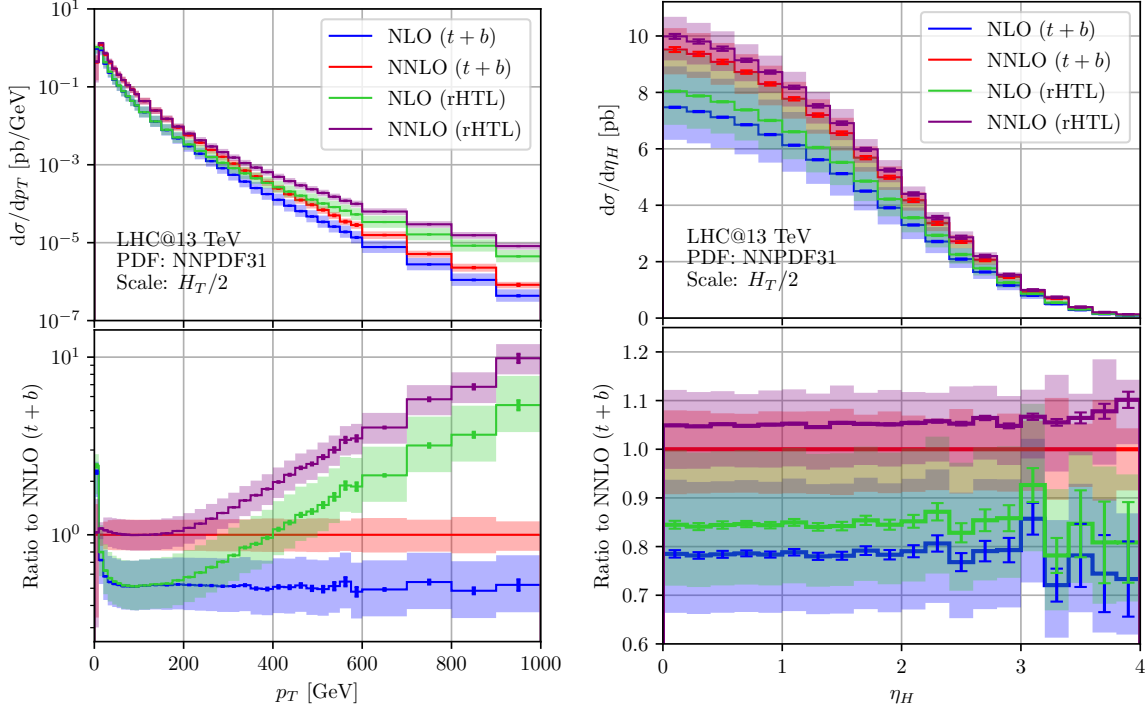


Figure D.1: Same as in Fig. 6.2 but for an OS renormalized bottom-quark mass.

OS and the $\overline{\text{MS}}$ scheme were limited to $p_T < 40$ GeV, and even here the differences were mild, the spectra are effectively identical to the ones presented in Fig. 6.2.

BIBLIOGRAPHY

- [1] Michał Czakon, Felix Eschment, and Tom Schellenberger. “Revisiting the double-soft asymptotics of one-loop amplitudes in massless QCD.” In: *JHEP* 04 (2023), p. 065. DOI: [10.1007/JHEP04\(2023\)065](https://doi.org/10.1007/JHEP04(2023)065). arXiv: [2211.06465 \[hep-ph\]](https://arxiv.org/abs/2211.06465).
- [2] Michał Czakon, Felix Eschment, and Tom Schellenberger. “Subleading effects in soft-gluon emission at one-loop in massless QCD.” In: *JHEP* 12 (2023), p. 126. DOI: [10.1007/JHEP12\(2023\)126](https://doi.org/10.1007/JHEP12(2023)126). arXiv: [2307.02286 \[hep-ph\]](https://arxiv.org/abs/2307.02286).
- [3] Michał Czakon et al. “Top-Bottom Interference Contribution to Fully Inclusive Higgs Production.” In: *Phys. Rev. Lett.* 132.21 (2024), p. 211902. DOI: [10.1103/PhysRevLett.132.211902](https://doi.org/10.1103/PhysRevLett.132.211902). arXiv: [2312.09896 \[hep-ph\]](https://arxiv.org/abs/2312.09896).
- [4] Michał Czakon et al. “Quark mass effects in Higgs production.” In: *JHEP* 10 (2024), p. 210. DOI: [10.1007/JHEP10\(2024\)210](https://doi.org/10.1007/JHEP10(2024)210). arXiv: [2407.12413 \[hep-ph\]](https://arxiv.org/abs/2407.12413).
- [5] Chen-Ning Yang and Robert L. Mills. “Conservation of Isotopic Spin and Isotopic Gauge Invariance.” In: *Phys. Rev.* 96 (1954). Ed. by Jong-Ping Hsu and D. Fine, pp. 191–195. DOI: [10.1103/PhysRev.96.191](https://doi.org/10.1103/PhysRev.96.191).
- [6] Murray Gell-Mann. “The Eightfold Way: A Theory of strong interaction symmetry.” In: (Mar. 1961). DOI: [10.2172/4008239](https://doi.org/10.2172/4008239).
- [7] S. L. Glashow. “Partial Symmetries of Weak Interactions.” In: *Nucl. Phys.* 22 (1961), pp. 579–588. DOI: [10.1016/0029-5582\(61\)90469-2](https://doi.org/10.1016/0029-5582(61)90469-2).
- [8] Abdus Salam and John Clive Ward. “Electromagnetic and weak interactions.” In: *Phys. Lett.* 13 (1964), pp. 168–171. DOI: [10.1016/0031-9163\(64\)90711-5](https://doi.org/10.1016/0031-9163(64)90711-5).
- [9] F. Englert and R. Brout. “Broken Symmetry and the Mass of Gauge Vector Mesons.” In: *Phys. Rev. Lett.* 13 (1964). Ed. by J. C. Taylor, pp. 321–323. DOI: [10.1103/PhysRevLett.13.321](https://doi.org/10.1103/PhysRevLett.13.321).
- [10] Peter W. Higgs. “Spontaneous Symmetry Breakdown without Massless Bosons.” In: *Phys. Rev.* 145 (1966), pp. 1156–1163. DOI: [10.1103/PhysRev.145.1156](https://doi.org/10.1103/PhysRev.145.1156).
- [11] G. S. Guralnik, C. R. Hagen, and T. W. B. Kibble. “Global Conservation Laws and Massless Particles.” In: *Phys. Rev. Lett.* 13 (1964). Ed. by J. C. Taylor, pp. 585–587. DOI: [10.1103/PhysRevLett.13.585](https://doi.org/10.1103/PhysRevLett.13.585).
- [12] Steven Weinberg. “A Model of Leptons.” In: *Phys. Rev. Lett.* 19 (1967), pp. 1264–1266. DOI: [10.1103/PhysRevLett.19.1264](https://doi.org/10.1103/PhysRevLett.19.1264).
- [13] Georges Aad et al. “Observation of a new particle in the search for the Standard Model Higgs boson with the ATLAS detector at the LHC.” In: *Phys. Lett. B* 716 (2012), pp. 1–29. DOI: [10.1016/j.physletb.2012.08.020](https://doi.org/10.1016/j.physletb.2012.08.020). arXiv: [1207.7214 \[hep-ex\]](https://arxiv.org/abs/1207.7214).
- [14] Serguei Chatrchyan et al. “Observation of a New Boson at a Mass of 125 GeV with the CMS Experiment at the LHC.” In: *Phys. Lett. B* 716 (2012), pp. 30–61. DOI: [10.1016/j.physletb.2012.08.021](https://doi.org/10.1016/j.physletb.2012.08.021). arXiv: [1207.7235 \[hep-ex\]](https://arxiv.org/abs/1207.7235).

- [15] M. Aaboud et al. “Search for an invisibly decaying Higgs boson or dark matter candidates produced in association with a Z boson in pp collisions at $\sqrt{s} = 13$ TeV with the ATLAS detector.” In: *Phys. Lett. B* 776 (2018), pp. 318–337. DOI: [10.1016/j.physletb.2017.11.049](https://doi.org/10.1016/j.physletb.2017.11.049). arXiv: [1708.09624 \[hep-ex\]](https://arxiv.org/abs/1708.09624).
- [16] Vardan Khachatryan et al. “Searches for invisible decays of the Higgs boson in pp collisions at $\sqrt{s} = 7, 8,$ and 13 TeV.” In: *JHEP* 02 (2017), p. 135. DOI: [10.1007/JHEP02\(2017\)135](https://doi.org/10.1007/JHEP02(2017)135). arXiv: [1610.09218 \[hep-ex\]](https://arxiv.org/abs/1610.09218).
- [17] Giuseppe Degrassi et al. “Higgs mass and vacuum stability in the Standard Model at NNLO.” In: *JHEP* 08 (2012), p. 098. DOI: [10.1007/JHEP08\(2012\)098](https://doi.org/10.1007/JHEP08(2012)098). arXiv: [1205.6497 \[hep-ph\]](https://arxiv.org/abs/1205.6497).
- [18] H. M. Georgi et al. “Higgs Bosons from Two Gluon Annihilation in Proton Proton Collisions.” In: *Phys. Rev. Lett.* 40 (1978), p. 692. DOI: [10.1103/PhysRevLett.40.692](https://doi.org/10.1103/PhysRevLett.40.692).
- [19] S. Dawson. “Radiative corrections to Higgs boson production.” In: *Nucl. Phys. B* 359 (1991), pp. 283–300. DOI: [10.1016/0550-3213\(91\)90061-2](https://doi.org/10.1016/0550-3213(91)90061-2).
- [20] A. Djouadi, M. Spira, and P. M. Zerwas. “Production of Higgs bosons in proton colliders: QCD corrections.” In: *Phys. Lett. B* 264 (1991), pp. 440–446. DOI: [10.1016/0370-2693\(91\)90375-Z](https://doi.org/10.1016/0370-2693(91)90375-Z).
- [21] Stefano Catani, Daniel de Florian, and Massimiliano Grazzini. “Higgs production in hadron collisions: Soft and virtual QCD corrections at NNLO.” In: *JHEP* 05 (2001), p. 025. DOI: [10.1088/1126-6708/2001/05/025](https://doi.org/10.1088/1126-6708/2001/05/025). arXiv: [hep-ph/0102227](https://arxiv.org/abs/hep-ph/0102227).
- [22] Robert V. Harlander and William B. Kilgore. “Next-to-next-to-leading order Higgs production at hadron colliders.” In: *Phys. Rev. Lett.* 88 (2002), p. 201801. DOI: [10.1103/PhysRevLett.88.201801](https://doi.org/10.1103/PhysRevLett.88.201801). arXiv: [hep-ph/0201206](https://arxiv.org/abs/hep-ph/0201206).
- [23] Charalampos Anastasiou and Kirill Melnikov. “Higgs boson production at hadron colliders in NNLO QCD.” In: *Nucl. Phys. B* 646 (2002), pp. 220–256. DOI: [10.1016/S0550-3213\(02\)00837-4](https://doi.org/10.1016/S0550-3213(02)00837-4). arXiv: [hep-ph/0207004](https://arxiv.org/abs/hep-ph/0207004).
- [24] Charalampos Anastasiou et al. “Higgs Boson Gluon-Fusion Production in QCD at Three Loops.” In: *Phys. Rev. Lett.* 114 (2015), p. 212001. DOI: [10.1103/PhysRevLett.114.212001](https://doi.org/10.1103/PhysRevLett.114.212001). arXiv: [1503.06056 \[hep-ph\]](https://arxiv.org/abs/1503.06056).
- [25] Bernhard Mistlberger. “Higgs boson production at hadron colliders at $N^3\text{LO}$ in QCD.” In: *JHEP* 05 (2018), p. 028. DOI: [10.1007/JHEP05\(2018\)028](https://doi.org/10.1007/JHEP05(2018)028). arXiv: [1802.00833 \[hep-ph\]](https://arxiv.org/abs/1802.00833).
- [26] G. Das, S. Moch, and A. Vogt. “Approximate four-loop QCD corrections to the Higgs-boson production cross section.” In: *Phys. Lett. B* 807 (2020), p. 135546. DOI: [10.1016/j.physletb.2020.135546](https://doi.org/10.1016/j.physletb.2020.135546). arXiv: [2004.00563 \[hep-ph\]](https://arxiv.org/abs/2004.00563).
- [27] U. Aglietti et al. “Two loop light fermion contribution to Higgs production and decays.” In: *Phys. Lett. B* 595 (2004), pp. 432–441. DOI: [10.1016/j.physletb.2004.06.063](https://doi.org/10.1016/j.physletb.2004.06.063). arXiv: [hep-ph/0404071](https://arxiv.org/abs/hep-ph/0404071).
- [28] Giuseppe Degrassi and Fabio Maltoni. “Two-loop electroweak corrections to Higgs production at hadron colliders.” In: *Phys. Lett. B* 600 (2004), pp. 255–260. DOI: [10.1016/j.physletb.2004.09.008](https://doi.org/10.1016/j.physletb.2004.09.008). arXiv: [hep-ph/0407249](https://arxiv.org/abs/hep-ph/0407249).
- [29] Stefano Actis et al. “NNLO Computational Techniques: The Cases $H \rightarrow \gamma\gamma$ and $H \rightarrow gg$.” In: *Nucl. Phys. B* 811 (2009), pp. 182–273. DOI: [10.1016/j.nuclphysb.2008.11.024](https://doi.org/10.1016/j.nuclphysb.2008.11.024). arXiv: [0809.3667 \[hep-ph\]](https://arxiv.org/abs/0809.3667).

- [30] Stefano Actis et al. “NLO Electroweak Corrections to Higgs Boson Production at Hadron Colliders.” In: *Phys. Lett. B* 670 (2008), pp. 12–17. DOI: [10.1016/j.physletb.2008.10.018](https://doi.org/10.1016/j.physletb.2008.10.018). arXiv: [0809.1301 \[hep-ph\]](https://arxiv.org/abs/0809.1301).
- [31] Charalampos Anastasiou, Radja Boughezal, and Frank Petriello. “Mixed QCD-electroweak corrections to Higgs boson production in gluon fusion.” In: *JHEP* 04 (2009), p. 003. DOI: [10.1088/1126-6708/2009/04/003](https://doi.org/10.1088/1126-6708/2009/04/003). arXiv: [0811.3458 \[hep-ph\]](https://arxiv.org/abs/0811.3458).
- [32] Charalampos Anastasiou et al. “Mixed QCD-electroweak corrections to Higgs production via gluon fusion in the small mass approximation.” In: *JHEP* 03 (2019), p. 162. DOI: [10.1007/JHEP03\(2019\)162](https://doi.org/10.1007/JHEP03(2019)162). arXiv: [1811.11211 \[hep-ph\]](https://arxiv.org/abs/1811.11211).
- [33] Marco Bonetti, Kirill Melnikov, and Lorenzo Tancredi. “Higher order corrections to mixed QCD-EW contributions to Higgs boson production in gluon fusion.” In: *Phys. Rev. D* 97.5 (2018). [Erratum: *Phys. Rev. D* 97, 099906 (2018)], p. 056017. DOI: [10.1103/PhysRevD.97.056017](https://doi.org/10.1103/PhysRevD.97.056017). arXiv: [1801.10403 \[hep-ph\]](https://arxiv.org/abs/1801.10403).
- [34] Matteo Bechetti et al. “Next-to-leading order corrections to light-quark mixed QCD-EW contributions to Higgs boson production.” In: *Phys. Rev. D* 103.5 (2021), p. 054037. DOI: [10.1103/PhysRevD.103.054037](https://doi.org/10.1103/PhysRevD.103.054037). arXiv: [2010.09451 \[hep-ph\]](https://arxiv.org/abs/2010.09451).
- [35] M. Czakon et al. “Exact Top-Quark Mass Dependence in Hadronic Higgs Production.” In: *Phys. Rev. Lett.* 127.16 (2021). [Erratum: *Phys. Rev. Lett.* 131, 179901 (2023)], p. 162002. DOI: [10.1103/PhysRevLett.127.162002](https://doi.org/10.1103/PhysRevLett.127.162002). arXiv: [2105.04436 \[hep-ph\]](https://arxiv.org/abs/2105.04436).
- [36] Stefan Weinzierl. *Feynman Integrals. A Comprehensive Treatment for Students and Researchers*. UNITEXT for Physics. Springer, 2022. DOI: [10.1007/978-3-030-99558-4](https://doi.org/10.1007/978-3-030-99558-4). arXiv: [2201.03593 \[hep-th\]](https://arxiv.org/abs/2201.03593).
- [37] Gerard ’t Hooft. “Renormalizable Lagrangians for Massive Yang-Mills Fields.” In: *Nucl. Phys. B* 35 (1971). Ed. by J. C. Taylor, pp. 167–188. DOI: [10.1016/0550-3213\(71\)90139-8](https://doi.org/10.1016/0550-3213(71)90139-8).
- [38] Gerard ’t Hooft and M. J. G. Veltman. “Regularization and Renormalization of Gauge Fields.” In: *Nucl. Phys. B* 44 (1972), pp. 189–213. DOI: [10.1016/0550-3213\(72\)90279-9](https://doi.org/10.1016/0550-3213(72)90279-9).
- [39] Andy Buckley et al. “LHAPDF6: parton density access in the LHC precision era.” In: *Eur. Phys. J. C* 75 (2015), p. 132. DOI: [10.1140/epjc/s10052-015-3318-8](https://doi.org/10.1140/epjc/s10052-015-3318-8). arXiv: [1412.7420 \[hep-ph\]](https://arxiv.org/abs/1412.7420).
- [40] Richard D. Ball et al. “Parton distributions from high-precision collider data.” In: *Eur. Phys. J. C* 77.10 (2017), p. 663. DOI: [10.1140/epjc/s10052-017-5199-5](https://doi.org/10.1140/epjc/s10052-017-5199-5). arXiv: [1706.00428 \[hep-ph\]](https://arxiv.org/abs/1706.00428).
- [41] John C. Collins, Davison E. Soper, and George F. Sterman. “Factorization of Hard Processes in QCD.” In: *Adv. Ser. Direct. High Energy Phys.* 5 (1989), pp. 1–91. DOI: [10.1142/9789814503266_0001](https://doi.org/10.1142/9789814503266_0001). arXiv: [hep-ph/0409313](https://arxiv.org/abs/hep-ph/0409313).
- [42] Yuri L. Dokshitzer. “Calculation of the Structure Functions for Deep Inelastic Scattering and e+ e- Annihilation by Perturbation Theory in Quantum Chromodynamics.” In: *Sov. Phys. JETP* 46 (1977), pp. 641–653.
- [43] V. N. Gribov and L. N. Lipatov. “Deep inelastic e p scattering in perturbation theory.” In: *Sov. J. Nucl. Phys.* 15 (1972), pp. 438–450.
- [44] Guido Altarelli and G. Parisi. “Asymptotic Freedom in Parton Language.” In: *Nucl. Phys. B* 126 (1977), pp. 298–318. DOI: [10.1016/0550-3213\(77\)90384-4](https://doi.org/10.1016/0550-3213(77)90384-4).

- [45] T. Kinoshita and A. Ukawa. “Mass Singularities of Feynman Amplitudes.” In: *Lect. Notes Phys.* 39 (1975). Ed. by Huzihiro Araki, pp. 55–58. DOI: [10.1007/BFb0013300](https://doi.org/10.1007/BFb0013300).
- [46] T. D. Lee and M. Nauenberg. “Degenerate Systems and Mass Singularities.” In: *Phys. Rev.* 133 (1964). Ed. by G. Feinberg, B1549–B1562. DOI: [10.1103/PhysRev.133.B1549](https://doi.org/10.1103/PhysRev.133.B1549).
- [47] Falko Dulat et al. “Higgs-differential cross section at NNLO in dimensional regularisation.” In: *JHEP* 07 (2017), p. 017. DOI: [10.1007/JHEP07\(2017\)017](https://doi.org/10.1007/JHEP07(2017)017). arXiv: [1704.08220 \[hep-ph\]](https://arxiv.org/abs/1704.08220).
- [48] Markus A. Ebert, Bernhard Mistlberger, and Gherardo Vita. “ N -jettiness beam functions at $N^3\text{LO}$.” In: *JHEP* 09 (2020), p. 143. DOI: [10.1007/JHEP09\(2020\)143](https://doi.org/10.1007/JHEP09(2020)143). arXiv: [2006.03056 \[hep-ph\]](https://arxiv.org/abs/2006.03056).
- [49] Daniel Baranowski et al. “Zero-jettiness soft function to third order in perturbative QCD.” In: (Sept. 2024). arXiv: [2409.11042 \[hep-ph\]](https://arxiv.org/abs/2409.11042).
- [50] Daniel Baranowski et al. “Triple real-emission contribution to the zero-jettiness soft function at $\text{N}3\text{LO}$ in QCD.” In: (Dec. 2024). arXiv: [2412.14001 \[hep-ph\]](https://arxiv.org/abs/2412.14001).
- [51] John M. Campbell et al. “The NNLO QCD soft function for 1-jettiness.” In: *Eur. Phys. J. C* 78.3 (2018), p. 234. DOI: [10.1140/epjc/s10052-018-5732-1](https://doi.org/10.1140/epjc/s10052-018-5732-1). arXiv: [1711.09984 \[hep-ph\]](https://arxiv.org/abs/1711.09984).
- [52] Thomas Becher and Guido Bell. “The gluon jet function at two-loop order.” In: *Phys. Lett. B* 695 (2011), pp. 252–258. DOI: [10.1016/j.physletb.2010.11.036](https://doi.org/10.1016/j.physletb.2010.11.036). arXiv: [1008.1936 \[hep-ph\]](https://arxiv.org/abs/1008.1936).
- [53] Thomas Becher and Matthias Neubert. “Toward a NNLO calculation of the anti-B \rightarrow X(s) gamma decay rate with a cut on photon energy. II. Two-loop result for the jet function.” In: *Phys. Lett. B* 637 (2006), pp. 251–259. DOI: [10.1016/j.physletb.2006.04.046](https://doi.org/10.1016/j.physletb.2006.04.046). arXiv: [hep-ph/0603140](https://arxiv.org/abs/hep-ph/0603140).
- [54] Radja Boughezal, Xiaohui Liu, and Frank Petriello. “ N -jettiness soft function at next-to-next-to-leading order.” In: *Phys. Rev. D* 91.9 (2015), p. 094035. DOI: [10.1103/PhysRevD.91.094035](https://doi.org/10.1103/PhysRevD.91.094035). arXiv: [1504.02540 \[hep-ph\]](https://arxiv.org/abs/1504.02540).
- [55] S. Frixione, Z. Kunszt, and A. Signer. “Three jet cross-sections to next-to-leading order.” In: *Nucl. Phys. B* 467 (1996), pp. 399–442. DOI: [10.1016/0550-3213\(96\)00110-1](https://doi.org/10.1016/0550-3213(96)00110-1). arXiv: [hep-ph/9512328](https://arxiv.org/abs/hep-ph/9512328).
- [56] Michał Czakon et al. “Single-jet inclusive rates with exact color at $\mathcal{O}(\alpha_s^4)$.” In: *JHEP* 10 (2019), p. 262. DOI: [10.1007/JHEP10\(2019\)262](https://doi.org/10.1007/JHEP10(2019)262). arXiv: [1907.12911 \[hep-ph\]](https://arxiv.org/abs/1907.12911).
- [57] M. Czakon. “A novel subtraction scheme for double-real radiation at NNLO.” In: *Phys. Lett. B* 693 (2010), pp. 259–268. DOI: [10.1016/j.physletb.2010.08.036](https://doi.org/10.1016/j.physletb.2010.08.036). arXiv: [1005.0274 \[hep-ph\]](https://arxiv.org/abs/1005.0274).
- [58] M. Czakon and D. Heymes. “Four-dimensional formulation of the sector-improved residue subtraction scheme.” In: *Nucl. Phys. B* 890 (2014), pp. 152–227. DOI: [10.1016/j.nuclphysb.2014.11.006](https://doi.org/10.1016/j.nuclphysb.2014.11.006). arXiv: [1408.2500 \[hep-ph\]](https://arxiv.org/abs/1408.2500).
- [59] Izaak Neutelings. *Izaak neutelings*. Mar. 2024. URL: https://tikz.net/sm_particles/.
- [60] Sidney R. Coleman and Erick J. Weinberg. “Radiative Corrections as the Origin of Spontaneous Symmetry Breaking.” In: *Phys. Rev. D* 7 (1973), pp. 1888–1910. DOI: [10.1103/PhysRevD.7.1888](https://doi.org/10.1103/PhysRevD.7.1888).
- [61] R. V. Harlander, S. Y. Klein, and M. Lipp. “FeynGame.” In: *Comput. Phys. Commun.* 256 (2020), p. 107465. DOI: [10.1016/j.cpc.2020.107465](https://doi.org/10.1016/j.cpc.2020.107465). arXiv: [2003.00896 \[physics.ed-ph\]](https://arxiv.org/abs/2003.00896).

- [62] Robert Harlander, Sven Yannick Klein, and Magnus C. Schaaf. “FeynGame-2.1 – Feynman diagrams made easy.” In: *PoS EPS-HEP2023* (2024), p. 657. DOI: [10.22323/1.449.0657](https://doi.org/10.22323/1.449.0657). arXiv: [2401.12778 \[hep-ph\]](https://arxiv.org/abs/2401.12778).
- [63] L. Bündgen et al. “FeynGame 3.0.” In: (Jan. 2025). arXiv: [2501.04651 \[hep-ph\]](https://arxiv.org/abs/2501.04651).
- [64] D. de Florian et al. “Handbook of LHC Higgs Cross Sections: 4. Deciphering the Nature of the Higgs Sector.” In: 2/2017 (Oct. 2016). DOI: [10.23731/CYRM-2017-002](https://doi.org/10.23731/CYRM-2017-002). arXiv: [1610.07922 \[hep-ph\]](https://arxiv.org/abs/1610.07922).
- [65] Armen Tumasyan et al. “A portrait of the Higgs boson by the CMS experiment ten years after the discovery.” In: *Nature* 607.7917 (2022). [Erratum: *Nature* 623, (2023)], pp. 60–68. DOI: [10.1038/s41586-022-04892-x](https://doi.org/10.1038/s41586-022-04892-x). arXiv: [2207.00043 \[hep-ex\]](https://arxiv.org/abs/2207.00043).
- [66] M. Cepeda et al. “Report from Working Group 2: Higgs Physics at the HL-LHC and HE-LHC.” In: *CERN Yellow Rep. Monogr.* 7 (2019). Ed. by Andrea Dainese et al., pp. 221–584. DOI: [10.23731/CYRM-2019-007.221](https://doi.org/10.23731/CYRM-2019-007.221). arXiv: [1902.00134 \[hep-ph\]](https://arxiv.org/abs/1902.00134).
- [67] Michał Czakon and Marco Niggetiedt. “Exact quark-mass dependence of the Higgs-gluon form factor at three loops in QCD.” In: *JHEP* 05 (2020), p. 149. DOI: [10.1007/JHEP05\(2020\)149](https://doi.org/10.1007/JHEP05(2020)149). arXiv: [2001.03008 \[hep-ph\]](https://arxiv.org/abs/2001.03008).
- [68] Tao Liu and Alexander A. Penin. “High-Energy Limit of QCD beyond the Sudakov Approximation.” In: *Phys. Rev. Lett.* 119.26 (2017), p. 262001. DOI: [10.1103/PhysRevLett.119.262001](https://doi.org/10.1103/PhysRevLett.119.262001). arXiv: [1709.01092 \[hep-ph\]](https://arxiv.org/abs/1709.01092).
- [69] Jean Zinn-Justin. “Renormalization of Gauge Theories.” In: *Lect. Notes Phys.* 37 (1975). Ed. by H. Rollnik and K. Dietz, pp. 1–39. DOI: [10.1007/3-540-07160-1_1](https://doi.org/10.1007/3-540-07160-1_1).
- [70] H. Kluberg-Stern and J. B. Zuber. “Ward Identities and Some Clues to the Renormalization of Gauge Invariant Operators.” In: *Phys. Rev. D* 12 (1975), pp. 467–481. DOI: [10.1103/PhysRevD.12.467](https://doi.org/10.1103/PhysRevD.12.467).
- [71] Satish D. Joglekar and Benjamin W. Lee. “General Theory of Renormalization of Gauge Invariant Operators.” In: *Annals Phys.* 97 (1976), p. 160. DOI: [10.1016/0003-4916\(76\)90225-6](https://doi.org/10.1016/0003-4916(76)90225-6).
- [72] Marc Henneaux, Axel Kleinschmidt, and Gustavo Lucena Gómez. “Remarks on Gauge Invariance and First-class Constraints.” In: *Ann. U. Craiova Phys.* 21 (2011), S1–S10.
- [73] David J. Gross and Frank Wilczek. “Ultraviolet Behavior of Nonabelian Gauge Theories.” In: *Phys. Rev. Lett.* 30 (1973). Ed. by J. C. Taylor, pp. 1343–1346. DOI: [10.1103/PhysRevLett.30.1343](https://doi.org/10.1103/PhysRevLett.30.1343).
- [74] H. David Politzer. “Reliable Perturbative Results for Strong Interactions?” In: *Phys. Rev. Lett.* 30 (1973). Ed. by J. C. Taylor, pp. 1346–1349. DOI: [10.1103/PhysRevLett.30.1346](https://doi.org/10.1103/PhysRevLett.30.1346).
- [75] *Proceedings, Colloquium on Renormalization of Yang-Mills Fields, Marseille, June 19-23, 1972.* 1972.
- [76] William E. Caswell. “Asymptotic Behavior of Nonabelian Gauge Theories to Two Loop Order.” In: *Phys. Rev. Lett.* 33 (1974), p. 244. DOI: [10.1103/PhysRevLett.33.244](https://doi.org/10.1103/PhysRevLett.33.244).
- [77] D. R. T. Jones. “Two Loop Diagrams in Yang-Mills Theory.” In: *Nucl. Phys. B* 75 (1974), p. 531. DOI: [10.1016/0550-3213\(74\)90093-5](https://doi.org/10.1016/0550-3213(74)90093-5).
- [78] E. Egorian and O. V. Tarasov. “Two Loop Renormalization of the QCD in an Arbitrary Gauge.” In: *Teor. Mat. Fiz.* 41 (1979), pp. 26–32.

- [79] Bernd A. Kniehl and Michael Spira. “Two loop $O(\alpha_s G(F) m(t)^2)$ correction to the $H \rightarrow b\bar{b}$ decay rate.” In: *Nucl. Phys. B* 432 (1994), pp. 39–48. DOI: [10.1016/0550-3213\(94\)90592-4](https://doi.org/10.1016/0550-3213(94)90592-4). arXiv: [hep-ph/9410319](https://arxiv.org/abs/hep-ph/9410319).
- [80] Bernd A. Kniehl and Michael Spira. “Low-energy theorems in Higgs physics.” In: *Z. Phys. C* 69 (1995), pp. 77–88. DOI: [10.1007/s002880050007](https://doi.org/10.1007/s002880050007). arXiv: [hep-ph/9505225](https://arxiv.org/abs/hep-ph/9505225).
- [81] K. G. Chetyrkin, Bernd A. Kniehl, and M. Steinhauser. “Decoupling relations to $O(\alpha_s^{**3})$ and their connection to low-energy theorems.” In: *Nucl. Phys. B* 510 (1998), pp. 61–87. DOI: [10.1016/S0550-3213\(97\)00649-4](https://doi.org/10.1016/S0550-3213(97)00649-4). arXiv: [hep-ph/9708255](https://arxiv.org/abs/hep-ph/9708255).
- [82] Thomas Appelquist and J. Carazzone. “Infrared Singularities and Massive Fields.” In: *Phys. Rev. D* 11 (1975), p. 2856. DOI: [10.1103/PhysRevD.11.2856](https://doi.org/10.1103/PhysRevD.11.2856).
- [83] K. G. Chetyrkin, Bernd A. Kniehl, and M. Steinhauser. “Strong coupling constant with flavor thresholds at four loops in the MS scheme.” In: *Phys. Rev. Lett.* 79 (1997), pp. 2184–2187. DOI: [10.1103/PhysRevLett.79.2184](https://doi.org/10.1103/PhysRevLett.79.2184). arXiv: [hep-ph/9706430](https://arxiv.org/abs/hep-ph/9706430).
- [84] Y. Schroder and M. Steinhauser. “Four-loop decoupling relations for the strong coupling.” In: *JHEP* 01 (2006), p. 051. DOI: [10.1088/1126-6708/2006/01/051](https://doi.org/10.1088/1126-6708/2006/01/051). arXiv: [hep-ph/0512058](https://arxiv.org/abs/hep-ph/0512058).
- [85] K. G. Chetyrkin, Johann H. Kuhn, and Christian Sturm. “QCD decoupling at four loops.” In: *Nucl. Phys. B* 744 (2006), pp. 121–135. DOI: [10.1016/j.nuclphysb.2006.03.020](https://doi.org/10.1016/j.nuclphysb.2006.03.020). arXiv: [hep-ph/0512060](https://arxiv.org/abs/hep-ph/0512060).
- [86] Charalampos Anastasiou et al. “High precision determination of the gluon fusion Higgs boson cross-section at the LHC.” In: *JHEP* 05 (2016), p. 058. DOI: [10.1007/JHEP05\(2016\)058](https://doi.org/10.1007/JHEP05(2016)058). arXiv: [1602.00695 \[hep-ph\]](https://arxiv.org/abs/1602.00695).
- [87] S. Catani and M. H. Seymour. “A General algorithm for calculating jet cross-sections in NLO QCD.” In: *Nucl. Phys. B* 485 (1997). [Erratum: Nucl.Phys.B 510, 503–504 (1998)], pp. 291–419. DOI: [10.1016/S0550-3213\(96\)00589-5](https://doi.org/10.1016/S0550-3213(96)00589-5). arXiv: [hep-ph/9605323](https://arxiv.org/abs/hep-ph/9605323).
- [88] Valentin Ahrens et al. “Origin of the Large Perturbative Corrections to Higgs Production at Hadron Colliders.” In: *Phys. Rev. D* 79 (2009), p. 033013. DOI: [10.1103/PhysRevD.79.033013](https://doi.org/10.1103/PhysRevD.79.033013). arXiv: [0808.3008 \[hep-ph\]](https://arxiv.org/abs/0808.3008).
- [89] Charalampos Anastasiou et al. “Higgs Boson GluonFfusion Production Beyond Threshold in N^3LO QCD.” In: *JHEP* 03 (2015), p. 091. DOI: [10.1007/JHEP03\(2015\)091](https://doi.org/10.1007/JHEP03(2015)091). arXiv: [1411.3584 \[hep-ph\]](https://arxiv.org/abs/1411.3584).
- [90] Charalampos Anastasiou et al. “Higgs boson gluon–fusion production at threshold in N^3LO QCD.” In: *Phys. Lett. B* 737 (2014), pp. 325–328. DOI: [10.1016/j.physletb.2014.08.067](https://doi.org/10.1016/j.physletb.2014.08.067). arXiv: [1403.4616 \[hep-ph\]](https://arxiv.org/abs/1403.4616).
- [91] Robert V. Harlander, Stefan Liebler, and Hendrik Mantler. “SusHi: A program for the calculation of Higgs production in gluon fusion and bottom-quark annihilation in the Standard Model and the MSSM.” In: *Comput. Phys. Commun.* 184 (2013), pp. 1605–1617. DOI: [10.1016/j.cpc.2013.02.006](https://doi.org/10.1016/j.cpc.2013.02.006). arXiv: [1212.3249 \[hep-ph\]](https://arxiv.org/abs/1212.3249).
- [92] Robert V. Harlander, Stefan Liebler, and Hendrik Mantler. “SusHi Bento: Beyond NNLO and the heavy-top limit.” In: *Comput. Phys. Commun.* 212 (2017), pp. 239–257. DOI: [10.1016/j.cpc.2016.10.015](https://doi.org/10.1016/j.cpc.2016.10.015). arXiv: [1605.03190 \[hep-ph\]](https://arxiv.org/abs/1605.03190).
- [93] Stefano Catani et al. “Soft gluon resummation for Higgs boson production at hadron colliders.” In: *JHEP* 07 (2003), p. 028. DOI: [10.1088/1126-6708/2003/07/028](https://doi.org/10.1088/1126-6708/2003/07/028). arXiv: [hep-ph/0306211](https://arxiv.org/abs/hep-ph/0306211).

- [94] George F. Sterman. “Summation of Large Corrections to Short Distance Hadronic Cross-Sections.” In: *Nucl. Phys. B* 281 (1987), pp. 310–364. DOI: [10.1016/0550-3213\(87\)90258-6](https://doi.org/10.1016/0550-3213(87)90258-6).
- [95] S. Catani and L. Trentadue. “Resummation of the QCD Perturbative Series for Hard Processes.” In: *Nucl. Phys. B* 327 (1989), pp. 323–352. DOI: [10.1016/0550-3213\(89\)90273-3](https://doi.org/10.1016/0550-3213(89)90273-3).
- [96] S. Catani and L. Trentadue. “Comment on QCD exponentiation at large x.” In: *Nucl. Phys. B* 353 (1991), pp. 183–186. DOI: [10.1016/0550-3213\(91\)90506-S](https://doi.org/10.1016/0550-3213(91)90506-S).
- [97] Andreas von Manteuffel, Erik Panzer, and Robert M. Schabinger. “Cusp and collinear anomalous dimensions in four-loop QCD from form factors.” In: *Phys. Rev. Lett.* 124.16 (2020), p. 162001. DOI: [10.1103/PhysRevLett.124.162001](https://doi.org/10.1103/PhysRevLett.124.162001). arXiv: [2002.04617 \[hep-ph\]](https://arxiv.org/abs/2002.04617).
- [98] Christian W. Bauer, Dan Pirjol, and Iain W. Stewart. “Soft collinear factorization in effective field theory.” In: *Phys. Rev. D* 65 (2002), p. 054022. DOI: [10.1103/PhysRevD.65.054022](https://doi.org/10.1103/PhysRevD.65.054022). arXiv: [hep-ph/0109045](https://arxiv.org/abs/hep-ph/0109045).
- [99] Christian W. Bauer et al. “Hard scattering factorization from effective field theory.” In: *Phys. Rev. D* 66 (2002), p. 014017. DOI: [10.1103/PhysRevD.66.014017](https://doi.org/10.1103/PhysRevD.66.014017). arXiv: [hep-ph/0202088](https://arxiv.org/abs/hep-ph/0202088).
- [100] J. A. M. Vermaseren, A. Vogt, and S. Moch. “The Third-order QCD corrections to deep-inelastic scattering by photon exchange.” In: *Nucl. Phys. B* 724 (2005), pp. 3–182. DOI: [10.1016/j.nuclphysb.2005.06.020](https://doi.org/10.1016/j.nuclphysb.2005.06.020). arXiv: [hep-ph/0504242](https://arxiv.org/abs/hep-ph/0504242).
- [101] S. Moch, J. A. M. Vermaseren, and A. Vogt. “The Longitudinal structure function at the third order.” In: *Phys. Lett. B* 606 (2005), pp. 123–129. DOI: [10.1016/j.physletb.2004.11.063](https://doi.org/10.1016/j.physletb.2004.11.063). arXiv: [hep-ph/0411112](https://arxiv.org/abs/hep-ph/0411112).
- [102] S. Moch, M. Rogal, and A. Vogt. “Differences between charged-current coefficient functions.” In: *Nucl. Phys. B* 790 (2008), pp. 317–335. DOI: [10.1016/j.nuclphysb.2007.09.022](https://doi.org/10.1016/j.nuclphysb.2007.09.022). arXiv: [0708.3731 \[hep-ph\]](https://arxiv.org/abs/0708.3731).
- [103] S. Moch, J. A. M. Vermaseren, and A. Vogt. “Third-order QCD corrections to the charged-current structure function $F(3)$.” In: *Nucl. Phys. B* 813 (2009), pp. 220–258. DOI: [10.1016/j.nuclphysb.2009.01.001](https://doi.org/10.1016/j.nuclphysb.2009.01.001). arXiv: [0812.4168 \[hep-ph\]](https://arxiv.org/abs/0812.4168).
- [104] J. Davies et al. “Non-singlet coefficient functions for charged-current deep-inelastic scattering to the third order in QCD.” In: *PoS DIS2016* (2016), p. 059. DOI: [10.22323/1.265.0059](https://doi.org/10.22323/1.265.0059). arXiv: [1606.08907 \[hep-ph\]](https://arxiv.org/abs/1606.08907).
- [105] J. Blümlein et al. “The massless three-loop Wilson coefficients for the deep-inelastic structure functions F_2 , F_L , xF_3 and g_1 .” In: *JHEP* 11 (2022), p. 156. DOI: [10.1007/JHEP11\(2022\)156](https://doi.org/10.1007/JHEP11(2022)156). arXiv: [2208.14325 \[hep-ph\]](https://arxiv.org/abs/2208.14325).
- [106] H. Kawamura et al. “On the next-to-next-to-leading order QCD corrections to heavy-quark production in deep-inelastic scattering.” In: *Nucl. Phys. B* 864 (2012), pp. 399–468. DOI: [10.1016/j.nuclphysb.2012.07.001](https://doi.org/10.1016/j.nuclphysb.2012.07.001). arXiv: [1205.5727 \[hep-ph\]](https://arxiv.org/abs/1205.5727).
- [107] Niccolò Laurenti. “Construction of a next-to-next-to-next-to-leading order approximation for heavy flavour production in deep inelastic scattering with quark masses.” In: (Jan. 2024). arXiv: [2401.12139 \[hep-ph\]](https://arxiv.org/abs/2401.12139).
- [108] Julien Baglio et al. “Inclusive production cross sections at N^3LO .” In: *JHEP* 12 (2022), p. 066. DOI: [10.1007/JHEP12\(2022\)066](https://doi.org/10.1007/JHEP12(2022)066). arXiv: [2209.06138 \[hep-ph\]](https://arxiv.org/abs/2209.06138).

- [109] Claude Duhr, Falko Dulat, and Bernhard Mistlberger. “Charged current Drell-Yan production at N³LO.” In: *JHEP* 11 (2020), p. 143. DOI: [10.1007/JHEP11\(2020\)143](https://doi.org/10.1007/JHEP11(2020)143). arXiv: [2007.13313 \[hep-ph\]](https://arxiv.org/abs/2007.13313).
- [110] Claude Duhr and Bernhard Mistlberger. “Lepton-pair production at hadron colliders at N³LO in QCD.” In: *JHEP* 03 (2022), p. 116. DOI: [10.1007/JHEP03\(2022\)116](https://doi.org/10.1007/JHEP03(2022)116). arXiv: [2111.10379 \[hep-ph\]](https://arxiv.org/abs/2111.10379).
- [111] Xuan Chen et al. “Dilepton Rapidity Distribution in Drell-Yan Production to Third Order in QCD.” In: *Phys. Rev. Lett.* 128.5 (2022), p. 052001. DOI: [10.1103/PhysRevLett.128.052001](https://doi.org/10.1103/PhysRevLett.128.052001). arXiv: [2107.09085 \[hep-ph\]](https://arxiv.org/abs/2107.09085).
- [112] Xuan Chen et al. “Transverse mass distribution and charge asymmetry in W boson production to third order in QCD.” In: *Phys. Lett. B* 840 (2023), p. 137876. DOI: [10.1016/j.physletb.2023.137876](https://doi.org/10.1016/j.physletb.2023.137876). arXiv: [2205.11426 \[hep-ph\]](https://arxiv.org/abs/2205.11426).
- [113] S. Moch et al. “Four-Loop Non-Singlet Splitting Functions in the Planar Limit and Beyond.” In: *JHEP* 10 (2017), p. 041. DOI: [10.1007/JHEP10\(2017\)041](https://doi.org/10.1007/JHEP10(2017)041). arXiv: [1707.08315 \[hep-ph\]](https://arxiv.org/abs/1707.08315).
- [114] S. Moch et al. “Low moments of the four-loop splitting functions in QCD.” In: *Phys. Lett. B* 825 (2022), p. 136853. DOI: [10.1016/j.physletb.2021.136853](https://doi.org/10.1016/j.physletb.2021.136853). arXiv: [2111.15561 \[hep-ph\]](https://arxiv.org/abs/2111.15561).
- [115] J. Davies et al. “Large-nf contributions to the four-loop splitting functions in QCD.” In: *Nucl. Phys. B* 915 (2017), pp. 335–362. DOI: [10.1016/j.nuclphysb.2016.12.012](https://doi.org/10.1016/j.nuclphysb.2016.12.012). arXiv: [1610.07477 \[hep-ph\]](https://arxiv.org/abs/1610.07477).
- [116] G. Falcioni et al. “The double fermionic contribution to the four-loop quark-to-gluon splitting function.” In: *Phys. Lett. B* 848 (2024), p. 138351. DOI: [10.1016/j.physletb.2023.138351](https://doi.org/10.1016/j.physletb.2023.138351). arXiv: [2310.01245 \[hep-ph\]](https://arxiv.org/abs/2310.01245).
- [117] Thomas Gehrmann et al. “Complete N_f^2 contributions to four-loop pure-singlet splitting functions.” In: *JHEP* 01 (2024), p. 029. DOI: [10.1007/JHEP01\(2024\)029](https://doi.org/10.1007/JHEP01(2024)029). arXiv: [2308.07958 \[hep-ph\]](https://arxiv.org/abs/2308.07958).
- [118] G. Falcioni et al. “Four-loop splitting functions in QCD – The quark-quark case.” In: *Phys. Lett. B* 842 (2023), p. 137944. DOI: [10.1016/j.physletb.2023.137944](https://doi.org/10.1016/j.physletb.2023.137944). arXiv: [2302.07593 \[hep-ph\]](https://arxiv.org/abs/2302.07593).
- [119] Thomas Gehrmann et al. “The NfCF3 contribution to the non-singlet splitting function at four-loop order.” In: *Phys. Lett. B* 849 (2024), p. 138427. DOI: [10.1016/j.physletb.2023.138427](https://doi.org/10.1016/j.physletb.2023.138427). arXiv: [2310.12240 \[hep-ph\]](https://arxiv.org/abs/2310.12240).
- [120] T. Jaroszewicz. “Gluonic Regge Singularities and Anomalous Dimensions in QCD.” In: *Phys. Lett. B* 116 (1982), pp. 291–294. DOI: [10.1016/0370-2693\(82\)90345-8](https://doi.org/10.1016/0370-2693(82)90345-8).
- [121] Richard D. Ball and Stefano Forte. “Summation of leading logarithms at small x.” In: *Phys. Lett. B* 351 (1995), pp. 313–324. DOI: [10.1016/0370-2693\(95\)00395-2](https://doi.org/10.1016/0370-2693(95)00395-2). arXiv: [hep-ph/9501231](https://arxiv.org/abs/hep-ph/9501231).
- [122] Richard D. Ball and Stefano Forte. “The Small x behavior of Altarelli-Parisi splitting functions.” In: *Phys. Lett. B* 465 (1999), pp. 271–281. DOI: [10.1016/S0370-2693\(99\)01013-8](https://doi.org/10.1016/S0370-2693(99)01013-8). arXiv: [hep-ph/9906222](https://arxiv.org/abs/hep-ph/9906222).
- [123] Marco Bonvini and Simone Marzani. “Four-loop splitting functions at small x.” In: *JHEP* 06 (2018), p. 145. DOI: [10.1007/JHEP06\(2018\)145](https://doi.org/10.1007/JHEP06(2018)145). arXiv: [1805.06460 \[hep-ph\]](https://arxiv.org/abs/1805.06460).
- [124] Xin Guan et al. “Splitting amplitudes at N³LO in QCD.” In: *JHEP* 01 (2025), p. 090. DOI: [10.1007/JHEP01\(2025\)090](https://doi.org/10.1007/JHEP01(2025)090). arXiv: [2408.03019 \[hep-ph\]](https://arxiv.org/abs/2408.03019).

- [125] J. McGowan et al. “Approximate N³LO parton distribution functions with theoretical uncertainties: MSHT20aN³LO PDFs.” In: *Eur. Phys. J. C* 83.3 (2023). [Erratum: Eur.Phys.J.C 83, 302 (2023)], p. 185. DOI: [10.1140/epjc/s10052-023-11236-0](https://doi.org/10.1140/epjc/s10052-023-11236-0). arXiv: [2207.04739 \[hep-ph\]](https://arxiv.org/abs/2207.04739).
- [126] Richard D. Ball et al. “The path to N³LO parton distributions.” In: *Eur. Phys. J. C* 84.7 (2024), p. 659. DOI: [10.1140/epjc/s10052-024-12891-7](https://doi.org/10.1140/epjc/s10052-024-12891-7). arXiv: [2402.18635 \[hep-ph\]](https://arxiv.org/abs/2402.18635).
- [127] Thomas Cridge et al. “Combination of aN³LO PDFs and implications for Higgs production cross-sections at the LHC.” In: (Nov. 2024). arXiv: [2411.05373 \[hep-ph\]](https://arxiv.org/abs/2411.05373).
- [128] Falko Dulat, Achilleas Lazopoulos, and Bernhard Mistlberger. “iHixs 2 — Inclusive Higgs cross sections.” In: *Comput. Phys. Commun.* 233 (2018), pp. 243–260. DOI: [10.1016/j.cpc.2018.06.025](https://doi.org/10.1016/j.cpc.2018.06.025). arXiv: [1802.00827 \[hep-ph\]](https://arxiv.org/abs/1802.00827).
- [129] D. Graudenz, M. Spira, and P. M. Zerwas. “QCD corrections to Higgs boson production at proton proton colliders.” In: *Phys. Rev. Lett.* 70 (1993), pp. 1372–1375. DOI: [10.1103/PhysRevLett.70.1372](https://doi.org/10.1103/PhysRevLett.70.1372).
- [130] Robert V. Harlander and Kemal J. Ozeren. “Finite top mass effects for hadronic Higgs production at next-to-next-to-leading order.” In: *JHEP* 11 (2009), p. 088. DOI: [10.1088/1126-6708/2009/11/088](https://doi.org/10.1088/1126-6708/2009/11/088). arXiv: [0909.3420 \[hep-ph\]](https://arxiv.org/abs/0909.3420).
- [131] Robert V. Harlander et al. “Higgs production in gluon fusion at next-to-next-to-leading order QCD for finite top mass.” In: *Eur. Phys. J. C* 66 (2010), pp. 359–372. DOI: [10.1140/epjc/s10052-010-1258-x](https://doi.org/10.1140/epjc/s10052-010-1258-x). arXiv: [0912.2104 \[hep-ph\]](https://arxiv.org/abs/0912.2104).
- [132] Alexey Pak, Mikhail Rogal, and Matthias Steinhauser. “Finite top quark mass effects in NNLO Higgs boson production at LHC.” In: *JHEP* 02 (2010), p. 025. DOI: [10.1007/JHEP02\(2010\)025](https://doi.org/10.1007/JHEP02(2010)025). arXiv: [0911.4662 \[hep-ph\]](https://arxiv.org/abs/0911.4662).
- [133] Peter Marquard et al. “Quark Mass Relations to Four-Loop Order in Perturbative QCD.” In: *Phys. Rev. Lett.* 114.14 (2015), p. 142002. DOI: [10.1103/PhysRevLett.114.142002](https://doi.org/10.1103/PhysRevLett.114.142002). arXiv: [1502.01030 \[hep-ph\]](https://arxiv.org/abs/1502.01030).
- [134] Peter Marquard et al. “Four-loop relation between the \overline{MS} and on-shell quark mass.” In: *PoS RADCOR2015* (2016), p. 094. DOI: [10.22323/1.235.0094](https://doi.org/10.22323/1.235.0094). arXiv: [1601.03748 \[hep-ph\]](https://arxiv.org/abs/1601.03748).
- [135] X. Chen et al. “Precise QCD predictions for the production of Higgs + jet final states.” In: *Phys. Lett. B* 740 (2015), pp. 147–150. DOI: [10.1016/j.physletb.2014.11.021](https://doi.org/10.1016/j.physletb.2014.11.021). arXiv: [1408.5325 \[hep-ph\]](https://arxiv.org/abs/1408.5325).
- [136] Kathrin Becker et al. “Precise predictions for boosted Higgs production.” In: *SciPost Phys. Core* 7 (2024), p. 001. DOI: [10.21468/SciPostPhysCore.7.1.001](https://doi.org/10.21468/SciPostPhysCore.7.1.001). arXiv: [2005.07762 \[hep-ph\]](https://arxiv.org/abs/2005.07762).
- [137] X. Chen et al. “Fully Differential Higgs Boson Production to Third Order in QCD.” In: *Phys. Rev. Lett.* 127.7 (2021), p. 072002. DOI: [10.1103/PhysRevLett.127.072002](https://doi.org/10.1103/PhysRevLett.127.072002). arXiv: [2102.07607 \[hep-ph\]](https://arxiv.org/abs/2102.07607).
- [138] Xuan Chen et al. “NNLO QCD Corrections for Higgs-plus-jet Production in the Four-lepton Decay Mode.” In: *PoS RADCOR2019* (2019), p. 003. DOI: [10.22323/1.375.0003](https://doi.org/10.22323/1.375.0003). arXiv: [1912.03560 \[hep-ph\]](https://arxiv.org/abs/1912.03560).
- [139] Massimiliano Grazzini and Hayk Sargsyan. “Heavy-quark mass effects in Higgs boson production at the LHC.” In: *JHEP* 09 (2013), p. 129. DOI: [10.1007/JHEP09\(2013\)129](https://doi.org/10.1007/JHEP09(2013)129). arXiv: [1306.4581 \[hep-ph\]](https://arxiv.org/abs/1306.4581).

- [140] Malte Buschmann et al. “Mass Effects in the Higgs-Gluon Coupling: Boosted vs Off-Shell Production.” In: *JHEP* 02 (2015), p. 038. DOI: [10.1007/JHEP02\(2015\)038](https://doi.org/10.1007/JHEP02(2015)038). arXiv: [1410.5806 \[hep-ph\]](https://arxiv.org/abs/1410.5806).
- [141] S. P. Jones, M. Kerner, and G. Luisoni. “Next-to-Leading-Order QCD Corrections to Higgs Boson Plus Jet Production with Full Top-Quark Mass Dependence.” In: *Phys. Rev. Lett.* 120.16 (2018). [Erratum: *Phys. Rev. Lett.* 128, 059901 (2022)], p. 162001. DOI: [10.1103/PhysRevLett.120.162001](https://doi.org/10.1103/PhysRevLett.120.162001). arXiv: [1802.00349 \[hep-ph\]](https://arxiv.org/abs/1802.00349).
- [142] Fady Bishara et al. “Constraining Light-Quark Yukawa Couplings from Higgs Distributions.” In: *Phys. Rev. Lett.* 118.12 (2017), p. 121801. DOI: [10.1103/PhysRevLett.118.121801](https://doi.org/10.1103/PhysRevLett.118.121801). arXiv: [1606.09253 \[hep-ph\]](https://arxiv.org/abs/1606.09253).
- [143] Gage Bonner and Heather E. Logan. “Constraining the Higgs couplings to up and down quarks using production kinematics at the CERN Large Hadron Collider.” In: (Aug. 2016). arXiv: [1608.04376 \[hep-ph\]](https://arxiv.org/abs/1608.04376).
- [144] Albert M Sirunyan et al. “Measurement and interpretation of differential cross sections for Higgs boson production at $\sqrt{s} = 13$ TeV.” In: *Phys. Lett. B* 792 (2019), pp. 369–396. DOI: [10.1016/j.physletb.2019.03.059](https://doi.org/10.1016/j.physletb.2019.03.059). arXiv: [1812.06504 \[hep-ex\]](https://arxiv.org/abs/1812.06504).
- [145] Vladimir Chekhovsky et al. “Combination and interpretation of differential Higgs boson production cross sections in proton-proton collisions at $\sqrt{s} = 13$ TeV.” In: (Apr. 2025). arXiv: [2504.13081 \[hep-ex\]](https://arxiv.org/abs/2504.13081).
- [146] Jonas M. Lindert et al. “Top-bottom interference effects in Higgs plus jet production at the LHC.” In: *Phys. Rev. Lett.* 118.25 (2017), p. 252002. DOI: [10.1103/PhysRevLett.118.252002](https://doi.org/10.1103/PhysRevLett.118.252002). arXiv: [1703.03886 \[hep-ph\]](https://arxiv.org/abs/1703.03886).
- [147] Fabrizio Caola et al. “Bottom-quark effects in Higgs production at intermediate transverse momentum.” In: *JHEP* 09 (2018), p. 035. DOI: [10.1007/JHEP09\(2018\)035](https://doi.org/10.1007/JHEP09(2018)035). arXiv: [1804.07632 \[hep-ph\]](https://arxiv.org/abs/1804.07632).
- [148] Roberto Bonciani et al. “Next-to-leading-order QCD corrections to Higgs production in association with a jet.” In: *Phys. Lett. B* 843 (2023), p. 137995. DOI: [10.1016/j.physletb.2023.137995](https://doi.org/10.1016/j.physletb.2023.137995). arXiv: [2206.10490 \[hep-ph\]](https://arxiv.org/abs/2206.10490).
- [149] Hendrik Mantler and Marius Wiesemann. “Top- and bottom-mass effects in hadronic Higgs production at small transverse momenta through LO+NLL.” In: *Eur. Phys. J. C* 73.6 (2013), p. 2467. DOI: [10.1140/epjc/s10052-013-2467-x](https://doi.org/10.1140/epjc/s10052-013-2467-x). arXiv: [1210.8263 \[hep-ph\]](https://arxiv.org/abs/1210.8263).
- [150] Keith Hamilton, Paolo Nason, and Giulia Zanderighi. “Finite quark-mass effects in the NNLOPS POWHEG+MiNLO Higgs generator.” In: *JHEP* 05 (2015), p. 140. DOI: [10.1007/JHEP05\(2015\)140](https://doi.org/10.1007/JHEP05(2015)140). arXiv: [1501.04637 \[hep-ph\]](https://arxiv.org/abs/1501.04637).
- [151] Emanuele Bagnaschi and Alessandro Vicini. “The Higgs transverse momentum distribution in gluon fusion as a multiscale problem.” In: *JHEP* 01 (2016), p. 056. DOI: [10.1007/JHEP01\(2016\)056](https://doi.org/10.1007/JHEP01(2016)056). arXiv: [1505.00735 \[hep-ph\]](https://arxiv.org/abs/1505.00735).
- [152] Emanuele Bagnaschi et al. “Resummation ambiguities in the Higgs transverse-momentum spectrum in the Standard Model and beyond.” In: *JHEP* 01 (2016), p. 090. DOI: [10.1007/JHEP01\(2016\)090](https://doi.org/10.1007/JHEP01(2016)090). arXiv: [1510.08850 \[hep-ph\]](https://arxiv.org/abs/1510.08850).
- [153] Rikkert Frederix et al. “Heavy-quark mass effects in Higgs plus jets production.” In: *JHEP* 08 (2016), p. 006. DOI: [10.1007/JHEP08\(2016\)006](https://doi.org/10.1007/JHEP08(2016)006). arXiv: [1604.03017 \[hep-ph\]](https://arxiv.org/abs/1604.03017).

- [154] Fabrizio Caola et al. “The Higgs transverse momentum spectrum with finite quark masses beyond leading order.” In: *JHEP* 08 (2016), p. 150. DOI: [10.1007/JHEP08\(2016\)150](https://doi.org/10.1007/JHEP08(2016)150). arXiv: [1606.04100 \[hep-ph\]](https://arxiv.org/abs/1606.04100).
- [155] Marco Niggetiedt and Marius Wiesemann. “Higgs-boson production in the full theory at NNLO+PS.” In: *Phys. Lett. B* 858 (2024), p. 139043. DOI: [10.1016/j.physletb.2024.139043](https://doi.org/10.1016/j.physletb.2024.139043). arXiv: [2407.01354 \[hep-ph\]](https://arxiv.org/abs/2407.01354).
- [156] Falko Dulat, Bernhard Mistlberger, and Andrea Pelloni. “Precision predictions at $N^3\text{LO}$ for the Higgs boson rapidity distribution at the LHC.” In: *Phys. Rev. D* 99.3 (2019), p. 034004. DOI: [10.1103/PhysRevD.99.034004](https://doi.org/10.1103/PhysRevD.99.034004). arXiv: [1810.09462 \[hep-ph\]](https://arxiv.org/abs/1810.09462).
- [157] Falko Dulat, Bernhard Mistlberger, and Andrea Pelloni. “Differential Higgs production at $N^3\text{LO}$ beyond threshold.” In: *JHEP* 01 (2018), p. 145. DOI: [10.1007/JHEP01\(2018\)145](https://doi.org/10.1007/JHEP01(2018)145). arXiv: [1710.03016 \[hep-ph\]](https://arxiv.org/abs/1710.03016).
- [158] Stefano Actis et al. “RECOLA: REcursive Computation of One-Loop Amplitudes.” In: *Comput. Phys. Commun.* 214 (2017), pp. 140–173. DOI: [10.1016/j.cpc.2017.01.004](https://doi.org/10.1016/j.cpc.2017.01.004). arXiv: [1605.01090 \[hep-ph\]](https://arxiv.org/abs/1605.01090).
- [159] Lucy Budge et al. “The one-loop amplitudes for Higgs + 4 partons with full mass effects.” In: *JHEP* 05 (2020), p. 079. DOI: [10.1007/JHEP05\(2020\)079](https://doi.org/10.1007/JHEP05(2020)079). arXiv: [2002.04018 \[hep-ph\]](https://arxiv.org/abs/2002.04018).
- [160] John Campbell and Tobias Neumann. “Precision Phenomenology with MCFM.” In: *JHEP* 12 (2019), p. 034. DOI: [10.1007/JHEP12\(2019\)034](https://doi.org/10.1007/JHEP12(2019)034). arXiv: [1909.09117 \[hep-ph\]](https://arxiv.org/abs/1909.09117).
- [161] John M. Campbell and R. Keith Ellis. “An Update on vector boson pair production at hadron colliders.” In: *Phys. Rev. D* 60 (1999), p. 113006. DOI: [10.1103/PhysRevD.60.113006](https://doi.org/10.1103/PhysRevD.60.113006). arXiv: [hep-ph/9905386](https://arxiv.org/abs/hep-ph/9905386).
- [162] John M. Campbell, R. Keith Ellis, and Ciaran Williams. “Vector Boson Pair Production at the LHC.” In: *JHEP* 07 (2011), p. 018. DOI: [10.1007/JHEP07\(2011\)018](https://doi.org/10.1007/JHEP07(2011)018). arXiv: [1105.0020 \[hep-ph\]](https://arxiv.org/abs/1105.0020).
- [163] R. Keith Ellis and Giulia Zanderighi. “Scalar one-loop integrals for QCD.” In: *JHEP* 02 (2008), p. 002. DOI: [10.1088/1126-6708/2008/02/002](https://doi.org/10.1088/1126-6708/2008/02/002). arXiv: [0712.1851 \[hep-ph\]](https://arxiv.org/abs/0712.1851).
- [164] Stefano Carrazza, R. Keith Ellis, and Giulia Zanderighi. “QCDLoop: a comprehensive framework for one-loop scalar integrals.” In: *Comput. Phys. Commun.* 209 (2016), pp. 134–143. DOI: [10.1016/j.cpc.2016.07.033](https://doi.org/10.1016/j.cpc.2016.07.033). arXiv: [1605.03181 \[hep-ph\]](https://arxiv.org/abs/1605.03181).
- [165] Kirill Melnikov, Lorenzo Tancredi, and Christopher Wever. “Two-loop $gg \rightarrow Hg$ amplitude mediated by a nearly massless quark.” In: *JHEP* 11 (2016), p. 104. DOI: [10.1007/JHEP11\(2016\)104](https://doi.org/10.1007/JHEP11(2016)104). arXiv: [1610.03747 \[hep-ph\]](https://arxiv.org/abs/1610.03747).
- [166] Kirill Melnikov, Lorenzo Tancredi, and Christopher Wever. “Two-loop amplitudes for $qg \rightarrow Hq$ and $q\bar{q} \rightarrow Hg$ mediated by a nearly massless quark.” In: *Phys. Rev. D* 95.5 (2017), p. 054012. DOI: [10.1103/PhysRevD.95.054012](https://doi.org/10.1103/PhysRevD.95.054012). arXiv: [1702.00426 \[hep-ph\]](https://arxiv.org/abs/1702.00426).
- [167] Lance J. Dixon. “Calculating scattering amplitudes efficiently.” In: *Theoretical Advanced Study Institute in Elementary Particle Physics (TASI 95): QCD and Beyond*. Jan. 1996, pp. 539–584. arXiv: [hep-ph/9601359](https://arxiv.org/abs/hep-ph/9601359).
- [168] Michał Czakon. “DiaGen/IdSolver.” In: (). unpublished.
- [169] J. A. M. Vermaasen. “New features of FORM.” In: (Oct. 2000). arXiv: [math-ph/0010025](https://arxiv.org/abs/math-ph/0010025).

- [170] Ben Ruijl, Takahiro Ueda, and Jos Vermaseren. “FORM version 4.2.” In: (July 2017). arXiv: [1707.06453 \[hep-ph\]](#).
- [171] S. Laporta. “High-precision calculation of multiloop Feynman integrals by difference equations.” In: *Int. J. Mod. Phys. A* 15 (2000), pp. 5087–5159. DOI: [10.1142/S0217751X00002159](#). arXiv: [hep-ph/0102033](#).
- [172] Philipp Maierhöfer, Johann Usovitsch, and Peter Uwer. “Kira—A Feynman integral reduction program.” In: *Comput. Phys. Commun.* 230 (2018), pp. 99–112. DOI: [10.1016/j.cpc.2018.04.012](#). arXiv: [1705.05610 \[hep-ph\]](#).
- [173] Philipp Maierhöfer and Johann Usovitsch. “Kira 1.2 Release Notes.” In: (Dec. 2018). arXiv: [1812.01491 \[hep-ph\]](#).
- [174] Jonas Klappert et al. “Integral reduction with Kira 2.0 and finite field methods.” In: *Comput. Phys. Commun.* 266 (2021), p. 108024. DOI: [10.1016/j.cpc.2021.108024](#). arXiv: [2008.06494 \[hep-ph\]](#).
- [175] U. Baur and E. W. Nigel Glover. “Higgs Boson Production at Large Transverse Momentum in Hadronic Collisions.” In: *Nucl. Phys. B* 339 (1990), pp. 38–66. DOI: [10.1016/0550-3213\(90\)90532-I](#).
- [176] Michał Czakon et al. “The $(Q_7, Q_{1,2})$ contribution to $\overline{B} \rightarrow X_s \gamma$ at $\mathcal{O}(\alpha_s^2)$.” In: *JHEP* 04 (2015), p. 168. DOI: [10.1007/JHEP04\(2015\)168](#). arXiv: [1503.01791 \[hep-ph\]](#).
- [177] Vladimir A. Smirnov. “Applied asymptotic expansions in momenta and masses.” In: *Springer Tracts Mod. Phys.* 177 (2002), pp. 1–262.
- [178] Marco Niggetiedt. “Quark mass effects in form factors and hadronic Higgs production.” PhD thesis. RWTH Aachen University, RWTH Aachen U., 2023. DOI: [10.18154/RWTH-2023-11198](#).
- [179] Simone Marzani et al. “Higgs production via gluon-gluon fusion with finite top mass beyond next-to-leading order.” In: *Nucl. Phys. B* 800 (2008), pp. 127–145. DOI: [10.1016/j.nuclphysb.2008.03.016](#). arXiv: [0801.2544 \[hep-ph\]](#).
- [180] Marco Niggetiedt and Johann Usovitsch. “The Higgs-gluon form factor at three loops in QCD with three mass scales.” In: *JHEP* 02 (2024), p. 087. DOI: [10.1007/JHEP02\(2024\)087](#). arXiv: [2312.05297 \[hep-ph\]](#).
- [181] M. Beneke and Vladimir A. Smirnov. “Asymptotic expansion of Feynman integrals near threshold.” In: *Nucl. Phys. B* 522 (1998), pp. 321–344. DOI: [10.1016/S0550-3213\(98\)00138-2](#). arXiv: [hep-ph/9711391](#).
- [182] Stefan Dittmaier, Michael Krämer, and Michael Spira. “Higgs radiation off bottom quarks at the Tevatron and the CERN LHC.” In: *Phys. Rev. D* 70 (2004), p. 074010. DOI: [10.1103/PhysRevD.70.074010](#). arXiv: [hep-ph/0309204](#).
- [183] Barbara Schmidt and Matthias Steinhauser. “CRunDec: a C++ package for running and decoupling of the strong coupling and quark masses.” In: *Comput. Phys. Commun.* 183 (2012), pp. 1845–1848. DOI: [10.1016/j.cpc.2012.03.023](#). arXiv: [1201.6149 \[hep-ph\]](#).
- [184] K. G. Chetyrkin, Johann H. Kuhn, and M. Steinhauser. “RunDec: A Mathematica package for running and decoupling of the strong coupling and quark masses.” In: *Comput. Phys. Commun.* 133 (2000), pp. 43–65. DOI: [10.1016/S0010-4655\(00\)00155-7](#). arXiv: [hep-ph/0004189](#).
- [185] R. L. Workman et al. “Review of Particle Physics.” In: *PTEP* 2022 (2022), p. 083C01. DOI: [10.1093/ptep/ptac097](#).

- [186] R. Tarrach. “The Pole Mass in Perturbative QCD.” In: *Nucl. Phys. B* 183 (1981), pp. 384–396. DOI: [10.1016/0550-3213\(81\)90140-1](https://doi.org/10.1016/0550-3213(81)90140-1).
- [187] N. Gray et al. “Three Loop Relation of Quark (Modified) Ms and Pole Masses.” In: *Z. Phys. C* 48 (1990), pp. 673–680. DOI: [10.1007/BF01614703](https://doi.org/10.1007/BF01614703).
- [188] M. Beneke and Vladimir M. Braun. “Heavy quark effective theory beyond perturbation theory: Renormalons, the pole mass and the residual mass term.” In: *Nucl. Phys. B* 426 (1994), pp. 301–343. DOI: [10.1016/0550-3213\(94\)90314-X](https://doi.org/10.1016/0550-3213(94)90314-X). arXiv: [hep-ph/9402364](https://arxiv.org/abs/hep-ph/9402364).
- [189] Ikaros I. Y. Bigi et al. “The Pole mass of the heavy quark. Perturbation theory and beyond.” In: *Phys. Rev. D* 50 (1994), pp. 2234–2246. DOI: [10.1103/PhysRevD.50.2234](https://doi.org/10.1103/PhysRevD.50.2234). arXiv: [hep-ph/9402360](https://arxiv.org/abs/hep-ph/9402360).
- [190] Ikaros I. Y. Bigi and N. G. Uraltsev. “Anathematizing the Guralnik-Manohar bound for anti-Lambda.” In: *Phys. Lett. B* 321 (1994), pp. 412–416. DOI: [10.1016/0370-2693\(94\)90268-2](https://doi.org/10.1016/0370-2693(94)90268-2). arXiv: [hep-ph/9311337](https://arxiv.org/abs/hep-ph/9311337).
- [191] Anna Kulesza and W. James Stirling. “Nonperturbative effects and the resummed Higgs transverse momentum distribution at the LHC.” In: *JHEP* 12 (2003), p. 056. DOI: [10.1088/1126-6708/2003/12/056](https://doi.org/10.1088/1126-6708/2003/12/056). arXiv: [hep-ph/0307208](https://arxiv.org/abs/hep-ph/0307208).
- [192] Matthew A. Lim and Rene Poncelet. “Robust estimates of theoretical uncertainties at fixed-order in perturbation theory.” In: (Dec. 2024). arXiv: [2412.14910 \[hep-ph\]](https://arxiv.org/abs/2412.14910).
- [193] Cappati et al. “ggF Status Report.” In: The 21st Workshop of the LHC Higgs Working Group. URL: <https://indico.cern.ch/event/1389221/contributions/6185912/attachments/2979973/5249263/241204-ggFWG1Update-3.pdf>. 2024.
- [194] R. L. Workman et al. “Review of Particle Physics.” In: *PTEP* 2022 (2022), p. 083C01. DOI: [10.1093/ptep/ptac097](https://doi.org/10.1093/ptep/ptac097).
- [195] Alexander Huss et al. “Les Houches 2023 – Physics at TeV Colliders: Report on the Standard Model Precision Wishlist.” In: (Apr. 2025). arXiv: [2504.06689 \[hep-ph\]](https://arxiv.org/abs/2504.06689).
- [196] Xiang Chen, Xin Guan, and Bernhard Mistlberger. “Three-Loop QCD corrections to the production of a Higgs boson and a Jet.” In: (Apr. 2025). arXiv: [2504.06490 \[hep-ph\]](https://arxiv.org/abs/2504.06490).
- [197] Bernhard Mistlberger and Adi Suresh. *RVV \times V: Interference contributions to inclusive Higgs boson and Drell-Yan production at N^4LO in QCD*. 2025. arXiv: [2504.10574 \[hep-ph\]](https://arxiv.org/abs/2504.10574). URL: <https://arxiv.org/abs/2504.10574>.

EIDESSTATTLICHE VERSICHERUNG

Ich, Tom Schellenberger, erkläre hiermit, dass diese Dissertation und die darin dargelegten Inhalte die eigenen sind und selbstständig, als Ergebnis der eigenen originären Forschung, generiert wurden.

Hiermit erkläre ich an Eides statt

1. Diese Arbeit wurde vollständig oder größtenteils in der Phase als Doktorand dieser Fakultät und Universität angefertigt;
2. Sofern irgendein Bestandteil dieser Dissertation zuvor für einen akademischen Abschluss oder eine andere Qualifikation an dieser oder einer anderen Institution verwendet wurde, wurde dies klar angezeigt;
3. Wenn immer andere eigene- oder Veröffentlichungen Dritter herangezogen wurden, wurden diese klar benannt;
4. Wenn aus anderen eigenen- oder Veröffentlichungen Dritter zitiert wurde, wurde stets die Quelle hierfür angegeben. Diese Dissertation ist vollständig meine eigene Arbeit, mit der Ausnahme solcher Zitate;
5. Alle wesentlichen Quellen von Unterstützung wurden benannt;
6. Wenn immer ein Teil dieser Dissertation auf der Zusammenarbeit mit anderen basiert, wurde von mir klar gekennzeichnet, was von anderen und was von mir selbst erarbeitet wurde;
7. Ein Teil oder Teile dieser Arbeit wurden zuvor veröffentlicht und zwar in:
 - [3] Michał Czakon u. a. “Top-Bottom Interference Contribution to Fully Inclusive Higgs Production”. In: *Phys. Rev. Lett.* 132.21 (2024), S. 211902. DOI: [10.1103/PhysRevLett.132.211902](https://doi.org/10.1103/PhysRevLett.132.211902). arXiv: [2312.09896 \[hep-ph\]](https://arxiv.org/abs/2312.09896)
 - [4] Michał Czakon u. a. “Quark mass effects in Higgs production”. In: *JHEP* 10 (2024), S. 210. DOI: [10.1007/JHEP10\(2024\)210](https://doi.org/10.1007/JHEP10(2024)210). arXiv: [2407.12413 \[hep-ph\]](https://arxiv.org/abs/2407.12413)

Aachen, den 1. Juli 2025

Tom Claus Rudolf
Schellenberger